Transient Models to Assess Transmission and Control of Airborne Infection Risks in a Respiratory Ward

ALEXANDER JON EDWARDS

SUBMITTED IN ACCORDANCE WITH THE REQUIREMENTS FOR THE DEGREE OF
DOCTOR OF PHILOSOPHY

THE UNIVERSITY OF LEEDS

EPSRC CENTRE FOR DOCTORAL TRAINING IN FLUID DYNAMICS

SEPTEMBER 2024

Publication Statement

The candidate, Alexander Jon Edwards, confirms that the work submitted is their own, except where work which has formed part of jointly authored publications has been included. The contribution of the candidate and the other authors to this work has been explicitly indicated below. The candidate confirms that appropriate credit has been given within the thesis where reference has been made to the work of others.

Chapter 2 contains material from the jointly authored publication:

> **Edwards AJ**, King M-F, Noakes CJ, Peckham D, López-García M. The Wells-Riley model revisited: randomness, heterogeneity, and transient behaviours. *Risk Analysis*, 2024, Volume 44, pp.2125-2147.
> `https://doi.org/10.1111/risa.14295`

Alexander Jon Edwards contributed the methodology, code, results, formal analysis, and writing of the manuscript. The Co-Authors of this manuscript provided guidance and supervision, and review and editing of the manuscript. The code and data for this manuscript are available at `https://github.com/scaje/stochastic_WR_paper_AJE.git`.

Chapter 3 contains material from the jointly authored publication:

> **Edwards AJ**, Benson L, Guo Z, López-García M, Noakes CJ, Peckham D, King MF, A mathematical model for assessing transient airborne infection risks in a multi-zone hospital ward, *Building and Environment*, 2023, Volume 238, p.110344.
> `https://doi.org/10.1016/j.buildenv.2023.110344.`

Alexander Jon Edwards contributed the methodology, code, model development, results, formal analysis, and writing of the manuscript. The Co-Authors of this manuscript provided guidance and supervision, and review and editing of the manuscript. The code and data for this manuscript are available at `https://github.com/scaje/Multi-zone_Hospital_conc_AJE.git`.

Chapter 4 contains material from the jointly authored publication:

> **Edwards, AJ**, King, MF, López-García, M, Peckham, D and Noakes, CJ, Assessing the effects of transient weather conditions on airborne transmission risk in naturally ventilated hospitals. *Journal of Hospital Infection*, 2024, Volume 148, pp.1-10.
> `https://doi.org/10.1016/j.jhin.2024.02.017`

Alexander Jon Edwards contributed the methodology, code, model development, results, formal analysis, and writing of the manuscript. The Co-Authors of this manuscript provided guidance and supervision, and review and editing of the manuscript. The code and data for this manuscript are available at `https://github.com/scaje/Contam_study_AJE`.

Acknowledgements

I would like to express my sincerest gratitude to my supervisors, Professor Catherine Noakes, Dr Martín López-García, Professor Daniel Peckham, and Dr Marco-Felipe King. Their continued support, invaluable guidance and breadth of experience has enriched my learning and understanding, facilitating my PhD journey. Their encouragement, enthusiasm, and mentoring has shaped me into the researcher I am today. Thank you for helping to make my project so enjoyable and rewarding, it has been a fantastic experience and a great privilege to work with you all.

Mum, I am eternally grateful for your unconditional love and unwavering support. Your constancy has given me the strength and freedom to focus solely on my PhD journey and take every opportunity given. I cannot thank you enough for all that you do. Dad, thank you for always being there. Your words of encouragement and guidance have helped me to stay on track throughout, and your phone calls have provided a much needed break from PhD work. Katie, the first Dr Edwards in the family, I think it is safe to say that I could not have done this without you. Your counsel has guided me throughout my PhD, and earned you an unofficial, but deserved role of external supervisor. I feel privileged to have shared this important life journey with you. Molly, thank you for joining me on this journey. I am lucky to have had your full commitment, patience and support to guide me throughout. Yatin, thank you for persuading me to carry on. This journey would not have been the same without you.

Thank you to the EPSRC Centre for Doctoral Training in Fluid Dynamics for funding my studies and giving me the opportunity to have many invaluable experiences. I would also like to acknowledge the support of the Leeds Teaching Hospitals NHS Trust.

Finally, Grandad, I would like to dedicate this thesis to you. A childhood enriched with your engineering knowledge and breadth of life experience has long fueled my drive for learning and problem solving. Although you are not here to see me finish this journey, I would not be the person I am today without you, and so this is for you.

Abstract

Modelling airborne transmission and associated infection risk to susceptible occupants in indoor environments is important for improving preparedness of emerging pathogens and future pandemics. This is especially the case in hospitals, notably respiratory wards in the United Kingdom (UK), where patients are particularly vulnerable to new infections. To date, many quantitative tools used to assess airborne infection risk are limited to very simplified scenarios that fail to capture common features of real life. This thesis aims to use airflow and airborne transmission models to better understand transient and multi-zone infection risks in indoor environments. Chapter 2 introduces novel mathematical formalisms, providing extensions to the existing Wells-Riley framework, a ubiquitous tool for assessing airborne infection risks. Results show the non-negligible infection risk to a susceptible individual who remains in the space after the infector leaves and highlight the importance of incorporating stochasticity. In Chapters 3 and 4, an adapted Wells-Riley model underpins a new transient multi-zone transmission model that simulates concentration of pathogen in the air, coupled with a compartmental epidemic model. This is applied to a naturally ventilated UK respiratory ward, where results from an airflow simulation are incorporated, better representing the space. The impact of transient occupancy, weather conditions and ventilation are illustrated. Chapter 5 extends this further by using a Monte Carlo simulation, enabling a random choice of outbreak parameters. A random day is chosen for the outbreak, influencing airflow, weather conditions and ventilation, alongside a random infectiousness of the infector, representing population heterogeneity. The findings presented in this thesis demonstrate the importance of considering transient effects, modelling multi-zone environments, and including stochasticity to capture outbreak-defining features that have previously been overlooked. Through exploration of specific scenarios, results highlight the likely impact of occupant behaviour, infectiousness, ventilation, weather conditions, and airflow on airborne transmission and consequent infection risk.

Contents

List of Figures

List of Tables

Nomenclature

ACH	Air Changes per Hour
AGP	Aerosol Generating Procedure
CFD	Computational Fluid Dynamics
CF	Cystic Fibrosis
CO_2	Carbon Dioxide
COVID-19	Coronavirus Disease 2019
HBN04-01	Health Building Note 04-01
HCAI	Healthcare Associated Infection
HCW	Healthcare Worker
HTM03-01	Health Technical Memorandum 03-01
IRP	Infectious Respiratory Particle
NHS	National Health Service
ODE	Ordinary Differential Equation
PPE	Personal Protective Equipment
ppm	Parts Per Million
QMRA	Quantitative Microbial Risk Assessment
RH	Relative Humidity

RI	Risk Index
SARS-CoV-2	Severe Acute Respiratory Syndrome Coronavirus-2
SARS	Sever Acute Respiratory Syndrome
SD	Standard Deviation
SEIR	Susceptible-Exposed-Infected-Recovered
SE	Susceptible-Exposed
SFIF	Spatial Flow Impact Factor
SIR	Susceptible-Infected-Recovered
SIS	Susceptible-Infected-Susceptible
SI	Susceptible-Infected
TB	*Mycobacterium tuberculosis*
TWF/TO	Two-way Flow/Two-opening
UK	United Kingdom
UVGI	Ultraviolet Germicidal Irradiation
WPC	Wind Pressure Coefficients

Chapter 1

Introduction

1.1 Background

The transmission of infectious pathogens has long played an important role in the health and well-being of humankind, with historical pandemics including the plague, cholera and Spanish flu (Piret and Boivin [2021]). There is an increasing likelihood of a pandemic occurring, influenced by many factors such as global connectivity, climate change, increased animal-to-human contact, and antimicrobial resistance (Sampath et al. [2021]). The recent Coronavirus Disease 2019 (COVID-19) pandemic has renewed the focus of emerging infectious diseases, with COVID-19 being the leading cause of death in the United Kingdom (UK) in 2020 and 2021 (Office for National Statistics (ONS) [2023]).

There are many modes of transmission for infectious pathogens including airborne, foodborne, waterborne, vector-borne (e.g., mosquitos), bloodborne, and sexually transmitted (World Health Organization [2012], UK Health Security Agency [2023]). In particular, airborne transmission is a common infection route for many respiratory infections, where an infectious pathogen is contained within small respiratory aerosols, typically around $5\,\mu\text{m} - 10\,\mu\text{m}$ or less in diameter (Bourouiba [2020]), that are produced during expiratory activities (Wang et al. [2021]). These aerosols are carried through the air and can be inhaled by an individual with the possibility of causing an infection. Other possible transmission routes for respiratory pathogens include fomite transmission (e.g., touching a contaminated surface and then transferring this to the facial mucosa i.e., mouth, nose and eyes) and droplet transmission (e.g., larger respiratory droplets that deposit on facial mucosa) (Li [2021]). Respiratory disease is one of the world's largest causes of morbidity and mortality (World Health Organization [2020]), with communicable diseases such as influenza, COVID-19, *Mycobacterium tuberculosis* (TB) and measles all being airborne (Wang et al. [2021]).

Airborne pathogens causing lower respiratory infections are of significance to many healthcare settings, particularly UK respiratory wards, where patients are already vulnerable to new infections and respiratory disease is a major contributor to pressure on the UK National Health Service (NHS) (NHS [2022]). In addition, healthcare-associated infections (HCAIs), defined as infections occurring in a healthcare setting that were not present prior to a patient entering that care setting, are estimated to have cost the NHS £2.1 billion in 2016/2017 from an estimation of $653,000$ HCAIs, with 22.8% causing respiratory infections (Guest et al. [2020]). Further, there is evidence to suggest that common bacterial pathogens causing HCAIs can be transmitted through the air such as *Staphylococcus aureus* (Kozajda et al. [2019]) and *Clostridium difficile* (Best et al. [2010]). In these cases, the transmission route is likely due to airborne dispersion, resulting in deposition onto surfaces and subsequent fomite transmission (King et al. [2015]).

On 18th April 2024, the World Health Organization published a technical report (World Health Organization [2024]) updating the terminology used for airborne transmission and particles containing infectious pathogens that travel in the air. The term "Infectious Particles" is introduced to represent particles containing the pathogen, along with water and other respiratory secretions. Once these particles are exhaled by an infectious person, they are then known as "Infectious Respiratory Particles (IRPs)". This replaces the terms "aerosol" and "droplet", where IRPs exist on a continuous size spectrum with no single cut off point distinguishing between larger and smaller particles. The report also defines "direct deposition" as IRPs that follow a short-range semi-ballistic trajectory before depositing on facial mucosa. The term "transmission through the air" now represents the transmission of IRPs through the air for both airborne transmission/inhalation or direct deposition over both long and short ranges and a range of particle sizes. However, the majority of this thesis was written before the publication of this technical report (World Health Organization [2024]), and thus for consistency, this thesis considers airborne transmission as the transmission of small respiratory aerosols only, as defined earlier.

The control of airborne transmission is impacted by the use of mitigation strategies such as ventilation and air cleaning, personal protective equipment (PPE), social distancing and vaccinations (Bueno de Mesquita et al. [2022]). Ventilation has previously been identified as playing an important role in airborne transmission (Li et al. [2007]). However, the ventilation guidance for general ward spaces in NHS hospitals is limited (Beggs et al. [2008]), and given that the NHS expresses a preference for the use of natural ventilation (NHS England [2021]), the consistent attainment of guideline ventilation rates is more difficult.

The successful implementation and assessment of mitigation strategies requires quantification of airborne transmission and an increased understanding of the factors that affect it. The COVID-19 pandemic highlighted the need for the development of modelling tools that can assess airborne infection risk as both a predictive (i.e., for future pandemics) and retrospective (i.e., for previous outbreaks) tool (Buonanno et al. [2020a]) to improve future preparedness against emerging outbreaks. This thesis aims to explore existing modelling tools and develop new methodology to improve the assessment of airborne transmission and the quantification of the associated infection risk. The aims and objectives of this thesis can be found in Section 1.8.

1.2 Airborne Disease Transmission

Understanding the fundamentals of airborne transmission is crucial to assess infection risk in different environments, as well as developing and implementing effective mitigation strategies. Airborne transmission is a common transmission route for many pathogens including Severe Acute Respiratory Syndrome Coronavirus-2 (SARS-CoV-2), measles virus, Severe Acute Respiratory Syndrome (SARS), influenza virus and TB (Wang et al. [2021]). Respiratory aerosols containing infectious material dry and stay suspended in the air, relying on buoyancy to drive their dynamics (Wells [1934]). There is a suggestion that the diameter size cut-off for aerosols should be 100 µm, with particles of diameter $10 - 100$ µm also capable of remaining airborne dependent on the ambient conditions, whereas particles with diameter > 100 µm typically fall to the ground relatively quickly (Prather et al. [2020]). It is possible for aerosols to become entrained within the ambient flow or ventilation systems and then transported throughout a room or to other connected spaces within the indoor environment (Bourouiba [2021]), facilitating long-range transmission. However, short-range transmission can still pose the highest risk, with close range infection occurring in a relatively short time (as little as 15 min for COVID-19) (Pringle et al. [2020]). Further, aerosols emitted in coughs and sneezes can rapidly travel as far as $7 - 8$ m (Fennelly [2020]), with this suspension due to entrainment within a turbulent gas cloud that is produced when breathing (Bourouiba

[2020]).

Air sampling is a technique used to detect pathogens in the air, explore how pathogens are dispersed in the air, and quantify the concentration (Tang et al. [2015]). This is important to develop a better understanding of pathogens that transmit through the air, especially as the COVID-19 pandemic highlighted that traditional distinctions between “droplet” and “aerosol” transmission has led to diseases being wrongly classified, with airborne transmission often being overlooked as a possible infection route for pathogens (Wang et al. [2021]). Whilst air samples can provide evidence of the presence of pathogens, it is cumbersome and time consuming to carry out, and it only provides a point sample which is significantly affected by ventilation, environmental conditions, occupancy and activity (Hathway et al. [2013], Hiwar et al. [2021b]). Without understanding of the airflow and occupancy, it is difficult to relate sampled concentrations to transmission risk.

The transmissibility of an infection can also be assessed by analysing the reproductive number, R_0, which gives an estimate of the expected number of secondary cases of the disease that occur due to one initial index case (the first identified infectious individual in a fully susceptible population) (Tang et al. [2015]). When $R_0 > 1$, this indicates that the number of cases grow exponentially and lead to an outbreak, however, when $R_0 < 1$ the outbreak dies out. Although most studies consider R_0 at a population scale, the concept can be used in local scale studies to consider the impact of measures such as ventilation (e.g., Noakes et al. [2006b])

1.2.1 Respiratory Emissions

The infectiousness of a given pathogen is another important factor that can vary from pathogen to pathogen. Where limited data exists, the infectious emission rate of a pathogen can be estimated using predictive methods along with comparisons to other airborne infections (Mikszewski et al. [2021]). The infectiousness of an individual can vary (Lloyd-Smith et al. [2005]), with large ranges between viral emission rates. Heterogeneity within the population can affect outbreak-defining factors such as herd immunity, emphasising its importance in epidemic models (Britton et al. [2020]). The infectiousness of virus-laden droplets may decay over time (Jayaweera et al. [2020]), with more recent studies showing the effects of relative humidity (RH), pH levels and ambient levels of Carbon Dioxide (CO_2) on the infectiousness and aerostability of airborne particles (Oswin et al. [2022], Haddrell et al. [2023, 2024]).

The emission rate of contagious individuals can be estimated based on the viral load in sputum from the mouth, the type of respiratory activity (e.g., breathing, speaking), respiratory physiological parameters (e.g., inhalation rate), and activity level (e.g., resting, standing, light exercise) (Buonanno et al. [2020b]). Other measurements such as source strength and indoor air characteristics can be used, as done by Bueno de Mesquita et al. [2020] using data from a human challenge study for influenza. Milton et al. [2013] measure influenza virus aerosols in exhaled breath, investigating larger aerosols ($> 5\,\mu\mathrm{m}$) and smaller aerosols ($< 5\,\mu\mathrm{m}$), generated by coughing and during normal breathing. The study found that smaller aerosols contained 8.8 times more viral copies than the larger aerosols. More recently, the same approach has been applied to SARS-CoV-2, again finding that smaller aerosols have a similar or higher level of viral copies compared to larger aerosols (Adenaiye et al. [2022]). This was also explored for different types of expiratory activities for SAR-CoV-2; breathing, talking and singing (Coleman et al. [2022]). Viruses may be transmitted by somebody quietly breathing through their nose, as well as by visibly coughing or talking (Stelzer-Braid et al. [2009]), with normal breathing sufficient to exhale enough infectious aerosols to cause an infection in another individual (Scheuch [2020]). Williams et al. [2020] measure exhaled levels of TB from patients with confirmed pulmonary tuberculosis using sampling from a face mask over a 24 h period, including sampling whilst the participant was sleeping, and no correlation was found with cough frequency, radiological characteristics, nor bacillary content of the sputum. Mitigation strategies such as face coverings (Verma et al. [2020]) could be useful in helping to prevent transmission of this kind, with previous studies showing the effectiveness of face masks in reducing emissions (Adenaiye et al. [2022], Lai et al. [2024]).

The variation between the diameters of aerosols produced by different activities such as talking, singing, coughing and normal breathing can be explored experimentally (Morawska et al. [2009]). This shows that depending on the activity and where within the respiratory tract the aerosol originated, the exhaled aerosols possess differing properties including size and infectiousness (Tung and Hu [2008]). These factors do not only affect the fluid mechanical properties of the aerosol itself, but the dynamics through the air and consequently, the associated risk of infection. The size of the particle can also affect the final destination. Foat et al. [2022] use computational fluid dynamics (CFD) investigations to explore evaporation effects on various droplet sizes and the deposition onto nearby surfaces. Hiwar et al. [2021a] develop an experimental tool, specifically designed for sampling deposited particles located close to a source.

Not only do the properties of aerosols vary due to the location of their production, but also depend on finer details of their host. For example, it is found that children generally produce fewer virus-laden aerosols than adults because their lungs are still developing and have fewer bronchioles and alveoli in which aerosols can form (Tung and Hu [2008]). This variation could also occur with respiratory diseases such as Cystic Fibrosis (CF). Patients with CF often have thicker mucus, higher sputum rates and weaker bronchioles and alveoli, and all of these factors can consequently affect the properties of the aerosols produced by these individuals (Sturm [2011]).

1.2.2 Non-respiratory Sources

When considering different types of diseases, it is often useful to highlight how these diseases transmit. Three different characterisations of airborne diseases are introduced: obligate, preferential, and opportunistic (Seto [2015]). Obligate diseases are solely airborne, and diseases which are characterised as preferential are those that are efficiently transmitted through the air but other routes are common (Seto [2015]). Finally, opportunistic diseases are mainly spread by alternative routes but can be aerosolised and transmitted under certain circumstances such as during aerosol generating procedures (AGPs). Examples of AGPs include intubation, tracheotomy and bronchoscopy (NHS [2021]). Initial ideas about re-aerosolisiation or aerosol generation were introduced by Wells [1934], who talks of aerosols re-entering the air when larger droplets settle, evaporate, and are lifted back into the air.

There are many different AGPs that can pose an increased risk to heathcare workers (HCWs) (Thompson et al. [2013]). However, it is important to understand how the risk from AGPs compares with everyday human activities such as coughing or sneezing. For example, transmission patterns of an outbreak of SARS in a major teaching hospital in Hong Kong indicated that one of the cases was originally believed to have been transmitted via a nebulizer procedure. However, it was later concluded that the transmission took place before the nebulizer was turned on (Wong et al. [2004]). Shrimpton et al. [2022] use particle sampling during upper airway suction, an AGP, to find that this did not increase aerosol concentration, and showed a much lower aerosol concentration when compared with coughing. Normal respiratory activities such as breathing and coughing, in many cases, can produce the same if not more aerosols than so-called AGPs (Hamilton et al. [2021]), with an absence of evidence to suggest that medical AGPs are associated with an increased risk of transmission of respiratory viruses beyond standard patient interactions (Wilson et al. [2021c]).

Pathogens which may not be naturally airborne but rather opportunistically airborne, such as *Clostridium difficile*, can become aerosolised after flushing a toilet, with lidless toilets increasing the risk of contamination in the surrounding environment (Best et al. [2012]). This opportunistic behaviour is further highlighted with examples of mycobacteria being aerosolised and transmitted in different locations such as hot tubs or swimming pools (Falkinham III [2003]).

1.3 Mathematical Models of Airborne Transmission

1.3.1 Single-Zone Models

A wide range of mathematical techniques are used to assess exposure to pathogens and subsequent infection risk, and this is often referred to as Quantitative Microbial Risk Assessment (QMRA). QMRA has many different approaches, common uses, and limitations (Haas [2020]). There are a variety of applicable scenarios for QMRA modelling and this is demonstrated in applications to foodborne pathogens (Pérez-Rodríguez et al. [2008], Pang et al. [2017], Ryan et al. [2018]), waterborne pathogens (Soller et al. [2010], De Man et al. [2014], Ramírez-Castillo et al. [2015]), and airborne pathogens, with more recent work focusing on the transmission of COVID-19 (Zhang et al. [2020], Buonanno et al. [2020a], Kitajima et al. [2020], Wilson et al. [2021b], Miller et al. [2022], Bate et al. [2024]).

The most common QMRA approach to airborne disease transmission is the Wells-Riley model (Wells et al. [1955], Riley et al. [1978]) giving an assessment of the probability of infection. The Wells-Riley equation is shown below:

$$E(t) = S_0(1 - e^{\frac{-I_0 pqt}{Q}}) \tag{1.1}$$

where $E(t)$ is the number of new infections or exposures, S_0 is the initial number of susceptible individuals, I_0 is the initial number of infected individuals, p [m^3 min^{-1}] is the pulmonary rate of individuals, q [quanta min^{-1}] is the infectious quanta production rate, and Q [m^3 min^{-1}] is the extract ventilation rate. The quanta production rate shown in the above equation is the rate at which an infected individual produces a quantum. A quantum is defined as the minimum number of infectious airborne particles required to infect an individual with probability $1 - e^{-1}$ (≈ 0.632) and may consist of one or more airborne particles (Sze To and Chao [2010]). The limitations of the Wells-Riley model, assuming well-mixed air and a steady-state concentration of pathogen within a space are tackled through various adaptations throughout the literature, some more successfully than others, presenting a need for these assumptions to be overcome (Zemouri et al. [2020]). However, a large number of studies still use the Wells-Riley model in the original form (Pavilonis et al. [2021], Zhao et al. [2022], Rowe et al. [2022]). For example, the Wells-Riley model was used to assess the probability of infection in a TB outbreak for different scenarios when varying cell occupancy, lock-up time and ventilation in a South African prison (Robertson et al. [2011]), showing that increased ventilation rates, and reduced occupancy and lock-up times are likely to reduce the probability of infection.

Whilst the Wells-Riley model is typically used for short-term interactions (and thus, with a Susceptible-Exposed (SE) model as in Chapter 2), it can be linked to more complex compartmental models to represent longer timescales. The Susceptible-Infected-Recovered (SIR) model,

$$\begin{aligned} \frac{dS(t)}{dt} &= -\psi S(t)I(t) \ , \\ \frac{dI(t)}{dt} &= \psi S(t)I(t) - \alpha I(t) \ , \\ \frac{dR(t)}{dt} &= \alpha I(t) \end{aligned}$$

originally introduced by Kermack and McKendrick [1927] is extended with a coupling to a Wells-Riley approach by Noakes et al. [2006b]. Here, $S(t)$, $I(t)$ and $R(t)$ represent the susceptible, infected and recovered individuals, respectively, ψ is the infection rate and α is the recovery rate. Other extensions include to a Susceptible-Exposed-Infected-Recovered (SEIR) model, where E represents exposed individuals, accounting for the latent period of an infectious disease (Noakes et al. [2006b], Chen and Liao [2008]).

An adapted Wells-Riley model is used to analyse a nosocomial outbreak of SARS in Hong Kong (Qian et al. [2009]). The adapted model aims to consider the variation in spatial concentration, building on previous work (Qian et al. [2007]) with an additional ordinary differential equation (ODE) characterising concentration with time. This adaptation allows for the mathematical model to be coupled with a CFD model to analyse the distribution and deposition of particles and visualise the variation in spatial risk. A CFD coupling with the Wells-Riley model is also explored in other work such as investigating COVID-19 transmission on long-distance trains in China (Wang et al. [2022]) or using CFD models to explore airflow patterns before using the Wells-Riley model to assess infection risk for diseases with a range of infectiousness (e.g., measles, influenza, and rhinovirus) (Tung and Hu [2008]).

There are many other adaptations of the Wells-Riley model such as using CO_2 as a proxy for exhaled breath that may contain infectious pathogens. Rudnick and Milton [2003] make adaptations where CO_2 is used as a marker for exhaled breath and ventilation effectiveness, with the re-breathed fraction used within the Wells-Riley model instead of the ventilation rate. This allows the model to be applied to settings where CO_2 has been measured, but ventilation rates are unknown. This model is also considered in Tung and Hu [2008] and Issarow et al. [2015], with other work building on this by using measured viral shedding and CO_2 data from a human challenge study (Bueno de Mesquita et al. [2020]), and including consideration of the infectious quanta dynamics in addition to the concentration based on exhaled CO_2 in a school, office and commercial setting (Cammarata and Cammarata [2021]). A more generalised version of Rudnick and Milton [2003], considering varying occupancy levels is presented by Burridge et al. [2022] in an application to an office scenario. A further study considers an application to schools and shows the likelihood of seasonal differences in infection risks due to lower ventilation rates in winter (Vouriot et al. [2021]).

Similar adaptations extend the Wells-Riley model by replacing the quanta parameter with a solution for the concentration of airborne pathogen in the space, and is demonstrated with assessments of risk in a single room (Boonmeemapasuk and Pochai [2022], Timpitak and Pochai [2022]) and with assessments of COVID-19 infection risk across fitness centres in Florida (Li et al. [2021a]), in a university campus in China (Li et al. [2021b]), and in a dining setting (Ding et al. [2022]). In an attempt to obtain the spatial distribution of the probability of infection, a spatial flow impact factor (SFIF) method is coupled with the Wells-Riley model (Guo et al. [2021]), and an advection–diffusion–reaction relationship is used to consider spatio-temporal infection risk through comparisons with real-life case studies, and a hypothetical study in a classroom (Lau et al. [2022]). Other methods include using a source-sink model within the Wells-Riley model exploring case studies in a restaurant and ballroom (Zhai and Li [2021]), and a dilution-based method, which does not come directly from the traditional Wells-Riley model, but the concentration of quanta, inhalation rate and a Poisson distribution to give an assessment of infection risk (Zhang and Lin [2021]). Pantelic and Tham [2012] use an adapted Wells-Riley model to incorporate results from an experimental study of an open plan office, where they assessed the effects of ventilation rates, infectiousness of the index case, and various exposure times.

Mitigation strategies are an important aspect of assessing an outbreak and infection risk, and the Wells-Riley model can be adapted to account for this, such as incorporating social distancing and ventilation as controls for transmission during the COVID-19 pandemic (Sun and Zhai [2020]), protection provided by face coverings (Zemouri et al. [2020]), mask effectiveness to assess infection risk and received dose from a TB infection (Nicas [1996], Fennelly and Nardell [1998], Nazaroff et al. [1998]), and more recently assessing COVID-19 infection risk (Dai and Zhao [2020], Fantozzi et al. [2022]). Other adaptations include the effects of particle filtration and air cleaning on infection risk (Nazaroff et al. [1998], Fisk et al. [2004]), and the deposition of infectious airborne particles (Fisk et al. [2004], Franchimon et al. [2008]).

In the work of Gammaitoni and Nucci [1997], a variation of the Wells-Riley model is presented and applied to an infection risk model of a TB outbreak, with their model allowing for varying quanta levels over time with a conservation equation, bringing their methodology closer to a dose-response type model, another QMRA technique. Dose-response models such as the one presented by Gammaitoni and Nucci [1997] have been commonly used in the literature such as to assess the risk of infection of TB, influenza and measles in healthcare waiting rooms (Beggs et al. [2010]), infection risk of influenza, TB, and rhinovirus within three different environments at a teaching hospital (Knibbs et al. [2012]), exploring the effects of ventilation on disease transmission in clinical rooms (King et al. [2021a]), and in the development of a stochastic web-based application that evaluates COVID-19 infection risk across specific settings (a classroom, a wedding venue, and a high intensity exercise class) (Rocha-Melogno et al. [2021]). Wood et al. [2023] explore a coupling of the quanta conservation equation with an SEIR epidemic model, where they analyse important timescales and features arising from the dimensionless dynamical system. The dimensional analysis explores key dimensionless timescales such as the dilution rate of the space, the quanta generation rate, the incubation period and removal rate, and demonstrates that these parameters can be used to assess the relevance of particular QMRA assumptions.

Dose-response approaches use a measurement of exhaled virions or bacteria in the air and produce a dose-response curve which gives an individual probability of infection given the inhalation of a specific dose, whereas the Wells-Riley approach uses quanta as a measure of infectious dose (Sze To and Chao [2010]). Dose-response models can be applied to a variety of transmission routes and can also be used to calculate the infectious source strength of an outbreak (Sze To and Chao [2010]). Despite sharing similar limitations, the Wells-Riley model allows for quick assessment and does not require as much prior data as a dose-response model, and so is often seen as a simpler approach (Zhao et al. [2022]).

1.3.2 Multi-zone Models

In many real-life outbreaks, it would often prove more useful and more realistic to model multiple zones. Studies acknowledge the need for considering multi-zonal spaces within infection risk models (Hodgson et al. [2004], Guyot et al. [2022]), and more recently, published work demonstrates evidence of contaminant transport of infectious particles and transmission to neighbouring zones with a study in a hospital ward (Jung et al. [2021]) and studies in quarantine hotels (Eichler et al. [2021], SAGE [2021]). There is also evidence to suggest transmission between an infectious individual and a susceptible individual who visits a shared bathroom up to 40 minutes after the infector has left (Jung et al. [2021]), and transmission of measles in a shared space where there was no direct contact between the infector and the susceptible individuals who later became infected (Bloch et al. [1985], Remington et al. [1985]). This emphasises that infection risk is still important despite the absence of an infector, especially between indoor spaces with connected airflow.

Noakes and Sleigh [2009] introduce a new zonal approach towards the Wells-Riley model in an attempt to deal with imperfect mixing in real environments. Zonal variations such as mixing, ventilation and concentration are included in the governing equation. This is then applied to a stochastic version of the Wells-Riley model using simulations to model various ventilation settings across a 9-zone hospital ward applied to a Susceptible-Infected (SI) epidemic model. An example of the 9-zone ward can be seen in Figure 1.1, illustrating the layout.

A two-patch Susceptible-Infected-Susceptible (SIS) epidemic model can be used in the form of a transport model, where people travel between those patches to give a zonal-type model that also allows for patch-specific parameters or boundary conditions between the patches (Arino et al. [2016]). The well-mixed Wells-Riley model can also be extended to consider multi-zone scenarios such as a multi-zone building (Pease et al. [2021]) and a multi-zone office scenario (Faulkner et al. [2022]) to investigate the use of ventilation and filtration systems and how these affect the probability of COVID-19 infection. Using mathematical techniques, the Wells-Riley model is also extended to account for multiple adjoining rooms and movement between these, capturing room-to-room air movement and differing ventilation rates (Melkumov et al. [2020]). Valida-

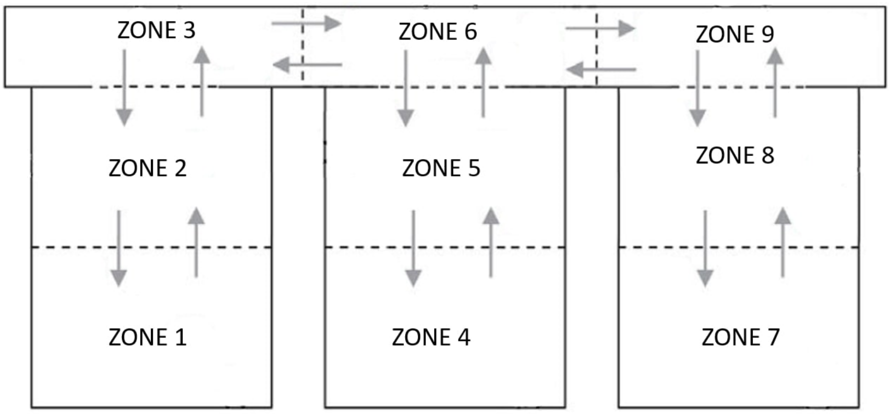

Figure 1.1: The geometric set-up for the 9-zone hospital ward based on the geometry provided in Noakes and Sleigh [2009] and López-García et al. [2019] with newly labelled zones.

tion in forms of CFD or experimental work can help to demonstrate the accuracy of any given model (Cheong and Lee [2018], Qian et al. [2009]).

A zonal SIS Markovian model is investigated by López-García et al. [2019] exploring the effects of ward ventilation, location of patients, ward over-occupancy, and outbreak detection management. This develops a more complex zonal stochastic model with the forward Kolmogorov equations and using a Gillespie Algorithm to simulate the stochastic process (Gillespie [1976]), building on the work presented by Noakes and Sleigh [2009]. The mathematical theory is presented with an application of the model to 6 various ventilation settings on the 9-zone ward layout in Figure 1.1, based on that originally introduced by Noakes and Sleigh [2009]. The work here suggests that detection time dominates the outbreak, but highlights noticeable effects on the airflow due to ventilation. A different approach using a Markov chain model focuses on particle deposition onto surfaces as opposed to airborne aerosol particles (Mei and Gong [2018]).

Ko et al. [2001] consider multiple zones but rather than neighbouring spaces, they take the approach of splitting a single room horizontally to help with better modelling of upper room ultraviolet germicidal irradiation (UVGI) effects on TB risk in a waiting room. However, other work explores splitting an airplane into multiple zones and modelling the space as 4 neighbouring passenger cabins to assess TB (Ko et al. [2004]). Noakes et al. [2015] assess the effects of UVGI on infection risk across a multi-zone hospital ward. However, not only is a multi-zone environment of connected neighbouring zones considered, but each zone is also split horizontally into a further 2 zones; a larger occupied section and a smaller upper section that contains the ultraviolet equipment.

1.4 Computational Airflow Models

Alongside mathematical risk models, it is important to gain an understanding of the surrounding airflow and how different factors may affect this. There are different methods that can be used to model airflow in indoor environments including using CFD techniques or with a network-based zonal model e.g., CONTAM.

1.4.1 Computational Fluid Dynamics (CFD)

CFD is a commonly used tool for modelling both indoor and outdoor airflow, and can be used to explore the spatial variation of velocity, pressure, temperature and contaminant transport. Example applications of CFD models include exploring indoor airflow patterns (Laitinen et al. [2023]), the removal efficiency of different ventilation strategies (Ren et al. [2021]), the effects of turbulence on airflow and contaminant transport (Li et al. [2021c]), modelling exhalations from a human source (Coldrick et al. [2022]), and the effects of spatial airflow distributions, temperature and RH on airborne transmission risk (Foat et al. [2022]).

When using CFD to model indoor environments, there are many different turbulence models, numerical schemes, and meshing techniques, each with different benefits and limitations depending on the application (Nielsen [2015]). Some of these numerical models and tools are more relevant to the modelling of pathogen transmission and associated applications (Peng et al. [2020]).

A CFD study using the Star-CCM+ (v10) software is used to analyse varying ventilation rates, the locations of the supply and extract vents, and including partitions between beds in a hospital (Cheong and Lee [2018]). The risk of infection is analysed using the Wells-Riley model, which shows that a higher ventilation rate significantly reduces the risk, while the other two factors made minimal difference and the best results are achieved when all three mitigation strategies were used in tandem. Adapted Wells-Riley models are also coupled with CFD approaches using ANSYS FLUENT in an application to a hospital ward (Qian et al. [2009]), in a restaurant and ballroom (Zhai and Li [2021]), and to simulate coughing passengers and the dispersion of droplets in an airplane cabin (Gupta et al. [2012]).

ANSYS FLUENT is a common CFD tool for modelling indoor environments in the context of airborne transmission. For example, ANSYS FLUENT is used to analyse the effects of hospital curtains as a mitigation on 2-bed and 4-bed hospital wards prior to the detection of an infection case (Ching et al. [2008]), to investigate airflow and infection risk in hospital anterooms and negative pressure isolation rooms (Tung and Hu [2008]), and to conduct tracer-gas simulations in high-rise flats, including other transmission factors such as wind and window opening schedules (Gao et al. [2008]). A similar tool, ANSYS-CFX is also used to explore the effects of ventilation, partitions and different design layouts on the transmission of TB on a real, 2-bed hospital ward (Noakes et al. [2006a]).

In addition to modelling airflow, ANSYS FLUENT can also be used to model particle deposition onto surfaces such as to predict spatial distributions of bio-aerosol deposition in single and double bed hospital environments by investigating the effects of different room layouts and the use of partitions in reducing neighbouring bed contamination (King et al. [2013], Wilson et al. [2021a]), and coupled with Monte Carlo simulations to visualise the infection risk of SARS-CoV-2 through the air and on surfaces in a negative-pressure ward (Guo et al. [2022]).

An advantage of using CFD as a tool for modelling airborne transmission is that it can enable high resolution of spatial and temporal variations in airflow and provide both detailed quantitative data and highly informative visualisation across a wide range of scenarios. However, CFD is computationally intensive and it can be particularly challenging to model transient effects or more complex geometries over longer time periods, whilst still achieving the same level of resolution.

1.4.2 Network-based Airflow Models

Although the majority of the previous studies use CFD, network models such as the software CONTAM allow for the simulation of airflow inside multi-zonal spaces and can model transient occupant and ventilation schedules, weather and wind effects such as wind pressure, wind speed, wind direction, RH, external temperatures, contaminant sources, and ambient air pollutants (National Institute of Standards and Technology [2022]). CONTAM assumes zones are fully mixed and deals with the flow across zones, rather than within them, sometimes known as a network model. Whilst the fully mixed assumption is a substantial simplification that cannot model the local spatial variation that a CFD model is capable of, network models are much quicker to run. This allows for larger scale building models and transient simulations over periods from hours to months. In the context of modelling disease transmission, this means that simulations can be carried out easily at a similar timeframe to an outbreak in an environment.

CONTAM is commonly used to model multi-zone indoor air and contaminant transport with applications including a multi-zone contaminant transport model in a general healthcare facility to assess the building design and the effects of various mitigation strategies such as room pressurisation, filtration, and UVGI (Emmerich et al. [2013]), and to explore the effects of different window and door opening settings on the airflow in buildings (Leprince and Carrie [2016]).

Larger geometries can also be modelled using CONTAM, such as modelling a high-rise residential building to investigate buoyancy-driven and wind-driven flow effects on gaseous pollutants (Mao et al. [2015]), to analyse contaminant transport to a multi-zone multi-storey building from an underground garage (Reichman and Dubowski [2021]), and to conduct a whole building simulation of two college halls of residence, alongside transient weather conditions to assess acute respiratory infection risk when comparing the high levels of ventilation offered by one building to the low levels of ventilation offered by the other (Zhu et al. [2020]). Shrestha et al. [2021] explore the use of CONTAM for a virtual multi-storey office space to model the aerosol dispersion of SARS-CoV-2 with both transient and steady-state simulations, exploring how different areas of the building may be affected by mitigation strategies such as mechanical ventilation.

Although CONTAM can be used for analysing contaminant transport and airflow directly, in the context of infection risk and disease transmission, it is common for CONTAM to be used for the airflow alone and then applied to other QMRA techniques. Cheong et al. [2018] use CONTAM to investigate mitigation strategies (e.g., increasing ventilation rates and isolating the patient) for an emergency department in a hospital, after which the Wells-Riley model is used to assess the probability of infection. The Wells-Riley model is also used following a multi-zone CONTAM simulation in other examples, including in a multi-zone prototype office building (Yan et al. [2022b]), in 5 prototype commercial buildings; a medium office, a large office, a small hotel, retail premises, and secondary school (Yan et al. [2022a]), and on a cruise ship (Xia et al. [2023]). Alternatively, CONTAM airflow simulations of a multi-zone building can be used with a state-space approach to assess risk of pollutant exposure and contaminant concentration (Parker et al. [2014]).

Although previous studies demonstrate the usefulness of CONTAM for airflow simulations and modelling contaminant transport, validation of more complex building models can be difficult, especially when considering occupant behaviour or movement. Most existing data is often limited to more simplified scenarios modelling a single tracer gas without transient occupants or long timescales, such as a single-zone building with errors less than 30% (Emmerich [2001]), a three-storey town house with errors less than 10% (Emmerich et al. [2004]), and a house with an attached garage with errors around $20 - 30\%$ (Emmerich and Dols [2016]).

It is also possible to combine different methods for modelling airflow, such as utilising the CFD capabilities of CONTAM. This is useful for scenarios where the well-mixed assumption is insufficient in a particular section of the building, but the remaining zones are assumed to be well-mixed. An example of this is shown using a residential home, where a leaking furnace producing Carbon Monoxide is modelled (Wang et al. [2010]).

As presented throughout Chapter 1, many modelling approaches consider fully mixed air in indoor spaces (e.g., CONTAM as above and the Wells-Riley model in Section 1.3). For the purpose of this thesis, where the focus is on assessing long-range airborne transmission across multiple zones with shared airflow, it is assumed that within-room features such as person-to-person interactions, close-range and fomite transmission, and the effects of turbulent mixing become less important and are dominated by the consideration of larger geometries across multiple rooms. Thus, the assumption of fully mixed air within a zone is an appropriate choice and will be considered throughout.

1.5 Weather and Ventilation

Another factor that can affect disease transmission is weather and seasonality, and this has been investigated in many recent studies that assess the effects of various weather conditions on COVID-19 transmission (Pani et al. [2020], Habeebullah et al. [2021]), demonstrating how weather conditions affect contaminant transport, particularly of infectious aerosols (Das et al. [2022]), and through epidemiological assessments (Dbouk and Drikakis [2021, 2022a]). Li et al. [2014] show that weather had a significant effect on the transmission of 'hand, foot and mouth disease' in China, and Sadyś [2017] shows the effects of various wind direction and wind speed on the airborne concentration of *Cladosporium spp.*. Although it can be difficult to identify which specific weather conditions dominate, the effects of various meteorological factors (e.g., RH, temperature, and wind speed) on virus transmission are often investigated (Pica and Bouvier [2012], Dbouk and Drikakis [2020]). Previous studies have highlighted the role that RH can play on airborne transmission (Pica and Bouvier [2012], Foat et al. [2022], Oswin et al. [2022], Haddrell et al. [2023]). However, in this thesis, it is assumed that aerosols carrying viruses are fully evaporated and that the timescales of changes in RH affecting the outcome of an infection are relatively small, and thus negligible, when compared to the timescales used to assess long-range airborne transmission across multiple connected rooms. As such, the role of RH on airborne transmission is not considered in this thesis.

Weather and wind conditions can consequently affect the efficiency of ventilation and airflow within indoor environments, particularly if the main source of ventilation is via natural means. Natural ventilation is commonly relied upon in UK hospitals, stemming from historical design and reducing carbon emissions (NHS England [2023]). Ventilation is defined as providing outdoor air to indoor environments and removing indoor air by means of mechanical or natural methods (Health and Safety Executive (HSE) [2023]). Natural ventilation usually occurs as a result of wind-driven flow, governed by external weather conditions such as wind speed and direction, or stack-driven which is governed by temperature differences between indoor and outdoor environments (Linden [1999]). Previous work suggests that there is a strong association between ventilation and the control of airborne infections indoors (Li et al. [2007]). As this form of ventilation is governed by natural phenomenon, it is difficult to predict and control, which affects its efficiency and makes it an uncertain method (Mao and Gao [2015]). It is suggested that natural ventilation can lead to an increase in the local dispersion of airborne pathogens, or take up to 4 h to be effective in removing infectious aerosols from the air (Dbouk and Drikakis [2022b]).

The uncertainty of natural ventilation is demonstrated through the disparities that are seen in reported ventilation rates achieved by means of natural ventilation. A small number of experimental studies measure natural ventilation rates in healthcare settings. Gilkeson et al. [2013] show rates of 3.4 - 6.5 air changes per hour (ACH) (i.e., the number of times that the total air volume in a zone or indoor space is completely removed and replaced in an hour) in UK hospital wards when using CO_2 as a tracer gas. Escombe et al. [2007] also conduct a study with CO_2 tracer gas, but instead find rates of up to 28 ACH in a Peruvian hospital. Whereas Qian et al. [2010] report observing rates of up to 69 ACH in a hospital ward in Hong Kong. A more recent study compared the efficacy of passive, natural ventilation with a newly retrofitted mechanical ventilation system that achieved 15 ACH in patient rooms and corridors and 6 ACH in other clinical areas by using a CO_2 tracer gas and aerosol samplers (Mingotti et al. [2021]).

To add to the uncertainty of natural ventilation, the effectiveness relies heavily on occupancy behaviour, with thermal comfort being an issue during colder weather periods, leading to closure of windows or doors, reducing natural ventilation (Stensballe et al. [2003], Pica and Bouvier [2012], Leprince and Carrie [2016], Park et al. [2021]).

When assessing ventilation, and the consequent effects of weather conditions, it is possible to use CO_2 as an indicator for the efficiency of the natural ventilation, in a similar way to using it as a proxy for airborne infections. This has been carried out in several studies that use measured CO_2 data from human respiratory sources in schools (Vouriot et al. [2021], Park et al. [2021], Burridge et al. [2023]) and in a hospital (Wilson et al. [2024]). Injected CO_2 tracer gas has also been used in hospitals to assess natural ventilation effects (Escombe et al. [2007], Gilkeson et al. [2013]). Qian et al. [2006] also use a tracer gas (Nitrous Oxide) to mimic the movement of a biological contaminant to investigate the effects of different ventilation systems and mixing on droplet dispersion in a 2-bed hospital ward.

Despite the importance of weather conditions in determining the efficiency of natural ventilation and disease transmission risk, many of the current models overlook transient effects and instead consider steady-state conditions (Emmerich et al. [2013], García-Tobar [2018]). The software CONTAM allows for easy incorporation of transient weather conditions into models, with studies considering the effects of this when using CONTAM to investigate the survival of influenza (Myatt et al. [2010]), model contaminant transport from an underground garage to a multi-storey building (Reichman and Dubowski [2021]), model ventilation and infection risk (Guyot et al. [2022]), and to model radon concentration in dwellings (García-Tobar [2019]).

1.6 UK Hospital Design

Ward design across hospitals in the UK is currently based on guidance set out in the 'Health Building Note 04-01 (HBN04-01): Adult in-patient facilities' (NHS England [2009]), with specifications on room dimensions, provision for equipment, privacy, hand hygiene, isolation facilities etc. As a result, many of the hospitals within the UK follow a similar layout. Over time, NHS policy has advocated towards moving away from Nightingale-style hospital wards, typically large open multi-bed bays without doors or partitions, towards a layout dominated more by single-occupant rooms or four-bedded bays (Short et al. [2014]). However, the majority of NHS hospital wards have developed by adopting a combination of both single-occupant rooms and multi-occupant rooms, due to the restrictions of retrofitting existing infrastructure and lack of funding (Gilkeson et al. [2013]).

In HBN04-01 (NHS England [2009]), the dimensional requirements for both a single-bed room and a 4-bed room are shown as $23.5\,\mathrm{m}^3$ and $72.5\,\mathrm{m}^3$ as of an update to the building note in 2009. Previously, from 1997, the requirements were $21\,\mathrm{m}^3$ for a single-bed room and $60\,\mathrm{m}^3$ for a multi-bed room. Other requirements for occupant spaces specify that the beds should be placed in such a way that they receive natural daylight and have suitable provisions for privacy (including during procedure or routine care, and visitation). Other dimensional requirements include bedside space, with the requirement of 3600 mm (width) × 3700 mm (depth) being deemed sufficient for the majority of activities carried out bedside to be accommodated.

In the 'Health Technical Memorandum 03-01 (HTM03-01): Part A' (NHS England [2021]) the design and validation requirements for ventilation in hospital environments are set out, where changes were made in 2021 following the COVID-19 pandemic to include a greater focus surrounding ventilation, airborne transmission, and indoor air quality in hospitals, particularly through the introduction of a ventilation safety group. The guidance in HTM03-01 Part A sets out requirements for air-exchange rates in particular spaces e.g., 6 ACH for a "general ward", 6 ACH for a "single room", and 10 ACH for an "infectious disease isolation room". There is no specific requirement on how these ventilation rates are achieved in general wards and single rooms, but the guidance does outline a preference for ventilation type with the first choice being natural ventilation, and the last choice being mechanical ventilation. Other specific guidance includes temperature, pressure and noise.

Although some of the benefits of natural ventilation are discussed in HTM03-01 Part A (i.e., the possibility of achieving high air-exchange rates), the reality is that the efficacy of natural ventilation becomes increasingly difficult to achieve when faced with barriers such as retrofitted internal sub-divisions of hospital settings (NHS England [2021]), restricted window openings and reduced wall vents and leakage for energy efficiency (Gilkeson et al. [2013]), concerns about infection control, safety and security (Lomas et al. [2012]), and its high dependency on occupant behaviour (Qian et al. [2010], Park et al. [2021]). With it being almost impossible to maintain consistent ventilation rates when relying solely on natural ventilation (NHS England [2021]) and the suggestion that mechanical ventilation may be a more reliable choice (Qian et al. [2010]), there is an increasing need for further modelling studies to investigate the efficacy of existing ventilation strategies, and better understand factors affecting airborne transmission risks in hospitals.

1.6.1 Ward J12, St. James' Hospital, Leeds, UK

An example of a traditionally designed hospital ward is J12, an adult respiratory ward at St James' Hospital NHS Trust, Leeds, UK. In later chapters, a 12-zone subset of Ward J12 at St. James' Hospital is the geometry of choice for the modelling scenarios, which was obtained from floor plans for Ward J12. This subset consisted of a ward layout containing patient single and multi-bed rooms, HCW and treatment room environments. The chosen 12-zone subset of Ward J12 is illustrated in Figure 1.2. Zones 1 and 2 represent 4-bed bays; Zones 3 and 4 represent single-occupant rooms; Zone 5 is the nursing station; Zone 6, 7 and 8 form a connecting corridor split into 3 zones; and Zones 9 - 12 are general clinical rooms including a sluice, staff room, treatment room and office.

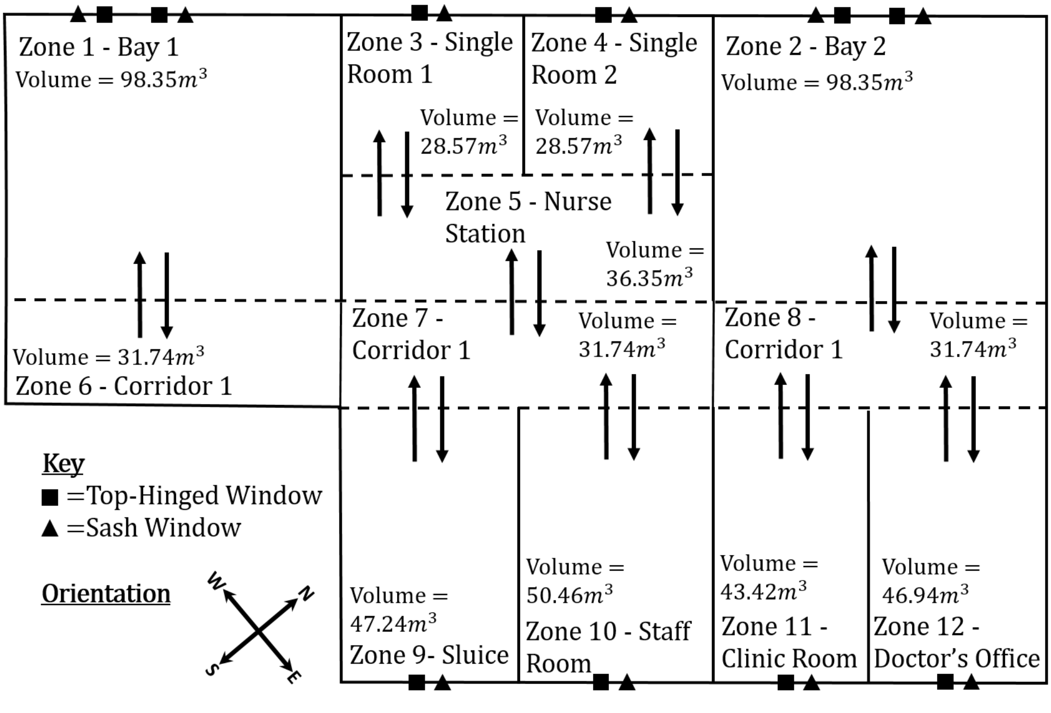

Figure 1.2: Illustration of the chosen geometry - a 12-zone subset of a UK respiratory ward showing the zone number, type and volume for each zone, the orientation of the geometry, and the location of windows.

This ward was originally designed to have open bays between a mixture of single-bed and multi-bed rooms, but over the years has been retrofitted with added doors to enable greater privacy for patients. Many of the original features of the hospital are still present including the window design. Sash windows were a common feature of older hospitals (Gilkeson et al. [2013]), however in recent years, the opening of sash windows has been restricted to 100 mm with a restrictor device being required to ensure patient safety, and to withstand possible deliberate attempts to open the window beyond this point (NHS England [2013]). Sash windows are often accompanied by a top-hinged window, which again has opening restrictions of 30 degrees. In Figure 1.3, an example of the window design on Ward J12 can be seen, with the sash window and an accompanying top-hinged window. This design is mirrored down the centre of a typical 4-bed bay with two sash windows and two top-hinged windows in each bay (Figure 1.4), and each single-bed room has a single sash window and top-hinged window (Figure 1.5).

Other features of Ward J12 can be seen with images of the nurses station (Figure 1.6), a 4-bed bay entrance with a smaller double door type (Figure 1.7), and a single-bed room door entrance (Figure 1.8). The images in Figures 1.3 - 1.8 were taken during an in-person visit to Ward J12.

Figure 1.3: An example of a sash and top-hinged window layout on Ward J12, St James' Hospital NHS Trust, Leeds, UK. Image taken during an in-person visit to the ward.

Figure 1.4: An example of windows in a 4-bed bay on Ward J12, St James' Hospital NHS Trust, Leeds, UK. Image taken during an in-person visit to the ward.

Figure 1.5: An example of a sash window in a single-bed room on Ward J12, St James' Hospital NHS Trust, Leeds, UK. Image taken during an in-person visit to the ward.

Figure 1.6: An example of the nurse station/reception on Ward J12, St James' Hospital NHS Trust, Leeds, UK. Image taken during an in-person visit to the ward.

Figure 1.7: An example of an entrance to a 4-bed bay with a smaller double door type on Ward J12, St James' Hospital NHS Trust, Leeds, UK. Image taken during an in-person visit to the ward.

Figure 1.8: An example of an entrance to a single-bed room on Ward J12, St James' Hospital NHS Trust, Leeds, UK. Image taken during an in-person visit to the ward.

1.7 Research Questions

As outlined in the above literature review, many of the current models used to assess airborne transmission risk are single zone and steady-state. This makes them unable to capture realistic features of environments that commonly vary with time such as occupancy, ventilation, and weather conditions, or an inability to accurately model indoor environments with multiple connected rooms. As a result, many important features that can affect airborne transmission are overlooked, and the resulting risk assessment may be inaccurate. QMRA techniques such as the Wells-Riley model, despite being quick and easy to implement, rely heavily on the knowledge of the outbreak parameters a priori and fail to account for randomness, stochasticity or unknown outbreak data. By having tools that incorporate a better understanding of the environmental and occupant factors that affect airborne transmission, better decisions can be made around the most effective mitigation measures. Therefore, this thesis aims to address the following research questions:

1. How can current QMRA techniques be developed to better represent real-life outbreak scenarios?
2. How important is the consideration of transient effects when modelling airborne transmission and associated infection risk?
3. How does airflow due to natural ventilation facilitate airborne transmission in multi-zone indoor environments, and what factors affect this?
4. Can we develop a successful coupling between airflow dynamics and QMRA techniques in order to provide a better informed risk assessment?
5. Can we extend modelling tools for increased versatility and adaptability, incorporating a broader set of outbreak scenarios?

1.8 Aims and Objectives

This thesis uses an approach combining mathematical models, airflow simulations and epidemiological understanding to develop transient multi-zone models for assessing airborne infection risk. The work then uses these models to explore specific scenarios, predominantly in healthcare settings, investigating further features of outbreak dynamics. The specific objectives for achieving this are:

1. Develop a broad understanding of disease transmission, epidemiology, and in-

fection prevention and control.

2. Develop QMRA techniques to include stochastic effects (e.g., randomness and unknown parameters) to better represent indoor environments and occupant factors (e.g., heterogeneity).
3. Develop models for assessing airborne transmission risk that consider transient effects and multi-zone environments.
4. Explore a coupling between the modelled infectious pathogen concentration in the air with computational epidemic modelling frameworks.
5. Develop airflow models of multi-zone indoor environments, and provide a coupling with a transmission model to understand the key features that affect airborne transmission and infection risk (e.g., ventilation and weather conditions).
6. Use a Monte Carlo approach to include stochastic effects and assess the relative importance of particular outbreak parameters (e.g., ventilation and infectiousness).
7. Apply the new modelling tools to realistic scenarios in healthcare and social settings to understand and quantify airborne transmission risk, and to explore the strengths and limitations of the model.

1.9 Thesis Outline

A brief introduction to the chapter layout is given:

Chapter 2: The Wells-Riley Model Revisited. In this chapter, focus is on the traditional Wells-Riley model, ubiquitous in providing risk assessments of airborne transmission in indoor environments. The fundamental principles of this model are explored and the limitations are considered. Methodological advances are then presented, using mathematical and probabilistic techniques to consider heterogeneity, randomness, stochasticity, and transient effects. The new methodology is demonstrated through applications to realistic scenarios in healthcare and social settings.

Chapter 3: A Transient Multi-zone Transmission Model. In this chapter, a tool is developed that uses a multi-zone transient concentration equation with an epidemic model, based on fundamental QMRA techniques similar to those presented in the Wells-Riley model in Chapter 2. Airflow is simulated using CONTAM and used to inform the transmission model, making it as realistic as possible. Using this modelling technique, transient versus steady-state approaches are compared when modelling airborne pathogen concentration, with an investigation into the effect that this has on consequent infection risk. This is illustrated through two multi-bed ward hospital case studies; one exploring a fixed location infectious HCW, and another exploring a transient infectious HCW moving around various zones completing a drug-round scenario.

Chapter 4: Transient Airflow, Weather and Airborne Transmission. In this chapter, the transmission model presented in Chapter 3 is used to explore the effects of variable ventilation flows, and its applicability is demonstrated through a healthcare ward scenario that explores the effects of transient weather conditions on airborne transmission and associated risks within indoor environments. CONTAM is used to simulate airflow in a naturally ventilated hospital ward allowing for varying weather conditions, whilst keeping all other factors fixed. These airflow simulations are then used to explore various scenarios including natural ventilation only, implementing mechanical ventilation, and open-bay scenarios enabling cross-ventilation flows.

Chapter 5: A Monte-Carlo Approach. In this chapter, the modelling tools presented in Chapters 3 and 4 are extended and used in a Monte-Carlo modelling approach to allow for the inclusion of everyday randomness into infection risk scenarios. In this study, airborne transmission risk is assessed with both natural and mechanical ventilation scenarios with random choices for weather conditions, natural ventilation and airflow, and infectiousness.

Chapter 6 - Conclusions. This chapter presents the conclusions from this thesis and highlights potential areas for further development in future work.

Chapter 2

The Wells-Riley Model Revisited

The Wells-Riley model has been widely used to estimate airborne infection risk, typically from a deterministic point of view (i.e., focusing on the average number of infections) or in terms of a per capita probability of infection. Some of its main limitations relate to considering well-mixed air, steady-state concentration of pathogen in the air, a particular amount of time for the indoor interaction, and that all individuals are homogeneous and behave equally. In this chapter, the Wells-Riley model is revisited, providing a mathematical formalism for its stochastic version, where the number of infected individuals is found to follow a Binomial distribution. Then, the Wells-Riley methodology is extended to consider transient behaviours, randomness and population heterogeneity. In particular, this chapter provides analytical solutions for the number of infections and the per capita probability of infection when: (i) susceptible individuals remain in the room after the infector(s) leave(s), (ii) the duration of the indoor interaction is random/unknown, and (iii) infectors have heterogeneous quanta production rates (or the quanta production rate of the infector present in the room is random or unknown). The applicability of our novel results are illustrated through three case studies: infection risk due to an infectious healthcare worker (HCW) visiting a patient, exposure during lunch for uncertain meal times in different dining settings, and a superspreader event where the emission rate of the infector is given as an estimate with uncertainty. Our results highlight that infection risk to a susceptible who remains in the space after the infector leaves can be non-negligible, and highlight the importance of incorporating uncertainty in the duration of the indoor interaction and the infectivity of the infector when estimating risk.

Chapter 2 contains material from the jointly authored publication:

Edwards AJ, King M-F, Noakes CJ, Peckham D, López-García M. The Wells-Riley model revisited: randomness, heterogeneity, and transient behaviours. *Risk Analysis*, 2024, Volume 44, pp.2125-2147.
`https://doi.org/10.1111/risa.14295`

The code and data for this manuscript are available at `https://github.com/scaje/stochastic_WR_paper_AJE.git`.

2.1 Introduction

In order to develop a better understanding of transmission mechanisms and to quantify the likely impact of different mitigation strategies, one can use a QMRA approach, as introduced in Chapter 1.

To date, the majority of QMRA models assessing airborne infection risk within indoor environments use the traditional Wells-Riley approach (Wells et al. [1955], Riley et al. [1978]), which estimates the number of infected individuals arising from an outbreak (see Equation (1.1)). This can be re-written in terms of the probability of each single susceptible individual (e.g., sharing an indoor space with a constant number I_0 of infectious individuals) becomes exposed (i.e., infected but not yet infectious) during a time interval [0,T],

$$P(T) = \frac{E(T)}{S_0} = 1 - e^{-\frac{I_0 q p}{Q}T}. \tag{2.1}$$

Here, $P(T)$ is the per capita probability of becoming exposed or infected, $E(T)$ is the estimated mean number of exposures (i.e., infections) during [0,T], S_0 is the initial number of susceptible people, p $[\mathrm{m}^3\,\mathrm{min}^{-1}]$ is the pulmonary breathing rate of each individual, Q $[\mathrm{m}^3\,\mathrm{min}^{-1}]$ is the extract ventilation rate in the space and q $[\text{quanta min}^{-1}]$ is the quanta production rate, as defined in Chapter 1. The quanta generation rate, q, cannot be experimentally measured, but estimated epidemiologically. If the exposure time, ventilation rate and number of exposures are known from a particular outbreak, then the quanta generation rate can be calculated using Equation (2.1) (Sze To and Chao [2010]).

The standard Wells-Riley Equation (2.1) relies on four key assumptions: (i) the air in the indoor space is well-mixed so that the concentration of pathogen in the air is spatially homogeneous, (ii) the concentration of pathogen in the air is at steady-state during [0,T], (iii) individuals behave equally, and (iv) susceptible and infectious individuals remain in the room for the whole time interval [0,T]. These are simplifying assumptions which allow for mathematical tractability but can lead to unrealistic predictions, especially in specific scenarios. The well-mixed assumption is commonly referred to as a major limitation of the Wells-Riley model in the literature (Rudnick and Milton [2003], Sze To and Chao [2010], Zemouri et al. [2020]), since it does not allow one to consider heterogeneities in the concentration of pathogen in the air within the indoor setting (Qian et al. [2009]). On the other hand, the steady-state approximation does not allow one to consider transient effects which can be especially relevant under specific environmental conditions (e.g., a moving population (Arino et al. [2016]), or under poor levels of ventilation and during small time scales (see Chapter 3)). Despite these limitations, it does however offer a quick and simple assessment of the risk in many spaces, often viewed as a simpler approach than other methods such as dose-response models or CFD methods (Sze To and Chao [2010], Zhao et al. [2022]).

There have been many adaptations made to the traditional Wells-Riley model over the years in an attempt to overcome these limitations arising due to the original assumptions, as highlighted in Chapter 1. These include considering the influence of spatial effects (Tung and Hu [2008], Qian et al. [2009], Pantelic and Tham [2012], Guo et al. [2021], Lau et al. [2022], Wang et al. [2022]), and using a transport equation for the concentration of pathogen in the space (Qian et al. [2009], Li et al. [2021a,b], Boonmeemapasuk and Pochai [2022], Timpitak and Pochai [2022], Ding et al. [2022]). Gammaitoni and Nucci [1997] allowed for varying quanta levels over time with a conservation equation, making the model closer to a dose-response approach, which has then been used extensively (Beggs et al. [2010], Knibbs et al. [2011], King et al. [2021a], Rocha-Melogno et al. [2021]).

Other adaptations look closer at individual aspects of the Wells-Riley model. For example, levels of excess CO_2 in the air, commonly considered as a proxy for amount of shared air in indoor spaces, was incorporated into the traditional Wells-Riley model (Rudnick and Milton [2003], Zemouri et al. [2020], Cammarata and Cammarata [2021], Burridge et al. [2022]). Other adaptions include accounting for the deposition of airborne particles (Fisk et al. [2004], Franchimon et al. [2008]), or the consideration of mitigation measures such as mask wearing (Nicas [1996], Fennelly and Nardell [1998], Nazaroff et al. [1998], Dai and Zhao [2020], Fantozzi et al. [2022]), social distancing (Sun and Zhai [2020], Shang et al. [2022]), and particle filtration or air cleaning (Nazaroff et al. [1998], Fisk et al. [2004]). The majority of the models mentioned above typically only consider single-zone environments, but multi-zone versions have also been developed (Ko et al. [2001, 2004], Noakes and Sleigh [2009], López-García et al. [2019]; see Chapter 3).

Despite the many different generalisations of the Wells-Riley model, many studies (Pavilonis et al. [2021], Zhao et al. [2022], Rowe et al. [2022]) still use the classical approach that was originally presented by Wells et al. [1955] and Riley et al. [1978]. Moreover, although the Wells-Riley model quantifies individual infection risk in terms of a per capita probability of infection, most of the applications in the literature typically use deterministic approaches focusing on mean quantities (e.g., mean number of individuals infected in an indoor space during [0,T]), typically for single zones and under the steady-state assumption. Stochastic formulations have been applied using Monte Carlo numerical approaches (Noakes and Sleigh [2009]), but those which can deal with more complex scenarios (multi-zone, transient concentration, random length of stay of the infectious individual, or heterogeneities across individuals), and which can allow estimation of the probability distribution of the number of exposed individuals during a specific time interval, are still to be properly formulated from a mathematical point of view. Having these tools would enable a more realistic approach to modelling real scenarios, better representing real-life behaviours and environments, and accounting for stochasticity, making the model more generalisable and applicable.

In this chapter, stochastic variations to the existing Wells-Riley framework are presented. Through these extensions that focus on probability distributions instead of mean quantities, it is possible to offer explicit analytical solutions that will allow for more general, and accurate applications of the Wells-Riley model when assessing risk. In particular, the non-negligible risk of infection to a susceptible person who remains in the space long after the infector leaves is analysed. The randomness in the duration of the indoor interaction is also incorporated, acknowledging that it is not always possible to know exactly how long an infectious individual may be present for, especially when trying to assess risk before the indoor gathering actually takes place. Finally, population heterogeneity is addressed by considering a probability distribution for the quanta generation rate, accounting for heterogeneous infectivity across individuals. These advancements will allow for a wider use of the traditional Wells-Riley model, increasing its applicability and providing a better representation of the heterogeneity and uncertainty that is present when assessing infection risk in real-life settings.

2.2 Developing a Stochastic Wells-Riley Model

The traditional Wells-Riley model allows one to estimate airborne infection risk in an indoor setting, typically during a fixed time period, say $[0, T]$ for some $T > 0$. One can classify individuals in the population (N individuals in an indoor setting) according to their disease status, typically Susceptible and Infectious, with $S_0 + I_0 = N$. Here, S_0 is the number of initially susceptible individuals and I_0 is the initial number of infectious individuals (usually $I_0 = 1$, although several infectious individuals could be involved in a given outbreak in some indoor environments).

If the time period under consideration, $[0, T]$, is relatively short (i.e., hours rather than days), individuals who become infected are not infectious during the indoor gathering, and the only infectious individuals are the ones initially in the room at time $t = 0$, I_0. It is then more precise to classify individuals as Susceptible ($S(t)$) and Exposed ($E(t)$), where individuals are exposed if they have been infected but are not yet infectious, whereas the number of infectious individuals remains constant, $I(t) = I_0$, and $S(t) + E(t) + I_0 = N$ for all $t \in [0, T]$. From now on, in this chapter, "infections" and "exposures" are used interchangeably, and focus on scenarios where the incubation period (i.e., time from infection to symptom onset) and the latent period (i.e., time from infection to becoming infectious) of the pathogen are longer than the time duration of the indoor interaction, so that individuals become infected but not infectious during the timescales of interest.

A deterministic version of the standard Wells-Riley model, or if one interprets $S(t)$ and $E(t)$ as mean quantities, can be obtained via the ODEs

$$\begin{aligned} \frac{dS(t)}{dt} &= -pC(t)S(t), \\ \frac{dE(t)}{dt} &= pC(t)S(t), \end{aligned} \tag{2.2}$$

which represent an SE compartmental epidemic model. Infectious quanta is defined in such a way that the rate at which individuals are infected is considered to be proportional to the concentration of pathogen in the air at any given time, $C(t)$ [quanta m^{-3}], where the constant of proportionality is the pulmonary breathing rate p [$\mathrm{m}^3\,\mathrm{min}^{-1}$], leading to the per capita infectivity rate $pC(t)$. Although an SE compartmental epidemic model is considered here to represent a duration of the indoor interaction which is shorter than the incubation and latent period of the pathogen (so that individuals become exposed but not yet infectious), the Wells-Riley methodology has also been linked to other types of compartmental epidemic models, such as SIS (López-García et al. [2019]) and SEIR (Wood et al. [2023]), to model alternative situations.

In particular, the concentration of pathogen in the air is modelled via the ODE

$$v\frac{dC(t)}{dt} = qI_0 - QC(t), \tag{2.3}$$

where v [m^3] is the room volume, q [quanta min^{-1}] is the quanta production rate, Q [$\mathrm{m}^3\,\mathrm{min}^{-1}$] is the extract ventilation rate and I_0 is the number of infectious individuals in the room during the time interval of interest.

Equation (2.3) can be solved analytically to obtain a transient solution for $C(t)$. If the initial condition is chosen to be $C(t=0)=C_0=0$ (e.g., time $t=0$ represents whenever the infector(s) enter(s) the room), then the following solution can be obtained:

$$C(t)=\frac{qI_0}{Q}\left(1-e^{-\frac{Qt}{v}}\right), \quad t\geq 0. \tag{2.4}$$

More general initial concentrations $C_0>0$ may be considered instead to represent specific situations. Moreover, Equation (2.3) can be solved for steady-state by setting $\frac{dC(t)}{dt}=0$, which leads to

$$C^*=\frac{qI_0}{Q}. \tag{2.5}$$

The following subsections show how to exploit these estimates of the concentration of pathogen in the air in order to estimate the number of exposures during the time interval of interest $[0,T]$. Finally, it is noted that although Q [$\text{m}^3\,\text{min}^{-1}$] represents an extract ventilation rate and is the parameter considered in most applications of the Wells-Riley model in the literature, there are other mechanisms that can contribute to the removal of pathogenic material from the air, and which can be easily incorporated into these models. In particular, in all equations in this chapter it is possible to substitute the extract ventilation rate Q by a more general removal rate R [$\text{m}^3\,\text{min}^{-1}$], which incorporates other mechanisms such as viral inactivation (biological decay in infectiousness of the pathogen) and viral deposition such as onto surfaces or the ground (Miller et al. [2021]), so that

$$R=Q+v\,r_i+v\,r_d \tag{2.6}$$

where v [m^3] is the volume of the space, r_i [min^{-1}] is the viral inactivation rate, and r_d [min^{-1}] is the viral deposition rate. Q is used from now on within the next sections to keep notation consistent, but the more general removal rate R can be used instead in all equations in this chapter, depending on the scenario under consideration. In fact, general removal rates are considered in the case studies analysed in Section 2.4.

2.2.1 Steady-state Concentration

If the steady-state concentration solution, Equation (2.5), is considered, then to estimate the number of exposed individuals during $[0,T]$ it is necessary to set $C(t)=C^*$ during the time interval of interest $[0,T]$, and substitute it back into Equation (2.2), leading to the solution

$$E(T) = S_0 \left(1 - e^{-\frac{pqI_0}{Q}T}\right),$$

so that the per capita probability of infection is $E(T)/S_0 = 1 - e^{-\frac{pqI_0}{Q}T}$; that is, the standard Wells-Riley per capita probability of infection given in Equation (2.1) under steady-state assumptions. From a stochastic point of view (i.e., if one interprets $E(T)$ as a random variable rather than as a deterministic or mean quantity), and since individuals become infected independently of each other, one can interpret this as a sequence of S_0 Bernoulli experiments, so that the number of exposed individuals in $[0, T]$ follows a Binomial distribution

$$E(T) \sim Bin\left(S_0\,,\,1 - e^{-\frac{pqI_0}{Q}T}\right), \tag{2.7}$$

which provides a stochastic interpretation of the deterministic estimate. It can be noted that the mean number of exposed individuals during $[0, T]$ is then $S_0\left(1 - e^{-\frac{pqI_0}{Q}T}\right)$. However, this stochastic interpretation also allows for the estimation of the probability of observing a specific number of exposures $E(T) = n$,

$$\mathbb{P}\{E(T) = n\} = \binom{S_0}{n}\left(1 - e^{-\frac{pqI_0}{Q}T}\right)^{n}\left(e^{-\frac{pqI_0}{Q}T}\right)^{S_0-n}, \quad n \in \{0, 1, \ldots, S_0\}. \tag{2.8}$$

It can be noted that, in fact, this distribution can be derived instead from first principles using the *master equation* (i.e., Kolmogorov differential equations) of the stochastic process, as is done next.

Consider here the stochastic version of the standard Wells-Riley model under steady-state concentration of pathogen in the air. In particular, consider $N = S_0 + I_0$ individuals in an indoor setting during $[0, T]$. The number of infectors over time remains constant, I_0, and the interest is in analysing the number of exposures that occur, $E(T)$. To do this, consider the random variable $S(t)$, representing the number of susceptible individuals at time t. According to Equation (2.2), consider that each susceptible individual becomes exposed independently of each other, at rate pC^*, with $C^* = \frac{qI_0}{Q}$. Thus, the variable $S(t)$ follows a pure death process (see [Allen, 2010, Section 6.4.2]) taking decreasing values in $\{S_0, S_0 - 1, \ldots, 2, 1, 0\}$, with initial condition $S(0) = S_0$.

The number of exposures in $[0, T]$ is a random variable which can be analysed in terms of the number of susceptibles, since $E(T) = S_0 - S(T)$. The number of susceptible individuals at any given time, $S(t)$, can be studied in terms of the probabilities $p_n(t) = \mathbb{P}\{S(t) = n\}$, $n \in \{0, 1, \ldots, S_0\}$, which obey the Forward Kolmogorov Equations [Allen, 2010, Section 5.6], typically referred to as the *master equation* of the stochastic process,

$$\begin{aligned} \frac{dp_n(t)}{dt} &= pC^*(n+1)p_{n+1}(t) - pC^* n p_n(t), \quad n \in \{0, 1, \ldots, S_0 - 1\}, \\ \frac{dp_{S_0}(t)}{dt} &= -pC^* S_0 p_{S_0}(t). \end{aligned}$$

These differential equations can be solved in $[0, T]$ using probability generating function techniques (see [Allen, 2010, Section 6.4.2]), leading to

$$p_n(T) = \mathbb{P}\{S(T) = n\} = \binom{S_0}{n} e^{-npC^*T} \left(1 - e^{-pC^*T}\right)^{S_0 - n}, \quad n \in \{0, 1, \ldots, S_0\}.$$

Finally, and since $E(T) = S_0 - S(T)$ so that $\mathbb{P}\{S(T) = n\} = \mathbb{P}\{E(T) = S_0 - n\}$, and $C^* = \frac{qI_0}{Q}$, one gets

$$\mathbb{P}\{E(T) = n\} = \binom{S_0}{n} \left(1 - e^{-\frac{pqI_0}{Q}T}\right)^n \left(e^{-\frac{pqI_0}{Q}T}\right)^{S_0 - n}, \quad n \in \{0, 1, \ldots, S_0\},$$

which proves Equation (2.8). This has also used the fact that $\binom{S_0}{n} = \binom{S_0}{S_0 - n}$. Thus, the distribution of the number of exposed individuals during $[0, T]$, under steady-state conditions, is indeed a Binomial distribution

$$E(T) \sim Bin\left(S_0, 1 - e^{-\frac{pqI_0}{Q}T}\right).$$

2.2.2 Transient Concentration

A particular limitation of the approach in Subsection 2.2.1 is that the transient concentration of pathogen in the air , $C(t)$, is approximated for $t \in [0, T]$, with the constant steady-state value C^*; this can lead to an overestimation of the predicted quanta concentration levels during early times and be particularly unrealistic in scenarios with low ventilation rates, larger room volumes or when the infector is only present for a short period of time (see Chapter 3). Alternatively, consider instead the transient solution of the concentration of airborne pathogen, Equation (2.4), and substitute it back into Equation (2.2) to reach the more precise estimate (Gammaitoni and Nucci [1997], Sze To and Chao [2010])

$$E(T) = S_0 \left(1 - e^{\frac{pqI_0}{Q^2}\left[v\left(1-e^{-\frac{Q}{v}T}\right)-QT\right]} \right).$$

Following the same arguments as before, $E(T)$ can be interpreted as a random variable in a stochastic version of the Wells-Riley model, and follows a Binomial distribution

$$E(T) \sim Bin\left(S_0\ ,\ 1 - e^{\frac{pqI_0}{Q^2}\left[v\left(1-e^{-\frac{Q}{v}T}\right)-QT\right]} \right),$$

so that the mean number of exposed individuals during $[0, T]$ is

$$S_0 \left(1 - e^{\frac{pqI_0}{Q^2}\left[v\left(1-e^{-\frac{Q}{v}T}\right)-QT\right]} \right),$$

and

$$\mathbb{P}\{E(T) = n\} = \binom{S_0}{n} \left(1 - e^{\frac{pqI_0}{Q^2}\left[v\left(1-e^{-\frac{Q}{v}T}\right)-QT\right]} \right)^n \left(e^{\frac{pqI_0}{Q^2}\left[v\left(1-e^{-\frac{Q}{v}T}\right)-QT\right]} \right)^{S_0-n},$$

for $n \in \{0, 1, \ldots, S_0\}$.

2.3 Randomness, Heterogeneity and Transient Behaviours

In this Section, extensions of the traditional Wells-Riley model to scenarios that are more representative of those experienced in real life are proposed. In Section 2.3.1, transient effects are incorporated by analysing the situation where the infectious individual(s) eventually leave(s) the room, whereas the susceptible individuals stay. In Section 2.3.2, the unknown duration of an interaction with an infectious individual is considered by incorporating a random time for the length of exposure, T. Finally, infectiousness heterogeneity across individuals is explored in Section 2.3.3 by considering a probability distribution for the quanta production rate q.

2.3.1 The Infector Leaves the Room

Section 2.2.2 provided an estimate of the risk to susceptible individuals who share the same room with the initial I_0 infectors during a time period of $[0, T]$ for some time $T > 0$. However, depending on the ventilation settings for the space, the environmental conditions (e.g., temperature, RH), or the biological properties of the airborne pathogen itself, susceptible individuals are also exposed to a (potentially non-negligible) residual risk even after the infector(s) leave(s) the room, if they remain in situ. For example, Chapter 1 highlighted evidence of transmission in a shared bathroom up to 40 minutes after the infector had left (Jung et al. [2021]), and evidence of transmission between neighbouring zones through connected airflow (Eichler et al. [2021], SAGE [2021]), demonstrating the possibility of airborne transmission despite the absence of an infector.

The focus here is on estimating infection risk for susceptible individuals who remain in the room during $[0, T+t]$, whereas the infector(s) leave(s) at time T, for some $T, t > 0$; in Section 2.4.1, this will apply to a scenario where an infected HCW visits the room of a susceptible hospital patient during a time interval $[0, T]$. However, the analysis here can be easily adapted to the situation where a susceptible individual enters the room after the infector has already left. It is clear that the overall infection risk for each susceptible individual during $[0, T+t]$, in terms of the per capita infection probability $P(T+t)$ of the individual being exposed/infected during $[0, T+t]$, can be split according to two distinct periods: the probability of the susceptible individual becoming exposed/infected during the time period during which the infector is present ($[0, T]$), $P_1(T)$, and if there was no infection in $[0, T]$, then the probability of the susceptible individual becoming exposed/infected during the time period after the infector leaves the room ($[T, T+t]$), $P_2(T, T+t)$, due to pathogenic material which remains in the air. In particular, the overall probability of infection during $[0, T+t]$ for a susceptible individual in the indoor setting is

$$\begin{aligned} P(T+t) &= \mathbb{P}\{\text{infection in } [0, T+t]\} \\ &= \mathbb{P}\{\text{"infection in } [0,T]\text{" or} \\ &\qquad \text{"no infection in } [0,T] \text{ and infection in } [T, T+t]\text{"}\} \\ &= P_1(T) + (1 - P_1(T)) P_2(T, T+t). \qquad (2.9) \end{aligned}$$

The per capita probability of each susceptible individual to become exposed during

$[0, T]$, $P_1(T)$, can be calculated as described in Section 2.2.2, using the transient concentration of pathogen in the air during $[0, T]$, so that

$$P_1(T) = 1 - e^{\frac{pqI_0}{Q^2}\left[v\left(1-e^{-\frac{Q}{v}T}\right)-QT\right]}. \tag{2.10}$$

To estimate exposure during the second period, when the infector is absent, consider

$$C(T) = \frac{qI_0}{Q}\left(1 - e^{-\frac{Q}{v}T}\right), \tag{2.11}$$

as the initial condition for the concentration of pathogen in the air during the period $[T, T + t]$, while considering $I_0 = 0$ during $[T, T + t]$ (since the infector(s) have left the room). Thus, Equation (2.3) becomes

$$v\frac{dC(T + t)}{dt} = -QC(T + t),$$

and solving this with the initial condition in Equation (2.11) gives

$$C(T + t) = \frac{qI_0}{Q}\left(1 - e^{-\frac{Q}{v}T}\right)e^{-\frac{Q}{v}t},\ t \geq 0.$$

Hence, to calculate the per capita exposure probability during $[T, T + t]$, $P_2(T, T + t)$, solve

$$\frac{dP_2(T, T + t)}{dt} = pC(T+t)(1 - P_2(T, T+t)) = \frac{pqI_0}{Q}\left(1 - e^{-\frac{Q}{v}T}\right)e^{-\frac{Q}{v}t}(1 - P_2(T, T+t)).$$

which gives

$$P_2(T, T + t) = 1 - e^{-\frac{pqvI_0}{Q^2}\left(1-e^{-\frac{Q}{v}T}\right)\left(1-e^{-\frac{Q}{v}t}\right)}, \quad t \geq 0. \tag{2.12}$$

As may be common in specific settings, such as hospitals or care homes, susceptible individuals (e.g., a patient) may stay in the room long after the infector(s) (e.g., a HCW) leave(s). Thus, it is possible to use the estimate

$$\lim_{t\to\infty} P_2(T, T + t) = 1 - e^{-\frac{pqvI_0}{Q^2}\left(1-e^{-\frac{Q}{v}T}\right)}. \tag{2.13}$$

Finally, combining Equations (2.9), (2.10) and (2.12) gives the overall probability of infection during $[0, T+t]$

$$P(T+t) = 1 - e^{\frac{pqvI_0}{Q^2}\left[e^{-\frac{Q}{v}t}\left(1-e^{-\frac{Q}{v}T}\right)-\frac{Q}{v}T\right]}, \quad t \geq 0. \tag{2.14}$$

As expected, by setting $t = 0$, the probability of infection during $[0, T]$, $P_1(T)$ in Equation (2.10) is recovered. Once again, if $t \to \infty$, that is, if the susceptible individual stays in the indoor space long after the infector has left, the overall per capita probability of infection can be estimated as

$$\lim_{t \to \infty} P(T+t) = 1 - e^{-\frac{pqI_0}{Q}T}. \tag{2.15}$$

It is worth highlighting that this solution is equal to the probability of infection in $[0, T]$ under the traditional Wells-Riley steady-state assumption (Equation (2.1)). This is directly related to the fact that the area under the steady-state concentration of pathogen $C^* = \frac{qI_0}{Q}$ in $[0, T]$ is equal to the area under the curve of the transient concentration of pathogen $C(t)$ in $[0, \infty)$ if the infector(s) leave(s) at time T; see Figure 2.1. Indeed, it can be checked that

$$\begin{aligned} \frac{qI_0}{Q}T &= \int_0^T C^* dt \\ &= \int_0^\infty C(t)dt \; = \; \int_0^T \frac{qI_0}{Q}\left(1 - e^{-\frac{Q}{v}t}\right)dt + \int_T^\infty \frac{qI_0}{Q}\left(1 - e^{-\frac{Q}{v}T}\right)e^{-\frac{Q}{v}(t-T)}dt. \end{aligned}$$

2.3.2 Uncertainty in the Duration of the Indoor Gathering

In some situations, it may be necessary to estimate exposure risk during $[0, T]$ when there is randomness or uncertainty in the duration of the event, T. This may be because the duration of the indoor gathering is unknown, or when assessing the risk for an event which has still not taken place, and for which duration is uncertain. In these scenarios, it is possible to consider that T is a random variable rather than a constant, which could represent the typical duration of a particular type of gathering (e.g., lunch across different hospitality venues in the results in Section 2.4.2) or when analysing a particular outbreak where the duration is not known. This scenario is now considered and the focus is on the steady-state modelling framework for simplicity, and it is considered that $T \sim G(\cdot)$ follows a probability distribution with density function $f_T(t)$.

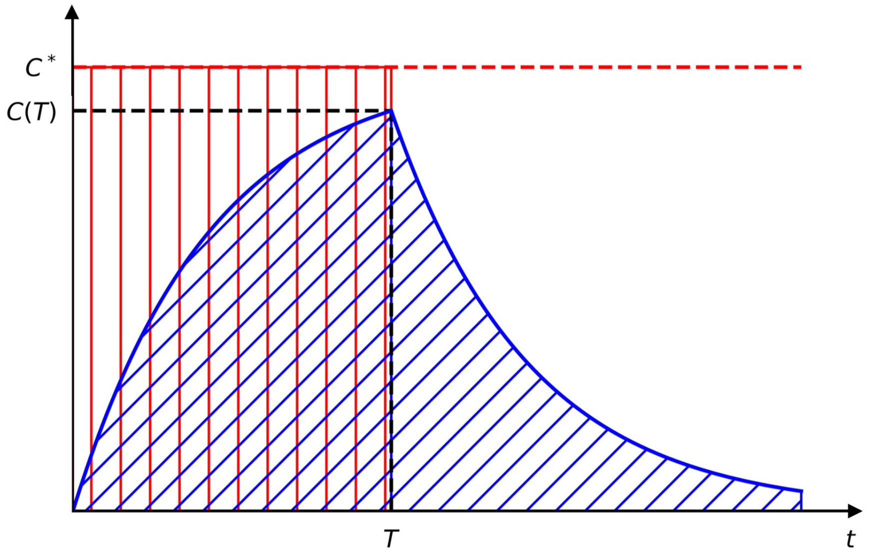

Figure 2.1: Comparison between the concentration of pathogen in steady-state during $[0, T]$ (red line), and the transient concentration during $[0, \infty)$ if the infector(s) leave(s) at time T (blue curve). The red and blue areas are equal, for any value of $T \geq 0$.

The per capita probability of infection in $[0, T]$ can be computed using Equation (2.1), as

$$P(T) = \int_0^\infty \left(1 - e^{-\frac{pqI_0}{Q}t}\right) f_T(t)\, dt\ . \tag{2.16}$$

Equation (2.16) represents the statistical mean of the steady-state per capita probability of infection weighted with the given probability distribution, $f_T(t)$. Whilst this expression provides quantification for the per capita infection risk (i.e., the probability of infection for an individual attending the indoor gathering, of duration $[0, T]$, where T is random and unknown), the distribution of the number of infections/exposures, $E(T)$, is trickier to find. Given that the time duration is random, infection events are no longer independent Bernoulli trials, and thus, $E(T)$ is not a Binomial random variable. This lack of independence can be noticed from the fact that, for example, if a particular individual gets infected during $[0, T]$, with T unknown, this increases the likelihood of the indoor gathering having lasted for a longer period (i.e., T being large), which increases the probability of other individuals having been exposed during the indoor gathering. Still, the probability distribution of the number of exposures can be computed in terms of probabilities $\mathbb{P}\{E(T)=n\}$ for $n \in \{0,1,\ldots,S_0\}$ by solving the integral

$$\mathbb{P}\{E(T)=n\} = \int_0^\infty \mathbb{P}\{E(T)=n|T=t\} f_T(t)\, dt\,.$$

Recall, from Equation (2.7), that $E(T|T=t) \sim Binomial(S_0\,,\ 1-e^{-\frac{pqI_0}{Q}t})$, and so

$$\mathbb{P}\{E(T)=n\} = \int_0^\infty \binom{S_0}{n} \left(1-e^{-\frac{pqI_0}{Q}t}\right)^n \left(e^{-\frac{pqI_0}{Q}t}\right)^{S_0-n} f_T(t)\, dt\,. \tag{2.17}$$

Although Equations (2.16) and (2.17) can easily be solved numerically for any density function $f_T(t)$ of interest, the next sections explore analytical expressions when specific distributions for T are considered; in particular, the Exponential and Erlang distributions as they are typically used to model waiting times in many applications.

2.3.2.1 Exponential Distribution

The duration of the indoor gathering can be modelled in terms of an Exponential distribution with rate λ, $T \sim Exp(\lambda)$, so that $f_T(t) = \lambda e^{-\lambda t}$ for $t \geq 0$. Then, the per capita probability of infection during $[0,T]$, Equation (2.16), becomes (see Appendix 2.A for the full derivation)

$$P(T) = 1 - \frac{\lambda}{\frac{pqI_0}{Q}+\lambda}. \tag{2.18}$$

On the other hand, the probability of observing n infections, $\mathbb{P}\{E(T)=n\}$, can be estimated using Equation (2.17), which gives

$$\mathbb{P}\{E(T)=n\} = \binom{S_0}{n} \sum_{i=0}^{n} (-1)^i \binom{n}{i} \frac{\lambda}{(S_0-n+i)\frac{pqI_0}{Q}+\lambda}, \quad n \in \{0,1,\ldots,S_0\}. \tag{2.19}$$

The reader is refered to Appendix 2.B for a detailed derivation and Appendix 2.C for numerical validation.

2.3.2.2 Erlang Distribution

Whilst the Exponential distribution has been widely used in the literature to model waiting times in many applications, partly due to its memoryless property, it can overestimate short times (since the density function decays exponentially from its maximum value at $f_T(0) = \lambda$), which may be unrealistic in specific situations. Alternatively, the Erlang distribution (which is a Gamma distribution with integer shape parameter) can be used, since it allows for a more Log-Gaussian-like shape (unimodal and defined on the positive real numbers); see for example Figure 2.5 where the Erlang distribution is used to model lunch times in different hospitality venues.

If $T \sim Erlang(k,\ \lambda)$ is considered, then $f_T(t) = \frac{\lambda^k\, t^{k-1}\, e^{-\lambda t}}{(k-1)!}$ for $t \geq 0$. Thus, the per capita probability of infection during $[0, T]$ becomes (Appendix 2.A)

$$P(T) = 1 - \left(\frac{\lambda}{\frac{pqI_0}{Q} + \lambda} \right)^k . \tag{2.20}$$

The number of exposures during $[0, T]$ can be estimated in terms of the probabilities (Appendix 2.B for the derivation; Appendix 2.C for the numerical validation)

$$\mathbb{P}\{E(T) = n\} = \binom{S_0}{n} \sum_{i=0}^{n} (-1)^i \binom{n}{i} \left(\frac{\lambda}{(S_0 - n + i)\frac{pqI_0}{Q} + \lambda} \right)^k , \quad n \in \{0, 1, \dots, S_0\}. \tag{2.21}$$

It is noted that since the $Erlang(k, \lambda)$ can be thought of as a sum of k independent, identically distributed exponential distributions with rate λ, it is clear that by setting $k = 1$ in Equations (2.20) and (2.21), Equations (2.18) and (2.19) for the exponential case are recovered, respectively, as expected.

2.3.3 Infectiousness Heterogeneity

The standard Wells-Riley model relies on the assumption that all infectors, I_0, release pathogenic material [quanta] at a constant and common rate q. However, population heterogeneity in infectiousness is common for many pathogens (Lloyd-Smith et al. [2005]), which is one of the reasons why estimates for the quanta production rate q for many pathogens often span significantly wide ranges (Mikszewski et al. [2021]). The infectivity of a given individual can depend on many different factors including their viral load (Kidd et al. [2021]), respiratory activity or behaviour (Buonanno et al. [2020b]), time since infection (Ma et al. [2021]) or symptoms (Wang et al. [2023]). Thus, it is of interest to consider the situation where the parameter q follows a probability distribution, $q \sim G(\cdot)$. If, for example, a single infector is in the room, $I_0 = 1$, the infectivity may be unknown and sampled from the corresponding distribution instead, which incorporates such heterogeneity at the population level.

As time T and the quanta production rate q both occur as linear terms in the exponent when calculating the steady-state per capita probability of infection, $P(T)$ in Equation (2.1), the results in Section 2.3.2 directly apply here when instead of a random duration T, a random quanta rate $q \sim G(\cdot)$ is considered, for some generic probability distribution with density function $f_q(q)$, whereas T is constant. In particular,

$$\begin{aligned} P(T) &= \int_0^\infty \left(1 - e^{-\frac{pqI_0}{Q}T}\right) f_q(q)\, dq\,, \\ \mathbb{P}\{E(T) = n\} &= \int_0^\infty \binom{S_0}{n} \left(1 - e^{-\frac{pqI_0}{Q}T}\right)^n \left(e^{-\frac{pqI_0}{Q}T}\right)^{S_0 - n} f_q(q)\, dq\,, \\ & \qquad\qquad\qquad\qquad\qquad\qquad\qquad\qquad n \in \{0, 1, \ldots, S_0\}. \end{aligned}$$

Thus, following the same arguments as in Section 2.3.2, and if $q \sim Exp(\lambda)$ with rate λ, so that $f_q(q) = \lambda e^{-\lambda q}$ for $q \geq 0$, the per capita probability of infection during $[0, T]$ is

$$P(T) = 1 - \frac{\lambda}{\frac{pI_0}{Q}T + \lambda},$$

and the number of exposures during $[0, T]$ can be estimated in terms of the probabilities

$$\mathbb{P}\{E(T) = n\} = \binom{S_0}{n} \sum_{i=0}^{n} (-1)^i \binom{n}{i} \frac{\lambda}{(S_0 - n + i)\frac{pI_0}{Q}T + \lambda}, \quad n \in \{0, 1, \ldots, S_0\}.$$

Alternatively, if instead $q \sim Erlang(k,\ \lambda)$ is considered, so that $f_q(q) = \frac{\lambda^k e^{-\lambda q}}{(k-1)!}\, q^{k-1}$ for $q \geq 0$, the per capita probability of infection during $[0, T]$ becomes

$$P(T) = 1 - \left(\frac{\lambda}{\frac{pI_0}{Q}T + \lambda}\right)^k, \tag{2.22}$$

and the number of exposures can be estimated via the probabilities

$$\mathbb{P}\{E(T) = n\} = \binom{S_0}{n} \sum_{i=0}^{n} (-1)^i \binom{n}{i} \left(\frac{\lambda}{(S_0 - n + i)\frac{pI_0}{Q}T + \lambda}\right)^k, \quad n \in \{0, 1, \ldots, S_0\}.$$

2.4 Results

This section considers three case studies to show the applicability of the methodology presented in Section 2.3 in real-life scenarios. Case Study 1 (Section 2.4.1) refers to exposure risk in a healthcare setting, and investigates risk once the infector has left the room. This uses measured HCW visit times to a single-bed room and explores the infection risk to the susceptible patient who remains in the room long after the infectious HCW leaves, exploiting our results in Section 2.3.1. Case Study 2 (Section 2.4.2) explores infection risk when the duration of the outbreak is unknown. In particular, Case Study 2 considers data from the different times spent eating in various restaurant environments, and explores how each hospitality setting can lead to different infection risk depending on the duration of lunch, using methodology from Section 2.3.2. The final Case Study 3 (Section 2.4.3) explores uncertainty in the infectiousness of an individual at a superspreader event, where the exact infectiousness of the infector is unknown but an estimate with uncertainty is provided. This estimate is used to generate an Erlang distribution to explore the methodology in Section 2.3.3.

2.4.1 Case Study 1 - Visit from a HCW

In many UK hospitals, it is common to have single-bed rooms that have a single patient present in them for a particular duration of time. In departments such as a respiratory ward, the majority of patients in single-bed rooms are inpatients for extended periods of time. This section models a scenario where an infectious HCW enters the single-bed room in order to complete a particular care activity with a given duration, and then leaves. The infection risk for the susceptible patient who remains in the room for long after the infector has left (i.e., $t \to \infty$) is estimated. This section leverages the analytical results in Section 2.3.1, and in particular Equation (2.15).

The HCW visit times used in this section were taken from a previous study (King et al. [2021b]) which observed actual care duration for a variety of activities including taking blood samples (“Bloods”, 13 visits recorded), intravenous care (“IV”, 20 visits recorded), general checks (“Check”, 13 visits recorded), observational care (“Obs”, 32 visits recorded) and doctors’ rounds (“Rounds”, 24 visits recorded), totaling 102 recorded visits. King et al. [2021b] then compared these real visit times with the duration of the equivalent care episodes but in a mock scenario. In this section, only the measured time data associated with the real care episodes observed are considered. In particular, 102 data points are used for the duration of actual care, which have mean $\mu = 4.37\,\text{min}$ and standard deviation (SD) $\sigma = 3.15\,\text{min}$.

The volume is chosen to be that of a single-bed room on a UK NHS Trust adult respiratory ward, $v = 28.57\,\text{m}^3$ (Section 1.6.1). For illustrative purposes, and since the quanta production rate for SARS-CoV-2 has been estimated to range from 15 to more than 4000 quanta h^{-1} (Mikszewski et al. [2021]), $q = 360\,\text{quanta}\,\text{h}^{-1}$ is used, equating to $q = 6\,\text{quanta}\,\text{min}^{-1}$ in the results. The pulmonary breathing rate of an individual is taken as $p = 0.01\,\text{m}^3\,\text{min}^{-1}$ (Noakes and Sleigh [2009]). A range of ventilation rates are explored representing 0.5 ACH, 1.5 ACH, 3 ACH and 6 ACH, giving $Q \in \{0.238, 0.714, 1.428, 2.856\}$ $[\text{m}^3\,\text{min}^{-1}]$. For the viral inactivation and deposition rates, plausible values in ranges proposed in Miller et al. [2021] are considered. In particular, the viral inactivation rates are $r_i \in \{0, 0.0035, 0.007, 0.0105\}$ $[\text{min}^{-1}]$, and the viral deposition rates are $r_d \in \{0.005, 0.0115, 0.01815, 0.025\}$ $[\text{min}^{-1}]$. These different removal mechanisms can result in removal rates ranging from $R = 0.381$ to $R = 3.870$ $[\text{m}^3\,\text{min}^{-1}]$, so in this section the values $R \in \{0.381, 1.143, 2.147, 3.870\}$ $[\text{m}^3\,\text{min}^{-1}]$ are explored.

2.4.1.1 HCW Visit Times

In Figure 2.2, the distribution of visit times (as a violin plot) from HCWs for the 5 different care types are plotted. Slight variations can be observed across the different activities, with "IV" and "Rounds" containing specific outliers (representing longer times) compared to the other activities. Also, "Check" typically has the shortest visit length, and a narrower distribution compared to other care types, with the shape of the violin plot concentrated around its mean. Apart from "Check", the quartiles for the other 4 types of care activity are similar in value, with a similar violin shape in the main body, suggesting a similar distribution of visit duration.

2.4.1.2 Total Probability of Infection

To visualise the risk of infection to the susceptible patient for the different care types and visit lengths, Figure 2.3 shows violin plots for the resulting infection risk probability $\mathbb{P}\{\text{infection in } [0, \infty)\}$ in Equation (2.15), for each care type and visit length. This probability estimates the total risk of infection to the susceptible patient, who remains in the room long after the infectious HCW has left. In Figures 2.3a-2.3d, removal rates

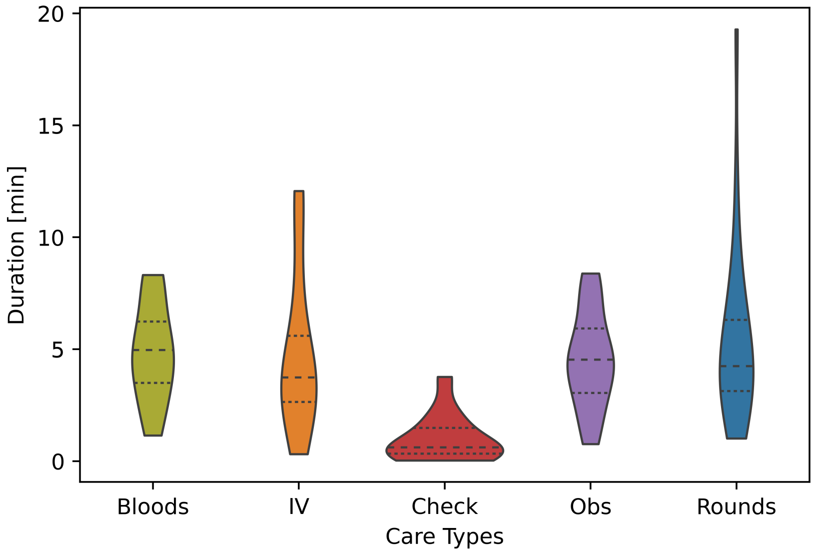

Figure 2.2: Violin plots illustrating the various durations of HCW visits when carrying out one of five care activities to a patient.

$R \in \{0.381, 1.143, 2.147, 3.870\}$ $[\mathrm{m}^3\,\mathrm{min}^{-1}]$ are explored. It can be noted that for each removal rate, “Check” typically leads to lower infection risk across care types, which is consistent with it typically having the lowest visit duration (Figure 2.2). As expected, increasing removal rates lead to decreasing infection risk regardless of the care type. It is clear that the violin plots in Figure 2.3 have similar shapes to those in Figure 2.2 for each care type. Increasing removal rates lead to decreasing variability (i.e., decreasing SD of the corresponding violin plots) in these, suggesting that increasing ventilation can lead to more homogeneous infection risk across different visits (especially within the same care type). However, it is interesting to note that the removal rates considered in this section are not able to completely mitigate large infection risk episodes represented by outliers corresponding to “IV” and “Rounds” type of care. This suggests that increasing ventilation might not be enough when HCW visits are significantly long, and that additional mitigation strategies, such as using masks, might be especially important in these cases (or during these visits).

2.4.1.3 The Importance of Each Time Period

The results above consider total infection risk, which accounts for the risk during the visit (i.e., during $[0, T]$, where $t = 0$ represents the infector HCW entering into the

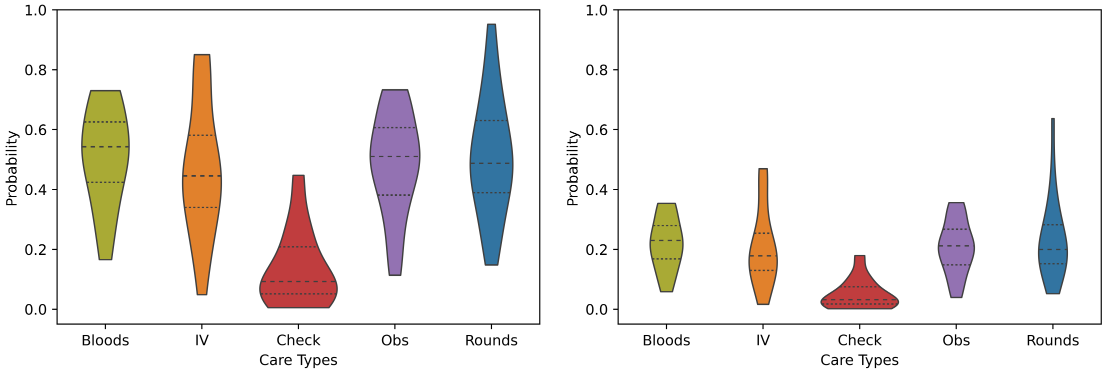

(a) $R = 0.381\,\mathrm{m}^3\,\mathrm{min}^{-1}$ (b) $R = 1.143\,\mathrm{m}^3\,\mathrm{min}^{-1}$

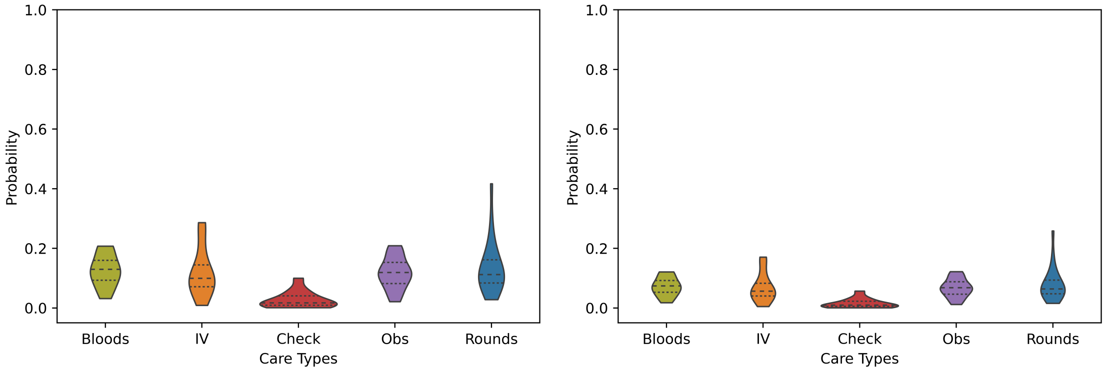

(c) $R = 2.147\,\mathrm{m}^3\,\mathrm{min}^{-1}$ (d) $R = 3.870\,\mathrm{m}^3\,\mathrm{min}^{-1}$

Figure 2.3: Violin plots for the distribution of total risk of infection to the susceptible patient due to the visit of an infector HCW (Equation (2.15) for $t \to \infty$), across different care types and removal rates: (a) $R = 0.381\,\mathrm{m}^3\,\mathrm{min}^{-1}$, (b) $R = 1.143\,\mathrm{m}^3\,\mathrm{min}^{-1}$, (c) $R = 2.147\,\mathrm{m}^3\,\mathrm{min}^{-1}$, and (d) $R = 3.870\,\mathrm{m}^3\,\mathrm{min}^{-1}$.

patient's room, and T is the time that the infector leaves the room), as well as after the visit (i.e., $[T, \infty)$). It is of interest then to analyse the relative importance of each of these two time periods. In Figure 2.4a, the total probability of infection during $[0, \infty)$ for the susceptible patient in the single-bed room is plotted, given by Equation (2.15), for all 102 observed visit times (without distinguishing care type) and the different removal rates. Also illustrated are the contributing probabilities which arise from each of the two time periods; Figure 2.4b shows the probability of infection during $[0, T]$ (that is, when the infector is present, Equation (2.10)), and Figure 2.4c shows the probability of infection after the infector has left (Equation (2.13)). In Figure 2.4d, the relative contribution of the infection risk during the time period after the infector has left on the total infection risk probability (Figure 2.4a) can be seen, that is

$$\frac{P_{total}(T) - P_1(T)}{P_{total}(T)} \text{ x } 100, \tag{2.23}$$

where $P_{total}(T)$ is computed via Equation (2.15), and $P_1(T)$ via Equation (2.10).

When analysing the results in Figure 2.4a, noting that a log-scale has been used for the y-axis, it can be seen that increasing the ventilation rate becomes more effective for longer HCW visits. For relatively short time periods (less than 5 min), small overall probabilities of infection can be observed, almost regardless of the removal rate considered. On the other hand, relatively longer times (more than 10 min) lead to significantly larger infection risk probabilities, and the impact of the removal rate becomes more noticeable. This feature is also seen in Figure 2.4b, when focusing on probability of infection during the specific time period when the infectious HCW is still in the room.

Importantly, the impact of increasing removal rates is more substantial when focusing on the probability of infection once the infector leaves; see Figure 2.4c. Despite the infector only being present for a relatively short period of time (up to 20 min), the infection risk in Figure 2.4c is not negligible, especially for larger values of T and smaller removal rates R. In particular, increasing removal rates have a considerable impact on the risk of infection after the infector leaves the room, with this difference growing with HCW visit length. When the infector is present for longer than 5 min, a greater benefit is seen in having a higher removal rate. This is directly related to the fact that the amount of pathogen which can accumulate in the air increases with T, and that in this type of scenario the susceptible individual remains in the room long after the infector has left (that is, $t \to \infty$ in Equation (2.15)).

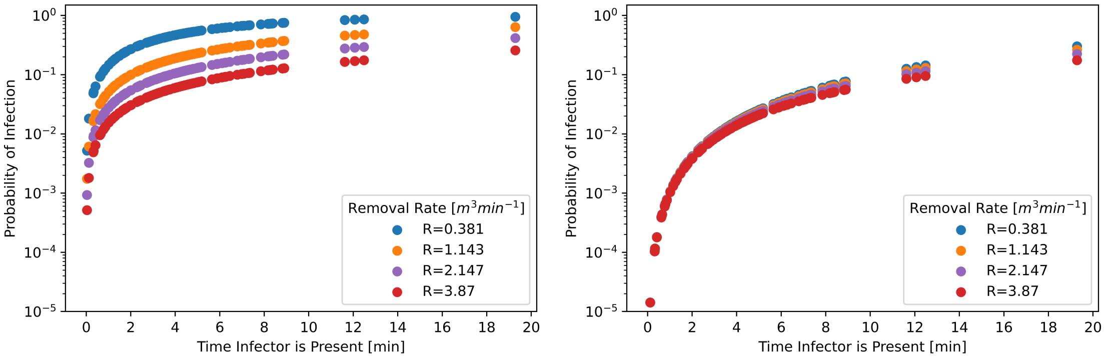

(a) Total probability (b) Infector is present

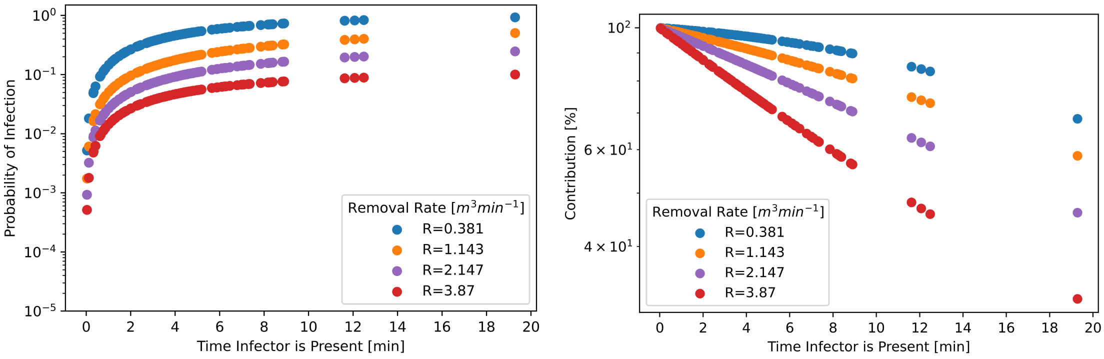

(c) Infector is absent (d) Relative contribution

Figure 2.4: Probabilities of infection for various HCW visit times, T, and varying removal rates for (a) the total period $[0, \infty)$ (Equation (2.15)), (b) the period for when the infector is present only, $[0, T]$ (Equation (2.10)), (c) the period after the infector has left, $[T, \infty)$ (Equation (2.13)), and (d) Relative contribution towards the total probability of infection from the probability of infection after the infector has left, defined in Equation (2.23).

Figure 2.4d plots the relative contribution to the total probability of infection from the infection risk during the time period after the infectious HCW has left. This is shown for all visit lengths and each of the four removal rates. It is worth noting that the removal rates have a similar effect here also, and is illustrated that with increasing removal rates, the percentage contributed from the second period gets smaller. That is to say, the period of time after the infector leaves becomes less important with larger removal rates (and thus, with increasing ventilation). This is due to the fact that the removal mechanisms will reduce the concentration of airborne pathogen faster, and thus reduce the risk to the susceptible individual still in the room after the infector leaves. It is clear that for short visit times, the infection risk after the HCW leaves is an important factor to consider, with the majority of the infection risk coming from this period, particularly for smaller removal rates and shorter visit times. Overall, this notes the non-negligible contribution to the overall risk of infection that comes from the period when the infector is not present.

A particular feature to highlight across all of the results in Figures 2.4 is the importance of considering transient effects, especially when modelling infection risk over small time scales. This section has illustrated the importance of the period once the infector leaves, when infectious pathogen may remain in the air and contribute to the infection risk for the susceptible patient. This would otherwise be overlooked when using the standard steady-state Wells-Riley model, since in this model the concentration would be considered to be zero as soon as the infector leaves.

2.4.2 Case Study 2 - Random Time Spent in Different Restaurant Settings

This section investigates the risk of infection posed by having lunch in different hospitality venues, and while considering an unknown (random) lunch duration T for different party sizes, leveraging the methodology in Section 2.3.2.

Erlang distributions are considered to model the duration $T \sim Erlang(k\ ,\ \lambda)$ of lunch, for some parameters (k, λ). In particular, these parameters are calibrated based on data from a study which investigates the impact of social factors on the duration of a meal time, which includes different party sizes in a selection of hospitality venues (Bell and Pliner [2003]). There are three different venues: a fast-food restaurant, a workplace cafeteria, and a moderately priced restaurant. The party sizes range from 1 person, to 5+ people. Since the focus is on analysing infection risk for the group having the meal together, due to an infector being present in this same group, only party sizes larger

	Observed		**Modelled** (Erlang(k , λ))			
Party Size	**Mean** μ [min]	**SD** σ [min]	**Mean** μ [min]	**SD** σ [min]	k	λ
2	18.2	6.0	17.8	5.9	9	0.5056
3	18.4	6.8	17.6	6.7	7	0.3979
4	19.7	7.2	18.4	7.0	7	0.3800
5	21.9	5.8	21.5	5.9	14	0.6510

Table 2.1: Observed average meal times, with standard deviation (SD), for various party sizes in a fast-food restaurant (Bell and Pliner [2003]), together with calibrated Erlang distributions to model these.

	Observed		**Modelled** (Erlang(k , λ))			
Party Size	**Mean** μ [min]	**SD** σ [min]	**Mean** μ [min]	**SD** σ [min]	k	λ
2	23.0	7.9	21.7	7.7	8	0.3685
3	33.0	11.3	34.8	11.6	9	0.2584
4	41.1	10.6	41.0	10.6	15	0.3658
5	44.0	14.2	45.8	14.5	10	0.2182

Table 2.2: Observed average meal times, with standard deviation (SD), for various party sizes in a workplace cafeteria (Bell and Pliner [2003]), together with calibrated Erlang distributions to model these.

than one will be considered here. For the illustrative results, meal duration for party sizes 5+ in Bell and Pliner [2003] have been used to consider a party size of exactly five individuals in this section. The mean meal duration, and its SD, for each party size can be seen for the fast-food restaurant, the workplace cafeteria, and the moderately priced restaurant in Table 2.1, Table 2.2, and Table 2.3, respectively.

As the data for the meal times in Bell and Pliner [2003] are given in the form of the mean and SD, instead of as raw data values, these summary statistics are used to calibrate the Erlang parameters k (shape) and λ (rate). In particular, an Erlang distribution has mean and SD given as:

$$\mu = \frac{k}{\lambda}, \quad \sigma = \sqrt{\frac{k}{\lambda^2}} \tag{2.24}$$

	Observed		**Modelled** (Erlang(k , λ))			
Party Size	**Mean** μ [min]	**SD** σ [min]	**Mean** μ [min]	**SD** σ [min]	k	λ
2	44.9	10.8	44.5	10.7	17	0.3849
3	47.2	10.1	47.6	10.1	22	0.4627
4	52.3	8.5	52.5	8.5	38	0.7239
5	58.5	13.1	58.7	13.1	20	0.3409

Table 2.3: Observed average meal times, with standard deviation (SD), for various party sizes in a moderately priced restaurant (Bell and Pliner [2003]), together with calibrated Erlang distributions to model these.

Thus, for each pair of observed (μ, σ) in Tables 2.1-2.3, for each party size, the simultaneous equations in Equation (2.24) are solved to get a corresponding value for k and λ. Since the shape parameter, k, takes integer values, the solution for k was then rounded to the nearest integer. Calibrated parameters are reported in Tables 2.1-2.3, and the resulting Erlang distributions are plotted in Figure 2.5. It is noted that the rounding method for k leads to a calibrated Erlang which does not precisely match the observed mean (and SD) meal durations, but the relative error is small, so the meal durations are relatively well captured by the resulting Erlang distributions. In particular, the relative error is less than 6.50% for the mean and less than 3.30% for the SD in the fast-food restaurant case, less than 5.65% for the mean and less than 2.85% for the SD in the workplace cafeteria case, and less than 1.64% for the mean and less than 0.83% for the SD in the moderately priced restaurant case, for all party sizes.

In Figure 2.5, the resulting Erlang distributions can be seen for each party size, for all of the dining locations. Figure 2.5a shows relatively small variability between the meal duration for different party sizes when dining in a fast-food restaurant, suggesting that, regardless of the number of people, the typical mean length remains the same. In the other two cases, there is evidence of more variability between the time spent across different party sizes. These results are rather intuitive to what would be expected in everyday life. Typically, fast-food settings are more informal and encourage a quicker dining experience regardless of the number of individuals present, whereas in more formal settings such as the workplace cafeteria or restaurant, once seated you may be more likely to stay for longer, especially for larger party sizes.

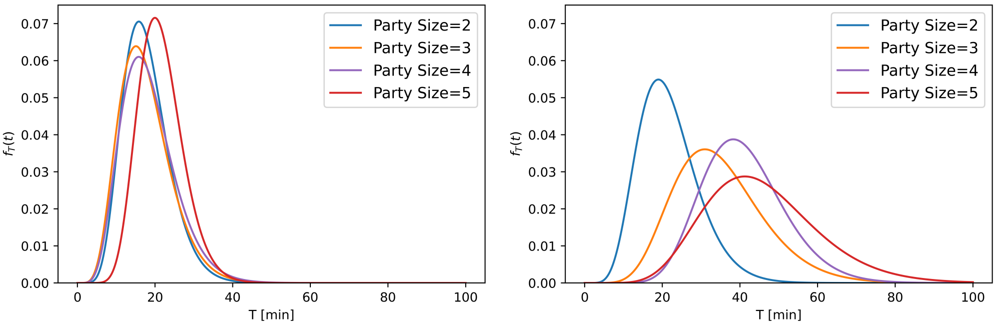

(a) Fast-Food Restaurant

(b) Workplace Cafeteria

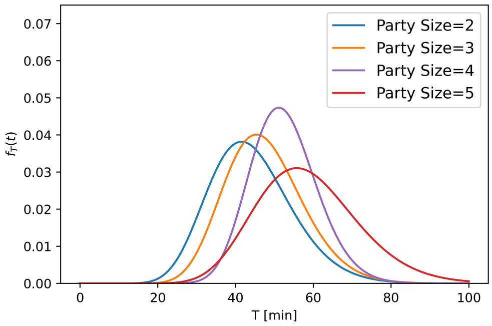

(c) Moderately Priced Restaurant

Figure 2.5: Calibrated Erlang density functions for each party size in the (a) fast-food restaurant, (b) workplace cafeteria, and (c) moderately priced restaurant.

2.4.2.1 Estimating the Number of Infections

Now, the aim is to explore the impact of these random meal durations, across different party sizes and hospitality venues, on the infection risk for the group (in terms of number of infections), if an infector is present in it. That is, for a party size N, the initial number of infectors is set to be $I_0 = 1$, and the initial number of susceptible individuals $S_0 = N - I_0$, and do not consider any interaction with other individuals in the venue. The pulmonary breathing rate is chosen to be $p = 0.01\,\mathrm{m}^3\,\mathrm{min}^{-1}$ (Noakes and Sleigh [2009]), and the quanta production rate $q = 6\,\mathrm{quanta}\,\mathrm{min}^{-1}$ as in the previous case study. The volumes of each space are considered to be equal, so that the results focus on analysing the impact of meal duration (which depends on hospitality venue type and party size) as the key factor of interest, while all other parameters/factors remain the same. In particular, for illustrative purposes space dimensions of $3 \times 10 \times 10$ (height [m] x width [m] x depth [m]) are considered, giving $v = 300\,\mathrm{m}^3$. Ventilation rates of 3 ACH and 1 ACH are explored, giving respective extract ventilation rates $Q = 15\,\mathrm{m}^3\,\mathrm{min}^{-1}$ and $Q = 5\,\mathrm{m}^3\,\mathrm{min}^{-1}$. For the viral inactivation and deposition rates, the mid-points of the ranges proposed in Miller et al. [2021] were chosen, leading to $r_i = 0.00525\ \mathrm{min}^{-1}$ and $r_d = 0.015\,\mathrm{min}^{-1}$, respectively. Combining these with the extract ventilation rates lead to removal rates $R = 21.075\,\mathrm{m}^3\,\mathrm{min}^{-1}$ (corresponding to 3 ACH) and $R = 11.075\,\mathrm{m}^3\,\mathrm{min}^{-1}$ (corresponding to 1 ACH).

The focus is on estimating the number of infections (as a random variable) in each scenario. In particular, Figure 2.6 shows the probability distribution of the number of infections for each party size and hospitality venue, when considering 3 ACH ventilation rate. The mean number of infections is plotted as a vertical line for each histogram, and these mean values are reported in the legend. Equivalent results are plotted in Figure 2.7 when considering 1 ACH instead. Results in Figure 2.6 suggest a relatively low risk for all scenarios, with the most likely outcome being zero infections (highest probability at zero). This is consistent across all three dining settings. In all of the cases, the mean number of exposures is less than 1, with the highest mean being 0.61 in the restaurant case with a party size of 5, as expected. In general, larger party sizes lead to higher risk of some infection(s) occurring; the probability of getting exactly one infection during the meal is 20-37% for a party size of 5, but less than 12% for a party size of 2. It is worth noting that, in reality, the probability of having an infector present would significantly increase for larger party sizes, which is not explored in these results (where we assume that a single infector is present, regardless of the scenario). Overall, the predicted number of infections in the moderately priced restaurant is larger than

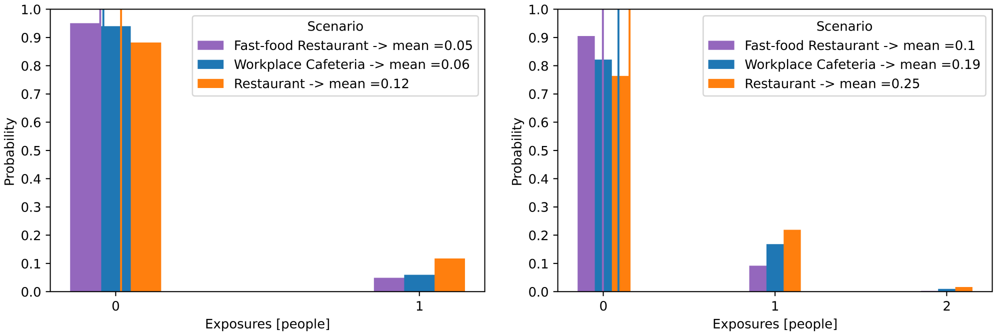

(a) Party Size = 2 (b) Party Size = 3

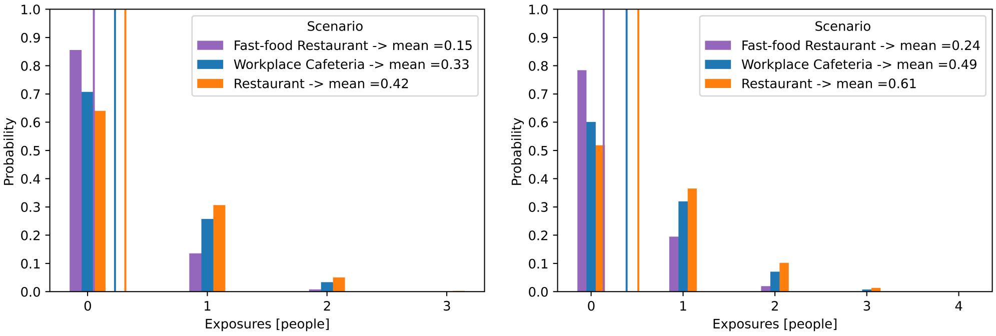

(c) Party Size = 4 (d) Party Size = 5

Figure 2.6: The probability of having a given number of exposures for different hospitality venues and party sizes. Volume of $v = 300\,\mathrm{m}^3$, and ventilation rate of 3 ACH. Mean numbers of infections are reported in the legend and plotted as vertical lines for each histogram.

in the workplace cafeteria, this one being larger than in the fast-food venue, which is directly related to the meal durations observed in Figure 2.5.

Another possibility of the low risk could be due to the good levels of ventilation. It is possible that the ventilation is muting some of the nuances due to the small variations present in the distributions. Here, the ventilation for this scenario is set to 3 ACH. In reality, this is probably unlikely for these spaces, and so for additional comparison, the probability of a given number of exposures for the three different restaurant cases can be seen for four different party sizes and a reduced ventilation rate of 1 ACH in Figure 2.7.

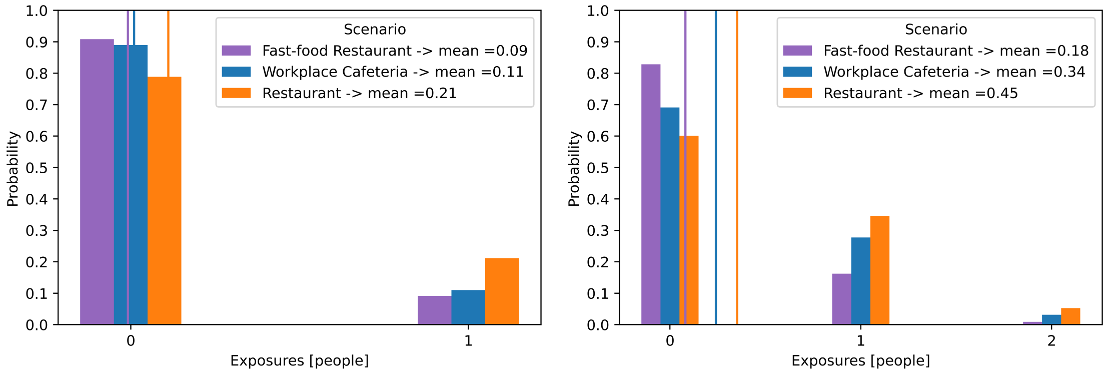

(a) Party Size = 2 (b) Party Size = 3

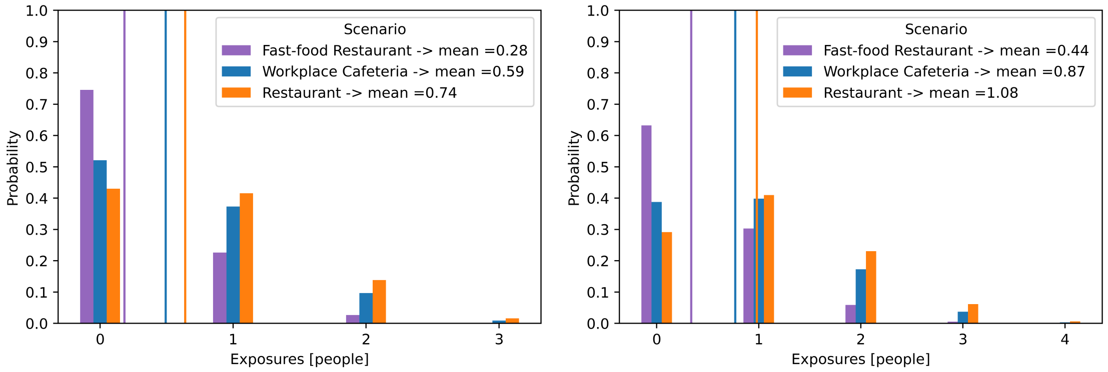

(c) Party Size = 4 (d) Party Size = 5

Figure 2.7: The probability of having a given number of exposures for different hospitality venues and party sizes. Volume of $v = 300\,\mathrm{m}^3$, and ventilation rate of 1 ACH. Mean numbers of infections are reported in the legend and plotted as vertical lines for each histogram.

When the ventilation is reduced in these spaces, the differences in risk becomes more noticeable, and it is possible to observe a larger probability across all non-zero predicted exposures, with a smaller probability of zero predicted exposures. In particular, the probability of zero exposures in a party size of 5 in a moderately priced restaurant has reduced from over 50% in the 3 ACH case, to less than 30% in the 1 ACH case. This increase in risk is also seen in the predicted mean number of exposures, where the highest mean across all scenarios is now 1.08, compared to 0.61 in the 3 ACH case.

2.4.2.2 Per Capita Infection Risk

In Figures 2.6 - 2.7, the focus is on the population level risk, in terms of the number of predicted exposures during the meal. It is possible to instead look at the risk posed to an individual who is attending the event (per capita probability), and study how this per capita risk is affected by the meal duration. The traditional Wells-Riley model (Equation (2.1)) offers a per capita probability of an individual becoming infected in a given scenario, for a given time duration T. Section 2.3.2 introduces the per capita probability for an individual when the exact time is not known, and can instead, be represented through an Erlang distribution (Equation (2.20)). Predictions given by these Equations (2.1) and (2.20) can now be compared when considering the meal duration times for the different hospitality venues. In the results that follow, the volume is set as $v = 300\,\mathrm{m}^3$, the pulmonary breathing rate as $p = 0.01\,\mathrm{m}^3\,\mathrm{min}^{-1}$, the quanta production rate as $q = 6\,\mathrm{quanta}\,\mathrm{min}^{-1}$, and removal rate as $R = 11.075\,\mathrm{m}^3\,\mathrm{min}^{-1}$.

To better understand the difference between per capita probabilities for known and unknown exposure times, a sample of 100 random time durations was taken from each Erlang distribution across each dining setting and party size in Figure 2.5. For each sampled meal duration, Equation (2.1) provides the per capita infection risk probability for that specific duration of the meal. Thus, Equation (2.1) applied to 100 sampled times (from each Erlang distribution in Figure 2.5, corresponding to each hospitality venue and party size) gives 100 values of $P(T)$, the per capita probability of infection estimated by the traditional Wells-Riley model. These 100 values of $P(T)$ are plotted as violin plots in Figure 2.8. On the other hand, each Erlang distribution in Figure 2.5 leads to a single overall prediction $P(T)$ from Equation (2.20), which estimates the per capita infection risk probability accounting for the uncertainty in meal duration encoded by the corresponding Erlang distribution. This single prediction of $P(T)$ is superimposed on each of the corresponding violin plots, as a black dot.

Figure 2.8 shows a similar pattern to that observed across the probability distributions for the number of exposures in Figures 2.6 - 2.7. In particular, the scenarios with the

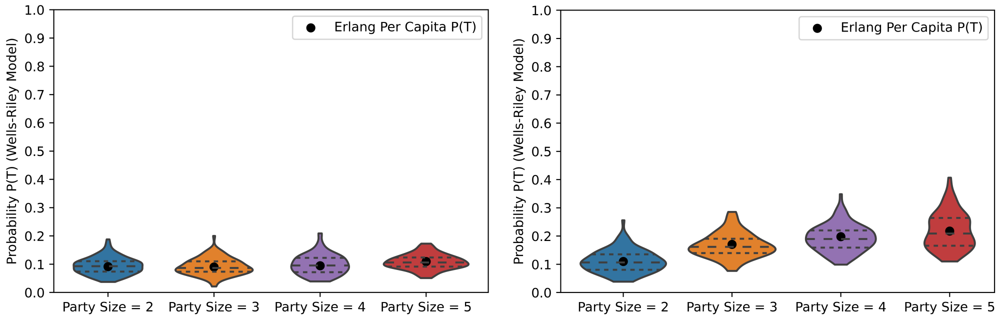

(a) Fast-Food Restaurant

(b) Workplace Cafeteria

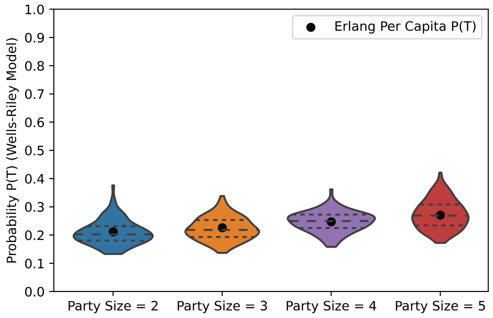

(c) Moderately Priced Restaurant

Figure 2.8: Violin plots for the distribution of per capita $P(T)$ for the traditional Wells-Riley model (Equation (2.1)) with duration T sampled from the Erlang distributions (Figure 2.5), along with the per capita $P(T)$ for unknown T using an Erlang distribution (Equation (2.20)) for each party size in the (a) fast-food restaurant, (b) workplace cafeteria, and (c) moderately priced restaurant.

typically shorter meal time durations experience the lowest per capita infection risk probability i.e., the fast-food restaurant has the lowest per capita risk. This is consistent also across the party sizes with larger groups typically experiencing a high individual per capita risk of infection, as expected. It can also be noted how the per capita probability obtained via Equation (2.20), which estimates infection risk while accounting for the uncertainty in the meal duration time encoded by the Erlang distribution, is able to summarise all of the distribution from the traditional Wells-Riley per capita (violin plot) into a single point (black dot), across Figures 2.8a - 2.8c. This is expected given that Equation (2.20) represents the statistical mean of the steady-state per capita probability of infection weighted by the Erlang distribution. Thus, by using the methodology in Section 2.3.2, it is possible to estimate infection risk in terms of $P(T)$ while accounting for the uncertainty in the time duration of the indoor interaction.

An interesting feature to highlight on these plots is the change in the per capita infection risk probability with party size. It is expected that the per capita infection risk probability may vary across the different dining settings (i.e., that the individual infection risk depends on the venue/indoor setting). However, one would expect that the individual infection risk does not depend on party size, if the number of infectors present is fixed to $I_0 = 1$; that is, Equation (2.1) and (2.20) are both independent of the total population size, N. However, through Figure 2.8, one can observe that as the party size increases, so does the per capita probability of infection. In this case, this is due to the fact that the Erlang distributions across the party sizes and settings account for the fact that individuals are likely to spend longer in a particular venue if there are more people dining (Figure 2.5). This highlights the importance of social and behavioural factors in determining infection risk, which is often overlooked when using traditional QMRA techniques such as the Wells-Riley model, but which can be better explored via the newly proposed methodology by integrating uncertainty in some model parameters.

2.4.3 Case Study 3 - Uncertainty in the Quanta Emission Rate

As described in Section 2.3.3, it is common for the quanta emission rate, q [quanta h^{-1}], to be random, unknown or vary between individuals when analysing an outbreak. In the case where the quanta emission rate is unknown, then an estimate can be used. However, as this is only an estimate, it may be useful to form a probability distribution around the quanta emission rate estimate to explore a broader range of possible values and associated infection risks, helping to account for any uncertainty or error in the parameter estimate. In the work of Miller et al. [2021], a Monte Carlo method is used to estimate the mean and SD of the quanta emission rate for the Skagit Valley chorale superspreading event during the COVID-19 pandemic with a given range of input values, with any unknown parameters represented by probability distributions. Here, the methodology from Section 2.3.3 is applied to explore an Erlang distribution formed around the mean and SD provided for the quanta emission rate estimate in Miller et al. [2021], allowing an exploration of a greater range of quanta emission rates and associated infection risk probabilities, better accounting for the fact that this quanta emission rate is an estimate and not an exact value.

In Miller et al. [2021], the mean is given as $970\,\text{quanta}\,\text{h}^{-1}$ and the SD is given as $390\,\text{quanta}\,\text{h}^{-1}$. As in Section 2.3.2, the mean and SD given here are used to calibrate Erlang distributions by solving Equation (2.24). Since the shape parameter, k, takes integer values, the solution for k was then rounded to the nearest integer. Calibrated parameters for the Erlang distribution are reported as $k = 6$ and $\lambda = 0.00638$. Due to the rounding method for k, the calibrated Erlang does not precisely match the mean (and SD) provided in Miller et al. [2021], but the relative error is small. In particular, the corresponding mean and SD from the Erlang are 940.825 and 384.09, respectively. This gives a relative error of less than 3.01% for the mean and less than 1.52% for the SD. In Figure 2.9, the calibrated Erlang for this scenario can be seen. This figure shows the uncertainty surrounding the estimated parameter as the distribution covers a large range of possible quanta generation rates.

2.4.3.1 Estimating the Number of Infections

To illustrate the methodology of using an Erlang distribution to represent a parameter estimate, a scenario is considered that represents an outbreak on a 4-bed bay on an adult respiratory ward in the UK, with the presence of an infectious visitor. That is, for a population of size $N = 5$, the initial number of infectors is set to be $I_0 = 1$, and the initial number of susceptible individuals $S_0 = N - I_0 = 4$. The pulmonary breathing rate is chosen to be $p = 0.01\,\text{m}^3\,\text{min}^{-1}$ ($p = 0.6\,\text{m}^3\,\text{h}^{-1}$; Noakes and Sleigh [2009]), and the outbreak is monitored over one hour ($T = 1\,\text{h}$). The quanta production rate is taken as random and defined by the calibrated Erlang distribution (Figure 2.9). The volume of the space is $98.35\,\text{m}^3$, equal to that of a 4-bed bay in a UK adult respiratory ward (Figure 1.2, Section 1.6). A ventilation rate of 3 ACH is explored, giving a respective extract ventilation of $Q = 4.9175\,\text{m}^3\,\text{min}^{-1}$ ($Q = 295.05\,\text{m}^3\,\text{h}^{-1}$). For the viral inactivation and

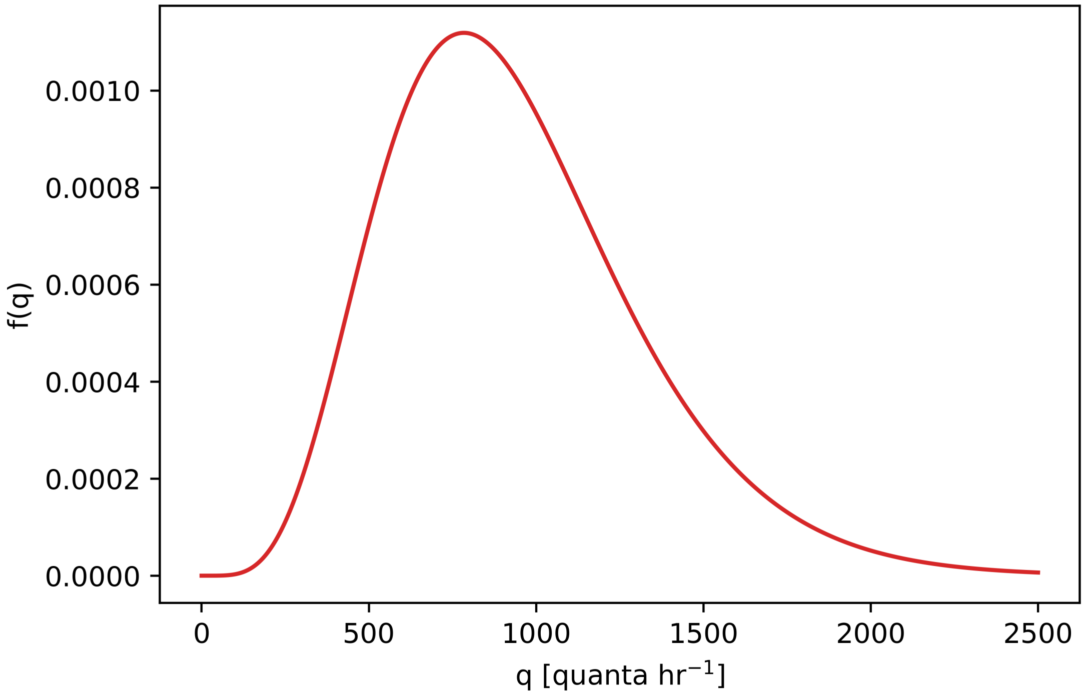

Figure 2.9: Calibrated Erlang density function for q [quanta h^{-1}] for the SARS-CoV-2 superspreading event in the Skagit Valley chorale.

deposition rates, the mid-points of the ranges proposed in Miller et al. [2021] were chosen, leading to $r_i = 0.00525\ \mathrm{min}^{-1}$ ($r_i = 0.315\,\mathrm{h}^{-1}$) and $r_d = 0.015\,\mathrm{min}^{-1}$ ($r_d = 0.9\,\mathrm{h}^{-1}$), respectively. Combining these with the extract ventilation rates lead to a removal rate of $R = 6.909\,\mathrm{m}^3\,\mathrm{min}^{-1}$ ($R = 414.5423\,\mathrm{m}^3\,\mathrm{h}^{-1}$). The parameters above are converted from min^{-1} to h^{-1} for the remainder of the calculations in this section, to be consistent with the units provided for q by Miller et al. [2021].

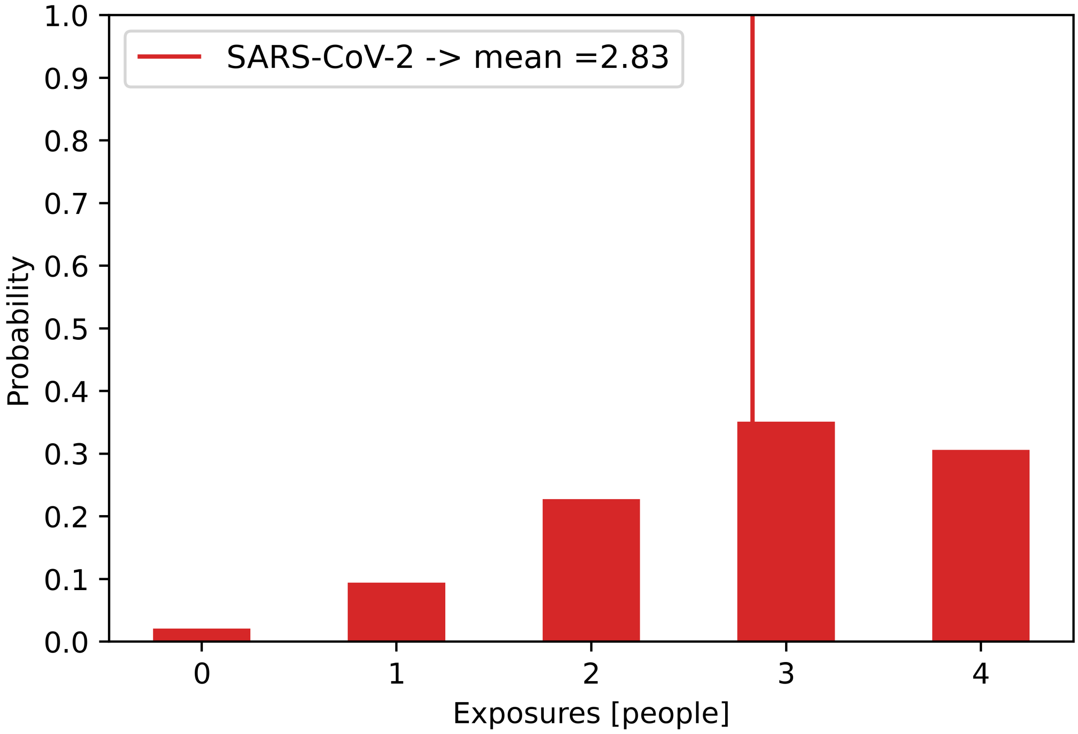

Figure 2.10: The probability of having a given number of exposures for q [quanta h^{-1}] for the SARS-CoV-2 superspreading event in the Skagit Valley chorale. Volume of $v = 98.35\,\mathrm{m}^3$, and ventilation rate of 3 ACH. Mean number of exposures is reported in the legend and plotted as a vertical line.

The probability histogram for $E(t)$, showing the probability of a given number of exposures for this SARS-CoV-2 superspreading event, is shown in Figure 2.10. As expected, given that this represents a superspreading event, the probability histogram predicts higher probabilities for larger numbers of exposures. For example, the probability of having zero exposures is 0.02074, whereas for 3 or 4 exposures, it is greater than 0.3. The mean number of exposures is 2.83, greater than 70% of the population. This illustrates high risk to the susceptible population, especially given that the outbreak only lasts for one hour. This shows that the predicted Erlang distribution is able to capture the increased risk when using estimated parameters for a superspreading event, displaying risk predictions that would suggest a highly infectious individual.

2.4.3.2 Per Capita Infection Risk

As in Section 2.4.2, it can be useful to look at the risk posed to each susceptible individual (per capita probability). In the same way as before, predictions given by the traditional Wells-Riley model (Equation (2.1)) and in this section, Equation (2.22), are compared when considering the Erlang distribution calibrated by an estimate for a superspreader's emission rate. The parameter choices for the scenario illustration remain the same as above.

A sample of 100 random emission rates was taken from the calibrated Erlang distribution (Figure 2.9) for the SARS-CoV-2 superspreading event. The traditional Wells-Riley model, Equation (2.1), provided the per capita infection risk probability for each of the sampled emission rates. These 100 values of $P(T)$ are plotted as a violin plot in Figure 2.11. On the other hand, the Erlang distribution in Figure 2.9 leads to a single overall prediction $P(T)$ from Equation (2.22), which estimates the per capita infection risk probability accounting for the uncertainty in the emission rate. This single prediction of $P(T)$ is superimposed on the violin plot, as a black dot, in Figure 2.11.

Figure 2.11 shows a similar pattern to that observed across the probability distributions for the number of exposures in that the violin plot from the Wells-Riley per capita illustrates relatively high risk, with the 25^{th}, 50^{th}, and 75^{th} distribution percentiles being equal to 0.6323, 0.7196, and 0.8054, respectively. The distribution also has a large spread, with predicted per capita probabilities ranging from 0.2193 to 0.9624, illustrating the uncertainty in the quanta emission rate prediction and consequently, the sample from the Erlang distribution contains a broad spectrum of possible quanta emission rates.

The prediction from the Erlang per capita probability, informed by the parameters of the calibrated Erlang distribution, gives a per capita probability of 0.7069. This is closely aligned to the mean (0.7025) and median (50th percentile; 0.7196) of the distribution formed from the Wells-Riley per capita probability, and is able to summarise a sample of 100 different quanta emission rates into a single point. This is consistent with the fact that Equation (2.22) represents the statistical mean of the steady-state per capita probability of infection weighted by the Erlang distribution. Therefore, when using the Erlang per capita probability from Equation (2.22), this accounts for the uncertainty of

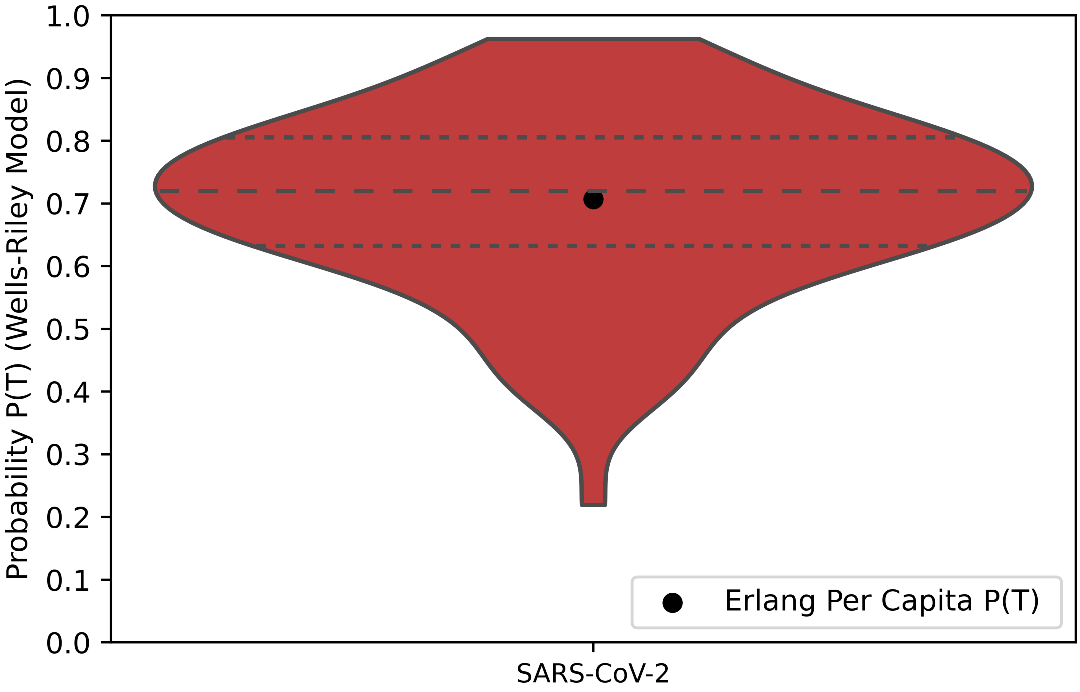

Figure 2.11: Violin plot for the distribution of per capita $P(T)$ for the traditional Wells-Riley model (Equation (2.1)) with 100 emission rates, q, sampled from the calibrated Erlang distribution (Figure 2.9), along with the per capita $P(T)$ for unknown emission rate (q [quanta h^{-1}]) using the Erlang distribution parameters (Equation (2.22)).

the parameter estimation when predicting infection risk and per capita probabilities, with this scenario demonstrating its applicability in scenarios where the exact quanta emission rate may be unknown or uncertain.

2.5 Discussion

This chapter has extended the traditional Wells-Riley framework, in order to assess risk in situations where the infector leaves the room but the susceptible individual remains, the duration of the indoor interaction is random/unknown, or with heterogeneity in infectivity across infectious individuals. The per capita probability of infection for each susceptible individual in these scenarios has been computed, and the probability distribution for the number of infections has been estimated.

When using the traditional Wells-Riley model under the steady-state assumption, the risk of infection is only non-zero when the infector is present. However, the suspension of infectious aerosols means that the risk remains possibly long after the infector leaves. By using a transient concentration of pathogen solution, it is possible to model the gradual growth and decay of the airborne pathogen concentration, and as a result, the accompanying infection risk. This allows for the computation of the probability of infection whilst the infector is present, and once they leave, giving a holistic risk assessment to a susceptible individual, acknowledging that the risk of infection stretches beyond the presence of an infector. This aids understanding of what governs infection risk, and how this may differ across the two time periods. This chapter provides the analytical solution for this probability for a single zone where the susceptible individual is present for a particular time period (Equation (2.14)) or for long after the infector leaves (Equation (2.15)).

The applicability of these results has been shown via a first case study (Section 2.4.1), where real-life HCW visit times data were leveraged, and used to estimate the risk experienced by the susceptible patient before and after the infector (HCW) leaves the space. The results show that the post-departure risk is non-negligible, and becomes even more important for shorter visit times, or under smaller removal rates. The results assume that the susceptible individual is present for $t \to \infty$ after the infector leaves. This is more relevant for hospitals wards, such as an adult respiratory ward where patients are often admitted as inpatients for longer periods. It is possible that the percentage contribution from the period after the infector leaves is much less if the susceptible individual also leaves shortly after.

It is possible that such a large contribution from the second period was seen due to the small time scales used for the presence of the infector. Even though these are realistic times (taken from measured data (King et al. [2021b])), if alternative scenarios were considered where the infector was present for longer periods, a smaller overall contribution from the second period may be seen. This would be scenarios where the first period displays steady-state-like behaviour. It is possible to see hints of this in Figure 2.4d, for example, in the case with the highest removal rate $(R = 3.87\,\mathrm{m}^3\,\mathrm{min}^{-1})$ and the longest visit time (19.28 min). This will most likely be the closest to steady-state behaviour out of all the modelled visit times and thus, the contribution from the second period is the smallest. Simultaneously, this further illustrates the importance of including the period after the infector leaves for shorter visits and poor removal rates, as its relevance can vary depending on the scenario parameters.

A limitation of the methodology in Section 2.3.1 is that only a single zone is considered. It is likely that when the infectious person leaves the room, they then enter a neighbouring zone, and so could still contribute to the infection risk in the original zone where the susceptible individual is situated. As previously discussed, transmission can occur across zones with shared airflow (Eichler et al. [2021], SAGE [2021]), with respiratory aerosols becoming entrained in the ambient airflow and transported to connected spaces. Chapter 3 shows that when extending models to consider multi-zone environments, it is possible to illustrate how an infector can have an impact on infection risk in connected zones.

An example of the stochasticity that exists in real life, which is overlooked by the traditional Wells-Riley model, is not knowing the duration of an outbreak, or the time that the infector is present in the space for. In these scenarios, it may be more suitable to consider a random duration, in the form of a distribution. This way, it is possible to estimate infection risk while accounting for realistic time distributions that are representative of typical behaviour experienced in the corresponding setting. This methodology was explored in Section 2.3.2, providing explicit solutions for steady-state concentration in a single room for two well-known distributions commonly used to model waiting times; Exponential and Erlang. A limitation of this methodology is the use of the steady-state solution for the concentration of airborne pathogen in the model, so future work should be devoted to generalise these results for a transient concentration of pathogen in the air. The importance of transient effects are demonstrated in Chapters 3 and 4.

Case Study 2 (Section 2.4.2) explored the possibility of not knowing the duration of the indoor interaction. In particular, infection risk during lunch in different dining settings was considered, and for different party sizes, by fitting an Erlang distribution to measured meal duration data. The resulting Erlang distributions varied across the scenarios with long meal durations experienced more so in the workplace cafeteria or in the moderately priced restaurant, whereas the fast-food restaurant had much smaller meal durations and less variation across the party sizes. This pattern was consistent with the infection risk, where settings of typically longer meal durations lead to a higher risk of infection, as does the increase in the party size. It can be observed how decreasing the removal rate increased the risk of infection across all scenarios, but the distribution of the risk of possible predicted exposures was still dominated by the distributions of meal durations.

When analysing the per capita probability of infection (Figure 2.8) the importance of considering social factors when assessing infection risk was illustrated. Intuitively, the per capita probability of infection should be unaffected by change in population size under the assumption that a single infector is present, but the results showed how the typical time spent in each scenario is highly influenced by social setting and party size, leading to variations in the per capita probability that are often overlooked when the exact exposure time is known. The per capita probability of infection for an Erlang-distributed time duration, represented as a single point in Figure 2.8, is closely aligned to the mean value of the standard Wells-Riley per capita probability of infection across 100 time durations sampled from the corresponding Erlang distribution, which is consistent with its derivation as the statistical mean weighted by an Erlang distribution. Thus, the single estimate is able to quantify infection risk while accounting for the uncertainty in the duration of the indoor interaction. This demonstrates the importance of incorporating uncertainty in the duration of the indoor interaction when estimating infection risk, rather than using a single estimate of this duration.

Case study 3 explored a scenario where the quanta emission rate was an estimate based on the Skagit Valley chorale superspreading event during the COVID-19 pandemic (Miller et al. [2021]). Here, a mean and SD were provided for a quanta emission rate, which was used to calibrate an Erlang distribution, following a similar approach to when exploring random meal duration (Section 2.3.2) given that both time and the quanta emission rate feature linearly in the exponent of the mathematical framework e.g., in the Wells-Riley model (Equation (2.1)). The results here were as expected given that this was an uncertain estimate of a superspreading event, with large variability seen in the per capita probability of infection distributed as a violin plot, with infection risk ranging from 21% to 96% from a 1 h outbreak. This illustrates the uncertainty in the quanta emission rate prediction and the resulting Erlang distribution. In addition, it is seen how the Erlang per capita probability for a random emission rate can quantify infection risk into a single value when compared to 100 Wells-Riley per capita probabilities, computed via Equation (2.1) by randomly sampling 100 Erlang-distributed emission rates. This single estimate encodes the variability of the distribution and offers a simple alternative for future analysis as opposed to working with distributions of highly variable per capita probabilities.

This case study further demonstrates the capability and ease of implementing the theory presented in Section 2.3.3, particularly in cases where the parameter estimation may be uncertain due to the nature of an outbreak. However, this methodology could be used in a similar way if a more accurate, representative distribution for a particular pathogen is known, but it is of interest to explore scenarios where the infectiousness (quanta emission rate) of a specific individual may be random, or vary between individuals (i.e., population heterogeneity). This could also be useful in allowing for general comparisons across different pathogens, for informative or exploratory modelling, and when investigating mitigation measures for future preparedness.

2.6 Conclusion

This chapter presented novel mathematical techniques to assess infection risk that build on the existing Wells-Riley framework. Through the inclusion of stochasticity, the existing methodology presented in the Wells-Riley model is taken and is used to derive the probability distribution of the number of exposures/infections. Moreover, the results were extended in order to assess risk of infection in the period after the infector leaves, and when considering an unknown random outbreak duration, or quanta generation rate, in terms of probability distributions. This chapter illustrated this methodology through three case studies: one case study that shows that the period after the infector leaves can contribute non-negligible risk, another case study which illustrates the risk for various restaurant scenarios where the exact duration of each outbreak is unknown, and a final case study exploring a scenario where an uncertain estimate is given for the quanta emission rate. This study successfully developed new, explicit formulas for the infection probability in these scenarios, increasing the applicability of the Wells-Riley framework, with a better representation of the characteristics that are faced when trying to model real-life outbreaks.

2.A Per capita probability of infection during $[0, T]$ under Exponentially distributed or Erlang distributed random times

Consider that T is exponentially distributed with rate λ, $T \sim Exp(\lambda)$, so that $f_T(t) = \lambda e^{-\lambda t}$ for $t \geq 0$. Then, the per capita probability of infection during $[0, T]$ is

$$\begin{aligned} P(T) &= \int_0^\infty \left(1 - e^{-(\frac{pqI_0}{Q})t}\right) \lambda e^{-\lambda t}\, dt \\ &= \int_0^\infty \lambda e^{-\lambda t}\, dt \;-\; \int_0^\infty \lambda e^{-(\frac{pqI_0}{Q}+\lambda)t}\, dt \\ &= 1 + \frac{\lambda}{\frac{pqI_0}{Q} + \lambda} \left[e^{-(\frac{pqI_0}{Q}+\lambda)t} \right]_{t=0}^{\infty} \end{aligned}$$

so that

$$P(T) \;=\; 1 - \frac{\lambda}{\frac{pqI_0}{Q} + \lambda}\,,$$

which corresponds to Equation (2.18).

If instead $T \sim Erlang(k,\; \lambda)$ is considered, so that $f_T(t) = \frac{\lambda^k\, t^{k-1}\, e^{-\lambda t}}{(k-1)!}$ for $t \geq 0$, the per capita probability of infection during $[0, T]$ is given by

$$\begin{aligned} P(T) &= \int_0^\infty \left(1 - e^{-(\frac{pqI_0}{Q})t}\right) \frac{\lambda^k\, t^{k-1}\, e^{-\lambda t}}{(k-1)!}\, dt \\ &= \int_0^\infty \frac{\lambda^k\, t^{k-1}\, e^{-\lambda t}}{(k-1)!}\, dt \;-\; \int_0^\infty \frac{\lambda^k\, e^{-(\frac{pqI_0}{Q}+\lambda)t}\, t^{k-1}}{(k-1)!}\, dt \\ &= \underbrace{\frac{\lambda^k}{(k-1)!} \int_0^\infty e^{-\lambda t}\, t^{k-1}\, dt}_{(\dagger)} \;-\; \underbrace{\frac{\lambda^k}{(k-1)!} \int_0^\infty e^{-(\frac{pqI_0}{Q}+\lambda)t}\, t^{k-1}\, dt}_{(\dagger\dagger)}\,. \end{aligned}$$

It is possible to compute $(\dagger)$

$$\int_0^\infty \frac{\lambda^k}{(k-1)!} e^{-\lambda t}\, t^{k-1}\, dt \;= 1$$

since it corresponds to integrating the density function of an $Erlang\,(k, \lambda)$. Also, computing (††)

$$\begin{aligned}\int_0^\infty \frac{\lambda^k\, t^{k-1}}{(k-1)!}\, e^{-(\frac{pqI_0}{Q}+\lambda)t} dt &= \left(\frac{\lambda}{\frac{pqI_0}{Q}+\lambda}\right)^k \underbrace{\int_0^\infty \frac{t^{k-1}}{(k-1)!} \left(\frac{pqI_0}{Q}+\lambda\right)^k e^{-(\frac{pqI_0}{Q}+\lambda)t}\, dt}_{\text{Equals 1, since it is the density of an } Erlang\left(k,\, \frac{pqI_0}{Q}+\lambda\right)} \\ &= \left(\frac{\lambda}{\frac{pqI_0}{Q}+\lambda}\right)^k.\end{aligned}$$

Thus,

$$P(T) = 1 - \left(\frac{\lambda}{\frac{pqI_0}{Q}+\lambda}\right)^k$$

which corresponds to Equation (2.20).

2.B Probability distribution of the number of exposures during $[0, T]$ for Exponentially distributed and Erlang distributed random times

Consider that T is exponentially distributed with rate λ, $T \sim Exp(\lambda)$, so that $f_T(t) = \lambda e^{-\lambda t}$ for $t \geq 0$. Then, the probability of observing exactly n exposures during $[0, T]$, for $n \in \{0, 1, \ldots, S_0\}$, is given by

$$\begin{aligned}
\mathbb{P}\{E(T) = n\} &= \int_0^\infty \binom{S_0}{n} \left(1 - e^{-\frac{pqI_0}{Q}t}\right)^n \left(e^{-\frac{pqI_0}{Q}t}\right)^{S_0 - n} \lambda e^{-\lambda t}\, dt \\
&= \binom{S_0}{n} \lambda \int_0^\infty \underbrace{\left(1 - e^{-\frac{pqI_0}{Q}t}\right)^n}_{\text{Use Binomial Expansion}} \left(e^{-\frac{pqI_0}{Q}t}\right)^{S_0 - n} e^{-\lambda t}\, dt \\
&= \binom{S_0}{n} \lambda \int_0^\infty \left(e^{-\frac{pqI_0}{Q}t}\right)^{S_0 - n} e^{-\lambda t} \sum_{i=0}^{n} (-1)^i \binom{n}{i} e^{-i\frac{pqI_0}{Q}t}\, dt \\
&= \binom{S_0}{n} \lambda \sum_{i=0}^{n} (-1)^i \binom{n}{i} \int_0^\infty e^{-\left[(S_0 - n + i)\frac{pqI_0}{Q} + \lambda\right] t}\, dt \\
&= -\binom{S_0}{n} \lambda \sum_{i=0}^{n} (-1)^i \binom{n}{i} \left[\frac{1}{(S_0 - n + i)\frac{pqI_0}{Q} + \lambda} e^{-\left[(S_0 - n + i)\frac{pqI_0}{Q} + \lambda\right] t}\right]_{t=0}^{\infty},
\end{aligned}$$

which leads to

$$\mathbb{P}\{E(T) = n\} = \binom{S_0}{n} \sum_{i=0}^{n} (-1)^i \binom{n}{i} \left(\frac{\lambda}{(S_0 - n + i)\frac{pqI_0}{Q} + \lambda}\right)^k, \quad n \in \{0, 1, \ldots, S_0\},$$

corresponding to Equation (2.19).

Alternatively, if $T \sim Erlang(k,\ \lambda)$ is considered, so that $f_T(t) = \frac{\lambda^k\, t^{k-1}\, e^{-\lambda t}}{(k-1)!}$ for $t \geq 0$, the probability of observing exactly n exposures during $[0, T]$, for $n \in \{0, 1, \ldots, S_0\}$, is given by

$$\mathbb{P}\{E(T) = n\} = \int_0^\infty \binom{S_0}{n} \left(1 - e^{-\frac{pqI_0}{Q}t}\right)^n \left(e^{-\frac{pqI_0}{Q}t}\right)^{S_0 - n} \frac{\lambda^k\, t^{k-1}\, e^{-\lambda t}}{(k-1)!}\, dt$$

$$
\begin{aligned}
&= \binom{S_0}{n} \frac{\lambda^k}{(k-1)!} \int_0^\infty \underbrace{\left(1 - e^{-\frac{pqI_0}{Q}t}\right)^n}_{\text{Use Binomial Expansion}} \left(e^{-\frac{pqI_0}{Q}t}\right)^{S_0-n} e^{-\lambda t}\, t^{k-1}\, dt \\
&= \binom{S_0}{n} \frac{\lambda^k}{(k-1)!} \int_0^\infty \left(e^{-\frac{pqI_0}{Q}t}\right)^{S_0-n} e^{-\lambda t}\, t^{k-1} \sum_{i=0}^{n} (-1)^i \binom{n}{i} e^{-i\frac{pqI_0}{Q}t}\, dt \\
&= \binom{S_0}{n} \frac{\lambda^k}{(k-1)!} \sum_{i=0}^{n} (-1)^i \binom{n}{i} \int_0^\infty \underbrace{e^{-\left[(S_0-n+i)\frac{pqI_0}{Q}+\lambda\right]t}}_{\text{Let } \gamma_i = (S_0-n+i)\frac{pqI_0}{Q}+\lambda} t^{k-1}\, dt \\
&= \binom{S_0}{n} \sum_{i=0}^{n} (-1)^i \binom{n}{i} \left(\frac{\lambda}{\gamma_i}\right)^k \underbrace{\int_0^\infty e^{-\gamma_i t} \frac{(\gamma_i)^k t^{k-1}}{(k-1)!}\, dt}_{\text{Equals 1, since it is the density of an } Erlang\,(k,\gamma_i)} \\
&= \binom{S_0}{n} \sum_{i=0}^{n} (-1)^i \binom{n}{i} \left(\frac{\lambda}{\gamma_i}\right)^k .
\end{aligned}
$$

Finally, recalling that $\gamma_i = (S_0 - n + i)\frac{pqI_0}{Q} + \lambda$, gives

$$
\mathbb{P}\{E(T) = n\} = \binom{S_0}{n} \sum_{i=0}^{n} (-1)^i \binom{n}{i} \left(\frac{\lambda}{(S_0 - n + i)\frac{pqI_0}{Q} + \lambda}\right)^k, \quad n \in \{0, 1, \ldots, S_0\},
$$

which corresponds to Equation (2.21).

2.C Numerical validation of the probability of a given number of exposures during $[0, T]$ for Exponentially distributed and Erlang distributed random times

To validate Equation (2.19), a mock outbreak was modelled with the quanta production rate $q = 30\,\text{quanta}\,\text{h}^{-1}$, pulmonary breathing rate $p = 0.6\,\text{m}^3\,\text{h}^{-1}$, the volume $v = 100\,\text{m}^3$, the extract ventilation rate $Q = 100\,\text{m}^3\,\text{h}^{-1}$ giving 1 ACH, the initial number of susceptible individuals $S_0 = 10$, and the initial number of infectors was $I_0 = 1$. $1,000,000$ samples of random times from an exponential distribution were taken, $Exp(\lambda)$, where $\lambda = \frac{S_0 pq I_0}{Q}$. These random times were then used to represent the outbreak duration. For each $1,000,000$ times, T, and the parameters defined above, the probability of each possible number of exposures for a binomial distribution for steady-state concentration (namely Equation (2.7)) was calculated. An average of these probabilities was taken and then compared against the analytical solution (Equation (2.19)). The result can be seen in Figure 2.12. As can be seen from the figure, both solutions are the same and thus, can conclude that Equation (2.19) has been validated numerically.

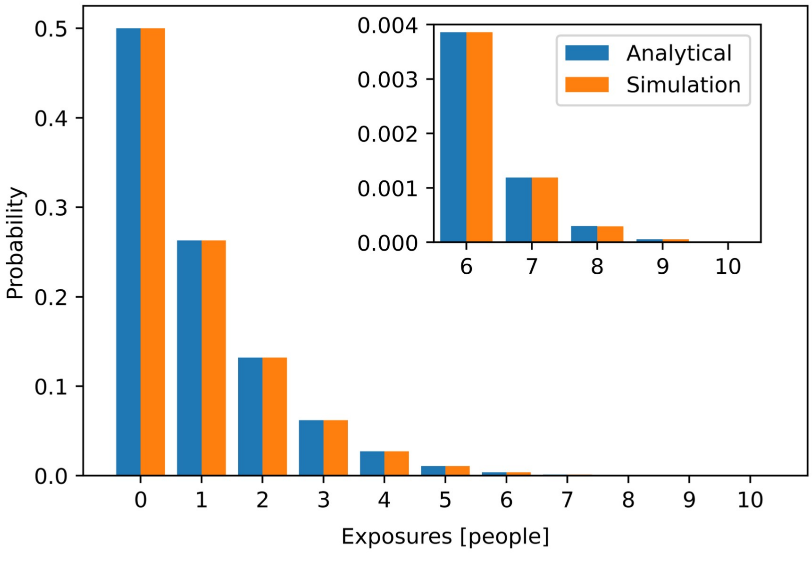

Figure 2.12: A comparison between Equation (2.19) and a result obtained by direct numerical simulation for validation of the probability of a given number exposures for Exponentially distributed random times.

An identical method to above was used to validate Equation (2.21). The only difference between the two methods is that the sample of random times was taken from an Erlang distribution, $Erlang(k, \lambda)$, where λ remained the same as in the previous case, and $k = 6$. The results can be seen in Figure 2.13. Again, both solutions are identical and thus, can conclude that Equation (2.21) has been validated numerically.

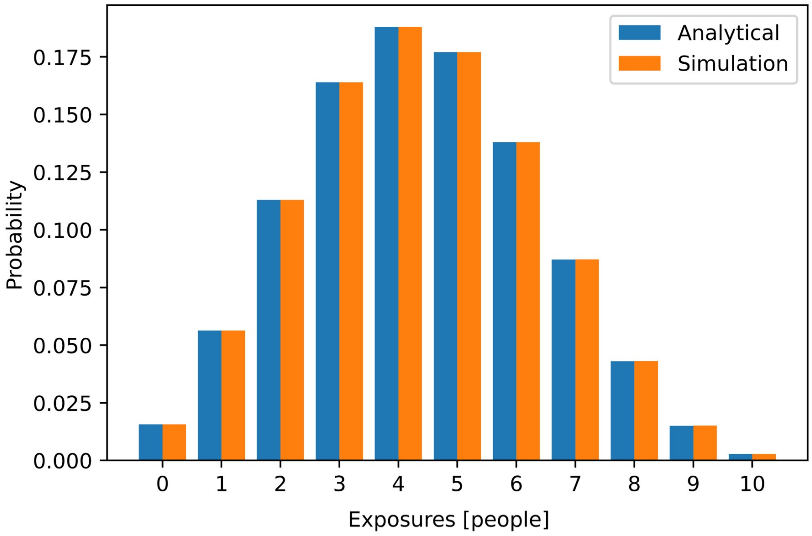

Figure 2.13: A comparison between Equation (2.21) and a result obtained by direct numerical simulation for validation of the probability of a given number exposures for Erlang distributed random times.

It is noted that as both time, T, and quanta production rate, q, occur as linear terms in the exponent when calculating the steady-state per capita probability of infection, $P(T)$ in Equation (2.1), the validations here also apply to the equivalent results stated in Section 2.3.3.

Chapter 3

A Transient Multi-zone Transmission Model

Quantification of the parameters influencing airborne infection risks associated with indoor activities in different settings can help in understanding outbreak dynamics and the effective implementation of mitigation strategies. This is particularly important in hospitals, where the consequence of infections amongst vulnerable individuals can be significant. Despite the transient occupancy and inter-connected nature of hospital wards, the majority of airborne risk models assume steady-state conditions and well-mixed air in a single zone. This chapter proposes a multi-zone model with both a fixed (i.e., stationary in one zone) and time-varying (i.e., moving between zones) infectious person. It uses an adapted version of the Wells-Riley model to estimate transient airborne virus concentration, and account for time-varying behaviour in the indoor setting. Through a coupling with a CONTAM airflow network model, the effects of ventilation patterns on inter-zonal flow rates are incorporated to represent likely airflow in a realistic hospital ward. This approach is used to explore the difference in predictions from transient versus steady-state models across several scenarios. Results suggest that a steady-state approach could lead to an overestimation of infection risk or underestimation of quanta emission, especially when the infectious person is only present for a short period of time. The difference between models is most apparent in poorly ventilated spaces, illustrating how risks can build over time when infectious occupant movement is more frequent than the removal rate due to ventilation. The model highlights the importance of considering transient factors when assessing infection risks to ensure that the most effective mitigation strategies are implemented to address long and short timescale risks.

Chapter 3 contains material from the jointly authored publication:

> **Edwards AJ**, Benson L, Guo Z, López-García M, Noakes CJ, Peckham D, King MF, A mathematical model for assessing transient airborne infection risks in a multi-zone hospital ward, *Building and Environment*, 2023, Volume 238, p.110344.
> `https://doi.org/10.1016/j.buildenv.2023.110344.`

The code and data for this manuscript are available at `https://github.com/scaje/Multi-zone_Hospital_conc_AJE.git`.

3.1 Introduction

The COVID-19 pandemic has highlighted the importance of understanding the factors which influence airborne transmission and how we manage the associated risk. With respiratory diseases already being a major contributor to pressure on hospital systems such as the NHS in the UK, even more so during the winter (NHS [2022]), it is especially important to minimise the transmission of nosocomial infections through the airborne route. Understanding the transport of pathogens in the air and the influence of the ward layout and ventilation system is a crucial part of designing and managing hospital environments to mitigate airborne transmission risks.

Real world hospital environments are complex and busy spaces with a considerable level of transient activity including behaviour of HCWs and visitors entering, leaving and moving around the space. The concentration of airborne pathogens is also transient in nature and may depend on the emission rate from an infected person (Buonanno et al. [2020b]) and governing airflow factors including ventilation within rooms and airflow between rooms. These factors must be considered in an appropriate way for the specific scenario in order to evaluate the concentration of pathogen in indoor spaces and thus, provide a better estimation of the epidemiological dynamics. However, many previous and current indoor transport and dispersion models only consider steady-state behaviour, both spatially and temporally, whether this be through CFD analysis (Qian et al. [2009], King et al. [2013], Cheong and Lee [2018]) or risk assessments using the Wells-Riley model (Noakes et al. [2006b], Robertson et al. [2011], Qian et al. [2009]).

The Wells-Riley model (Wells et al. [1955], Riley et al. [1978]) is widely used to estimate the influence of ventilation on the number of newly infected individuals during the time interval $[0, T]$ in an indoor setting, and is given by Equation (1.1). The model aims to provide an assessment of the risk of infection for a given single zone, for a particular emission rate of infectious doses expressed through q [quanta min^{-1}], as previously stated. It is widely recognised that the use of quanta to describe infectious dose emitted is a simplification of the transmission process. Some studies have looked to relate this directly to emitted virus either through measurement (Bueno de Mesquita et al. [2020]) or through calculation (Buonanno et al. [2020b]), and a recent analysis has shown that quanta emission rates for different diseases can have very large ranges (Mikszewski et al. [2021]). However, quanta based steady-state models have been shown to compare well to COVID-19 super-spreading outbreaks suggesting that the approach can be valuable for assessing risk (Peng et al. [2022]).

Previous studies have used multi-zone models (Noakes and Sleigh [2009], López-García et al. [2019]). However, these use idealised airflow assumptions with steady-state quanta concentrations to demonstrate model behaviour rather than consider the ventilation in a realistic environment. A better approximation of indoor airflow can be modelled using ventilation network models, such as CONTAM, as introduced in Chapter 1.

In this chapter, an adaptation of the Wells-Riley model is used to develop a transient multi-zonal approach to model the concentration of pathogen in the air and infection risk in a hospital scenario. This is illustrated through two case studies: (i) a scenario with a fixed patient infector who is stationary in one of the ward zones and (ii) a scenario with a transient infector, representing an infectious HCW completing a drug round. The first scenario uses an idealised ventilation assumption to compare to Noakes and Sleigh [2009] and López-García et al. [2019]. The second transient infector case assumes that the infectious person moves from one zone to another in time within a geometry based on a UK respiratory ward, with inter-zonal flow values extracted from a CONTAM airflow simulation.

3.2 Methodology

3.2.1 Transmission Model

Modelling transmission and outbreak dynamics is traditionally based on the SIR model, originally introduced by Kermack and McKendrick [1927]. There have been many variations of this compartmental model, for example SIS assumes no immunity on recovery (Arino et al. [2016], López-García et al. [2019]) and SEIR includes the latent period (Noakes et al. [2006b], Chen and Liao [2008], Sun and Hsieh [2010]). These models have also been coupled to the Wells-Riley model (Noakes et al. [2006b], López-García et al. [2019]) to explore the impact of indoor conditions on outbreak dynamics. These epidemic models are suited to population scale simulations with a duration of several days or weeks, however in indoor settings such as a hospital ward, the complexity of interactions between people and admission-discharge patterns makes modelling the whole outbreak challenging.

Here, an SE model is used, as introduced in Chapter 2 (Equation (2.2)), where one considers the transmission dynamics in an indoor setting during a time interval $[0, T]$. In this time interval, $[0, T]$, it is assumed that newly infected individuals are taken to be exposed and infected but are not yet infectious due to being in the latent period. This allows for a simplified compartmental model without the added complexity of new infectors or accounting for changes in the population size in the setting, allowing for focus purely on the model dynamics in the early stages. The equations, re-written in a slightly different form to Chapter 2, are:

$$\begin{aligned}\frac{dS(t)}{dt} &= -\psi S(t),\\ \frac{dE(t)}{dt} &= \psi S(t),\end{aligned} \tag{3.1}$$

where $S(t)$ represents the number of susceptible individuals at time t, and $E(t)$ the number of exposed (i.e., infected but not infectious) individuals at time t. The infection rate ψ contains the parameter defining the number of infectious individuals in the indoor setting, $I(t) = I_0$, which is assumed to be constant during the time interval of interest $[0, T]$. To model transient effects, the infection rate is considered to be time-dependent, and given by $\psi(t) = pC(t)$, where p [$\mathrm{m^3\,min^{-1}}$] is the pulmonary breathing rate and $C(t)$ [quanta $\mathrm{m^{-3}}$] is the concentration of airborne pathogen at time t, which is characterised by the conservation Equation (2.3).

The standard Wells-Riley methodology defines a constant infection rate $\psi = pC^*$, where $C^* = \frac{qI}{Q}$ is the steady-state solution (Equation (2.5)). On the other hand, a transient version involves defining $\psi(t) = pC(t)$, where $C(t)$ is the transient solution of Equation (2.3), as shown in Equation (2.4).

Following the approach in López-García et al. [2019], the single-zone model can be extended to a transient multi-zone case for M zones:

$$v_k \frac{dC_k(t)}{dt} = q_k I_k - Q_k C_k(t) - \sum_{j=1}^{M} \beta_{kj} C_k(t) + \sum_{j=1}^{M} \beta_{jk} C_j(t)\ , \quad k = 1, \ldots, M \tag{3.2}$$

where $C_k(t)$ is the quanta concentration in the air in Zone k, I_k is the number of infectious individuals in Zone k, Q_k [$\mathrm{m^3\,min^{-1}}$] represents the extract ventilation rate in Zone k, and q_k [$\mathrm{quanta\,min^{-1}}$] represents the per capita quanta production rate for infectious individuals in Zone k. β_{kj} [$\mathrm{m^3\,min^{-1}}$] is the inter-zonal flow rate from Zone k to j, which is only non-zero if Zone k is connected to Zone j (López-García et al. [2019]). The individual zones represent single spaces such as rooms, bays, or corridors which are connected to other zones to form a multi-zone environment via doors or openings. Larger rooms may also be split up into multiple zones themselves, which are connected directly through an opening from floor-to-ceiling and wall-to-wall. Multiple connected single zones form a multi-zone geometry.

In addition to Equation (3.2), it is also necessary to extend the SE model presented in Equation (3.1) for a multi-zone case of M zones:

$$\begin{aligned}\frac{dS_k(t)}{dt} &= -\psi_k S_k(t),\\ \frac{dE_k(t)}{dt} &= \psi_k S_k(t),\end{aligned} \tag{3.3}$$

for $k = 1, \dots, M$, where the infection rate becomes $\psi_k = p_k C_k(t)$.

The system of equations given by Equation (3.2), which models the concentration of pathogen in the air in each zone $k = 1, \dots, M$, can be written in matrix form as

$$\mathbf{v}\frac{d\mathbf{C}(t)}{dt} = \mathbf{q} \circ \mathbf{I} - \mathbf{V}\mathbf{C}(t), \tag{3.4}$$

where **C**(t) is the column vector of concentrations in each zone, which is spatially constant for any given time, inside a given zone. **V** is the ventilation matrix, **v** is the column vector of volumes for each zone, **q** is the column vector of quanta production rate for each zone and **I** is the column vector for the number of infectious individuals for each zone, where the symbol ∘ represents the element-wise product of the two column vectors. This gives the ventilation matrix **V** as:

$$\mathbf{V} = \begin{pmatrix} Q_1 + \sum_k \beta_{1k} & -\beta_{21} & -\beta_{31} & \cdots & -\beta_{M1} \\ -\beta_{12} & Q_2 + \sum_k \beta_{2k} & -\beta_{32} & \cdots & -\beta_{M2} \\ -\beta_{13} & -\beta_{23} & \ddots & \ddots & -\beta_{M3} \\ \vdots & \vdots & \vdots & \vdots & \vdots \\ -\beta_{1M} & -\beta_{2M} & \cdots & -\beta_{M-1,M} & Q_M + \sum_k \beta_{Mk} \end{pmatrix}.$$

The inter-zonal flow rates, β_{kj} [$\mathrm{m^3\,min^{-1}}$], can be approximated, informed by experiments, or extracted from other airflow simulations. In Case Study 1 (Section 3.3.1), constant and idealised values were used for both ventilation rates and inter-zonal flow rates for the whole simulation time. These were followed by models where the CONTAM software was used to determine the values of β_{kj} for a naturally ventilated hospital (Case Study 2 in Section 3.3.2). The theoretical details of the CONTAM model and the way in which the inter-zonal flow values are extracted can be seen in Section 3.2.2.

In a similar way, the steady-state system of zonal concentration of airborne pathogen can be recovered from Equation (3.4) to give:

$$\mathbf{C}^{*} = \mathbf{V}^{-1}\mathbf{q} \circ \mathbf{I}, \tag{3.5}$$

which will be used as a comparison to the transient solution, obtained from numerically solving Equation (3.4), in Sections 3.3.1 and 3.3.2.

It is worth noting that the equations for the concentration of pathogen in the air (Equations (2.3), (3.2) and (3.4)) do not include a turbulence flux term. This study aims to model long-range exposure across multi-connected zones rather than focus on short-range exposure, where turbulence fluxes would dominate. To evaluate short-range exposures, alternative approaches such as CFD modelling (Foat et al. [2022]) or analytical approximation of aerosol size distributions with distance (Miller et al. [2022]) would be needed.

3.2.2 Airflow Simulations

CONTAM 3.4.0.3 (Dols and Polidoro [2015], National Institute of Standards and Technology [2022]) is used alongside the transmission model, described in Section 3.2.1, to determine inter-zonal flow values β_{kj}, used within the transmission model in Case Study 2 (Section 3.3.2). This allows for added complexity in the model, and allows for the simulation of a naturally ventilated multi-zonal scenario, incorporating transient behaviour. To extract the inter-zonal flow rates, the results of each simulation are processed using the CONTAM *Results Export Tool* (Polidoro et al. [2016], NIST [2022]). This allows for the export of the airflow results through each airflow element, which can then be used as the values for β_{kj} in Equation (3.2), demonstrating the successful coupling of the two separate approaches.

A multi-zone hospital ward is considered, where each zone is set to have an ambient temperature of 20°C. For each Zone k, the air mass balance equation is considered:

$$m_{0,k} - m_{k,0} + m_{v,k} - m_{k,v} + \sum_{j} m_{k,j} - \sum_{j} m_{j,k} = 0, \tag{3.6}$$

where $m_{k,j}$ [kg min^{-1}] is the mass airflow entering Zone j from Zone k, and $m_{j,k}$ [kg min^{-1}] is the mass airflow entering Zone k from Zone j. $m_{0,k}$ [kg min^{-1}] is the total mass airflow entering Zone k from the outside environment and $m_{k,0}$ [$\mathrm{kg\,min^{-1}}$] is the total mass airflow leaving Zone k into the outside environment (e.g., natural ventilation). These can include through means of openings, leaks, doors and windows. $m_{k,v}$ [$\mathrm{kg\,min^{-1}}$] is the total mass airflow extracted from Zone k due to mechanical extract ventilation and $m_{v,k}$ [$\mathrm{kg\,min^{-1}}$] is the total mass airflow for the mechanical supply ventilation to Zone k.

In this case, the inter-zonal flow rates in Section 3.2.1 can be linked with those above extracted from the CONTAM model, as

$$\beta_{kj} = \frac{m_{k,j}}{\rho_k}, \tag{3.7}$$

where ρ_k [$\mathrm{kg\,m^{-3}}$] is the air density in Zone k.

When modelling windows, doors and other openings it is necessary to consider airflow rates through the opening as well as through surrounding gaps and leakage. This can help to capture any unintentional or accidental introduction of outside air into a building (i.e., infiltration air (Younes et al. [2012])). In this case, the mass flow rate is calculated from the pressure gradients using an orifice assumption in the power law equation (Guyot et al. [2022])

$$m_{k,j} = \rho_k C_d \Delta P_{k,j}^{n_{fe}}. \tag{3.8}$$

Here ρ_k [$\mathrm{kg\,m^{-3}}$] is the air density in Zone k, C_d [$\mathrm{m^3\,min^{-1}\,Pa^{-1}}$] is the discharge coefficient, $\Delta P_{k,j}^{n_{fe}}$ [Pa] is the pressure difference between Zone k and Zone j with n_{fe} as the flow exponent.

Throughout the simulations in Section 3.3.2, the discharge coefficient is set as $C_d = 46.8\ \mathrm{m^3\,min^{-1}\,Pa^{-1}}$ (equivalent to $C_d = 0.78\ \mathrm{m^3\,s^{-1}\,Pa^{-1}}$). This is the default value given by CONTAM, which is an experimentally determined value shown to work well for most applications (Weber and Kearney [1980], Dols and Polidoro [2015]). The flow exponent is also kept at the default value for CONTAM, $n_{fe} = 0.5$. Flow exponents vary from $n_{fe} = 0.5$ for large openings, where the flow is dominated by dynamic effects, to $n_{fe} = 1$ for narrow openings dominated by viscous effects (Dols and Polidoro [2015]).

The pressure in each zone is calculated based on the differences in air densities. This accounts for any temperature differences and consequent stack effects, based on the hydrostatic equation. Additionally, this requires the input of external pressures acting on the walls which is linked to the wind conditions as follows (Persily and Ivy [2001], Guyot et al. [2022]):

$$P_k = \frac{1}{2}\rho_0 C_{P,k} u^2, \tag{3.9}$$

where P_k $[\mathrm{kg\,m^{-1}\,min^{-2}}]$ is the wind pressure on an external wall of Zone k, ρ_0 $[\mathrm{kg\,m^{-3}}]$ is the external air density, $C_{P,k}$ is the pressure coefficient at a leakage point in Zone k and u $[\mathrm{m\,min^{-1}}]$ is the velocity of the wind at the given altitude.

In Section 3.3.2, a leakage flow path was modelled alongside each external window and each internal door using Equation (3.8). This represents gaps around these elements or any reduction in air-tightness since fitting. Increased leakage helps to account for the fact that this subset of the ward is part of a much larger building with airflow that is not accounted for in the modelling. Windows remained closed for the full duration of the numerical simulation, so flow at the windows is via the leakage values only. It is assumed that doors between zones remained closed throughout, apart from when they were open for a 1-minute period to simulate the transient infectious HCW moving in and out of that particular zone. In Section 3.3.1, since this does not include a coupling with a CONTAM simulation, no comments are made on the opening state of the windows and doors. These are represented quantitatively only through the inter-zonal mixing rates as presented in Setting A in Noakes and Sleigh [2009] and López-García et al. [2019].

3.3 Results

This section presents two case studies where the methodology introduced in Section 3.2 is applied. These two scenarios aim to explore the influence of both an infector in a fixed location (an infectious patient), and a transient infector, representing an infectious HCW who completes a drug round, on the predictions of concentration of airborne pathogen and infection risk when using a steady-state model versus a transient model.

3.3.1 Case Study 1: Bed-bound Infectious Patient

3.3.1.1 The 9-zone Hospital Ward

To explore the case with a fixed infector who becomes infectious (or is admitted whilst being infectious) at $t = 0$ at a single location, the same idealised hospital ward scenario was used as in Noakes and Sleigh [2009] and López-García et al. [2019]. The geometry shown in Figure 1.1 consists of 3 bays, each split up into two zones and an adjoining corridor which is split up into 3 zones, connecting the end of each bay.

The model assumes a steady-state ventilation scenario with the same amount of air supplied to and extracted from each zone (Setting A in Noakes and Sleigh [2009] and López-García et al. [2019]). Airflow between adjacent Zones k and j is represented by an inter-zonal flow rate of $\beta_{k,j} = 9\,\mathrm{m}^3\,\mathrm{min}^{-1}$. The supply and extract ventilation in each zone is $Q_k = 3\,\mathrm{m}^3\,\mathrm{min}^{-1}, \quad \forall k$, which leads to an overall ward ventilation rate of $27\,\mathrm{m}^3\,\mathrm{min}^{-1}$ ($1620\,\mathrm{m}^3\,\mathrm{h}^{-1}$). The volume of each zone is $v_k = 60\,\mathrm{m}^3, \quad \forall k$, leading to a total ward volume of $v = 540\,\mathrm{m}^3$ and a total ventilation rate over the whole ward of 3 ACH (i.e., total ward ventilation rate divided by total ward volume). The inter-zonal flow set-up gives a case of homogeneous mixing in each zone i.e., the net boundary flow is zero. It is assumed that there are 3 individuals in each zone, with the infector located in Zone 1, giving $S_0 = (2, 3, 3, 3, 3, 3, 3, 3, 3)$, $E_0 = 0$ for each zone, and $I_0 = 1$ in Zone 1 only, and is zero for all other zones. The quanta emission rate of the infector is taken to be $q_1 = 0.5\,\mathrm{quanta\,min}^{-1}$ (Noakes and Sleigh [2009]). The pulmonary breathing rate of all individuals is taken to be $p_k = 0.01\,\mathrm{m}^3\,\mathrm{min}^{-1}, \quad \forall k$. The total population is 27 individuals, leaving 26 susceptibles when accounting for the infectious person in Zone 1. The initial concentration of pathogen in the air is taken to be $C_0 = 0$ in each zone.

Equations (3.3) and (3.4) were solved over a time period of $< 8\,\mathrm{h}$ meaning that it is reasonable to assume that the occupancy does not change and that this is within the incubation and latent period of the individuals who become exposed i.e., there are no new infectious individuals.

3.3.1.2 Effect of Ventilation Rate

Figure 3.1c shows the solution to the transient system (Equation (3.4)) for concentration of airborne quanta at 3 ACH (as used in Noakes and Sleigh [2009]) for each zone. This is plotted together with the steady-state (Equation (3.5)) concentration of pathogen in the air (dashed lines) in each zone. The results show that there is a substantial difference between the steady-state solution and transient solution within the first hour. When using the steady-state model, as commonly used within the Wells-Riley model (Wells et al. [1955], Riley et al. [1978]), there is an overestimation of the likely concentration, which is due to the time taken for the concentration to build up in the space. For example, the infectious person is fixed in Zone 1, however for the steady-state assumption at time $t = 0$ in Zone 2, the concentration level is non-zero and is in fact, over half of the value of the zone where the infectious person is present. This is clearly unrealistic and is better approximated by the transient solution, as it takes a non-negligible amount of time for the concentration of pathogen to flow into the adjoining Zone 2 from Zone 1 and begin to increase.

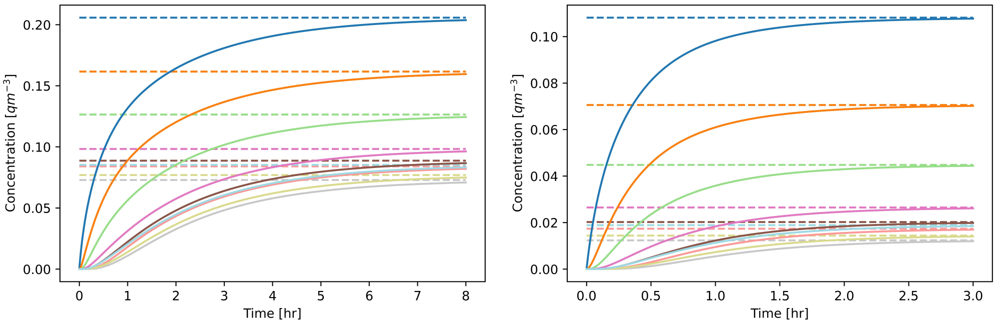

(a) 0.5 ACH

(b) 1.5 ACH

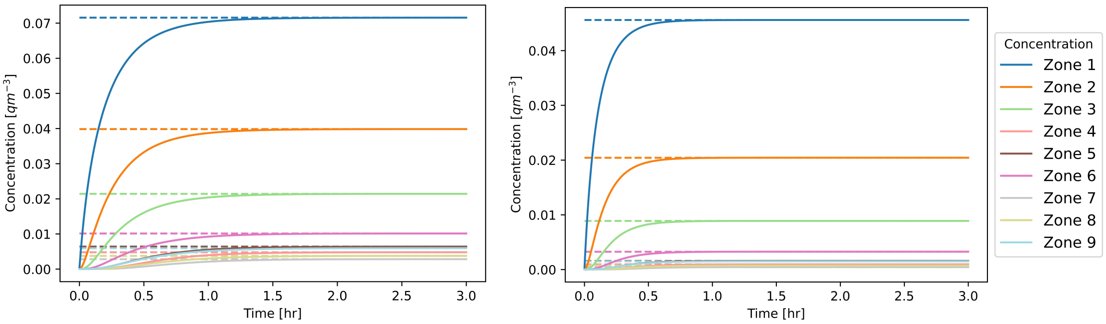

(c) 3 ACH

(d) 6 ACH

Figure 3.1: The solution for the quanta concentration in the air with the transient solution (solid) and the steady-state solution (dashed) for various ventilation rates for the fixed infector case.

The solutions for the quanta concentration with two lower ventilation rates are plotted in Figure 3.1a and Figure 3.1b, where the extract ventilation is changed to $Q_k = 0.5\,\text{m}^3\,\text{min}^{-1}$ and $Q_k = 1.5\,\text{m}^3\,\text{min}^{-1}$, equating to 0.5 ACH and 1.5 ACH, respectively. As expected, as the ventilation rate in the space reduces, the overestimation in the steady-state model becomes more significant. In Figure 3.1a, the simulation was extended to 8 h to illustrate that the transient concentration solution does not reach steady-state until close to $7 - 8\,\text{h}$, which is considerably longer than in the initial case of 3 ACH and even the case of 1.5 ACH, regardless of the fact that the steady-state value is much lower with both 3 ACH and 1.5 ACH. In addition to the effects on the accuracy of the model used, the change in ventilation rate also affects the absolute value of the transient and steady-state concentration of quanta in the space. For example, in the case of 3 ACH, even though the steady-state is reached significantly faster than for a lower ACH, the predicted steady-state quanta concentration is much lower, illustrating the positive effect of ventilation on the mean concentration of quanta.

A fourth case with $Q_k = 6\,\mathrm{m}^3\,\mathrm{min}^{-1}$ equating to 6 ACH is also presented in Figure 3.1d, showing the transient quanta concentration solution. This case was included as 6 ACH is the recommended ventilation rate in UK NHS hospital wards (NHS England [2021]). At 6 ACH, the transient model reaches the steady-state value in around 30 min, considerably faster than in the other cases, although it is important to note that the steady-state value is lower than in the other cases. This would further increase in specialist environments such as intensive care wards where ventilation rates of 10 ACH are typically recommended. Although in reality many hospital wards do not reach the recommended standard, particularly where they are naturally ventilated, the results here suggests that should hospital wards be ventilated at 6 ACH, the transient effects become less significant and the steady-state model gives a reasonable approximation.

To illustrate this difference further, if the first 30 min of an outbreak on a hospital ward are considered, which is sufficiently prior to the stage at which any of the ventilation scenarios reach the steady-state value, then the relative difference between the transient concentration solution and that of the steady-state at $t = 30\,\mathrm{min}$ can be compared; this is shown in Figure 3.2 for 3 different zones plotted against increasing ventilation rate.

The results in Figure 3.2 show that how appropriate the steady-state model is depends on both the ventilation rate and the zone. The higher the ventilation rate, the smaller the difference is between the two models and so the better the steady-state approximation becomes. However, a significant overestimation is evident in some zones. The steady-state approximation is closest to the transient model when the infectious individual is present in the same space. At 3 ACH, Zone 7, which is furthest from the infected individual, is overestimated by almost 80% using a steady-state model, compared to less than 10% difference in Zone 1. At 6 ACH, it can be seen that although the transient effects are are less important close to the infectious individual (i.e., in Zone 1 or 2), as one moves further away, these effects again become more significant. In Zone 7, there is a difference of over 40% between the two models. This being said, as the steady-state concentration is lower at a higher air change rate, as can be seen from Figure 3.1d, the quanta concentration value in this zone is very small compared to all other cases.

These results demonstrate that when using these models in complex multi-zone en-

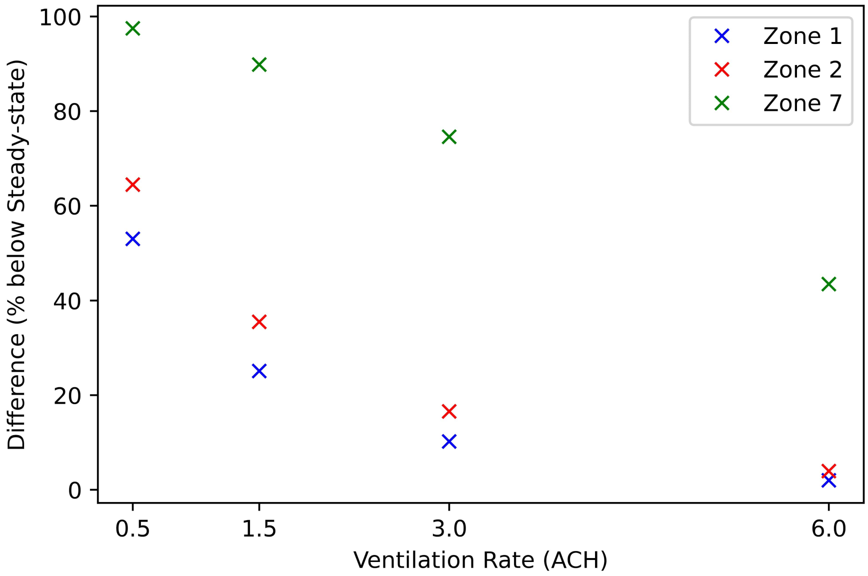

Figure 3.2: The relative difference between the concentration values of the steady-state and the transient solution at $t = 30\,\text{min}$ for Zone 1 (zone with infector present), Zone 2 (zone adjacent to the infector), and Zone 7 (zone furthest from the infector) with 4 different ventilation settings for the fixed infector case.

vironments, there will still likely be zones or time periods for which a steady-state assumption gives an overestimation. Although in terms of a risk assessment this potentially errs on the side of caution, it can also lead to underestimates in quantifying outbreak parameters. If the zonal flows are not considered, as shown in Noakes and Sleigh [2009], it can result in a significant underestimation of infectious quanta emission where models are used to "back calculate" from an outbreak. Although not explicitly demonstrated here, the converse would also be true. Once an infectious person has left a space, the steady-state model returns immediately to zero, which would therefore underestimate the transient model, failing to capture the decay curve that would be experienced in reality.

The consequences of the overestimation of the transient quanta concentration solution translates into the expected cumulative exposures over time. Figure 3.3 shows the solution for the exposures compartment of the SE model for four different ventilation rates in terms of total exposures across all susceptible people within the respiratory ward rather than in each zone. This illustrates the overall difference between using the steady-state concentration model versus the transient model and how this affects the number of estimated exposures, which again is being overestimated when using the solution from the steady-state concentration.

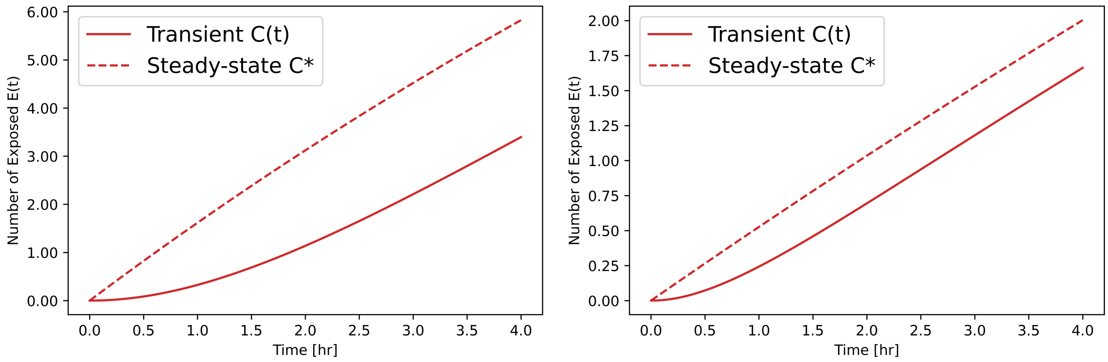

(a) 0.5 ACH

(b) 1.5 ACH

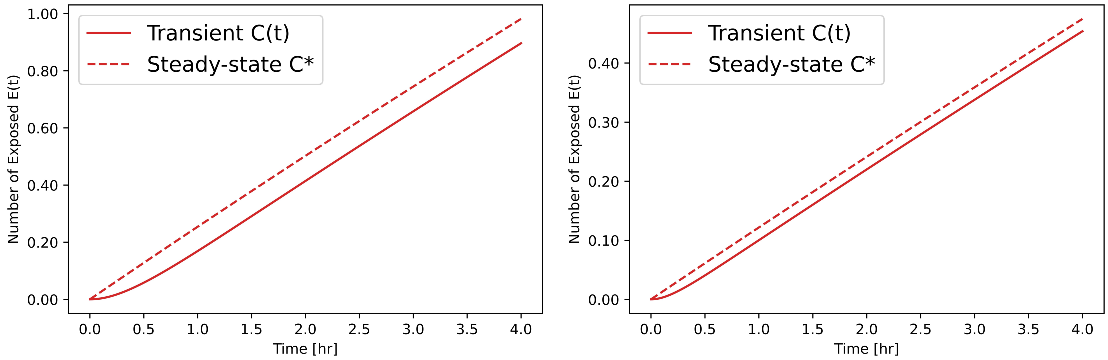

(c) 3 ACH

(d) 6 ACH

Figure 3.3: The solution for the exposed compartmental model using the transient solution for concentration of pathogen in the air (solid) and the steady-state solution (dashed) for various ventilation rates for the fixed infector case.

When considering lower ventilation rates, as previously done in Figure 3.1a and Figure 3.1b, where the overestimation for the concentration is higher, this consequently translates into a larger difference between the estimated exposures compartmental model when using the steady-state concentration versus the transient (Figure 3.3a and Figure 3.3b). It is also worth highlighting the increase in the overall quanta concentration in each space and thus, an increased number of exposures. Despite this being an expected consequence, it illustrates the effects that ventilation has on an outbreak, reducing the overall risk of transmission.

As expected, at the recommended ventilation rate of 6 ACH (Figure 3.3d), there is very little difference between the predictions for the number of exposed individuals and that after the 4 h period, not even 1 exposure is predicted. This highlights the benefits of good ventilation within spaces when trying to reduce transmission.

3.3.1.3 Varying The Quanta Emission Rate

Figure 3.4 explores the relative difference between the cumulative number of exposed individuals by time $t = 4\,\text{h}$ plotted against increasing ventilation rate, when using the steady-state concentration solution versus the transient solution for varying quanta emission rates.

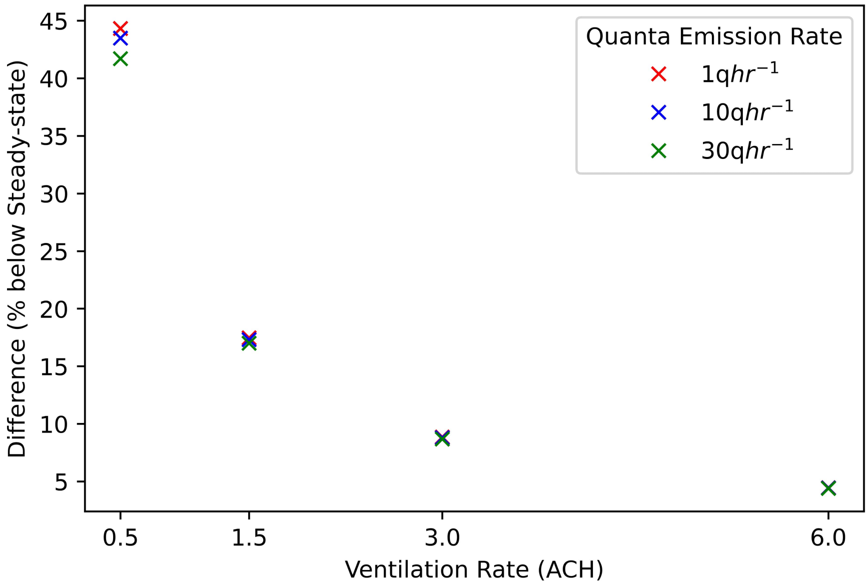

Figure 3.4: The relative difference between the predicted exposures from the epidemic model when using the steady-state versus the transient solution for concentration of airborne pathogen for 3 different quanta emission rates across 4 different ventilation settings for the fixed infector case.

As seen previously in the concentration data in Figure 3.2, overestimation using the steady-state model is also seen in the exposures. This decreases as the ventilation rate increases with a difference of more than 40% in predicted exposures between the two models with a ventilation rate of 0.5 ACH compared to around 10% when the ventilation rate is 3 ACH. The results in Figure 3.4 show a small effect of the quanta emission rate, with the greatest difference at low ventilation rates; as the ventilation rate increases to 3 ACH and beyond, there is negligible difference between the two models for different emission rates. At 6 ACH, the relative difference between the two models is $< 5\%$, regardless of the infectiousness of an individual, again suggesting that the recommended ventilation rates for hospital wards in the UK likely eliminate the need for consideration of transient effects, except for very short duration events, regardless of the quanta emission rate. However, in scenarios with poor ventilation, it is possible to experience different accuracy when using steady-state versus the transient assumptions and it is important to consider the infectiousness of an infector. Results for the concentration solution, exposure solution and the relative difference between the steady-state solutions and transient solutions, illustrate that ventilation rates in a scenario are the main driving factor that are likely to determine the outcome of an airborne outbreak and also whether a transient or steady-state approximation is most appropriate.

3.3.2 Case Study 2: Transient Infectious HCW

3.3.2.1 A Real Respiratory Ward

In this second case, a different, more realistic geometry was used. A 12-zone geometry subset was chosen that consisted of a ward layout containing patient single and multi-bed wards, HCW and treatment room environments. The geometry (Figure 1.2) is used for the simulations with a transient infector where: Zones 1 and 2 represent 4-bed bays (with 4 susceptible people in each); Zones 3 and 4 represent single rooms (with 1 susceptible person in each); Zone 5 is the nursing station (with 4 susceptible people and 1 initial infector); Zone 6 is a connecting corridor split into 3 zones, namely Zone 6a, 6b, and 6c (with 4 susceptible people in total, representing staff); and Zones 7-10 are clinical treatment rooms (with 6 susceptible people across these zones - 3 in Zone 8, 2 in Zone 9 and 1 in Zone 10). There are a total of 24 fixed susceptible people, with 1 infector who is allowed to move through the space following a pre-defined schedule. This gives initial conditions for the epidemic model as $S_0 = (4, 4, 1, 1, 4, 1, 2, 1, 0, 3, 2, 1)$, $E_0 = 0$ for each zone, and $I_0 = 1$ in Zone 5 only and is zero for all other zones. The transient infector moves from one zone to another in time, but once they are in a particular zone, the interaction with specific patients is not considered and the focus is on modelling the airborne concentration and exposure in the whole zone.

In order to allow the infector to move around the space, it was necessary to have a realistic schedule. Information provided by a senior clinician on the typical number of times a HCW visited a patient was used to define typical activities, as shown in Table 3.1. This is not based on observational data, but is instead designed to be representative

Bed	Observations	Drug round	Medical review	Total Visits
Bay 1 - Bed 1	7	4	1	12
Bay 1 - Bed 2	8	4	1	13
Bay 1 - Bed 4	8	4	1	13
Single Room 1	4	3	1	8
Single Room 2	7	4	1	12

Table 3.1: Frequency of HCW visits to patients for chosen zones on a UK Respiratory ward for a typical 24 hour period.

and demonstrate the effects of movement.

From Table 3.1, the average number of visits to a bed per day is 11.6 per 24 hour period. Taking this as $\approx$ 12 per day, it was assumed that $\frac{1}{3}$ of the visits were at night and $\frac{2}{3}$ of the visits during a 12 hour daytime period. This gave an estimate of 8 visits throughout a 12 hour daytime period which is approximately one visit every 90 min to each bed. Working on the basis that across two 4-bed bays and two single rooms there are 10 beds in total from the chosen geometry (Figure 1.2), this gives an approximate time of 9 minutes per visit per bed. For a 4-bed bay it was assumed that approximately 35 minutes were spent on each at one time, and a single-bed room taken as 10 minutes per round. This then leads to the following schedule:

1. Infectious HCW sets up at nurse station for 30 min - Zone 5
2. Infectious HCW visits Bay 1 to complete round lasting 35 min - Zone 1
3. Infectious HCW visits Bay 2 to complete round lasting 35 min - Zone 2
4. Infectious HCW visits Single Room 1 to complete round lasting 10 min - Zone 3
5. Infectious HCW visits Single Room 2 to complete round lasting 10 min - Zone 4

This schedule lasts for 2 hours, which is then repeated creating a 4 hour simulation, with 2 visits to each bed within the period of modelling. Movements such as between zones through corridors have been ignored and assumed to be sufficiently short in duration to have no significant effect.

Elements	**Number**	**CONTAM Airflow Type**
Top-hinged Window	1,4,7,10,34,37,40,43	TWF/TO
Sash Window	2,5,8,11,35,38,41,44	TWF/TO
Double Door	13,15,17,20	TWF/TO
Single Door	26,28,30,32	TWF/TO
Under-door Gap	14,16,18,21,27,29,31,33	TWF/TO
Leakage	3,6,9,12,36,39,42,45	One-way Flow Using Powerlaw/Crack Description
Corridor End	22,25	One-way Flow Using Powerlaw/Orifice Area Data
Corridor (Long)	19,23,24	TWF/TO

Table 3.2: Airflow element descriptions, corresponding element number in Figure 3.5, and the boundary condition defined within the CONTAM model for the 12-zone respiratory ward in this chapter (Chapter 3). TWF/TO, Two-way Flow/Two-opening

A CONTAM model of the airflow was used to obtain realistic inter-zonal flow rates, β_{kj}, following the methodology in Section 3.2.2. The CONTAM set-up in Figure 3.5 shows the location of airflow openings with an arrow illustrating the positive airflow direction. Table 3.2 shows the corresponding description to each of the openings. The building orientation, windows, and doors were used to determine ward inter-zonal flows for three steady-state ventilation rates, 0.5 ACH, 1.5 ACH and 3 ACH. In the CONTAM model, the windows remained closed for the full duration of the simulation. It is assumed that doors between zones remained closed throughout, apart from when they were open for a 1-minute period to simulate the transient infectious HCW moving in and out of that particular zone. The inter-zonal flow rates were then used in the equation for multi-zone concentration of airborne pathogen (Equation (3.2)) as discussed in Section 3.2.2. As previously, the quanta emission rate of infectious individuals is taken to be $q_k = 0.5$ quanta $\text{min}^{-1}, \quad \forall k$ (Noakes and Sleigh [2009]) and the pulmonary breathing rate of all individuals is taken to be $p_k = 0.01\,\text{m}^3\,\text{min}^{-1}, \quad \forall k$. The initial concentration of pathogen in the air is taken to be $C_0 = 0$ in each zone.

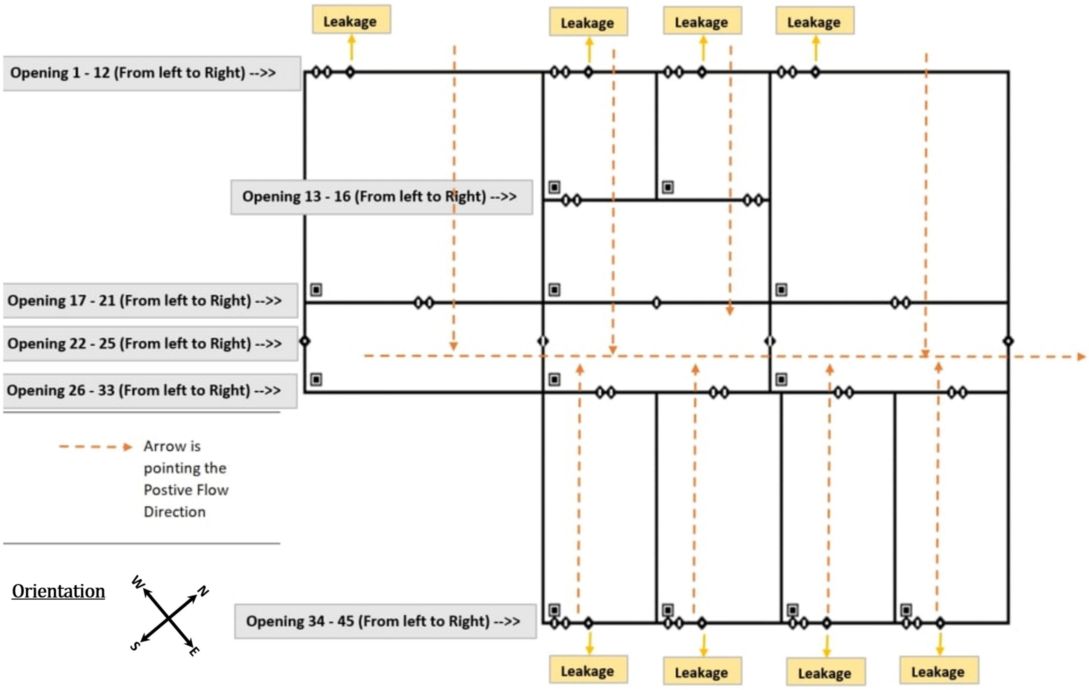

Figure 3.5: CONTAM model set-up, illustrating the geometry, airflow elements (small diamonds) and corresponding number (opening numbers on the left of the figure) and the arrow illustrating the direction taken as positive for the airflow. The corresponding airflow element type to each number can be seen in Table 3.2 and Table 4.1 for the appropriate model in this chapter and Chapter 4, respectively. The square icon in each zone contains the zonal set-up.

3.3.2.2 Effect of Ventilation Rate

Figure 3.6 shows solutions for the transient concentration of airborne quanta for three ventilation rates, alongside the steady-state solution. For clarity, only the solution for the 5 zones in which the infector visits have been included on this plot. Due to the transient infector moving through the zones at different time periods, different dynamics to the concentration solutions seen in the fixed infector case (Figure 3.1) can be observed.

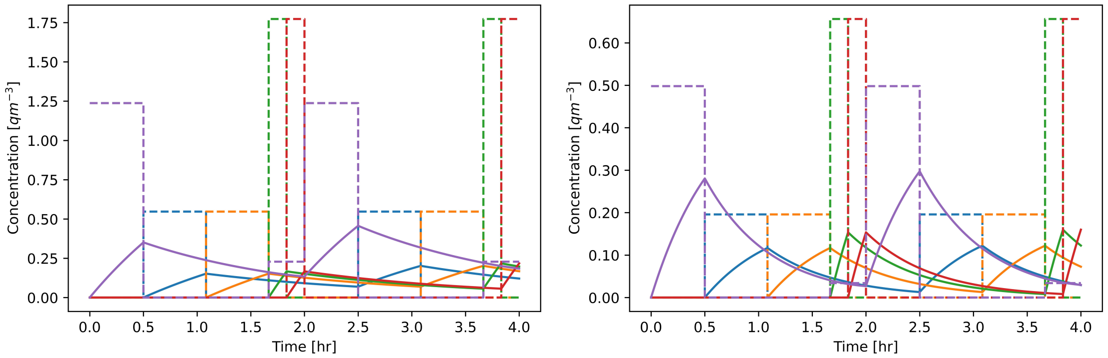

(a) 0.5 ACH

(b) 1.5 ACH

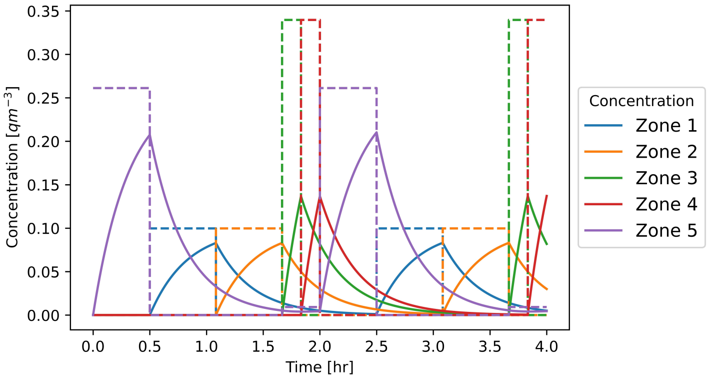

(c) 3 ACH

Figure 3.6: Modelled concentration of pathogen in the air for the transient solution (solid) and the steady-state solution (dashed) for three ventilation rates for the transient infector case.

The overestimation by the steady-state approximation is still present, but is much more varied than when the infectious individual is at a fixed location. For example, when the infectious person is in Zone 1, the transient quanta concentration almost reaches the steady-state value by the time the infectious person leaves, whereas in Zone 3, the peak transient concentration is less than half of the steady-state value.

Unlike the steady-state approximation which immediately returns to zero concentration when the infectious person leaves, the transient model captures the dilution rate of the quanta in the air over time. The time period for this dilution depends on ventilation rate, and for lower ventilation rates it is possible to see that the concentration never returns to zero (e.g., Figure 3.6a). By the time the infectious person returns for the second ward visit, the quanta concentration is compounded and thus, upon leaving for the second time the airborne concentration is higher than after the first visit.

A similar effect can also be seen with zones where the infectious person is not present, but are linked through airflow to the zone where the infectious person is. Here, an opposite effect can be seen where the concentration of pathogen is non-zero and begins to increase despite the absence of an infector. This is due to the effects of mixing, ventilation and inter-zonal airflow. The steady-state model fails to capture this gradual increase in other zones. The steady-state model does show a non-zero concentration in connected zones but these are small, and the presence of an infector dominates. For example, in Figure 3.6a, when the infector is in Zones 3 and 4, it is possible to observe a non-zero concentration in Zone 5, a directly connected zone.

Figure 3.7 shows the relative difference between the steady-state and transient models for Zone 5 (the nurse station), and Zone 3 (a single-bed room) for the concentration of pathogen solution. By using these two different zones, it allows for a different room volume in each case and a different length of visit by the infectious person. In both cases, the relative difference has been calculated at the end of the first visit and at the end of the second visit to explore the effects of compounding and dilution due to the movement of the transient infector and inter-zonal flow connections in a multi-zone system.

Zone 5 (Nurse Station) has a smaller relative difference between models and is therefore better approximated by the steady-state than Zone 3 (single-bed room). The difference between the two rooms increases with the ventilation rate. However, the infectious person spends only 10 minutes in the single room, as opposed to 30 minutes in the nurse station which is also likely to be a major contributor to the difference between the two models. The longer the infectious person stays in a zone, the closer the quanta concentration will get to the steady-state value; since the focus is on the relative difference, the zone with the infectious person present for the longest time will have a smaller relative difference between the two models. As previously, the higher ventilation rate, the better the approximation by the steady-state model regardless of the time spent in the zone, and this can be seen for both zones. Other factors such as volume and time can also

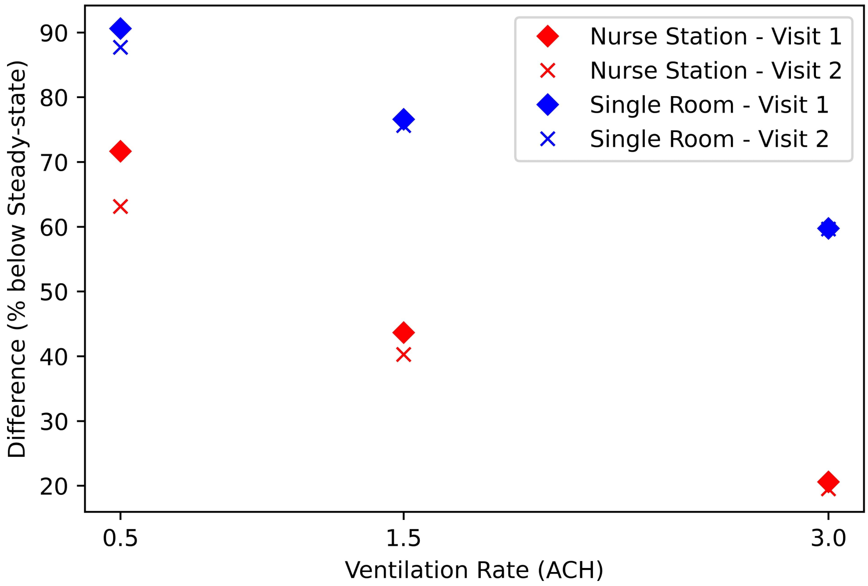

Figure 3.7: The relative difference between the concentration values of the steady-state and the transient solution for Zone 5 (the Nurse station), and Zone 3 (a single-bed room) after the first and last visit with 3 different ventilation settings for the transient infector case.

increase the effects of ventilation on the accuracy of the steady-state approximation for a particular zone. For example, in the single room, upon increasing the ventilation rate from 0.5 ACH to 3 ACH, the steady-state model is around 30% more accurate, whereas in the case of the slightly bigger volume and longer visitation of the nurse station, this increase is closer to around 50%.

As previously mentioned, there is evidence that other zones are affected by the infectious air transported from connecting zones when the infector is not necessarily present, or that the transient model describes a decaying airborne concentration when the infectious individual leaves a zone. This can be illustrated by focusing on each zone in turn in Figure 3.7. When comparing the relative difference at the end of the first ward visit compared to the second visit, at higher ventilation rates the steady-state approximation for the first and second visit is very similar. However, at the lowest ventilation rate, the overestimation by the steady-state model decreases from the first visit to the second. This demonstrates the uncertainty of a steady-state model for approximating transient multi-zone environments. For scenarios with low or varying ventilation in multi-zone spaces of varying geometry, it would be difficult to characterise the accuracy of the steady-state approximation due to the added transient effects from the infectious person moving around the space. This difference is eliminated with increasing ventilation rate, where the steady-state approximation not only becomes better, but there is little difference between each visit during the simulated time period. This analysis demonstrates the added complexity that is introduced by an infectious person moving around a space which is ubiquitous in real-life scenarios, and how the transient model is able to capture this with greater consistency.

In a similar way to Case Study 1, any overestimation experienced through using a steady-state model for the concentration of pathogen instead of the more accurate transient version leads to an overestimation in the predicted number of exposures as well. This is illustrated in Figure 3.8, showing the solution for both steady-state and transient models of the exposed compartment of the SE model across the whole ward for three different ventilation rates.

It is worth noting that in Chapter 2, specifically Figure 2.1, the steady-state concentration solution is equal to that of the transient solution when considering a period that extends long after the infector leaves. Although the period after the infector leaves is considered here, the infector returns to the same zone $< 2\,\mathrm{h}$ after they initially left. Additionally, this is a multi-zone scenario (compared to a single zone scenario in Section 2.3.1) where the concentration in a given zone is also influenced by possible concentration flux to or from connected neighbouring zones, which in this scenario, also have the possible presence of an infector. This further contributes to the difference in the transient and steady-state solutions for the concentration of pathogen in the air.

These results show that the differences between steady-state and transient model concentrations are translated into the risks predicted through the epidemic model. This follows the same pattern observed in the fixed infector case with the steady-state model overestimation becoming greater as the ventilation rate decreases. Another notable feature in Figure 3.8 is the variation as the transient infector moves around. Unlike the case with the fixed infector, the periods where the infector moves are reflected with varying overestimation at each period. For example in the first 30 minutes in Figure 3.8b, it is possible to observe the steady-state solution begin to look like it could diverge from the transient model as opposed to being a linear overestimation. This gives motivation for further analysis into a zonal-level analysis rather than on a population level. For example, by looking into the effects of extending the period of time when an infectious person is present during a drug round.

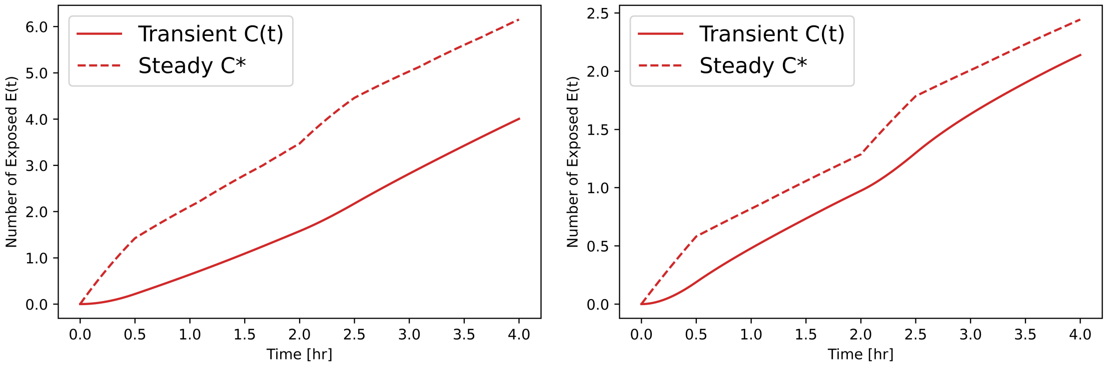

(a) 0.5 ACH

(b) 1.5 ACH

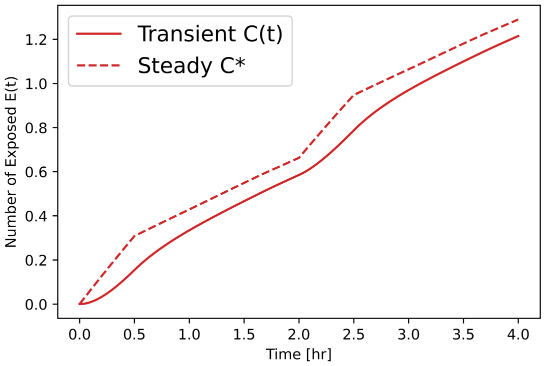

(c) 3 ACH

Figure 3.8: The solution for the exposed compartmental model using the transient solution for quanta concentration in the air (solid) and the steady-state solution (dashed) across the whole ward for three ventilation rates for the transient infector case.

The effects of the ventilation rate on the overall number of exposures can also be seen in Figure 3.8. As in the fixed infector case, increasing the ventilation rate reduces the quanta concentration in each zone and thus, potentially the total number of exposures in an outbreak.

3.3.2.3 Varying Quanta Rates

In Figure 3.9, the relative difference of the final exposed value ($t = 4\,\mathrm{h}$) from the exposed compartment of the SE model across the whole ward can be seen for three ventilation rates, and for three different quanta production rates.

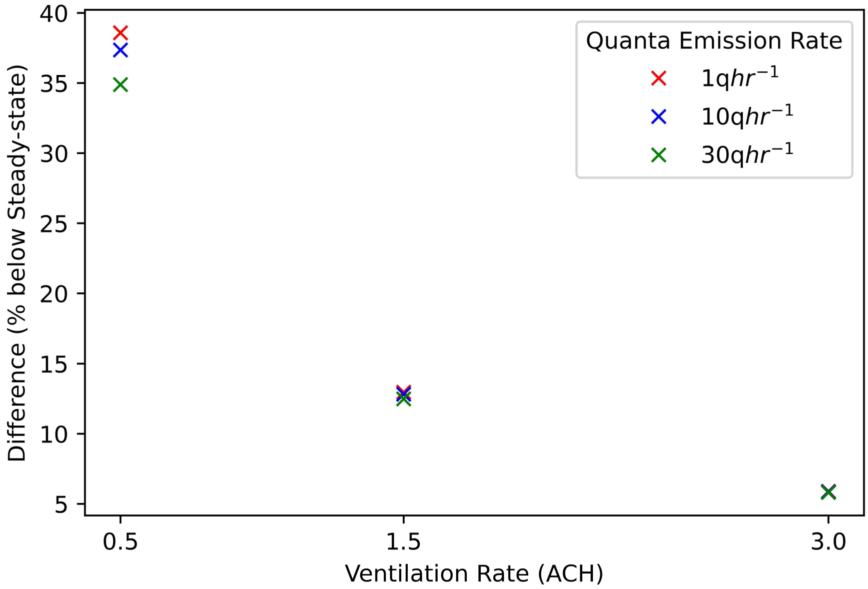

Figure 3.9: The relative difference between the predicted exposures from the epidemic model when using the steady-state versus the transient solution for concentration of airborne pathogen across the whole ward for 3 different quanta emission rates across 3 different ventilation settings for the transient infector case.

A very similar outcome to the fixed infector case can be seen. The difference between models decreases as the ventilation rate is increased, and the relative difference for each quanta production rates align; for the well-ventilated case, all three quanta production rates display an almost identical overestimation when using a steady-state approximation. Despite having a transient infector moving around the space, the model accuracy for the well-ventilated case is similar when predicting exposures whether using a transient or steady-state concentration model. Given that the transient infector case uses more realistic inter-zonal flow values than in the fixed infector model, a greater difference in the two results may have been expected. This provides motivation for further analysis into the inter-zonal flows and mixing rates, and the possible effects these could have on the outbreak dynamics.

3.4 Discussion and Conclusion

Through extension of an equation for the concentration of airborne pathogen to a multi-zonal environment and a coupling with an SE epidemic model, this chapter has demonstrated the ability to analyse the potential importance of transient effects on outbreaks in multi-zone indoor spaces. By considering a transient solution of the multi-zone concentration, rather than the more commonly applied steady-state Wells-Riley model, one can better predict the likely quanta concentration in indoor environments and how this may affect the transport of airborne pathogens to neighbouring spaces. Through various occupancy, ventilation and quanta emission scenarios, a comparison of the two models has shown the importance of considering transient effects and the ability of the transient model to capture some of the complexities experienced when attempting to model real-life scenarios. Additionally, even when considering the transient solution, the numerical model has a computational time of 1.23 s for the fixed infector case, and 1.59 s for the transient infector case. Given that this includes the steady-state model calculation and comparison as well, it demonstrates no computational benefit in using the steady-state model in place of the transient model for these scenarios. This consequently leads to a better prediction of exposures during an outbreak, and thus, the potential for better implementation of mitigation strategies and resources to situations which would benefit the most.

It is important to highlight that the steady-state model may result in a "worst-case" style of analysis which may be applicable and even favourable in certain scenarios. Using the steady-state approach when planning interventions such as ventilation design can result in a "safety factor" to provide resilience in design. It is also likely to be appropriate for longer time period scenarios where the infector can be assumed to be fixed in one location, although the zonal variation in concentration still needs to be considered. However, when this is applied to short timescale events, and a moving infector, the differences between the models are non-negligible. In using such models to inform management or temporary environmental interventions in a hospital setting, where resources are often scarce and bed occupancy is high (Dowd [2021]), it is important that methods can offer efficient and realistic assessments to pragmatically deploy resources. Using a transient approach can allow for a more realistic representation of complex scenarios, where the model presented is versatile and adaptable, making it suitable for many outbreak scenarios and disease settings.

With the use of ventilation rates between 0.5 and 6 ACH, the benefits of increased ventilation rates on various scenarios have been shown. Increasing the ventilation rate leads to an overall reduction in the total quanta concentration in a given space and the consequent number of exposures resulting from an infector. At higher ventilation rates, there is less variability between the model predictions, with the expected exposures in an environment less dependent on the choice of parameters in models. It is also worth noting that despite the variation in ventilation rates through the models, the inter-zonal flow rates remained fixed for each scenario. This assumption may not hold in reality, and the inter-zonal flow rates would most likely change alongside the ventilation rates, which is something that should be considered in future work.

One of the main limitations of a study such as this is validation. Although sensitivity to ventilation rates, emission rates and the behaviour of an infector were explored, the work presented in this study is based on a model calculation. Previous work has shown that the Wells-Riley model can match transmission rates observed in large outbreaks (Peng et al. [2022]). There is also evidence of airborne transmission between neighbouring spaces including for COVID-19 in quarantine hotels (SAGE [2021]) and hospital wards (Jung et al. [2021]). Airflow models such as CONTAM have also had prior validation (Haghighat and Megri [1996]), and initial comparison between the CONTAM model of the respiratory ward and CO_2 measurements in the ward suggest that the airflow used in this chapter is realistic. Although it is clear that this work would benefit from observational validation of an outbreak, this is extremely difficult in complex multi-zone settings in a busy hospital ward. In practice, it is almost impossible to identify exactly where an infection originated and the direct and indirect contacts of an infector, especially when considering long-range exposure in a hospital environment. Exposure is complicated by multiple shift patterns, staff changes, movement within and between rooms, multiple zones and identifying whether the infection was airborne or contracted via an alternative route such as fomite transmission. The models in this chapter also only consider the far-field airborne exposure, and do not include the potential for exposure to higher concentrations of aerosols and droplets when an infector has close-range interaction with a susceptible individual. In the future, this work could explore validation and close-range exposures via a CFD study, but this would likely be limited to a single room split into multiple zones as a multi-zone ward geometry such as the one used here would be impractical and computationally expensive to replicate over an extended time period.

Despite the successful demonstration of the transient model, it is likely that there are certain scenarios where a steady-state approximation would be sufficient. However, this chapter has demonstrated that these need careful consideration, with the duration of time the infector spends in the room, the ventilation rate and the inter-zonal flows all affecting whether the model is appropriate. Further work should apply these models to a much broader set of scenarios exploring further the effects of variable ventilation rates with weather and season (see also Chapter 4), inter-zonal flows and mixing, and occupancy behaviours. However, through this approach, the ability to better represent more realistic scenarios has been illustrated and future work on specific outbreak scenarios will hopefully establish its value further.

Chapter 4

Transient Airflow, Weather and Airborne Transmission

Driven by historical design, many UK hospitals rely heavily on natural ventilation as their main source of airflow in patient wards. This uncertain method of ventilation leads to unpredictable flow patterns between indoor spaces, potentially causing the unexpected transport of infectious material between connecting zones. However, effects such as weather conditions are often overlooked by steady-state transmission models. To analyse the effect on inter-zonal airflow, a multi-zone CONTAM model of a naturally ventilated hospital respiratory ward is proposed in this chapter, incorporating transient weather. In addition to the inter-zonal flow rates, the ventilation rates from the CONTAM model are coupled to the transmission model presented in Chapter 3 to give an assessment of the risk in inter-connected spaces, focusing particularly on occupancy, disease and ventilation scenarios based on a UK respiratory ward. The results suggest that natural ventilation with varying weather conditions can cause irregularities in the ventilation rates and inter-zonal flow rates of connected zones and thus, lead to infrequent but high peaks in the predicted concentration of airborne pathogen in particular rooms. This transient behaviour is shown to significantly increase the risk of infection, particularly through movement of airborne pathogens between rooms, and highlights that under certain conditions large outbreaks may be more likely. It is also shown how the ventilation rates achieved by natural ventilation are likely to fall below the recommended guidance, and that the implementation of supplemental mechanical ventilation can both increase ventilation rates and reduce the variability in infection risks. These results emphasise the need for consideration of transient external conditions when assessing the transmission risk of airborne infection in indoor environments.

Chapter 4 contains material from the jointly authored publication:

> **Edwards, AJ**, King, MF, López-García, M, Peckham, D and Noakes, CJ, Assessing the effects of transient weather conditions on airborne transmission risk in naturally ventilated hospitals. *Journal of Hospital Infection*, 2024, Volume 148, pp.1-10.
> `https://doi.org/10.1016/j.jhin.2024.02.017`

The code and data for this manuscript are available at `https://github.com/scaje/Contam_study_AJE`.

4.1 Introduction

In order to successfully model infection risk in indoor spaces, it is important to use the most representative models. However, the majority of the current models overlook the importance of transient effects and a multi-zone approach (as discussed in Chapter 3). Modelling studies have begun to consider multi-zone approaches (Noakes and Sleigh [2009], López-García et al. [2019]), highlighting the importance of connected spaces when considering airborne contaminant transport (Hodgson et al. [2004], Guyot et al. [2022]) with more recent work providing evidence of transmission to neighbouring zones (Jung et al. [2021], SAGE [2021]).

There is a strong association between ventilation and the control of indoor airflow in preventing the transmission of airborne infections (Li et al. [2007]). UK guidance states that most hospital wards should have fresh air ventilation rates of 6 ACH (NHS England [2021]). However, a large proportion of hospital wards rely heavily on natural ventilation, and this can be problematic as the ventilation rate is highly dependent on conditions such as external climatic and weather conditions, and the opening sizes of windows, doors or leakage (Park et al. [2021]). Although some experimental studies have reported high levels of natural ventilation (Escombe et al. [2007], Qian et al. [2010]), these discuss how natural ventilation is uncertain and difficult to control, accompanied with the suggestion that mechanical ventilation may be a more reliable choice (Qian et al. [2010]). In addition to these factors, the behaviour of the occupants should also be considered with thermal discomfort being an issue (Qian et al. [2010], Park et al. [2021]), and efforts to improve energy efficiency and safety features reducing the efficacy of natural ventilation (Gilkeson et al. [2013]).

One of the main factors affecting natural ventilation and the resulting airflow is external weather conditions. Previous studies have considered the impact of seasonality and various weather conditions on disease transmission (Pica and Bouvier [2012], Li et al. [2014], Mao et al. [2015], Sadyś [2017], Dbouk and Drikakis [2020, 2021, 2022a], Pani et al. [2020], Habeebullah et al. [2021], Das et al. [2022]), suggestive of the need for the use of varying weather effects within models. CONTAM allows for the use of transient weather conditions within models (Myatt et al. [2010], García-Tobar [2019], Zhu et al. [2020], Reichman and Dubowski [2021]), as highlighted in Chapter 1.

In this chapter, CONTAM is used to simulate airflow in a multi-zone naturally ventilated respiratory ward and a previous infection risk model is then used, which allows for the coupling of the airflow solution with an SE-based transmission model (Chapter

3). Through this coupling, the effects of transient weather conditions on indoor airflow and risk of infection were assessed, applying the methodology to a specific fixed-occupancy scenario over longer time scales, and the variability in exposure to infection under different ventilation conditions was explored.

4.2 Methodology

4.2.1 Airflow Simulations

The airflow approach and the chosen geometry (Figure 1.2) are the same as those previously used in Chapter 3. The CONTAM model set-up is illustrated in Figure 3.5 with the corresponding description of each airflow element seen in Table 4.1, which is based on the same model used in Chapter 3. It is worth noting that the CONTAM set-up differs slightly to that used in Chapter 3, hence an updated version of Table 3.2 is included here (Table 4.1). In addition, no movement of people was modelled in this chapter. The windows were assumed to remain open and doors closed for the full duration of the simulation. There was a corresponding leakage element for the windows and doors in each zone. It is important to highlight the restriction of the window openings, meaning that when these are modelled as “fully open”, this is much smaller than may be initially imagined (see Section 1.6.1). In addition, the discharge coefficient for a “top-hinged window” was reduced to 0.4 to mimic this opening limitation.

The full dimensions can be found in Table 4.1, including updates from the model presented in Chapter 3 such as the distinction between double door types, the open bay nurse station, and the choice of flow path for the end of corridor. The flow element to represent the end of each corridor (numbers 22 and 25), which in reality leads to the rest of the building, was represented as a leakage flow element the same size and airflow type as the “under-door gap”, to the ambient environment. This is a reasonable assumption as in reality, a door would be here that leads to other parts of the building, meaning that this airflow element is essentially modelled as a closed door, consistent with the rest of the model. Additional calculations or further assumptions were not necessary to implement this, and this still allows for the removal of contaminants and the entry of ambient air, which would be expected if modelling the building as a whole. Internal zones (zones without windows; namely Zones 5-8) have an internal temperature of 25 °C, External Zones (zones with windows; namely Zones 1-4 and 9-12) have an internal temperature of 22 °C.

Elements	**Number**	**Size** (Height x Width [m])	**CONTAM Airflow Type**
Top-hinged Window	1,4,7,10,34,37,40, 43	0.57 x 0.97	TWF/TO
Sash Window	2,5,8,11,35,38,41, 44	0.20 x 0.79	TWF/TO
Double Door A	17,20	2.18 x1.80	TWF/TO
Double Door B	13,15	2.06 x 1.40	TWF/TO
Single Door	26,28,30,32	2.06 x 0.90	TWF/TO
Under-door Gap A	18,21,22,25	0.01 x 1.80	TWF/TO
Under-door Gap B	14,16	0.01 x 1.40	TWF/TO
Under-door Gap (single)	27,29,31, 33	0.01 x 0.90	TWF/TO
Window Leakage	3,6,9,12,36,39,42, 45	1.76 x 0.01	One-way Flow Using Powerlaw/Crack Description
Open Bay	19	2.39 x 6.03	TWF/TO
Corridor (Long)	23,24	2.39 x 2.04	TWF/TO

Table 4.1: Airflow element descriptions, corresponding element number in Figure 3.5, and the boundary condition defined within CONTAM model for the 12-zone respiratory ward in this chapter (Chapter 4). TWF/TO, Two-way Flow/Two-opening

Let us recall the fundamental equations that are used in the CONTAM simulation presented, but are not re-stated here; Equation (3.6) representing the air mass balance equation, and Equation (3.8) representing the power law equation for calculating the mass flow rate, both originally presented in Chapter 3.

In this chapter, the airflow simulations were solved transiently over a period of 6-months from April 1st - September 30th 2021 and the calculation time step was 30 min. A transient weather file was used to represent the external environmental conditions throughout the simulation such as wind speed [$\mathrm{m\,s^{-1}}$], wind direction [°], outdoor air temperature [°C], and barometric pressure [Pa]. This was a local weather file for the Leeds area for the year of 2021 (Climate.OneBuilding [2022]). The weather data has an average air temperature of 10.18 °C, an average barometric pressure of 100 785.61 Pa, an average wind speed of $4.40\,\mathrm{m\,s^{-1}}$, and an average wind direction of 226.68° (south-westerly wind). A wind rose plot of the weather data can be seen in Figure 4.1. The weather file was converted to the correct format required for CONTAM using the *Weather File Creator 2.0* (NIST [2023b]).

In order to convert the wind speeds to pressures on the facade of the building, CONTAM uses wind pressure coefficients (WPC) for each zone k, $C_{P,k}$. These coefficients are related to the wind pressure as shown in Equation (3.9) (Persily and Ivy [2001]). If no WPC are used then the pressure difference across the opening is unaffected by wind speed, which is not realistic. CONTAM provides a library of wind pressure profiles (Persily and Ivy [2001], NIST [2023a]), specifically for low-rise rectangular buildings based on the work by Swami and Chandra [1988]. In this study, *S&C_3_long* & *S&C_3_short* are used on the longest and shortest side of the building, respectively, with the choice based on the ratio of each wall size with $Length = 3 \times Width$, where $C_{P,k}(0) = 0.6$. It is important to emphasise that the only factors varied within the simulations were the weather conditions, and all other boundary conditions remained constant.

4.2.2 Transmission Model

The airborne infection transmission model used in this study is outlined in Chapter 3, which couples the transient concentration of a pathogen in the air with an SE epidemic compartmental model, shown in the Equation (3.3) and accompanying solution from Equation (3.2).

The transmission model allows for the use of airflow simulation results to be exported

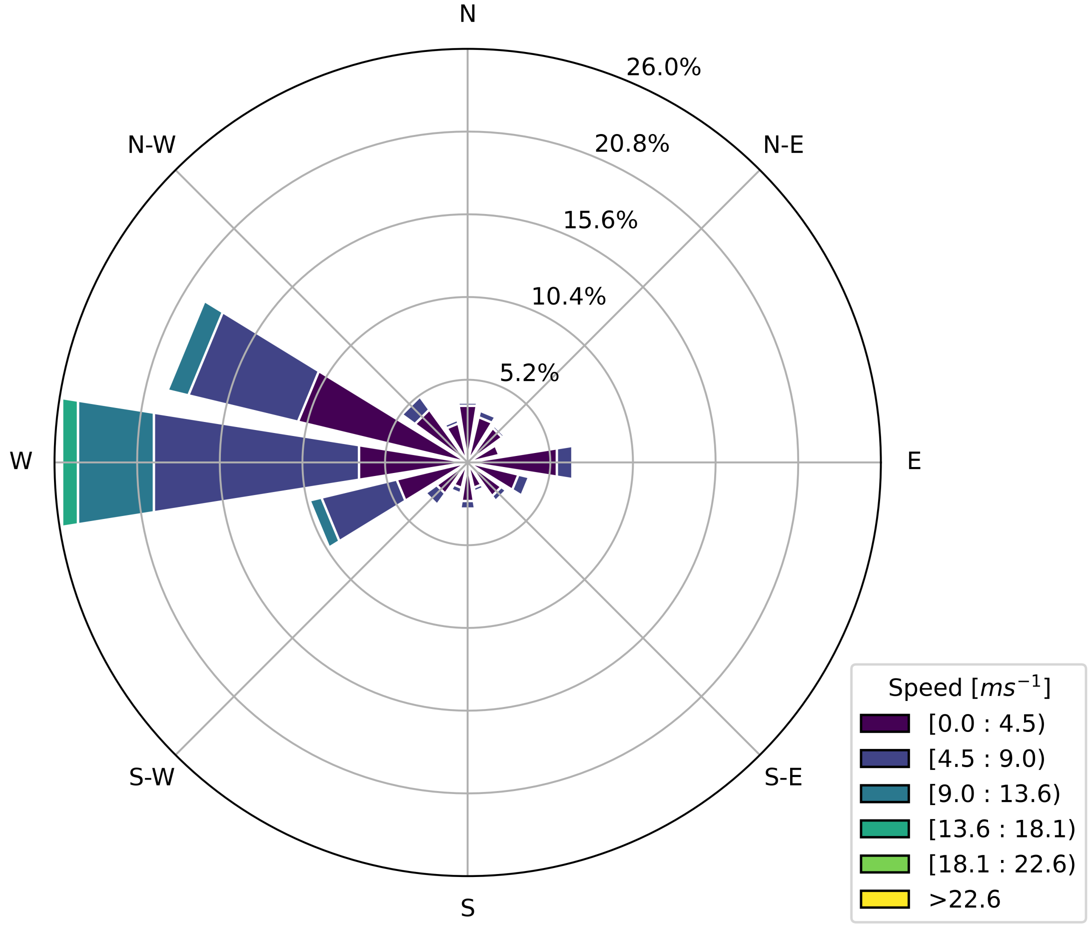

Figure 4.1: A wind rose plot illustrating the wind speed and wind direction from the weather file for the Leeds area for the year of 2021.

from the CONTAM model and used within the system of equations to inform parameter choice. In Chapter 3, only the inter-zonal flow values (β_{kj}) were imported and the relationship between this and the air mass balance equation (Equation (3.6)) can be seen in Equation (3.7). However, in this chapter, a fully coupled transient version is used. In the same way as the inter-zonal flow values, the airflow from the windows and corresponding leakage elements in the CONTAM solution are now exported. These values are then used in the transmission model as the extract ventilation rates (Q_k), representing the natural ventilation. For the case of natural ventilation only, the following relationship between the CONTAM simulation (Equation (3.6)) and the extract ventilation in the transmission model is provided:

$$Q_k = \begin{cases} \frac{m_{k,0} - m_{0,k}}{\rho_k} & \text{if } m_{k,0} \geq m_{0,k} \text{ ,} \\ 0 & \text{otherwise.} \end{cases} \tag{4.1}$$

In Section 4.3.2.2, natural ventilation is explored alongside mechanical ventilation. For the mechanical ventilation, an air handling system is used in CONTAM to define the extract ventilation, which uses fresh air from the ambient environment to supply the required volume to the system, with the ventilation distributed equally across the zone. A balance of supply and extract ventilation was assumed in each zone, so as not to create any additional pressure differences in the ward. For the case of natural ventilation with mechanical ventilation, Equation (4.1) becomes:

$$Q_k = \begin{cases} \frac{(m_{k,0} - m_{0,k}) + m_{k,v}}{\rho_k} & \text{if } m_{k,0} \geq m_{0,k} \text{ ,} \\ \frac{m_{k,v}}{\rho_k} & \text{otherwise.} \end{cases}$$

Although not considered here, if the model had a scenario for mechanical ventilation only, then:

$$Q_k = \frac{m_{k,v}}{\rho_k}.$$

In each case, these values are updated every two hours in the transmission model, using the exported CONTAM airflow solution.

In order to assess the total number of predicted exposures, the simulation is split into weekly periods. As the 6-month airflow simulation is an unrealistically long period to have a single infectious person present with no treatment or new secondary infections emerging, the total predicted exposures from the exposed compartment of the SE model were recorded at the end of each week, considering whole-person exposures only, and then the initial conditions reset. This used the transient quanta concentration, based on the airflow and corresponding weather conditions for that given week. This was repeated across the 26 weeks within the 6-month period of the simulation. These values were then used to form a distribution showing the probability of a particular number of predicted exposures on a given week across the ward assuming that one infected person was present for the duration of the week.

In addition to the probability distribution for predicted exposures, a Risk Index (RI) was calculated. The RI represents the average fraction of individuals exposed across the whole ward and can be calculated as

$$RI = \mathbb{E}\left[\frac{\mathbf{E}(t)}{S_0}\right] \tag{4.2}$$

Here $\mathbf{E}(t)$ is a random variable which represents the predicted number of exposures during $t = 1$ week, and S_0 represents the total number of initially susceptible individuals in the ward. To calculate the RI, $\mathbb{P}\{E(t) = x\}$ is estimated as the proportion out of all 26 weeks, that there are $E(t) = x$ predicted whole-person exposures. This probability is then multiplied by x and divided by the total number of initially susceptible individuals, S_0. This is done for all possible values of x, and then the sum is taken as

$$\mathbb{E}\left[\frac{\mathbf{E}(t)}{S_0}\right] = \sum_{x=0}^{n} \frac{x}{S_0}\mathbb{P}\{E(t) = x\}.$$

This is applied in Sections 4.3.2 and 4.3.4.

4.3 Results

4.3.1 Comparison to CO_2 Measurements

To ensure the modelled airflow was realistic, predicted CO_2 values were exported from the CONTAM simulation and compared against real measurements provided by a previous study. To model the relationship between people, ventilation rates and airflow, all of the individuals present are represented by sources of CO_2 with a generation rate of 0.005L/s (Persily and de Jonge [2017]). The individuals are assumed to be in a fixed location for the full duration of the simulation. Although this is unrealistic in terms of specific individuals being present at the same location for the full duration, it is representative of the average ward occupancy over that period, e.g., if a patient is discharged or moved, it is assumed that they are replaced. The outdoor ambient concentration of CO_2 is taken to be 400 parts per million (ppm) (Adzic et al. [2022]).

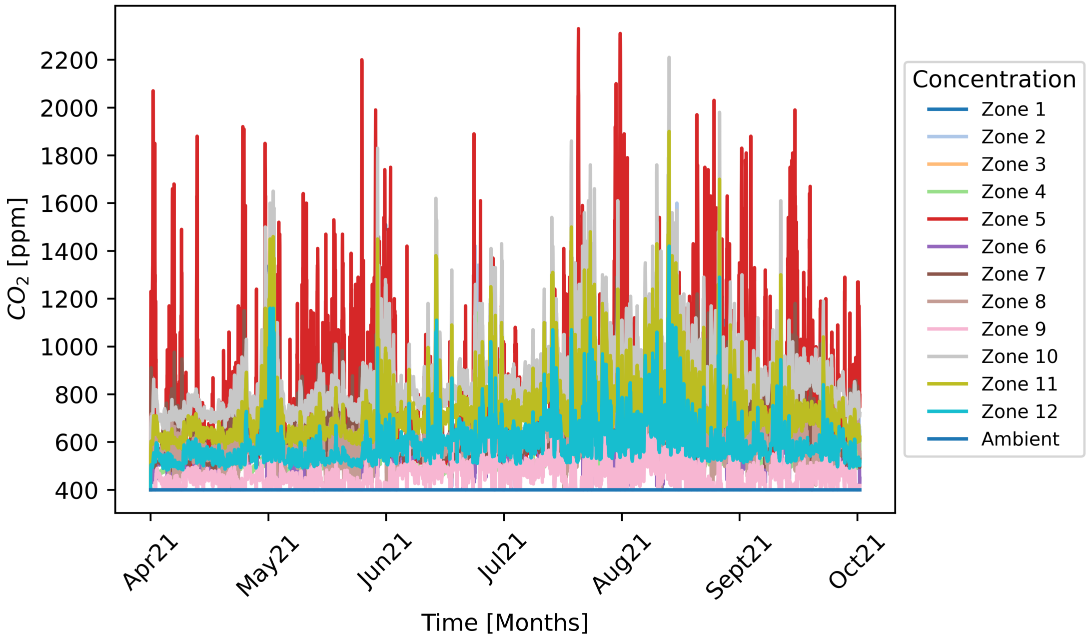

Figure 4.2: The simulated CO_2 concentration levels from the CONTAM airflow simulation on a 12-Zone UK respiratory ward. Modelled occupancy included 4 individuals in Zone 1 & 2, 3 in Zone 10, 2 in Zone 11, 1 in Zones 3, 4, 5 & 12, and 0 in Zones 6, 7, 8 & 9.

By having the external weather conditions as the only varying parameter, it is possible to directly assess the consequences of this on predicted CO_2 concentrations for each zone (Figure 4.2). Illustrated here are sharp, infrequent rises in the CO_2 levels at various points in time. This is apparent in all of the zones, with the highest peaks in Zone 5, an internal zone without windows.

CO_2 measurements, provided by a previous study, had been taken for a single internal zone using an Airvisual pro (IQAir) sensor at 10 second intervals during October 2019. The sensor was located on the nursing station in the ward (an equivalent location to Zone 5), and continuously recorded temperature, humidity, particulates and CO_2, although only the CO_2 data is considered in this study. The sensor range for CO_2 measurement is 400-10,000 ppm with an accuracy of 70 ppm ±3% at temperatures up to 50 °C and RH up to 95%. In order to compare the two as effectively as possible, the CONTAM simulation was extended to also include the month of October, as it was important to compare against the experimental data using simulated airflow from the same time of year. This is because the simulations use real weather data, which is highly dependent on the month and season. The CO_2 concentration levels were exported for the month of October and both simulated and measured data plotted as a bar chart, which was separated into 3 categories; 400-800 ppm, 800-1200 ppm, and >1200 ppm. The results can be seen in Figure 4.3. In addition to the case with all the doors closed, a case with only patient doors closed (Zones 1, 2, 3, and 4) and all other doors open was simulated and included in Figure 4.3. This was in an attempt to provide a more realistic scenario for comparison, as in reality it is unlikely that all the doors remained closed for the full duration.

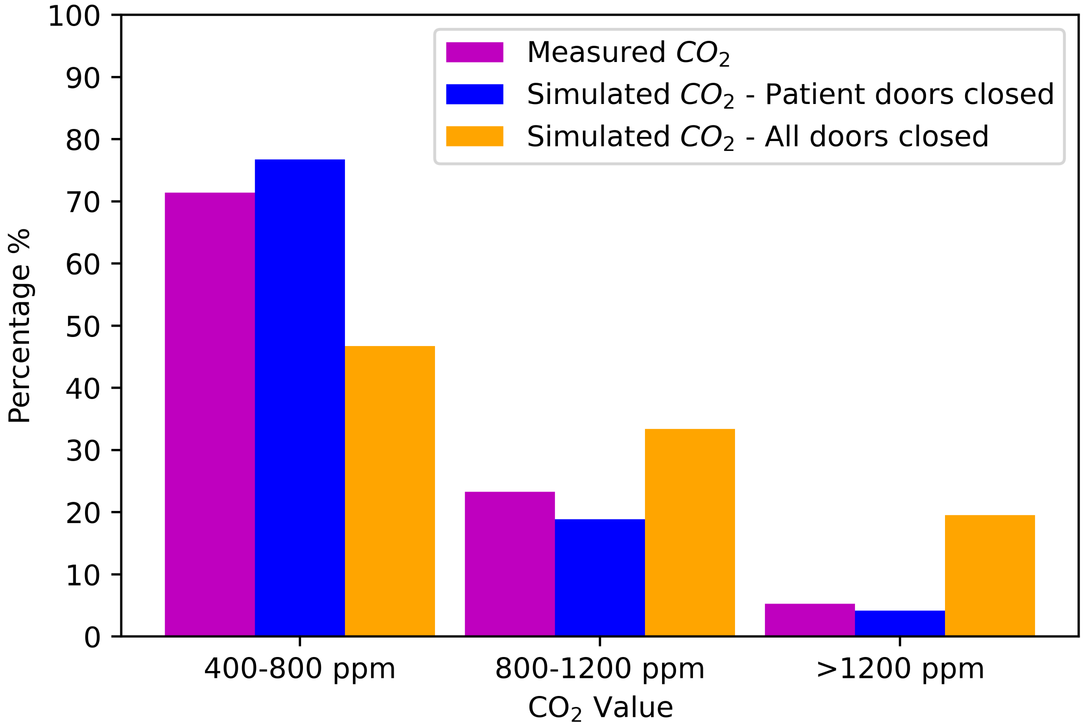

Figure 4.3: A bar chart showing the comparison between simulated CO_2 values (ambient CO_2 level of 400 ppm) for two door schedules for Zone 5 in October 2021 with measured CO_2 values for October 2019 for the nursing station (an equivalent location to Zone 5).

Despite the inability to model the exact transient occupancy, window opening behaviour or weather conditions that the real ward experienced, the simulated and measured data show a reasonably good agreement. In the case with only the patient zone doors closed, a difference smaller than ±5.5% is seen which is considered sufficiently close to conclude that the CONTAM model is able to realistically represent the airflow within this multi-zone space. Although this is not a validation, due to the difficulty in replicating the exact conditions of the measured data, this offers sufficient reassurance that the airflow simulation captures the features of this hospital ward.

In addition to this, to assess the importance of the choice of ambient CO_2 level, a case with an ambient CO_2 level of 450 ppm was explored. In Figure 4.4, a bar chart showing the comparison between the simulated and measured CO_2 values can be seen with this alternative ambient CO_2 level of 450 ppm.

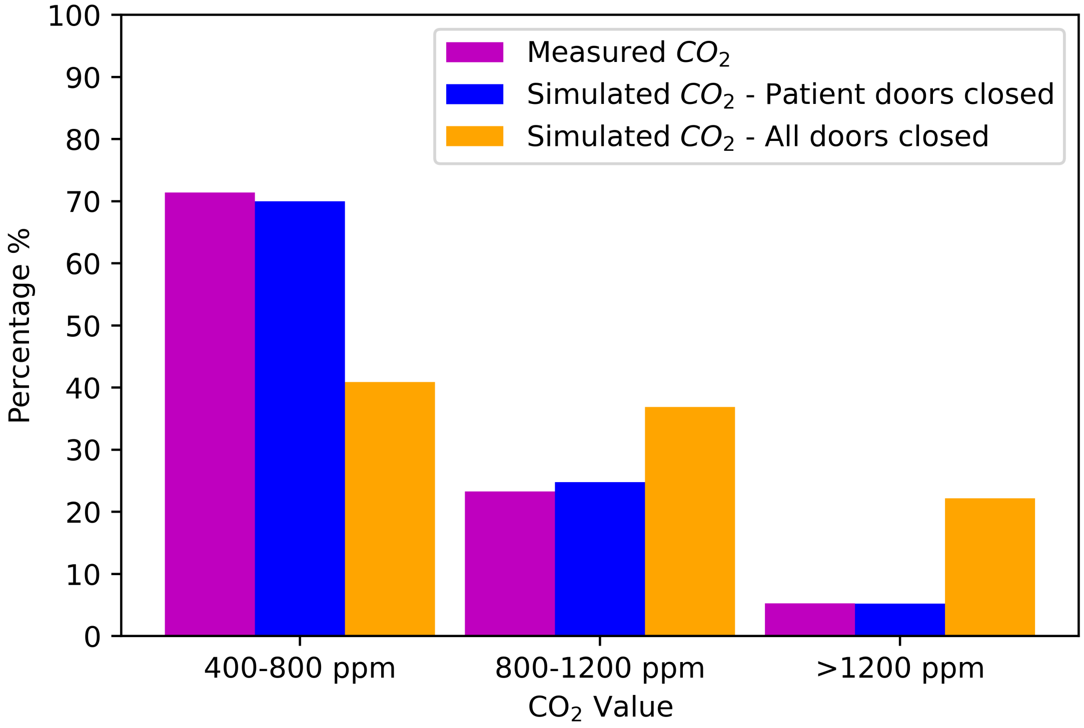

Figure 4.4: A bar chart showing the comparison between simulated CO_2 values (ambient CO_2 level of 450 ppm) for two door schedules for Zone 5 in October 2021 with measured CO_2 values for October 2019 for the nursing station (an equivalent location to Zone 5).

Across both scenarios, the agreement is similar but with a shift in the values, as expected. In the 400 ppm case, it can be observed that with the patient doors closed the difference between the measured and simulated CO_2 data was less than ±5.5%, and with all the doors closed smaller than ±24.67%. For 450 ppm ambient CO_2 level, it can be seen that with patient doors closed the difference is now less than ±1.48%, which is much closer in agreement. However, when all of the doors are closed, a difference of less than ±30.51% is seen, giving a worse agreement.

For this study, the ambient CO_2 level was kept at 400 ppm for two reasons: (i) this is a widely used choice for outdoor ambient CO_2 levels, and (ii) although there is not measured outdoor data to compare to, the real hospital ward considered in this study is on an upper floor of a building away from traffic sources and so it is unlikely that the external environment CO_2 levels would be significantly elevated. It is also important to note that the aim here is to use the model to give representative airflow dynamics to explore scenarios more realistically, rather than to simulate the exact ventilation and infection risk on a particular ward, meaning it is not necessary to exactly replicate measured data.

4.3.2 Transmission Model Analysis

To assess the potential influence of the transient airflow on infection risk, the airflow solution from the CONTAM model is extracted and used to provide both the inter-zonal flow values and the extract ventilation rates to the transmission model, as described in Section 4.2.2. The outbreak scenario for the transmission model is assumed to have the same occupancy as for the CO_2 analysis resulting in 17 individuals (see Figure 4.2). The infector is set to be the individual in Zone 5, giving 16 initially susceptible individuals, 0 initially exposed individuals and 1 initially infectious individual. The number of infectious individuals remains constant throughout. The quanta emission rate of the infector is taken to be $q_5 = 0.5\,\text{quanta}\,\text{min}^{-1}$ and the pulmonary breathing rate of all individuals is taken to be $p_k = 0.01\,\text{m}^3\,\text{min}^{-1}$ for all k (Noakes and Sleigh [2009]). The initial concentration is taken to be $C_k(0) = 0$ in each zone.

4.3.2.1 Variability of Natural Ventilation

The solution for the transient concentration of airborne pathogen can be seen in Figure 4.5a for a 6-month period from April 1st - September 30th 2021. The prominent feature of this figure is the sharp spikes and peaks in quanta concentration in the air. This suggests that particular days and weeks may pose a higher infection risk than others as a result, and that infection risk on a naturally ventilated ward may be pre-determined by the weather conditions. Since the transmission model only imports the airflow from

CONTAM, this also emphasises that these peaks happen as a direct result of the airflow within the space, driven only by the transient weather conditions. To illustrate the infrequency of the peaks of the quanta concentration, a probability density histogram for the quanta concentration can be seen in Figure 4.5b. The majority of the concentration values fall below 0.5 quanta m^{-3} with only 4.57% of values above this threshold. In fact, the zoomed portion of this plot only makes up 0.35% of all concentration values. This is useful in showing that although it is possible to capture the occurrence of these spikes, and that they may even look the dominant feature in Figure 4.5a, the higher concentration values are highly infrequent in comparison to the majority of concentration values over time.

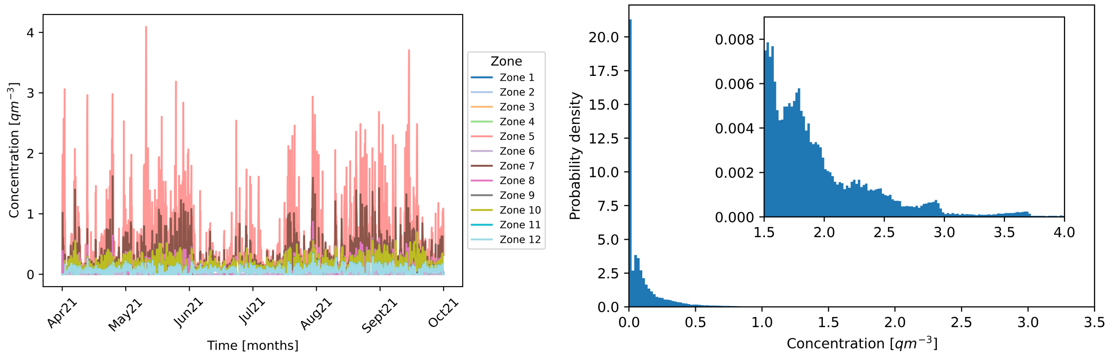

(a) Quanta concentration over time

(b) Probability density of quanta concentration

Figure 4.5: Simulated concentration of pathogen in the air for "Natural Ventilation Only": (a) Concentration in each zone for a 6-month period; (b) probability density histogram of the quanta concentration values with a zoomed portion showing the infrequent higher values.

The resulting predicted exposure distribution for a typical week can be seen in Figure 4.6a, with the RI value superimposed. The RI value comes from solving Equation (4.2) for the given scenario. There is a relatively high risk of exposures across the ward, with the possibility of up to 12 of the susceptible population becoming exposed during the week. This is surprising as the doors to each zone are closed with the infector remaining fixed in one zone, and so the risk here is solely driven by the inter-zonal airflow as a response to external conditions, leading to contaminant transport through the leakage around doors, and a low ventilation rate. This illustrates the importance of considering multi-zone models with connected airflow, as there may be a non-zero risk of transmission despite the absence of an infector in a given zone. The large spread of the distribution is also noticeable with the predicted exposures ranging from 4 to

12 individuals. This suggests that there is significant variability in the exposures that are predicted on a weekly basis, highlighting the uncertainty that is occurring due to the weather conditions. These results also suggest the possibility of elevated risk on particular days or weeks over the 6-month period, meaning that part of the risk experienced when visiting or being admitted to a hospital ward may be pre-determined by the weather.

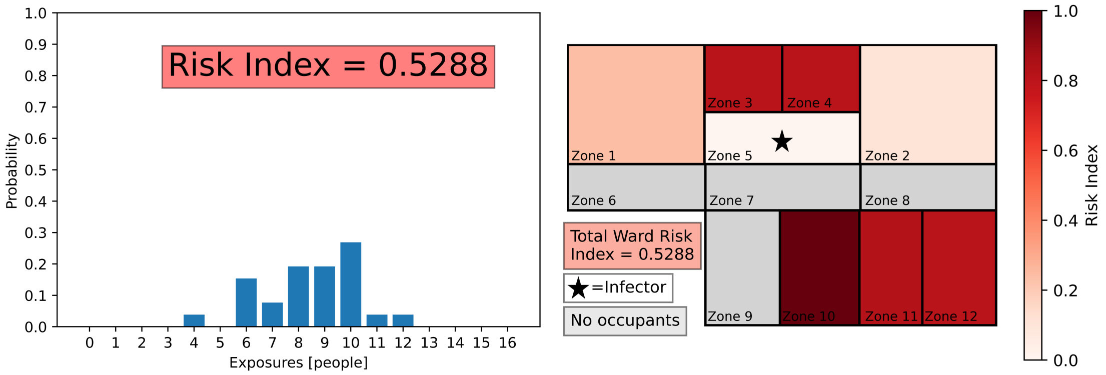

(a) Probability Distribution

(b) Heat Map of the RI

Figure 4.6: Predicted exposures for "Natural Ventilation Only": (a) probability distribution showing predicted weekly exposures and RI across the whole ward; (b) heat map showing the zonal RI value based on predicted exposure.

In this scenario, $RI = 0.5288$ translating to an expectation of 52.88% of individuals becoming exposed across the whole ward on a typical week. This appears to be a high value, however it is likely to be representative of a worst-case scenario as it is assumed that the infector is present in the ward for the whole time period (i.e., for the full week, not taking into account working shifts). In Figure 4.6b, the RI for each zone is illustrated as a heat map across the ward, giving an insight into the relative risk in each individual zone rather than a ward as a whole. The RI for each zone uses the corresponding number of initially susceptible individuals for that zone as S_0 in Equation (4.2), instead of the ward population as used for the ward RI. This gives the risk as a proportion of the number of people typically in the space. The risk is clearly variable across various zones, with particular zones having higher risk than others. This could be suggestive of a particular airflow pattern emerging, where the infectious material is more likely to be transported to particular zones, particularly as Zone 10 has a considerably higher risk than the other zones, and also has a larger typical occupancy of 3 individuals when compared to the other rooms. This airflow pattern is evident again in that Zone 2 experiences almost zero risk from the infector in Zone 5, but adjacent rooms have an elevated risk. The geometry (Figure 1.2) shows that Zones 1 to 4 are north-west facing, and so it is likely that they would catch the predominantly westerly wind (Figure 4.1) and be the reason for this emerging airflow pattern. The results here illustrate the uncertainty caused by the use of natural ventilation and the dominance of the weather conditions on determining the airflow and risk in indoor environments.

4.3.2.2 Addition of Mechanical Ventilation

This section explores the effects of including mechanical ventilation through the addition of 3 ACH and 6 ACH mechanical ventilation alongside open windows (i.e., natural ventilation and mechanical ventilation), and all doors closed as before. As mentioned in Section 4.2.2, for the required mechanical ventilation, an air handling system is used in CONTAM, where a balance of supply and extract ventilation distributed equally in each zone is assumed, so as not to create any additional pressure differences in the ward. Fresh air was taken to supply the required amount of air. The probability distribution for the predicted exposures together with the RI across the ward on a given week, and the heat map illustrating the RI value for each zone within the ward can be seen respectively for the case with 3 ACH mechanical ventilation in Figures 4.7a and 4.7b, and the case of 6 ACH mechanical ventilation in Figures 4.7c and 4.7d. In Figure 4.7a, results show a substantial reduction in risk with the predicted exposures now ranging from 0 to 2, illustrating a much smaller spread to the distribution and thus, less uncertainty. In addition, the $RI = 0.0769$, which is over an 85% reduction compared to the original case with natural ventilation alone. This can also be illustrated in the heat map of the ward (Figure 4.7b) with the RI for each corresponding zone, suggesting the pathogen would be better contained with less affected zones. The reduction in risk is also noticeable from the heat map with only one zone now affected, compared to all 7 occupied zones in the original case. This shows how the implementation of mechanical ventilation can lead to a reduction in infection risk and uncertainty across the space.

In the case with 6 ACH mechanical ventilation (Figure 4.7c), the recommended rate for NHS patient wards (NHS England [2021]), an even further reduction in the risk is seen with $RI = 0.0168$, over 96% less than the original case, around an additional 11% reduction from the 3 ACH scenario, showing the lowest risk in any scenario. The zonal RI heat map (Figure 4.7d) indicates low risk across all zones, with only one zone having a non-zero risk (less than 9%). Interestingly, in both cases, the mechanical ventilation has

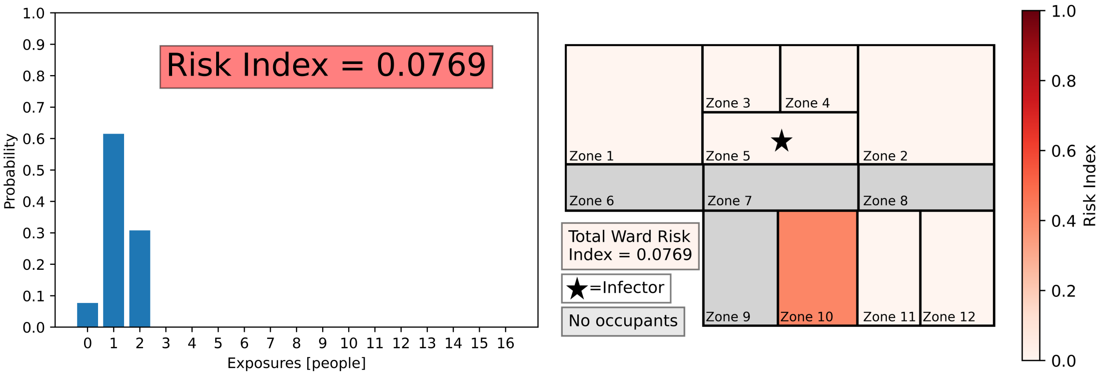

(a) 3 ACH (b) 3 ACH

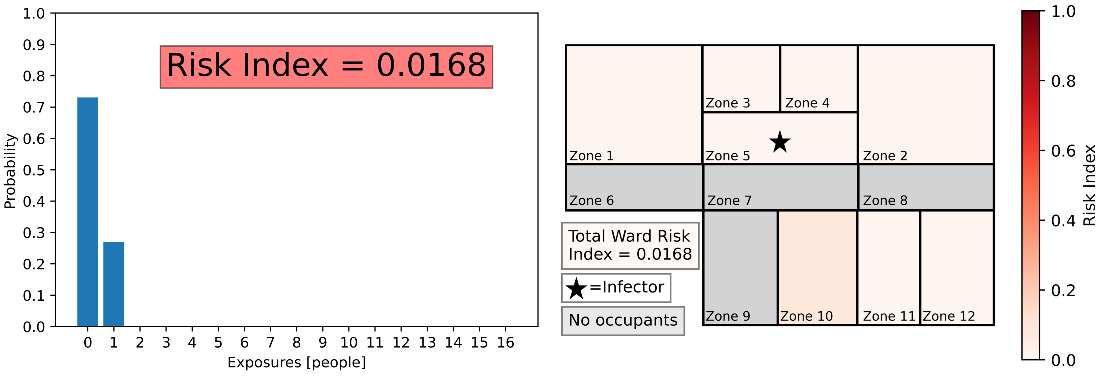

(c) 6 ACH (d) 6 ACH

Figure 4.7: Predicted exposures with the addition of mechanical ventilation, for two ventilation rates, illustrated as: (a) & (c) weekly probability distribution across the whole ward together with the RI value; (b) & (d) heat map showing the zonal RI value based on predicted exposures.

contained the infectious quanta concentration and reduced the contaminant transport much better than relying on weather-driven natural ventilation alone, eliminating the uncertainty and reducing the risk that was originally present. It is possible that natural ventilation and the consequent airflow contributes more to the transport of contaminant into connected spaces, rather than being efficient at the removal of the infectious quanta concentration. This further demonstrates that the effects seen in the original scenario (Section 4.3.2.1) were a direct consequence of the transient weather conditions. It is important to note that this is an idealised scenario, and in reality imperfect balancing of mechanical ventilation systems and the behaviour of people will likely mean that the difference between natural ventilation and mechanical ventilation is not as stark.

4.3.2.3 Ventilation Rates

Figure 4.8a presents a probability density plot illustrating the ventilation rates predicted across the ward by the CONTAM model for a period of 6-months of both the "Natural Ventilation Only" case and the "Natural Ventilation + 3 ACH Mechanical Ventilation" case. In addition, the average ventilation rate over the simulation period is plotted for both cases, along with the recommended ventilation rate of 6 ACH proposed in the UK HTM03-01 guidance (NHS England [2021]).

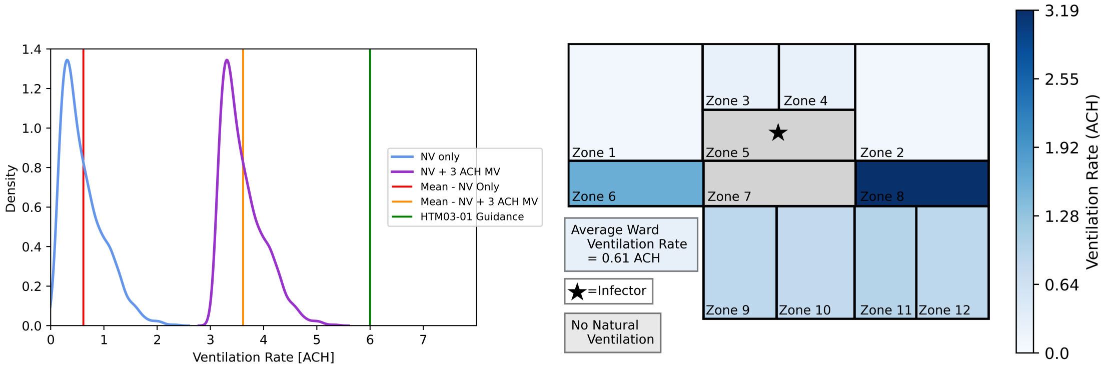

(a) Probability Density (b) Heat Map

Figure 4.8: (a) A probability density plot showing the overall ventilation achieved across the ward for both the "Natural Ventilation (NV) only" case and the "Natural Ventilation + 3 ACH Mechanical Ventilation (MV)" case, and (b) a heat map illustrating the average ventilation rates achieved for the scenario of "Natural Ventilation Only" for each zone.

In the "Natural Ventilation Only" case, the majority of the predicted ventilation rates fall below 1 ACH (82%) and 99.5% below 2 ACH, with the highest not surpassing 2.6 ACH, which is not even half of the recommended rate. The average ventilation rate achieved across the ward is 0.61 ACH. This illustrates not only the variability in natural ventilation rates, but also that they are not likely to be sufficient for healthcare settings based on the recommendation of 6 ACH provided in the guidance (NHS England [2021]). In addition to the density plot, it is possible to also visualise the average ventilation rates achieved in each zone by the heat map that can be seen in Figure 4.8b. This clearly indicates that the south-easterly side of the building is much better ventilated than the other, giving an insight into the airflow pattern across this subset of zones. This could be useful in informing healthcare professionals of the best zones in which to place an infectious individual or which zones may most need additional intervention with mitigation strategies, for example air cleaners.

It is also possible to consider how the ventilation rates may compare to healthcare guidance with the addition of 3 ACH mechanical ventilation to the natural ventilation provided through windows and leakage. In Figure 4.8a, a probability density curve is also shown for the ward ventilation rates for the case of "Natural Ventilation and 3 ACH Mechanical Ventilation". This results in the same shaped distribution as in the original case, but shifted to a higher value. However, it is still evident that all of the ventilation rates fall below the recommended rate of 6 ACH (NHS England [2021]). The simulation predicts that the model is still not reliably achieving the recommended ventilation rates across the ward. However, the addition of partial mechanical ventilation leads to a reduction in the risk (over 85%), and reduced uncertainty across the ward, mitigating some of the effects due to weather. This shows that even in spaces where it is not possible to reach the recommended rate, any additional mechanical ventilation device, or the implementation of air cleaners, could reduce infection risk. This may encourage some hospitals to implement what they can, where they can, rather than taking no action due to the recommended rate being problematic in retrofitting.

4.3.2.4 Open Bay Scenario

To fully assess the capabilities of natural ventilation alone, an "Open Bay" scenario was simulated. In this case, the windows and doors were both fully open for the duration of the simulation. This aimed to mimic a "Nightingale-style" hospital ward, which is fully open. The probability distribution for the predicted exposures together with the RI across the ward on a given week, and the heat map illustrating the RI value for each zone within the ward can be seen in Figures 4.9a and 4.9b, respectively.

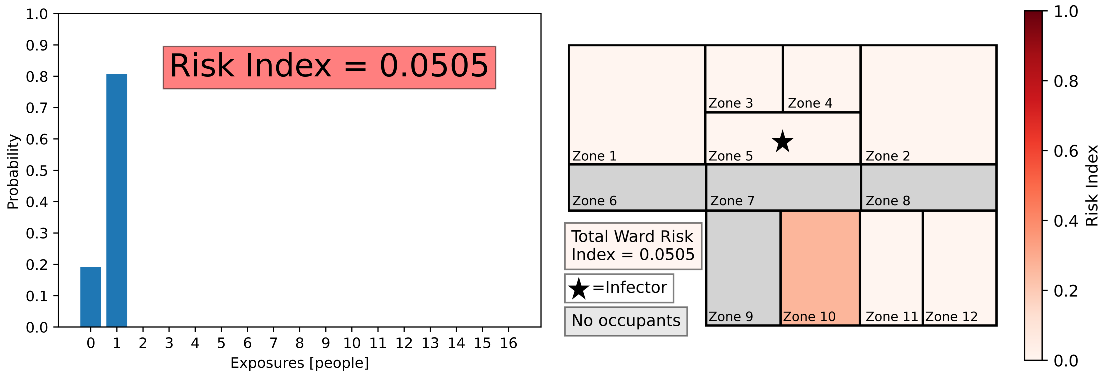

(a) Probability Distribution

(b) Heat Map of the RI

Figure 4.9: Predicted exposures for the "Open Bay" scenario (natural ventilation only with windows and doors open): (a) probability distribution showing the weekly predicted exposures across the whole ward; (b) heat map showing the zonal RI value based on predicted exposure.

In the exposure probability distribution (Figure 4.9a), a large reduction in the RI value is seen ($RI = 0.0505$), one of the lowest values that has been seen across any of the scenarios, with over a 90% reduction in risk from the original scenario with doors closed. Interestingly, this is lower than that in the case with natural ventilation and 3 ACH of mechanical ventilation, and almost equivalent to natural ventilation with 6 ACH mechanical ventilation, with the heat map (Figure 4.9b) almost identical to that scenario. This demonstrates that when natural ventilation is used in the way that it was most likely designed to be originally, on an open bay allowing for cross-flow across the whole ward, it is an effective tool. The simulations predicted up to 48 ACH average ventilation rates in particular zones in the ward, which is comparable to measurements in Peru (Escombe et al. [2007]) and Hong Kong (Qian et al. [2010]). However, in practical terms, when window openings are restricted for safety and thermal comfort, and doors are installed and closed for privacy or infection prevention and control, natural ventilation rates are reduced significantly.

4.3.3 Correlation with Weather Conditions

An investigation into the correlation between the varying weather conditions and the spikes in predicted quanta concentration is presented here. As the weather file data used in the simulations above was hourly, for consistency, the hourly concentration values from the transmission model were compared against each weather parameter; wind speed [$\mathrm{m\,s^{-1}}$], wind direction [°], outdoor air temperature [°C], and barometric pressure [Pa]. The results for each comparison can be seen in Figure 4.10.

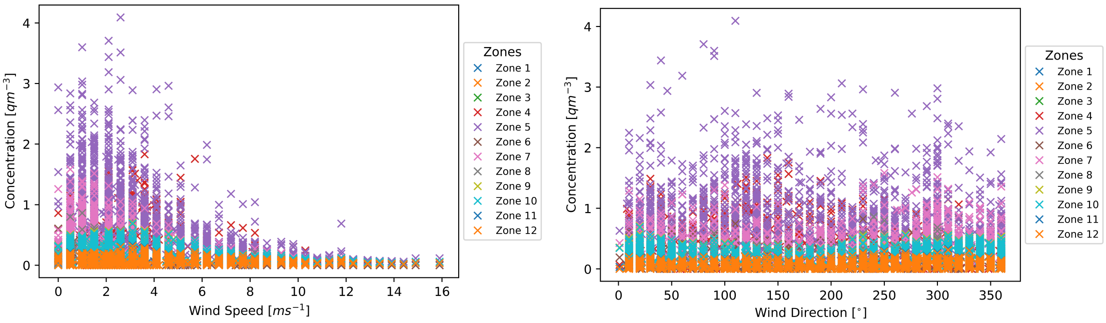

(a) Wind Speed [$\mathrm{m\,s^{-1}}$]

(b) Wind Direction [°]

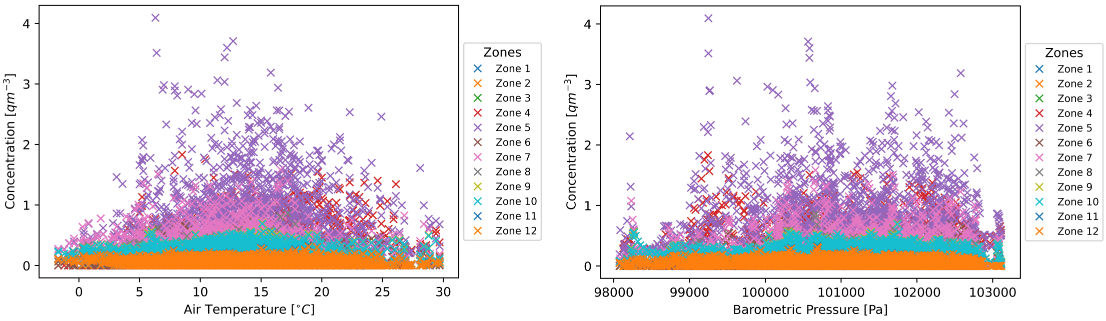

(c) Outdoor Air Temperature [°C]

(d) Barometric Pressure [Pa]

Figure 4.10: A comparison between the hourly weather data with the predicted quanta concentration solution for each zone for a period of 6-months from April 1st 2021 - September 30th 2021, inclusive, for each of the individual weather parameters.

As is shown in Figure 4.10, it is difficult to highlight clear correlations between the predicted quanta concentration values across the ward and the various weather parameters. However, when comparing the predicted quanta concentration value with wind speed (Figure 4.10a), the highest concentration values are associated with lower wind speeds (typically $< 6\,\mathrm{m\,s^{-1}}$). This is not surprising, as it is common to associate good natural ventilation with the ability to flush air throughout the indoor space, which is much harder to do at lower wind speeds. If there are lower wind speeds present, more stagnant air indoors would also be expected. However, it is possible that although this may increase the risk in the zone with the infector present or directly connected zones, it may reduce contaminant transport to the rest of the ward, which could be a reason why the correlation between these is not as strong. Also, there is a higher proportion of time where the wind speeds are at a lower value, which could be influencing the correlation that can be observed.

Another pattern that can be highlighted is the higher predicted concentration values being associated with temperatures (Figure 4.10c) in the range of $4.85 - 24.85\,^{\circ}\mathrm{C}$. Given that the indoor temperature is set at $22\,^{\circ}\mathrm{C}$ for zones with windows, and $25\,^{\circ}\mathrm{C}$ for zones without windows, there should be a more noticeable stack effect from the temperature differences, causing the colder outdoor air to be drawn into the building, with it rising and warming and exiting the building at a higher point, creating a more prominent temperature-driven flow. It would be expected that this would increase the flow through the building, however this is associated with higher predicted concentration levels here. It could be possible that although the flow is being driven by temperature differences, it is leading to more contaminant transport but is not strong enough to be efficient in removing the contaminant, particularly if this is also associated with lower wind speeds. It is also important to note that the CONTAM model does not enable the modelling of the full thermal performance of a building, with fixed internal temperatures assumed regardless of outdoor conditions. In reality, there would be temperature variations in indoor spaces, which could help or hinder the ventilation flow depending on the relative difference to the outdoor environment.

As for the comparison with barometric pressure (Figure 4.10d) and wind direction (Figure 4.10b), it is difficult to highlight any stand-out features at all. It seems that the comparison with each of the weather parameters fail to capture any strong correlation between these and the higher predicted concentration values, demonstrating that it may be more nuanced and related to the combination of all of these factors applied together over a longer time period to cause the spikes in predicted quanta concentration that are observed (Figure 4.5a). For completeness, the weather data was also compared to the predicted concentration values with a 1hr, 2hr, 1 day, 2 day and 3 day lag to see if the weather conditions had a delayed effect on the concentration value, and also cases with co-variables for each possible combination e.g., wind speed versus temperature coloured by concentration values were explored, all of which led to very similar results to the ones presented here, showing no strong correlation between particular weather parameters and concentration value, and so are not included here.

4.3.4 Alternative Infector Locations

In order to explore how risk might vary when the infectious source is in different locations, a further 3 additional cases were considered; an infector in Zone 1, an infector in Zone 2, and an infector in Zone 10. In each scenario, all other parameters remained the same including the original occupancy. The original infector in Zone 5 was now modelled as a susceptible individual and the susceptibles were reduced to account for the infector present in either Zone 1, Zone 2 or Zone 10 in each respective case. Simulations were carried out for the case with natural ventilation only, with all doors remaining closed and all windows open for the full duration of the simulation. Figure 4.11 shows the probability distribution for the predicted exposures together with the RI across the ward on a given week for the infector in Zones 1, 2 and 10.

When modelling the infector in a different location, each scenario has a similar overall RI value. However, as is visible from the distributions, this does not imply similar behaviour. For example, when the infector is in Zone 1 or Zone 2 (Figures 4.11a and 4.11c, respectively), both large 4-bed patient bays with windows, much more certainty is seen in the predictions, through a smaller range of possible exposures. This is suggestive that week to week, the infection risk and contaminant transport is less affected by weather variations and so the number of predicted exposures varies less than it does in the original case (e.g., Figure 4.6a), but also in the case where the infector is in Zone 10 (Figure 4.11e).

When the infector is in Zone 10 (Figure 4.11e), although the RI for this scenario is in between that of the other two locations, a different behaviour is illustrated by the exposure distribution. There is a much larger spread of the number of possible exposures ranging from 2 to 12. This demonstrates the uncertainty in infection risk when the infector is in Zone 10 and shows how the predicted number of exposures vary substantially week to week, as a result of the transient weather conditions.

Interestingly, Zone 10 is on the south-easterly side of the building, whereas Zones 1 and 2 are on the north-westerly side of the building. Given that Zone 10 also has windows present, this is suggestive that although higher risk is observed, the infection risk and contaminant transport predictions are lower if the infector is on the north-westerly side of the building (Zones 1 and 2), as much smaller ranges for the predicted exposures are seen. This suggests that the south-easterly side (Zone 10) of the building is also more sensitive to changes in weather conditions, which could be indicative of the flow pattern experienced across this hospital ward, with it likely being more dominant on that

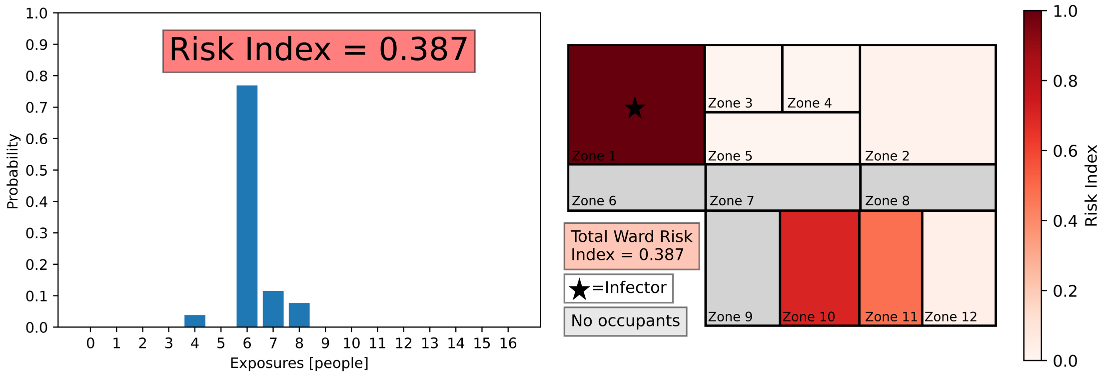

(a) Infector in Zone 1

(b) Infector in Zone 1

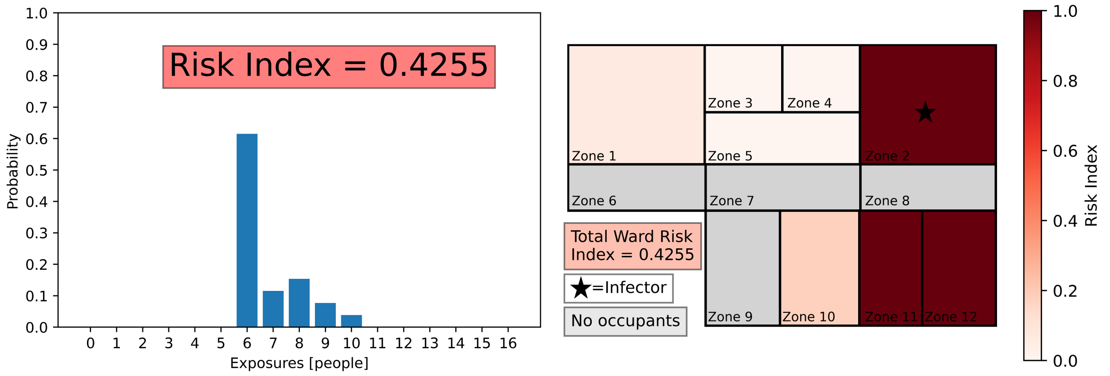

(c) Infector in Zone 2

(d) Infector in Zone 2

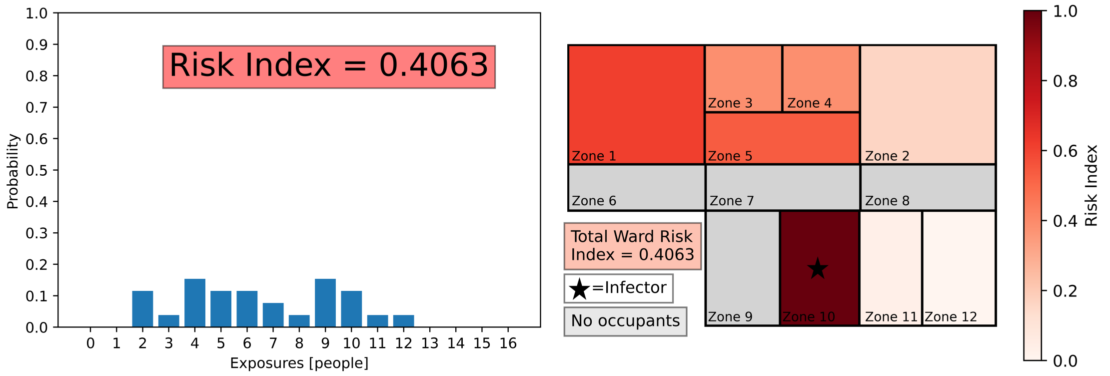

(e) Infector in Zone 10

(f) Infector in Zone 10

Figure 4.11: Predicted exposures illustrated as (a), (c) & (e) probability distribution for a given week across the whole ward together with the RI value, and (b), (d) & (f) heat map showing the RI value for each individual zone based on predicted exposure for three different infector locations.

side of the building. This is consistent with the heat map showing the natural ventilation rates in each zone across the ward. As is shown in Figure 4.8b, the ventilation rates on the south-easterly side are higher than those on the north-westerly, suggesting that this is the dominant flow direction.

When the infector is in Zone 1, despite seeing a high level of risk for Zone 1, the heat map (Figure 4.11b) shows that the risk elsewhere is reduced, especially when comparing with the original scenario (Figure 4.6b). The heat map also predicts a particular pattern of contaminant transport to the south-easterly side of the ward. This is, again, suggestive that prevailing wind conditions mean that the majority of the air is flowing towards the opposite side of the building with very little contaminant transport back into the zones on the north-westerly side. It also seems to display a diagonal pattern, where there is no risk visible in Zone 2 or Zone 12. This suggests these zones in particular may be at a stagnation point, or even form a separate airflow pattern that is isolated from the rest of the ward.

When the infector is in Zone 2, the heat map displays a very distinct pattern of risk, with high risk to Zones 2, 11, and 12, and only low risk to Zone 1 and Zone 10, with zero risk in other zones. This shows that the airflow in Zone 2 is not stagnant but is instead part of a separate airflow or re-circulation pattern including Zones 2, 11 and 12. However, the ventilation does not appear to be as efficient in these zones as the risk is much higher than in other scenarios, with the darkest red colour seen across the heat maps. However, this is not reflected in the RI value for the whole ward ($RI = 0.4255$), which is less than that in the original case, but this is likely due to nuances in the defined occupancy.

For the infector in Zone 10 (Figure 4.11f), low risk is predicted in Zones 2 and 11, with zero risk in Zone 12, again suggestive of a separate airflow pattern to the rest of the ward. As expected, the highest risk is in the zone with the infector present. However, there is non-zero risk on the opposite side of the ward too, suggesting that airflow and contaminant is travelling back towards the north-westerly side in sufficient quantities to cause exposures, contrary to the lack of back-flow presented in Figure 4.11b. These heat maps could help to inform patient locations when considering infection prevention and control. However, it is important to highlight that this is likely a direct consequence of the weather conditions, and so is subject to variations depending on the particular weather conditions experienced.

4.3.5 Orientation Study

St. James' Hospital in Leeds, UK, is a symmetrical building that has mirrored ward layouts on either side. Through the previous models in the chapter, the airflow was simulated on a geometry based on Ward J12, however, for completeness the geometry in the opposite orientation is explored here, that is flipped 180°, as though it were situated on the other side of the building. This allows for an investigation into whether the results observed are an artifact of the chosen ward's orientation, or a feature of weather effects interacting with airflow regardless of ward location. As in previous cases, the airflow results were exported from the CONTAM simulation and used within the transmission model. The outbreak parameters remained the same, with the infector in Zone 5; the set-up is identical to the case described in Section 4.3.2.1 but now with the geometry rotated 180°.

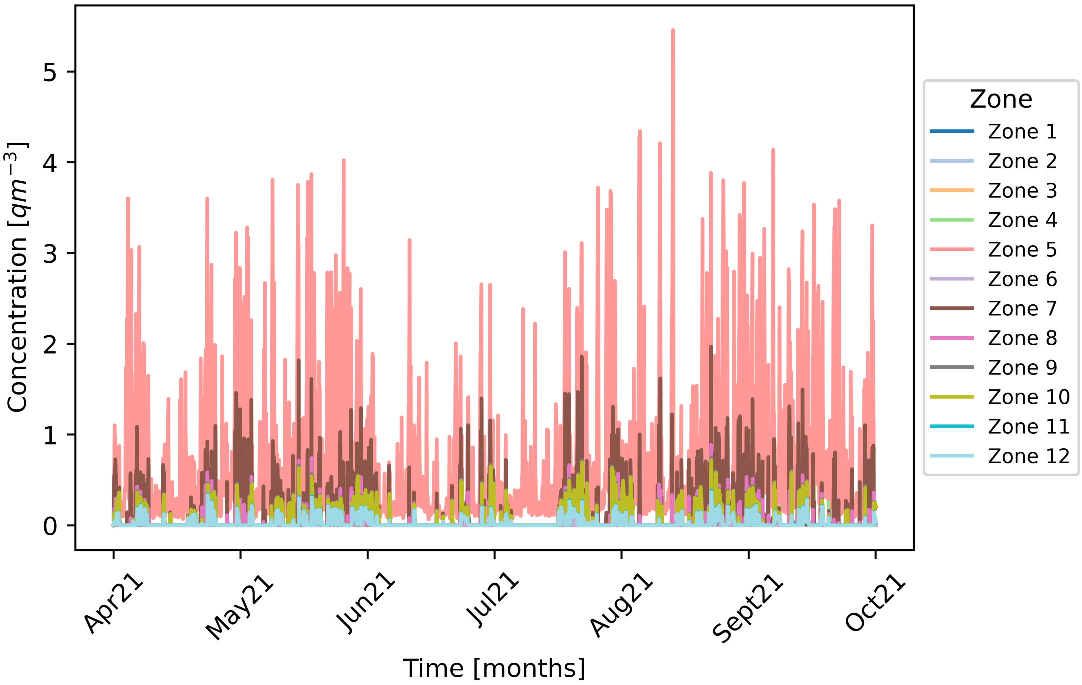

Figure 4.12: The full modelled solution for the concentration of pathogen for a 6-month period from April 1st to September 30th 2021 in the air for the orientation study, where the orientation is rotated 180°.

Figure 4.12 shows the solution for the predicted concentration of airborne pathogen in the ward. As can be seen in this figure, it is still possible to observe the spikes in the infectious quanta concentration, as before. This demonstrates that the airflow is displaying the same features as in the original case. Again, these peaks are mainly occurring in Zone 5, where the infector is located. When comparing this figure with the original orientation in the natural ventilation only case in Figure 4.5a, the peaks look more frequent in the case of the orientation study, but display similar behaviour.

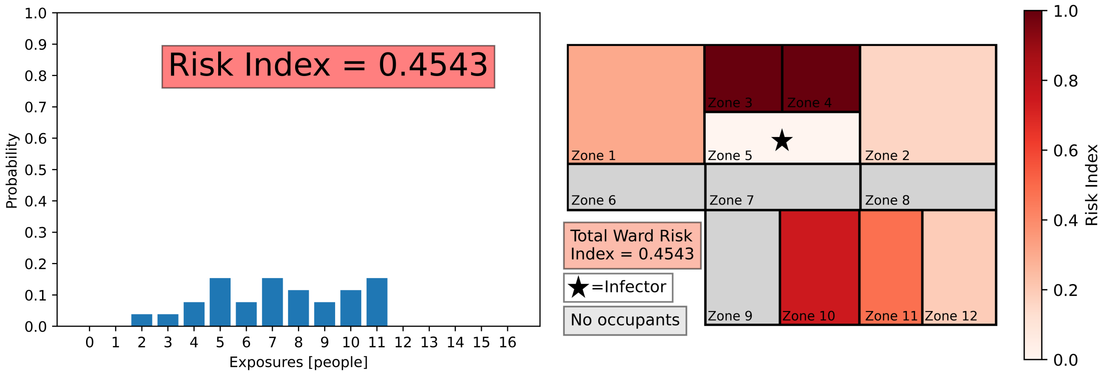

(a) Probability Distribution

(b) Heat Map of the RI

Figure 4.13: Predicted exposures for the orientation study, where the orientation is rotated 180°: (a) probability distribution showing the predicted weekly exposures and RI value across the whole ward; (b) heat map showing the zonal RI value based on predicted exposure.

To further compare between the different orientations, it is helpful to look at the predicted infection risk. Figure 4.13 illustrates the probability distribution of predicted exposures with the given ward RI, and a heat map of the ward illustrating the RI for each zone. The ward RI for this scenario is given as $RI = 0.4543$, which is lower than the original orientation scenario. However, in the probability distribution for the orientation study (Figure 4.13a), a larger range of possible predicted exposures (2 to 11 in this case) can be seen when compared with the original case (4 to 12). This is suggestive of greater uncertainty in the orientation study, showing that the ward may be more affected by transient weather conditions, with risk varying more on a weekly basis. In the heat map (Figure 4.13b), the highest risk zones are now in Zones 3 and 4, which are now on the the south-easterly side of the building due to the change in orientation. So although the orientation has been flipped, the south-easterly side of the building still experiences the highest risk, as in previous scenarios with natural ventilation alone, affecting different zones in each respective case. This is a possible feature of using the same weather file as the wind direction remained the same across both of the scenarios. It is possible that if the simulation was extended or a different weather file was used, the comparison of the two wards may be different again. Although the results do differ slightly, the same features are observed in both cases with sharp peaks in predicted quanta concentration, leading to increased infection risk and uncertainty across the ward.

4.3.6 Other Door Opening Scenarios

In addition to the scenarios presented above, a variety of alternative cases were modelled to explore variation in overall ward infection risk when varying the door opening schedules to various zones. Since the focus of this study was on the effects of transient weather conditions, throughout each simulation all other factors remained fixed. This limited the variation within each scenario, and meant that for example, the doors were fixed for the full 6-month modelling period. In reality, it is likely that the door opening schedule would change frequently due to other transient behaviours such as occupant movement, which was not modelled here.

In order to consider alternative door opening scenarios, in addition to the case presented above (all doors closed), two other door schedules were explored; half of the doors closed (only doors to patient zones were closed), and all doors open. In Table 4.2, the ward RI for all of the scenarios which have been discussed so far are presented, but now for all of the three door opening schedules.

Consistently across all cases, apart from those with mechanical ventilation, these show that an increase in door opening leads to lower risk and thus, the more effective the natural ventilation. This was seen specifically in Section 4.3.2.4, which showed a considerable reduction in risk, and ventilation rates as high as 48 ACH in some zones, demonstrating how effective natural ventilation can be when it is not obstructed by closed doors. Again, this is illustrated here with considerable lower risk across all scenarios when all of the doors are open. This shows that when a design permits full cross-flow of airflow on the ward, the natural ventilation is highly effective in reducing infection risk. However, it is once again worth highlighting that this is not always possible, nor practical.

An interesting feature to highlight is the case where mechanical ventilation has been added to the natural ventilation. In these cases, when half of the doors are open the RI is higher than when all of the doors are closed. This is likely due to the fact that when all of the doors are closed, the contaminant is better contained allowing for the full effect of mechanical ventilation in each zone. However, when half of the doors are open,

Scenario	All doors Closed	Half of the doors closed	All doors open
NV only - Infector in Zone 5 (original case)	RI = 0.5288	RI = 0.3582	RI = 0.0505
NV only - Infector in Zone 1	RI = 0.387	RI = 0.3774	RI = 0.1635
NV only - Infector in Zone 2	RI = 0.4255	RI = 0.3726	RI = 0.149
NV only - Infector in Zone 4	RI = 0.4832	RI = 0.3317	RI = 0.0505
NV only - Infector in Zone 10	RI = 0.4063	RI = 0.3149	RI = 0.1082
Orientation Study	RI = 0.4543	RI = 0.3269	RI = 0.0192
NV + 3 ACH MV	RI = 0.0769	RI = 0.101	RI = 0.0264
NV + 6 ACH MV	RI = 0.0168	RI = 0.0409	RI = 0.0024

Table 4.2: The ward RI for various modelled scenarios with three different door opening schedules. NV, Natural Ventilation; MV, Mechanical Ventilation.

it allows for enough contaminant transport to increase the risk, but neither containing the contaminant enough for the mechanical ventilation to be effective, nor enough open doors to allow for natural ventilation to be as effective as possible. All of these scenarios highlight the difficulties in choosing the most effective form of ventilation or removal mechanisms, and emphasise the importance of carefully considering the environment in which it is being implemented, with models such as the one presented here offering a useful tool to help assess this.

4.4 Discussion

The simulation results here illustrate the effects of weather conditions, building design and behavioural factors on airborne transmission when relying on natural ventilation. The initial scenario with natural ventilation only illustrates how weather conditions can vary the risk of infection. As shown in Figure 4.5, the highest quanta concentrations happen infrequently, but may be important for the transmission of infection. Other key factors will include the presence, type, and transmissibility of infection. This model represents a worst-case scenario where the infected person is present for a whole week at a time and with a quanta emission rate of $0.5\,\text{quanta}\,\text{min}^{-1}$ which is representative of a more infectious COVID-19 or influenza case (Mikszewski et al. [2021]). However, the results illustrate that when a set of conditions come together, such as the sustained presence of a more infectious individual combined with particular weather conditions, the chances of an outbreak become more likely.

The positive effects of mechanical ventilation are already well-known and this is further illustrated in the model when 3 ACH and 6 ACH are added to the natural ventilation. Despite 3 ACH of mechanical ventilation being half that of the recommended rate, it still dominates over the natural ventilation and dampens the effects of external weather conditions, reducing risk and uncertainty in both scenarios (over 85% reduction in RI value). The addition of 6 ACH does have an added benefit (additional 11% reduction in RI value) but the majority of the reduction comes from the initial 3 ACH. So although both cases demonstrate the benefits of mechanical ventilation, and that the recommended rate of 6 ACH has the bigger risk reduction, this shows that 3 ACH delivers the majority of this initial reduction, suggesting that even an underspecified mechanical ventilation system will provide better dilution and consistency as opposed to not acting at all. While the application of air cleaners have not been modelled explicitly, a similar result would likely be obtained.

Results also demonstrated that poor ventilation rates are likely to be achieved when relying on natural ventilation alone. Section 4.3.2.3 shows that all ventilation rates are less than 2.6 ACH (82% less than 1 ACH and 99.5% less than 2 ACH), far below that of the recommended rate of 6 ACH in the hospital guidance (NHS England [2021]). This is also illustrated on a heat map (Figure 4.8b), which could be useful in identifying zones which suffer from poorer ventilation and need further intervention. This is in part due to the internal design of the hospitals and limited access to the ambient environment. Buildings contain many internal zones, which do not have windows, leakage, or vents to outside air, and so unless other mitigation strategies are put in place, these locations could suffer from no ventilation at all. Many hospitals which were designed with open bays have had doors added for patient privacy, and in older buildings, existing windows or outlets have more recently been reduced in size due to safety measures, or removed completely in an effort to improve energy efficiency (Gilkeson et al. [2013]). Despite the original hospital design being able to provide sufficient ventilation, it is now likely that over time many of these conditions are no longer met. It is critical that internal airflow is considered as part of retrofit, and where modifications restrict window openings or reduce flow paths, additional ventilation should be considered to compensate.

An unintentional positive with the age of a building is the gaps, leakage and reduction in air tightness that naturally occurs. If left unmaintained, these can help to contribute towards natural ventilation rates and potentially improve the quality of air in indoor spaces. However, as this is unplanned, it is also highly uncertain and unreliable. Due to the inclusion of leakage in the CONTAM modelling, it is possible this is contributing to the natural ventilation rates achieved in Figure 4.8, meaning the air exchange rates through originally intended sources are even lower.

Another feature of this study is the possibility of identifying dominant airflow patterns, and locations around the hospital which may prove to have consistently lower risk than others. The use of a heat map presenting the RI for each zone can be a useful tool to help indicate any patterns. This was particular noticeable when plotting the natural ventilation rates in Figure 4.8b. The zones on the south-easterly side of the building display higher ventilation rates than those on the north-westerly side, suggesting that the air is flowing towards the south-easterly side more dominantly. Additionally, in every scenario throughout this paper, the RI in Zone 10 has been consistently higher than in any other zone, again suggesting that this zone often receives the highest amount of infectious concentration, and is susceptible to a dominant flow path. This analysis could prove useful when choosing patient or mitigation locations. Despite the ventilation rates in some zones being higher than others, the risk is still high. It is possible that the internal airflow rates governed by the natural ventilation are having a large impact on contaminant transport to these zones, but are not efficient nor fast enough with the removal of the infectious material. This further supports the use of mechanical ventilation or approaches such as air cleaners, contrary to solely relying on natural methods.

As this study is based on a model, it has a number of limitations. The model is based on the floor plan, occupancy, windows and representative weather conditions for a single UK respiratory ward. However, the model does not aim to quantify risks explicitly on that ward. The scenarios were designed to be realistic, but only considered the influence of ventilation and not the complexities that exist in a real ward. The model is idealised and does not fully capture all the factors that create internal flows, including turbulent mixing, which is not present in the CONTAM airflow model, and variations in internal temperatures. However, the comparison of the airflow with CO_2 data suggests that the mixing achieved is realistic.

The use of a local transient weather file (Climate.OneBuilding [2022]), using real historical data, enabled the modelling of possible scenarios. As with any transmission model, validation against infection cases is almost impossible, as identifying where the source of an outbreak originated, and replicating the exact transient behaviours, occupancy and external conditions at the time is difficult. Also, the contribution of other transmission routes (i.e., close range and fomite) are not considered here. The limitations of transmission models are discussed in Chapter 3. The choice of the infectiousness of an individual will adjust the risk index values in these scenarios. For example, in the first scenario with natural ventilation only, simulations with a pathogen emission rate of $q = 1\,\text{quanta}\,\text{h}^{-1}$ and $q = 10\,\text{quanta}\,\text{h}^{-1}$ result in RI values of 0.0337and 0.2644, respectively. However, this does not alter the relative risk in each space nor the overall spatial behaviour of the pathogen transport to inter-connected zones. In this chapter, the same infectiousness of $q = 30\,\text{quanta}\,\text{h}^{-1}$ ($q = 0.5\,\text{quanta}\,\text{min}^{-1}$) was used, as in Chapter 3. This is a realistic choice given that Mikszewski et al. [2021] present ranges of $15 - 4213\,\text{quanta}\,\text{h}^{-1}$ for SARS-CoV-2, $18 - 8640\,\text{quanta}\,\text{h}^{-1}$ for measles virus, and $0.11 - 79\,\text{quanta}\,\text{h}^{-1}$ for influenza virus. In this chapter, the intention is not to predict exact outbreak patterns, but rather by using the modelling approach, develop a much better understanding of the long-term effects of natural ventilation and weather conditions on airflow and the potential for an outbreak.

The heat map illustrating the zonal RI could be used to help healthcare professionals identify areas of high risk, and to translate the complex modelling and mathematical assessment more easily into usable features for healthcare systems. This could be particularly useful in distinguishing between the ward or zone which requires intervention. In the scenario of a pandemic where the hospital is under elevated pressure with a scarcity of resources such as PPE, the heat map could help to assess whether the ward as a whole is high risk or whether it is only particular zones. For example, in Figure 4.6b, there are numerous zones with elevated risk and so it may be easier to apply a blanket mitigation of PPE to the whole ward. Whereas in Figure 4.7d, only Zone 10 has increased risk, but the rest of the ward has little to no risk. So here it would be more appropriate to only apply PPE to the visitors to this particular zone, rather than everyone visiting the ward. This would help to reduce resource waste and save it for the scenarios that need it most. Although this study does not directly investigate the implementation of outputs (e.g., the heat maps) into healthcare systems, this accessibility and comprehensible illustration of the results is a priority. Without valuable output methods, it may be difficult or too time consuming for healthcare professionals to translate this research into practical terms, alongside completing often chaotic schedules, highlighting the need for more consideration into the applicability and implementation of informative research.

4.5 Conclusion

In conclusion, through the use of transient weather conditions within an airflow and transmission model, this chapter has highlighted how weather conditions have a significant influence on internal airflow, and can lead to uncertainty and periods of higher pathogen concentrations within ward environments. When these conditions are combined with the presence of a more infectious person on the ward, the probability of a large outbreak increases. This uncertainty also extends to ventilation rates, with many naturally ventilated spaces falling far below the recommended standard. Reliance on closed internal doors and restricted window openings is not likely to provide sufficient ventilation for wards based on the recommendation of 6 ACH provided in the guidance (NHS England [2021]).

Mechanical ventilation or other similar approaches, such as the use of air cleaners, can help to reduce the effects of transient weather on natural ventilation. This includes ensuring a more consistent in-room ventilation rate, and reducing the unwanted transfer of air between spaces, and can, in turn, decrease the risk to patients. Through illustrative outputs such as heat maps, the aim is to be able to advise engineering and healthcare professionals of the risk distribution of their multi-room hospital wards, and help make informed choices of mitigation strategies.

Chapter 5

A Monte Carlo Approach

As discussed in previous chapters, QMRA is a well-established framework for assessing the risk of airborne transmission and the importance of outbreak parameters. However, many current approaches are often constrained by the availability of outbreak data, or fail to identify the relative importance of factors affecting infection risk. In this chapter, a Monte Carlo approach, extending a deterministic QMRA model to incorporate stochastic effects, is presented. This allows for the variation of outbreak parameters such as the infectiousness of the infector, accounting for population heterogeneity, and the day of the outbreak, influencing the weather conditions and resulting natural ventilation. Through 10,000 runs in a Monte Carlo simulation, the role of these varying parameters on the predicted number of resulting exposures is assessed. As expected, the results show that typical behaviour from the full Monte Carlo simulation predicts higher infection risk for poorer ventilation rates and higher infectiousness. However, when investigating individual days of the simulation, it is observed that particular days (i.e., certain weather conditions) can cause inherently high or low risk, regardless of the infectiousness of the infector. This highlights the nuances present when assessing outbreaks, and further shows the important role that ventilation plays in influencing the transmission of airborne pathogens. By extending existing QMRA models to include stochastic effects, it is possible to investigate a wider range of scenarios, and thus provide a more realistic quantification of infection risk and the factors that affect airborne transmission.

5.1 Introduction

QMRA has been used to provide risk assessments for a broad range of applications, as highlighted in Chapter 1, with recent work identifying potential future research areas to ensure the continued advancement of QMRA techniques (Hamilton et al. [2024]). Although QMRA is a well-established tool (Haas et al. [1999], Haas [2020]), many current approaches are often constrained by the availability of outbreak data, or fail to capture the multitude of factors affecting infection risk (Beaudequin et al. [2015]).

Stochastic techniques such as Monte Carlo simulations allow for unknown outbreak parameters to be represented as a probability distribution (e.g., a lognormal distribution (Chen et al. [2011]) or a uniform distribution (Miller et al. [2021])) or a set of defined choices a priori, better reflecting everyday life by accounting for uncertainty and variability. The Monte Carlo simulation then repeatedly simulates the model, each time drawing a different, random set of input values from the predefined parameter distributions, with the results shown as a set of possible outcomes with different probabilities (Bonate [2001]).

An increasingly common approach in airborne transmission modelling is to use Monte Carlo approaches to explore infection risk with uncertainty and variability in different outbreak parameters (Chen et al. [2011], Wilson et al. [2021b], Guo et al. [2022], Wilson et al. [2022]). In particular, these can include but are not limited to emission rates and dose (Buonanno et al. [2020a], Chen et al. [2021]), pathogen concentration (Shi et al. [2018]), and outbreak duration or infector location (Noakes and Sleigh [2009]), with the Monte Carlo simulation resulting in a probability distribution for infection risk (Liao et al. [2005], Shi et al. [2018], Buonanno et al. [2020a], Yan et al. [2021]). It is also possible to use Monte Carlo simulations to estimate unknown parameters (e.g., emission rates (Buonanno et al. [2020a], Miller et al. [2021]), virions in an aerosol (Guo et al. [2022]) or the reproductive number (Chen et al. [2011])), find the best-fit probability distributions for a given parameter (Liao et al. [2005]), or to confirm predictions of analytical models (Juher et al. [2009]).

In this chapter, a Monte Carlo simulation is used on an transient multi-zone transmission model (as presented in Chapter 4) to explore variability in infection risk predictions of a 24 h outbreak on a naturally ventilated UK respiratory ward, where the quanta emission rate of the infector is unknown and sampled from a distribution, and the ventilation setting, representing a given day within a 6-month period (April 1st 2021 - September 30th 2021), is chosen at random.

5.2 Methodology

The Monte Carlo simulation consists of repeatedly solving a transmission model coupled with airflow simulation results over a 24 h period, whilst sampling some input parameters from relevant probability distributions. To model the airflow, the same methodology and simulation results are used as described in Section 4.2.1. In this chapter, the results from the 6-month simulation are divided into airflow results for individual days, totalling 183 days from April 1st 2021 to September 30th 2021, inclusive. The transmission model in this chapter uses the same methodology as described in Section 4.2.2. The simulation is repeated $N_{mc} = 10,000$ times, each time recording the total number of predicted exposures after selecting a random quanta emission rate for the infector, and selecting a random day between April 1st 2021 to September 30th 2021, representing the airflow and ventilation setting for that day. By choosing a random day for the ventilation setting, this allows for a variety of different weather conditions and natural ventilation rates to be modelled.

The geometry, defined zones and volumes can be seen in Figure 1.2. As before, there are assumed to be 4 individuals in Zones 1 and 2, 1 individual in Zones 3 and 4, 1 individual in Zone 5, 3 individuals in Zone 10, 2 individuals in Zone 11 and 1 individual in Zone 12, totalling 17 individuals. The infector is set to be the individual in Zone 5, giving 16 initially susceptible individuals, 0 initially exposed individuals and 1 initially infectious individual. The number of infectious individuals remains constant throughout.

A lognormal distribution, $LN(184.64, 2.1)$, is used to define the quanta emission rate of the infector, q, with geometric mean and geometric SD given as 184.64 and 2.1, respectively, as given in Chen et al. [2021], estimated for SARS-CoV-2 from the Diamond Princess cruise ship outbreak. The resulting probability density function can be seen in Figure 5.1. A sample of size N_{mc} is taken from the distribution and a value chosen at random in each Monte Carlo run, allowing for the possibility of a unique value on each run. The quanta emission rate is capped at 1000 quanta h^{-1}, to limit the infectiousness of the individual within a realistic range. Any values in the sample that are greater than 1000 quanta h^{-1} are discarded and re-sampled until the value is less than or equal to 1000 quanta h^{-1}. It is often challenging to select an appropriate quanta emission rate to represent an infectious individual as it cannot be experimentally measured, but is instead estimated epidemiologically from outbreak data (Sze To and Chao [2010]). Recent approaches have attempted to improve the accuracy of quanta emission rate predictions through estimations based on the viral load present in sputum from the mouth

(Buonanno et al. [2020b]), and through measurements from a human challenge study (Bueno de Mesquita et al. [2020]), but this still remains a challenge with data showing that quanta emission rates can have large variations (Mikszewski et al. [2021]).

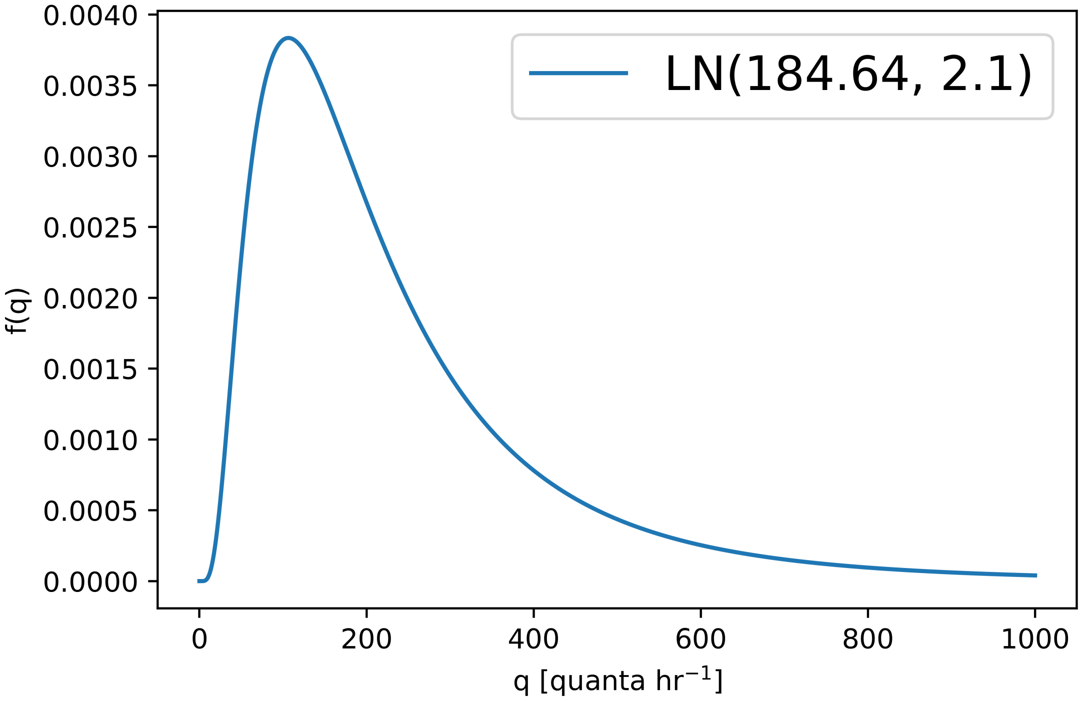

Figure 5.1: The probability density function of a lognormal distribution $LN(184.64, 2.1)$ with geometric mean and geometric SD given as 184.64 and 2.1, for SARS-CoV-2 quanta emission rate, q. The distribution is truncated at $q = 1000\,\text{quanta}\,\text{h}^{-1}$.

The pulmonary breathing rate was set to $p = 0.01\,\text{m}^3\,\text{min}^{-1}$ (Noakes and Sleigh [2009]). For the removal rate, the models in Chapters 3 and 4 were modified and the extract ventilation rate Q was replaced by a more general removal rate, R, as defined in Equation (2.6). The extract ventilation rate, Q, was defined by the airflow simulation results, as in Section 4.2.2, and is dependent on the day chosen at random in each run of the Monte Carlo simulation. For the viral inactivation and deposition rates, the mid-points of the ranges proposed in Miller et al. [2021] were chosen, leading to $r_i = 0.00525\ \text{min}^{-1}$ and $r_d = 0.015\,\text{min}^{-1}$.

5.3 Results

5.3.1 Sensitivity Analysis

Sensitivity analysis was conducted to investigate whether $N_{mc} = 10,000$ runs of the Monte Carlo solution was sufficient to provide a representative distribution for the model output (i.e., number of exposures). To conduct the sensitivity analysis, the Monte Carlo simulation was performed four different times with $N_{mc} = 10,000$ runs; one forming the solution base for this chapter, and three additional simulations to compare with. Additionally, this was repeated for a Monte Carlo simulation with $N_{mc} = 100$ runs and $N_{mc} = 1,000$ runs, for completeness.

Figures 5.2a - 5.2c illustrate the full solution for the predicted mean number of exposures for 4 Monte Carlo simulations modelling a 24 h outbreak for $N_{mc} = 100$ runs, $N_{mc} = 1,000$ runs, and $N_{mc} = 10,000$ runs, randomly choosing an emission rate and day (for the ventilation setting). In addition, the shaded regions in each plot represent the region between the 5^{th} and 95^{th} percentile of each solution in the respective colour, where the opacity parameter has been decreased to allow the visualisation of any overlapping.

Figure 5.2a illustrates variation across the predicted mean number of exposures for the four different Monte Carlo simulations with $N_{mc} = 100$ runs, with visible differences in the overlapping shaded regions, showing that these solutions do not align and that more runs would be required. An improved comparison can be seen in Figure 5.2b for $N_{mc} = 1,000$ runs, particularly in the solutions for the predicted mean number of exposures. However, there is still a lack of overlap visible in the shaded regions across the four different Monte Carlo simulations, showing that $N_{mc} = 1,000$ runs are not sufficient to provide solutions that are robust against the random sampling of selected input parameters.

However, as can be seen in Figure 5.2c with $N_{mc} = 10,000$ runs, the solution for the mean number of exposures and each shaded region across all 4 simulations show very good agreement, with almost no difference between them. This figure offers reassurance that $N_{mc} = 10,000$ runs of the Monte Carlo simulation is sufficient to provide solutions that are robust against the random sampling of selected input parameters. It is also noted that $N_{mc} = 10,000$ runs has been used as a benchmark in other studies (Shi et al. [2018], Guo et al. [2022]).

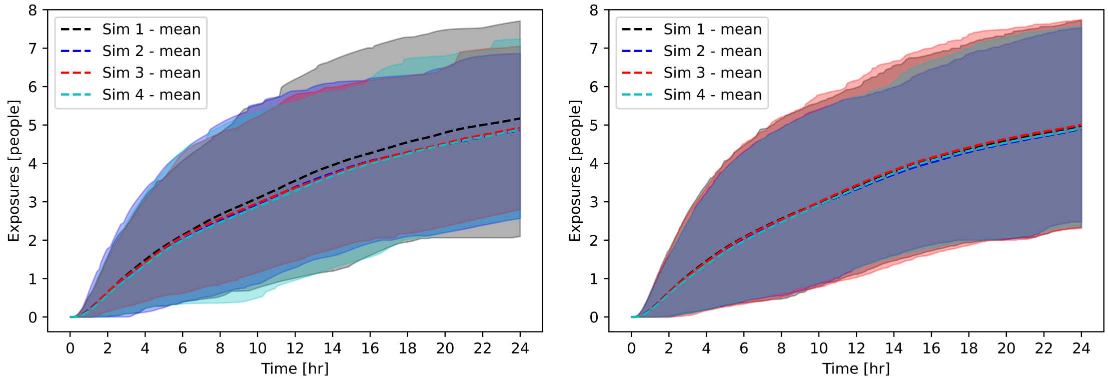

(a) $N_{mc} = 100$

(b) $N_{mc} = 1,000$

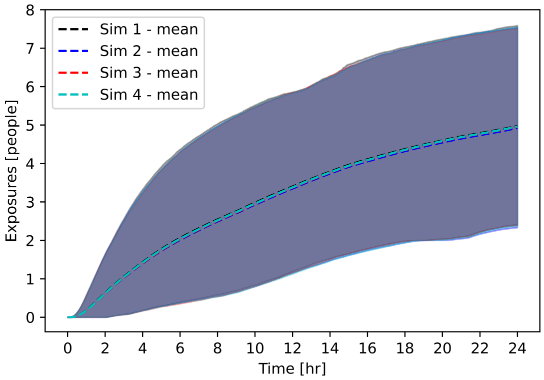

(c) $N_{mc} = 10,000$

Figure 5.2: A comparison of the solution for the predicted mean number of exposures for a 24 h outbreak from four different Monte Carlo simulations with (a) $N_{mc} = 100$ runs, (b) $N_{mc} = 1,000$ runs, and (c) $N_{mc} = 10,000$ runs. The shaded regions represent the region between the 5th and 95th percentile of each simulation in the respective colour.

5.3.2 Natural Ventilation Only

In the same way as in Chapter 4, a case of natural ventilation only is assessed, but in this chapter, a 24 h period is considered instead. To assess the predicted number of exposures under natural ventilation only, a probability distribution of the predicted number of exposures from the Monte Carlo simulation can be seen alongside a RI value (Equation (4.2)) in Figure 5.3a. In Figure 5.3b, a heat map of the geometry can be seen illustrating the RI value for each zone, and the ward as a whole.

From the heat map in Figure 5.3b, all zones with susceptible patients present have a non-zero RI value, albeit small. However, it is clear that the risk is highly concentrated to two zones in this scenario; Zone 10 and 11. The probability distribution in Figure 5.3a is a unimodal distribution centred around 5 predicted exposures, with a mean number of predicted exposures equal to 4.973. This is likely due to the fact that the total susceptible population in Zone 10 and Zone 11 combined is equal to 5, the zones with the highest RI.

The relatively symmetric shape of the probability distribution can also be seen through Figure 5.4, which shows the mean, median, a red shaded region between the 5th and 95th percentiles, and a purple shaded region between the 25th and 75th percentiles for the full solution of the predicted number of exposures for a 24 h period. This figure shows that the mean and median show good agreement, consistent with the symmetric features of the probability distribution seen in Figure 5.3a.

The other feature to highlight in Figure 5.4 is the size of the shaded region between the 5th and 95th percentiles. This illustrates the large variability between predicted exposure solutions across the $10,000$ simulations when using different days and quanta emission rates, also visible with the large spread of the probability distribution with a range of 1 to 8 possible exposures (Figure 5.3a). Both of these figures show the uncertainty present in airborne transmission risk when relying on natural ventilation alone and allowing for uncertainty in parameter values, illustrating the variability that exists in real-life outbreaks.

Figure 5.5 investigates the role of the two parameters that were randomly chosen in each run of the Monte Carlo simulation, with a scatter plot of the chosen quanta emission rate and ventilation day, with the points coloured by the predicted number of exposures at the end of the 24 h period.

In Figure 5.5, the overall pattern shows dominance from the quanta emission rate, with

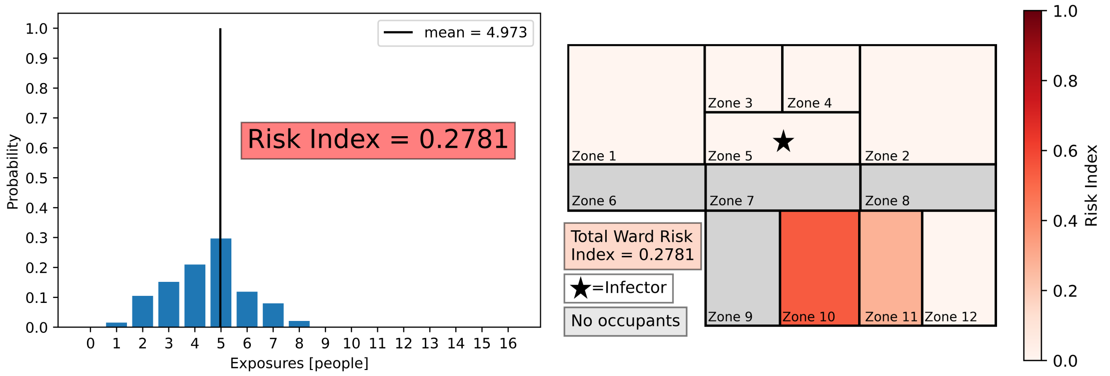

(a) Probability Distribution

(b) Heat Map of the RI

Figure 5.3: Predicted exposures from the 10,000 Monte Carlo simulations for natural ventilation only: (a) probability distribution showing predicted weekly exposures and RI across the whole ward; (b) heat map showing the zonal RI value based on predicted exposure.

an increased number of predicted exposures as the quanta emission rate gets larger for the majority of the days chosen for the ventilation setting. However, it is possible to observe a pattern horizontally as well, where it appears that particular days manage to limit the number of exposures regardless of how high the quanta emission rate gets, suggesting that these particular days benefit from a higher overall natural ventilation rate or a particularly beneficial airflow pattern. It is also possible to observe the opposite behaviour, suggesting that some particular days have a lower natural ventilation rate or airflow pattern facilitating contaminant transport to zones with a larger occupancy, leading to an increased number of exposures across all quanta emission rates. This highlights the additional uncertainty present in infection risk modelling when relying on natural ventilation alone and the possibility of inconsistent airflow.

Finally, Figure 5.6 illustrates a scatter plot with a direct comparison between the total number of predicted exposures with the quanta emission rate used for the simulation, coloured this time by the ventilation day used. This figure displays a cone-like shape, where the number of predicted exposures increases with increased quanta emission rate, as would be expected. However, it is also evident that on particular days, the number of predicted exposures is limited and follows a distinctive trajectory regardless of the quanta emission rate, suggesting that the ventilation rate or flow pattern observed on particular days are either affecting contaminant transport to particular zones, or varying in removal efficiency, as indicated in Figure 5.5. It is possible that this

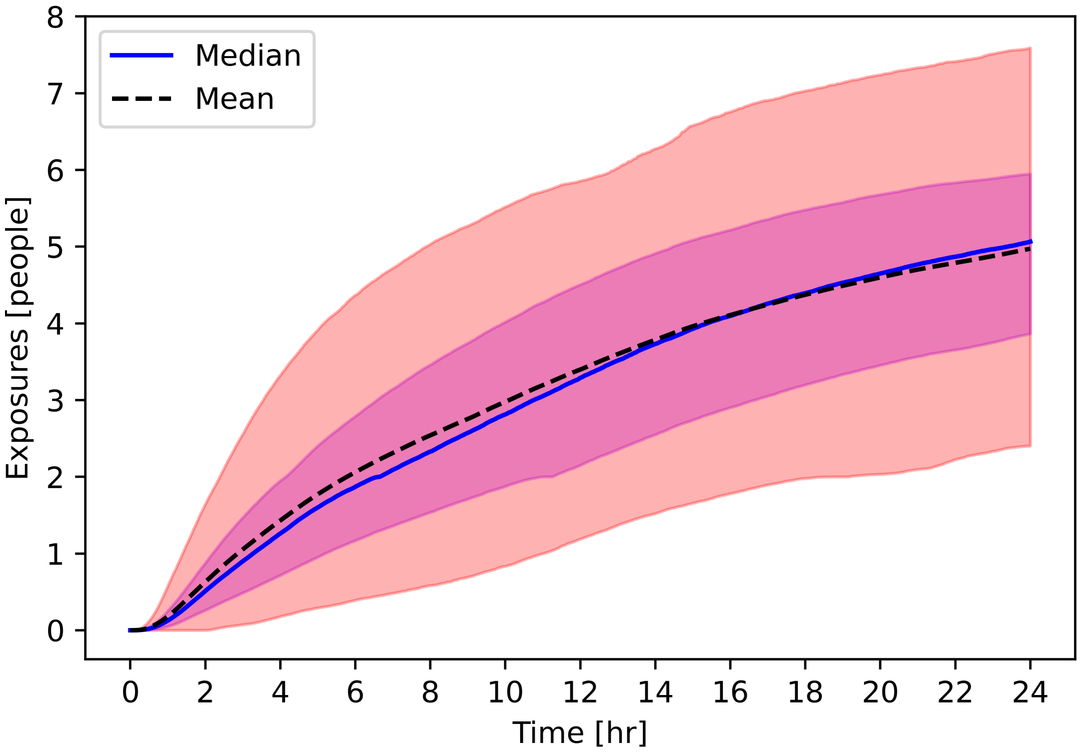

Figure 5.4: The predicted number of exposures over a 24 h period from the 10,000 Monte Carlo simulations shown as the mean, median, a red shaded region between the 5th and 95th percentiles, and a purple shaded region between the 25th and 75th percentiles for natural ventilation only.

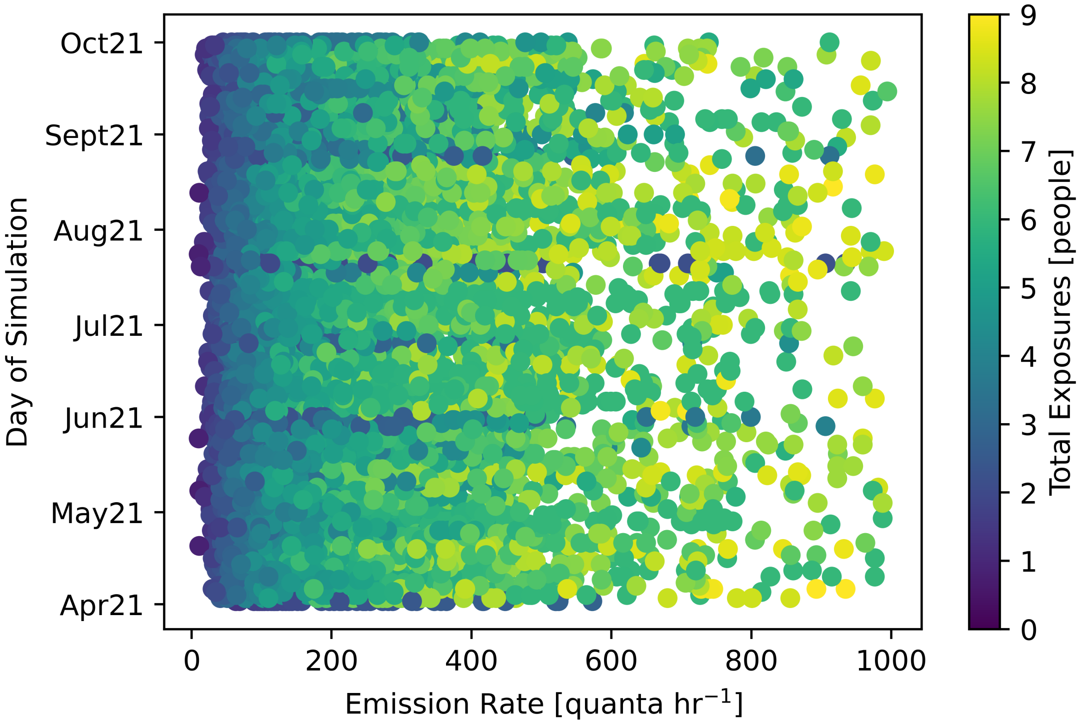

Figure 5.5: A scatter plot comparing the randomly chosen day (ventilation setting) and quanta emission rate for the 10,000 Monte Carlo simulations, coloured by the resulting total number of predicted exposures for natural ventilation only.

is also influenced by nuances with the susceptible population defined in certain zones, but it indicates that the exposure trajectory for a given day is predefined based on the weather conditions, and thus, the resulting natural ventilation and airflow.

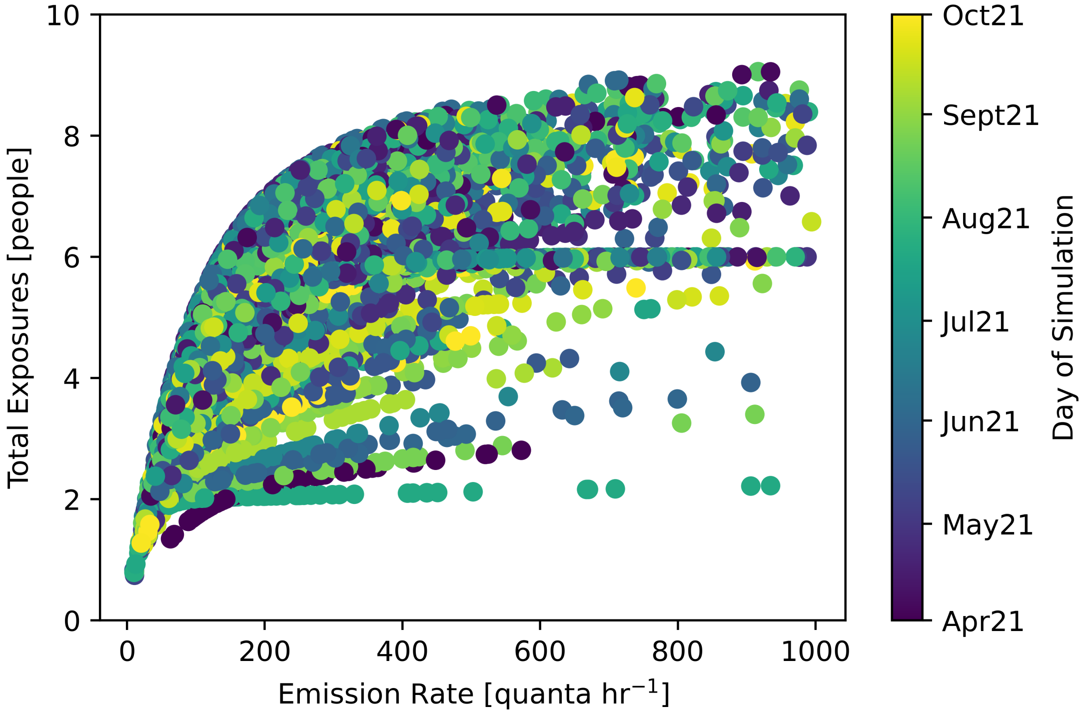

Figure 5.6: A scatter plot comparing the total number of predicted exposures and quanta emission rate for the 10, 000 Monte Carlo simulations, coloured by the randomly chosen day (ventilation setting) for natural ventilation only.

Despite the set-up of this natural ventilation only case being similar to the one presented in Chapter 4, it is worth highlighting that the results in this chapter (Figure 5.3) are different to those previously presented (Figure 4.6). This is because of the random sampling used to determine the input parameters. In particular, the simulations in this chapter allow for a variable quanta emission rate, sampled from a probability distribution, in each modelled 24 h period. Additionally, although the airflow results from the 6-month CONTAM simulation presented in Chapter 4 are used here, this is instead considered over 24 h periods rather than weekly periods, and the day used for the simulation is randomly sampled from the 6-month period, as opposed to being considered chronologically.

5.3.3 Addition of Mechanical Ventilation

In addition to the random selection of day and thus, natural ventilation setting in Section 5.3.2, 3 ACH of mechanical ventilation is now added. Additionally, this allows for a comparison of the results obtained here via Monte Carlo methods with those in Section 4.3.2.2. Figure 5.7a shows a probability distribution for predicted number of exposures from the $10,000$ Monte Carlo simulations alongside a RI value (Equation (4.2)), with Figure 5.7b showing a heat map of the geometry illustrating the zonal RI value.

The probability distribution for the case with the addition of 3 ACH mechanical ventilation is now asymmetric and long tailed, compared to the symmetric distribution seen in the case with natural ventilation alone (Figure 5.3a). Additionally, there is $> 62\%$ reduction in RI, and only one zone (Zone 10) has a noticeably increased risk, with the other zones displaying non-zero, but relatively small RI values. A substantial reduction in infection risk is observed when providing an additional 3 ACH of mechanical ventilation. However, the range of predicted exposures is from 0 to 5, instead of 2 to 8 in Section 5.3.2. So although the infection risk has reduced, the uncertainty in infection risk prediction is still present, likely due to the use of a Monte Carlo simulation approach incorporating randomness.

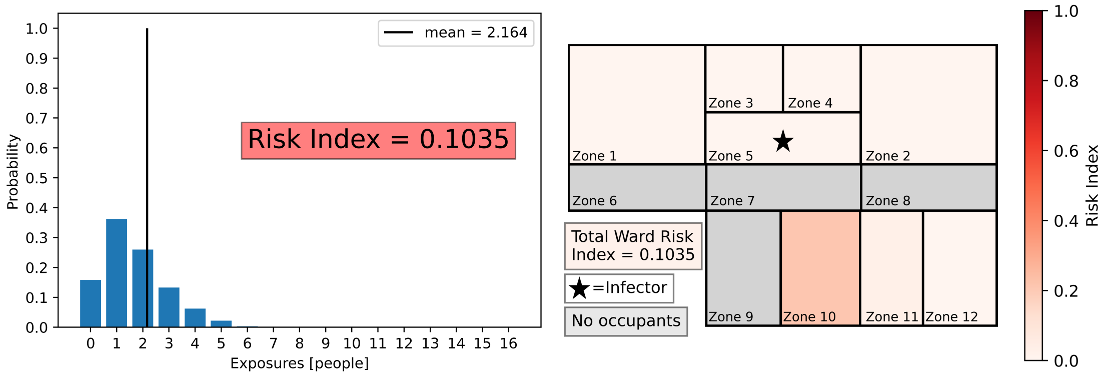

(a) Probability Distribution

(b) Heat Map of the RI

Figure 5.7: Predicted exposures from the $10,000$ Monte Carlo simulations for natural ventilation with 3 ACH mechanical ventilation: (a) probability distribution showing predicted weekly exposures and RI across the whole ward; (b) heat map showing the zonal RI value based on predicted exposure.

In Figure 5.8, the predicted number of exposures with the addition of 3 ACH mechanical ventilation can be observed with the mean, median, a red shaded region between the 5th and 95th percentiles, and a purple shaded region between the 25th and 75th percentiles. The mean and median solutions deviate more than the case with natural ventilation alone (Figure 5.4), which is consistent with the asymmetric shape of the probability distribution (Figure 5.7a). It is also possible to observe the reduction in overall infection risk with a much smaller number of predicted exposures. A reduction in uncertainty is also observed, with a reduced shaded region between the 5th and 95th percentiles. This suggests that the addition of mechanical ventilation does provide a more consistent airflow pattern compared with natural ventilation alone.

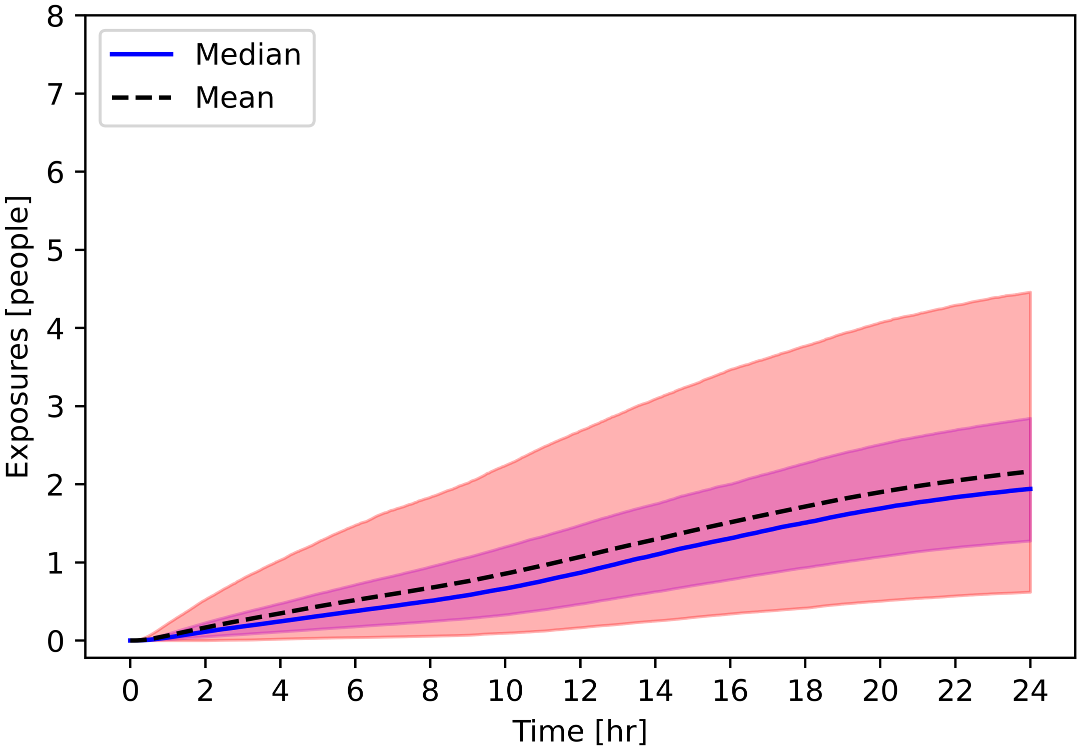

Figure 5.8: The predicted number of exposures over a 24 h period from the 10,000 Monte Carlo simulations shown as the mean, median, a red shaded region between the 5th and 95th percentiles, and a purple shaded region between the 25th and 75th percentiles for natural ventilation and 3 ACH mechanical ventilation.

When comparing the choice of ventilation day with the quanta emission rate (Figure 5.9), there is a similarity in the horizontal pattern as was seen when modelling natural ventilation alone (Figure 5.5), where particular days have a distinct effect on the predicted exposures regardless of the quanta emission rate, but it is much harder to identify with the overall reduction in infection risk. This shows that despite 3 ACH

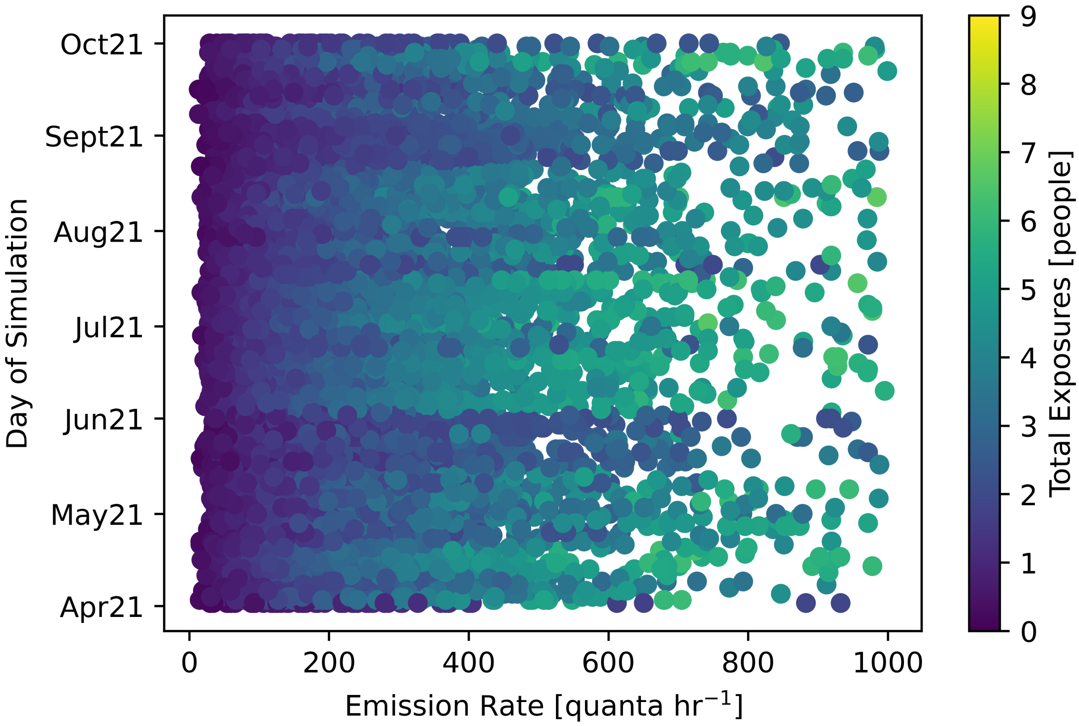

Figure 5.9: A scatter plot comparing the randomly chosen day (ventilation setting) and quanta emission rate for the 10,000 Monte Carlo simulations, coloured by the resulting total number of predicted exposures for natural ventilation and 3 ACH mechanical ventilation.

mechanical ventilation offering a more consistent airflow, it is still impacted by natural ventilation and weather conditions, and can lead to increased risk depending on the day of the outbreak.

If instead, the quanta emission rate and the predicted number of exposures are compared (Figure 5.10) as before, it is possible to observe the same cone-like pattern, with an increase in predicted exposures for increasing quanta emission rate. Focusing on the colour of these points, based on the day chosen for the ventilation setting, it is possible to observe particular days following more defined and distinctive trajectories, as before, with it being clearer for the mechanical ventilation case (Figure 5.10) than in the case with natural ventilation only (Figure 5.6). For example, the most dominant line acting as the lower bound to the cone-like structure is in a dark blue/purple colour, showing results from the same day, and it can be seen that although increased quanta emission rate does increase the overall predicted exposures, these points follow a distinctive curve. This suggests that regardless of the increase in quanta emission rate, due to the ventilation setting or airflow pattern on this particular day, the number of predicted exposures are capped and follow a predefined trajectory. Equally, it is possible to pick out similar trajectories at the upper bound of the cone-like shape. Additionally, it is worth highlighting that the cone-like shape with the addition of mechanical ventilation (Figure 5.10) is much more pronounced, giving further evidence of the decreased uncertainty and increased consistency in the airflow patterns.

5.4 Discussion

Through the results presented in this chapter, the use of Monte Carlo methods for assessing airborne transmission risk has been explored. Through a Monte Carlo approach, $N_{mc} = 10,000$ simulations were computed, and in each run a random quanta emission rate and outbreak day (weather and ventilation setting) were sampled from relevant distributions. Although the number of runs in a Monte Carlo simulation can be a limitation to a study such as this, the results in Figure 5.2 offer verification that the number of runs chosen for the simulation ($N_{mc} = 10,000$) provide solutions that are robust against the random sampling of selected input parameters.

To set up the Monte Carlo simulation, it was necessary to define a probability distribution for the quanta emission rate so that a sample could be taken and a value chosen at random in each simulation. The probability distribution chosen was taken from

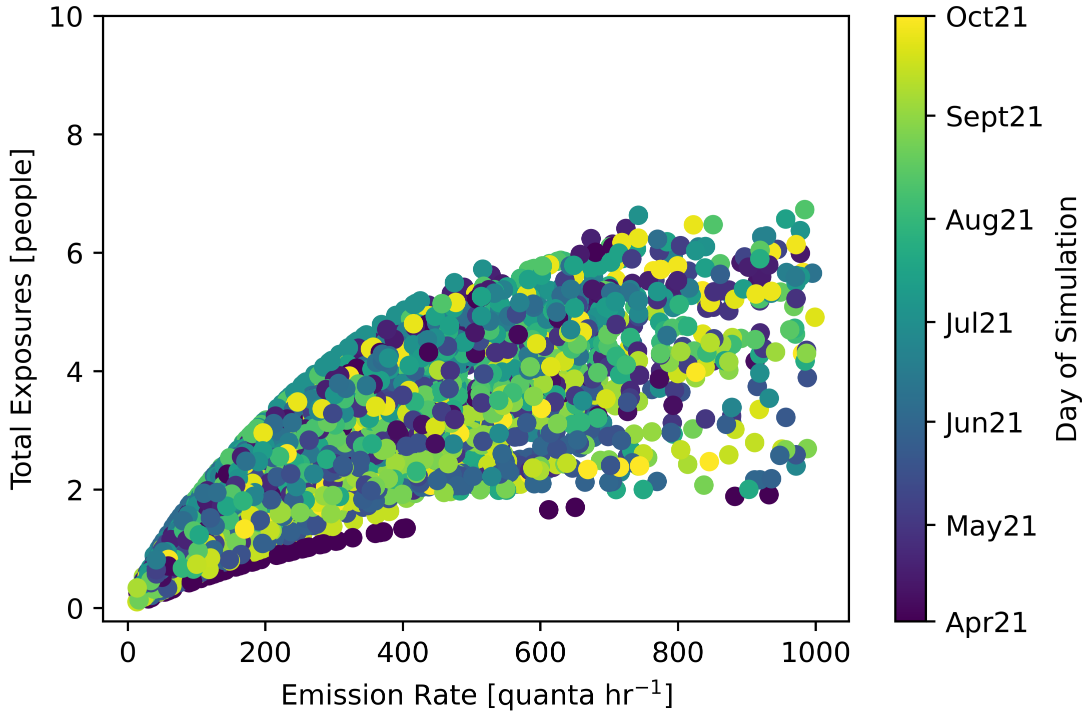

Figure 5.10: A scatter plot comparing the total number of predicted exposures and quanta emission rate for the 10, 000 Monte Carlo simulations, coloured by the randomly chosen day (ventilation setting) for natural ventilation and 3 ACH mechanical ventilation .

Chen et al. [2021]. When defining the methodology, a modelling choice was made to limit the quanta emission rate value to $\leq 1000\,\text{quanta}\,\text{h}^{-1}$. This was chosen as the cap based on a study by Miller et al. [2021], where the mean quanta emission rate of a highly infectious individual at a the Skagit Chorale superspreader event was given as $970\,\text{quanta}\,\text{h}^{-1}$. It is worth highlighting that both of these studies (Chen et al. [2021], Miller et al. [2021]) estimated the quanta emission rate based on large outbreak events (the Diamond Princess cruise ship (Chen et al. [2021]), and the Skagit Chorale (Miller et al. [2021])). Additionally, both of these outbreaks occurred in the early stages of the COVID-19 pandemic, and so it is likely that there was limited guidance in place, and that it was the first infection for many susceptible individuals, who had no immunity from prior infections or vaccinations. However, when used in this study, the aim is not to reproduce exact outbreaks, but to illustrate airborne transmission features and methods for quantifying infection risk.

When assessing infection risk, natural ventilation alone displays a RI value of 0.2781, with infection risk highly concentrated into two zones (Zone 10 and Zone 11). This is suggestive of a particular airflow path leading to increased contaminant transport in these zones. This is similar behaviour to what was observed in Chapter 4, Section 4.3.2.1, where Zone 10 was also the riskiest zone and was caused due to a dominant flow path from north-west to south-east of the geometry. Another similar behaviour to the previous chapter was the uncertainty present when relying solely on natural ventilation. This was seen in both the range of possible predicted exposures (1 to 8 in Figure 5.3a) and the large size of the shaded region in Figure 5.4. Both of these figures are consistent with the findings from Chapter 4, where weather conditions can affect the natural ventilation, leading to inconsistent airflow and thus, infection risk predictions.

When 3 ACH mechanical ventilation is added to the natural ventilation, over a 62% reduction in RI from the scenario with natural ventilation alone can be seen, once again demonstrating the benefits of mechanical ventilation. Interestingly, however, there is still increased variability in possible predicted exposures (range of 0 to 5 possible exposures in Figure 5.7a). This is different to what was observed in Chapter 4 (possible exposures ranging from 0 to 2 in Figure 4.7a), which showed that the uncertainty and variability in infection risk prediction reduced substantially when adding 3 ACH mechanical ventilation, providing a more consistent airflow path and more efficient removal mechanism. This suggests that although in Figure 5.7a, the reduction in risk is observed when adding mechanical ventilation, since a Monte Carlo approach is being used, stochastic effects and randomness are being included in the solution and hence, able to capture a greater range of possible outcomes. This shows the strength of Monte Carlo modelling approaches for QMRA, since the model here is able to capture the overall behaviour (i.e., reduction in risk due to better removal mechanisms) whilst still accounting for the randomness and variability that exists in real life, offering a more realistic modelling tool.

In the Monte Carlo simulation approach, the quanta emission rate and the day of the outbreak are both varied. When comparing these factors, there remained a strong relationship by where the larger the quanta production rate, the higher the number of predicted exposures. However, in Figures 5.5 and 5.9, in both cases it is possible to observe the effects of particular days where the infection risk is high across all quanta emission rates, and the converse also evident, although not as clear in Figure 5.9 as Figure 5.5. Although the final predicted exposures are not the same across these two cases, it is possible to see that this feature is mirrored across the two scenarios, with them both showing a similar horizontal pattern of days which have inherently lower risk, and days which have higher risk. These figures illustrate the importance of weather conditions and the resulting natural ventilation on the overall infection risk, and show that this is highly dependent on the day of which the outbreak occurs, regardless of the quanta emission rate, and as in this study, whether there is mechanical ventilation or not.

This same feature is present across Figures 5.6 and 5.10, where a cone-like pattern is seen when comparing the quanta emission rate with the number of predicted exposures, coloured by the day of the outbreak. This time, more visible in Figure 5.10 than Figure 5.6, but it can be seen that the cone shape is capped by curves formed by points of the same colour i.e., the same day used for the outbreak. This is clearer at the lower bound of the cone shape, but it suggests that an outbreak on a particular day already follows a defined trajectory regardless of the choice of quanta emission rate. It is likely that this is a direct consequence of the weather conditions, natural ventilation and consequent flow patterns on the ward on a given day, resulting in a particular pattern of removal and contaminant transport to particular zones where the predicted exposures happen. This is also influenced by the defined susceptible populations in each zone, which causes nuances in the possible combinations available for the number of predicted exposures. For example, if a given day predicts a higher risk in Zones 3 and 4 only, each with a single susceptible person, then the maximum number of exposures resulting from this is two (one from Zone 3 and one from Zone 4), which is why there are defined trajectories that appear to reach a steady-state maximum without exposing the total susceptible population across the whole ward.

This study has further demonstrated the importance of the interplay between quanta emission rate (i.e., the infectiousness of an individual) and the role of ventilation and airflow in airborne transmission, and the consequent quantification of the infection risk. Through the results in this chapter, it can be seen that even when a highly infectious individual is present, the number of exposures can be limited to a defined maximum as a direct result of the ventilation and airflow pattern, which determines the transport of the airborne pathogen concentration to particular zones and thus, where possible exposures can take place. The converse is also true, where an individual may have a low quanta emission rate, but predicted infection risk is high due to the ventilation and airflow on the day of the outbreak. This becomes much more complex in environments where individuals are not modelled as fixed and are allowed to move around the indoor environment, but it once again highlights the effects of ventilation, weather and resulting airflow on airborne transmission, and in particular the importance of having a reliable and consistent method of ventilation.

5.5 Conclusion

By constructing a Monte Carlo version of the modelling tools presented in Chapter 4, the extension presented here is able to include stochasticity and the randomness of real life by allowing for parameter variation, such as choosing a random quanta emission rate for the infector from a representative probability distribution, and choosing a random day for the outbreak, influencing the natural ventilation and weather conditions. By allowing for parameter variability in each simulation, it has been possible to assess the relative importance of these factors on infection risk, and see how these stochastic effects play a role in airborne transmission risk in reality.

Although this chapter has shown that when considering a full Monte Carlo simulation, predictions for a typical day show that poorer ventilation or higher emission rates lead to increased risk, it also highlighted that when focusing on shorter time scales or investigating individual days, the ventilation (i.e., weather conditions and resulting natural ventilation) plays an important role and can highly influence the outcome of an outbreak, regardless of the infectiousness of an individual. The model presented here highlights the difficulty of investigating airborne pathogen outbreaks and quantifying the nuanced features of outbreak parameters. However, by extending existing deterministic QMRA techniques to stochastic methods such as a Monte Carlo simulation, it is possible to investigate a wider range of realistic scenarios, developing a better understanding of the factors that affect airborne transmission and associated infection risk.

Chapter 6

Conclusions and Future Work

The importance of airborne transmission has been highlighted by the recent COVID-19 pandemic, and given its key role in the transmission of many other common respiratory pathogens, emphasis is made on the need for further development of the modelling tools and risk assessments associated with it. To be an effective modelling approach, it must be able to accurately represent indoor environments and successfully capture realistic outbreak characteristics such as multiple connected zones, occupant behaviour, and disease specific properties, with easy applicability to a wide range of scenarios; particularly important to environments such as hospitals and other healthcare settings given the prevalence of various infectious pathogens, the presence of vulnerable individuals and often limited resources.

This thesis uses an approach combining airflow analysis, mathematical techniques, building physics and numerical models to provide developments to existing modelling frameworks through the inclusion of transient effects, extensions to multi-zone environments, incorporating randomness and stochasticity, and couplings with airflow simulations. A variety of outbreak scenarios are used to illustrate their applicability, exploring various ventilation, occupancy and disease scenarios. In this chapter, the key findings of the thesis are highlighted, with the discussion of limitations, implications and any potential areas for consideration in the future.

6.1 Summary

As highlighted throughout this thesis, there are many different modelling approaches that can be used to assess airborne transmission risk. However, these are often constrained by limiting assumptions and an inability to capture the full complexity of real-life scenarios (e.g., the Wells-Riley model as highlighted in Chapter 1). In an attempt to overcome these limitations and bring the modelling tools closer to reality, Chapter 2 provided a stochastic adaptation of the Wells-Riley framework, allowing for the consideration of unknown or uncertain parameters in the model, as many QMRA approaches are often limited by the availability of outbreak data (Beaudequin et al. [2015]). Chapter 5 also considered stochastic effects through a Monte Carlo simulation, allowing for variable input parameters representing heterogeneity within the population (e.g., the infectiousness of an individual may vary (Lloyd-Smith et al. [2005])).

Chapter 2 highlighted the importance of considering transient effects by exploring infection risk in the period after an infectious person has left a room but the susceptible individual remains in situ. This period would be overlooked when using steady-state models, where infection risk is not considered when there is no infector present. However, research shows that the presence of an infector is not needed for transmission to take place (Jung et al. [2021], Eichler et al. [2021], SAGE [2021]). This also emphasises the importance of considering multi-zone environments, as an infector may move around the space, entering and leaving particular zones, or never enter a zone but contribute to the quanta concentration in that zone through shared airflow. In Chapter 3, a transient multi-zone transmission model was developed. This demonstrated the importance of considering transient effects instead of using steady-state models, and illustrated that shared airflow contributes to the quanta concentration and thus, infection risk in a multi-zone environment.

Despite this thesis considering airborne transmission within indoor environments, it is also important to consider the effects of external conditions. Chapter 1 illustrated the role that external weather conditions can play in airborne transmission and on the consequent airflow indoors, with this being particularly important in naturally ventilated spaces, although the majority of models overlook these factors. As such, Chapter 4 provided an extension to the transmission model developed in Chapter 3 to include results from a multi-zone airflow simulation that included transient weather conditions. This chapter demonstrated the effects of weather conditions on airflow in naturally ventilated spaces. Due to the variability in weather conditions, Chapter 5 sampled a random day for each Monte Carlo simulation, showing the airflow and resulting ventilation to be an outbreak-defining feature. Chapters 4 and 5 highlighted that airborne infection risk may be pre-determined by weather conditions in spaces that predominately rely on natural ventilation as their main source of airflow.

6.2 Key Findings

6.2.1 The Wells-Riley Model Revisited

1. The consideration of transient effects becomes more important over smaller time scales or with smaller removal rates.
2. The infection risk to a susceptible individual who remains in the room long after the infector has left is non-negligible. This demonstrates the importance of considering infection risk despite the absence of an infector (whether they have since left, or were never present to begin with but instead in a neighbouring zone)
3. The importance of considering social factors and social behaviour when assessing infection risk. Various social factors such as the setting type or the number of individuals present can affect the time individuals spend in a social setting, and can therefore influence the infection risk.
4. The inclusion of uncertainty, randomness and stochasticty into risk assessment tools can help to account for any unknown parameters or outbreak information.

6.2.2 A Transient Multi-zone Transmission Model

1. Steady-state models can overestimate the quanta concentration in the space, and thus, the infection risk and predicted number of exposures. A transient model is able to better capture the growth and decay of infectious quanta concentration, and therefore provide a more accurate risk assessment. This is particularly important over smaller time scales or smaller removal rates.
2. A steady-state model represents a “worst case scenario” and there may be some scenarios where using a steady-state model is sufficient, and possibly even favourable such as longer time periods or high levels of ventilation.

3. Increasing extract ventilation rates lead to a reduction in infectious quanta concentration and thus, a reduction in predicted exposures and infection risk in the indoor environment.

4. The use of a transient model allows for a better representation of an outbreak with the capability of capturing realistic transient features such as changes in occupancy, ventilation, and disease settings.

6.2.3 Transient Airflow, Weather and Airborne Transmission

1. When coupled with airflow results, the transmission model presented in Chapter 3 is able to capture spikes and peaks in predicted quanta concentration occurring due to the transient weather effects and natural ventilation used on the ward, showing the benefits of a successful coupling between an airflow simulation with a transmission risk model.

2. Natural ventilation can lead to uncertainty in the predicted quanta concentration across the ward due to the varying weather conditions, with unexpected contaminant transport to connected indoor spaces. This consequently can lead to increased infection risk, with particular weeks or zones experiencing a higher risk than others.

3. The implementation of mechanical ventilation can lead to a large reduction in the infection risk on the ward and provide a more reliable airflow, dominating the effects of the transient weather conditions. The addition of 3 ACH mechanical ventilation lead to over an 85% reduction in risk compared to the natural ventilation only case.

4. Predicted natural ventilation rates across the ward average 0.61 ACH, falling far below the recommended standard of 6 ACH. This illustrates the uncertainty and the caution needed when relying on natural ventilation as the main source of airflow. Even with higher ventilation rates being attainable by natural ventilation, it is possible that it is not as efficient at removing infectious concentration as the alternative of mechanical ventilation.

5. Despite the addition of mechanical ventilation at 3 ACH, the overall ward ventilation rate can still fall below the recommended rate of 6 ACH. However, a large risk reduction was observed, illustrating that “something is better than nothing”

and that even if the recommended ventilation rate can not be achieved, an effort should be made to implement whatever is possible.

6. The heat maps are a useful tool in identifying particular airflow patterns or locations of higher risk across the ward. This could be a particularly valuable resource to have on a hospital ward for HCWs, clinicians and estates teams to refer to when making decisions about patient location, mitigation strategies such as PPE, or rooms that could benefit from additional ventilation intervention.

6.2.4 A Monte Carlo Approach

1. Stochasticity and randomness were incorporated into the coupled airflow and transmission model (Chapters 3 and 4), extending this to be more representative and better account for the uncertainty of real life. This also demonstrates the versatility of the models presented in Chapter 4, with the capability of them being extended using stochastic methods.
2. The Monte Carlo simulation used a probability distribution for the quanta emission rate, and randomly chose a day from a 6-month period to represent the weather conditions and airflow for the outbreak. Random parameter choices allow for a wider range of modelling scenarios and for the importance of each random parameter in the outcome of an outbreak to be assessed.
3. The Monte Carlo model highlights the importance of ventilation effects and the ability of weather conditions and resulting natural ventilation to influence the outcome of an outbreak, regardless of the infectiousness of an individual.

6.3 Future Work

The work in this thesis has developed and illustrated the use of new modelling tools to better understand airborne transmission and associated risks through a combination of airflow simulations, mathematical techniques and numerical analysis. However, through this, existing gaps within the area have been identified and addressed for future consideration.

Validation: A consistent limitation across all of the work in this thesis is the complexity of characterising an outbreak to allow for modelling and quantification of the infection risk. In many cases, the origin of the outbreak is unknown and difficult to identify, including the original transmission route, and factors that vary with the heterogeneity of the population such as infectiousness, immune response, the incubation and latent period, symptoms, behaviour and movement, and even efficiency of implementing mitigation measures between individuals. The environment itself contributes to the complexity with large buildings, outdated plans for building design or the age of the building affecting its current state, varying weather conditions, and occupant behaviour altering internal factors (e.g., door and window opening). Each of these factors make validation extremely difficult.

Validation of the models that are presented in this thesis would not only add further emphasis to the results and findings, but also encourage the development of these models further knowing that they are as accurate and representative as possible. Whether this be through additional complexities, better quantifying factors that characterise an outbreak, or through output and extension of the models to a tool that can be used in practice on these hospital wards to influence real life decisions or future policy.

A proposed approach to directly extend the work in this thesis includes a combined numerical and experimental study. The study should look to utilise the modelling approaches presented in Chapter 4, which presents a coupled transmission model and airflow simulation of an adult respiratory ward. Measured CO_2 data across that same ward can be used to validate the airflow results from the CONTAM simulation, extending the initial comparison presented in Section 4.3.1. Additionally, outbreak data from the hospital ward that records symptom onset, predicts likely transmission routes (e.g., location, time and suspected infector), and includes contact tracing and testing would provide sufficient data to validate the transmission model including predicted infection risk (i.e., number of exposures), and consequently, the accuracy of the predicted quanta concentrations.

Short-range Exposure: The research in this thesis focuses on long-range transmission of the smaller infectious aerosols contributing to exposure and infection risk primarily through connected zones, suspension and transport in the ambient air or ventilation systems. However, airborne transmission or more generally disease transmission is possible, and sometimes favourable from a much closer distance with a higher infectious dose possible. It is important for future research to consider this route of transmission and its contribution to the overall predicted infection risk and number of exposures.

As such, this work would benefit from the inclusion of a broader, more realistic representation of the exhaled droplet distribution and the inclusion of parameters that better represent particle physics and dynamics e.g., more accurate quantification of particle deposition, inactivation and evaporation. This would help increase the accuracy in the predicted concentration of airborne pathogen, and also acknowledge the possibility of transmission via alternative routes (e.g., fomite transmission, close-range transmission) more explicitly.

Turbulent Mixing: Turbulent mixing was not included in the airflow simulations or transmission model presented in this thesis. However, it is possible that as a result, the inter-zonal flows to connected zones are slightly reduced and in reality, there would have been a greater amount of mixing and contaminant transport. Even though it is possible to assume that turbulent mixing plays a negligible role when focusing only on long-range transmission, it would be beneficial in future work to explore turbulent mixing using CFD, particularly around internal doors and between connected zones, windows, and occupant movement to better understand its contribution. Although turbulent mixing is not included in the CONTAM modelling tool, if required, this could be incorporated into the transmission model presented in Chapters 3 and 4 directly, further illustrating the benefit of the coupled approach.

Human Behaviour: Throughout this thesis, each chapter has highlighted the importance and value of considering additional complexities in modelling tools. For example, transient behaviours, multi-zone environments, and stochasticity in parameter choices. Despite these factors increasing the complexity of QMRA approaches and improving the accuracy of the overall risk assessment, all of these factors are highly dependent on human behaviour. Future work should build on the modelling tools presented by including human behaviour, such as modelling probabilities of a given occupant location, interaction between occupants, distance between occupants and time occupants are present in a given location. Modelling tools such as these would allow for the simulation of outbreaks across a broader range of healthcare settings (e.g., wards, waiting rooms, A&E departments) and bring QMRA techniques even closer to reality, increasing the chances of future validation.

Software Infrastructure: Through this work, various numerical tools and outputs were developed that could inform practice and help to influence policy in healthcare settings such as the UK respiratory ward explored in this thesis. However, due to the time constraints involved, it was not possible to develop the numerical tools to a better level of automation for the set-up of different scenarios. Future work should address this, helping to make the numerical models more versatile and applicable to a greater variety of scenarios. If this process could be automated in the future, it would allow healthcare settings to use the tool directly after inputting some specific set-up parameters (e.g., geometry, geographical location, occupancy information etc.), making the tool more intuitive and easily disseminated. This would then facilitate the implementation of this tool into healthcare settings, where it could be of direct benefit to others, offering live predictions of infection risk.

A Monte Carlo Approach: Following the findings presented in Chapter 5, where the choice of day, and consequent ventilation and indoor airflow, highly influenced the outcome of the outbreak, further analysis should be focused on investigations into the specific factors that contributed to these effects. For example, this should include understanding the role of specific weather conditions (e.g., wind speed, wind direction and temperature), and the consideration of a broader set of external conditions such as exploring seasonality (e.g., summer versus winter). Dependent on data availability, this could also include the seasonal effects of RH.

The occupancy in each zone should also be explored, as it is likely that depending on the airflow across the ward and thus, which zones experience increased levels of airborne pathogen concentration, the defined occupancy in those zones may provide a limit for the number of possible exposures.

The location of the infector will also contribute to the eventual levels of quanta concentration in particular zones and so varying infector location, either through multiple simulations that each model a fixed infector (i.e., stationary in one zone for the full duration) in different locations or a single simulation that models a transient infector (i.e., moving between zones with a pre-defined schedule or probability) should be considered in future work.

6.4 Practical Implications

Section 1.6 highlighted the inconsistencies of hospital guidance in terms of recommendations on how these spaces are ventilated (e.g., preference for natural ventilation) and what ventilation rates should be achieved (e.g., 6 ACH for patient wards), whilst also providing guidance that can inhibit these recommendations such as restricted window opening, privacy, and safety. When incorporating all these features into the modelling approaches, Chapter 4 highlighted that many wards within the NHS are subject to insufficient ventilation rates, with the possibility of some wards suffering from no ventilation at all.

Through continued engagement with both St James' Hospital (Section 1.6.1) and a senior consultant on the ward, it has been possible to undertake numerous visits to Ward J12, an adult respiratory ward, to engage with staff and patients, assess window and door conditions, measure geometries, and compare the blueprints to the current ward design. This has enabled the modelling tools to be shaped by first-hand experience, with a clear personal view on the value of the findings presented throughout this work. Observing daily ward activities has incited the desperate need for action that not only improves the air quality of these spaces, with mitigating airborne transmission in mind, but also in a way that does not contribute to the already elevated workload of staff.

Throughout this thesis, new modelling tools have been developed and existing approaches extended to consider features ubiquitous to these spaces, but through a way which is tractable to all manner of stakeholders in healthcare settings such as HCWs, clinicians or NHS estate managers. The collaboration between engineers and mathematicians with healthcare personnel is crucial to ensuring that future developments in modelling tools are purpose built with application in mind so that they can be seamlessly implemented into daily activities without additional burden to front-line staff, and can start to play a role in reducing airborne transmission risk and improving air quality in UK hospital wards.

6.5 Final Remarks

In conclusion, this thesis has developed new methodology for assessing the factors that affect airborne transmission and associated infection risk. Healthcare settings such as those discussed in this work are in need of models that are practical, usable, and accurate to help provide comprehensible risk assessments and inform mitigation choices. Through the consideration of transient effects, multi-zone environments, stochasticity, and randomness, the work in this thesis presents modelling tools that can be used to assess a wide range of realistic scenarios. Explorations using these models gives emphasis to the importance of carefully considering building design, retrofits, guidance, and policy to provide resilient indoor environments of the future, increasing preparedness of emerging infectious diseases and limiting health impacts to building occupants.

References

O. O. Adenaiye, J. Lai, P. J. Bueno de Mesquita, F. Hong, S. Youssefi, J. German, S. S. Tai, B. Albert, M. Schanz, S. Weston, et al. Infectious severe acute respiratory syndrome coronavirus 2 (SARS-CoV-2) in exhaled aerosols and efficacy of masks during early mild infection. *Clinical Infectious Diseases*, 75(1):e241–e248, 2022.

F. Adzic, B. M. Roberts, E. A. Hathway, R. K. Matharu, L. Ciric, O. Wild, M. Cook, and L. Malki-Epshtein. A post-occupancy study of ventilation effectiveness from high-resolution CO2 monitoring at live theatre events to mitigate airborne transmission of SARS-CoV-2. *Building and Environment*, 223:109392, 2022.

L. J. Allen. *An introduction to stochastic processes with applications to biology*. CRC press, 2010.

J. Arino, C. Sun, and W. Yang. Revisiting a two-patch SIS model with infection during transport. *Mathematical medicine and biology: a journal of the IMA*, 33(1):29–55, 2016.

A. M. Bate, D. Miller, M.-F. King, K.-A. Moseley, J. Xu, I. Hall, M. López-García, S. T. Parker, and C. J. Noakes. A quantitative microbial risk assessment approach to estimate exposure to SARS-CoV-2 on a bus. *Journal of Transport & Health*, 38:101829, 2024.

D. Beaudequin, F. Harden, A. Roiko, H. Stratton, C. Lemckert, and K. Mengersen. Beyond QMRA: Modelling microbial health risk as a complex system using Bayesian networks. *Environment international*, 80:8–18, 2015.

C. B. Beggs, K. G. Kerr, C. J. Noakes, E. A. Hathway, and P. A. Sleigh. The ventilation of multiple-bed hospital wards: Review and analysis. *American journal of infection control*, 36(4):250–259, 2008.

C. B. Beggs, S. J. Shepherd, and K. G. Kerr. Potential for airborne transmission of infection in the waiting areas of healthcare premises: Stochastic analysis using a Monte Carlo model. *BMC infectious diseases*, 10(1):1–8, 2010.

R. Bell and P. L. Pliner. Time to eat: The relationship between the number of people eating and meal duration in three lunch settings. *Appetite*, 41(2):215–218, 2003.

E. Best, J. Sandoe, and M. Wilcox. Potential for aerosolization of Clostridium difficile after flushing toilets: The role of toilet lids in reducing environmental contamination risk. *Journal of Hospital Infection*, 80(1):1–5, 2012.

E. L. Best, W. N. Fawley, P. Parnell, and M. H. Wilcox. The potential for airborne dispersal of Clostridium difficile from symptomatic patients. *Clinical Infectious Diseases*, 50(11):1450–1457, 2010.

A. B. Bloch, W. A. Orenstein, W. M. Ewing, W. H. Spain, G. F. Mallison, K. L. Herrmann, and A. R. Hinman. Measles outbreak in a pediatric practice: Airborne transmission in an office setting. *Pediatrics*, 75(4):676–683, 1985.

P. L. Bonate. A brief introduction to Monte Carlo simulation. *Clinical pharmacokinetics*, 40:15–22, 2001.

W. Boonmeemapasuk and N. Pochai. A risk model of airborne transmission and vaccine efficacy in an outpatient room with a ventilation system. *Engineering Letters*, 30(2), 2022.

L. Bourouiba. Turbulent Gas Clouds and Respiratory Pathogen Emissions: Potential Implications for Reducing Transmission of COVID-19. *JAMA*, 323(18):1837–1838, 05 2020. ISSN 0098-7484.

L. Bourouiba. The fluid dynamics of disease transmission. *Annual Review of Fluid Mechanics*, 53:473–508, 2021.

T. Britton, F. Ball, and P. Trapman. A mathematical model reveals the influence of population heterogeneity on herd immunity to SARS-CoV-2. *science*, 369(6505): 846–849, 2020.

P. J. Bueno de Mesquita, C. J. Noakes, and D. K. Milton. Quantitative aerobiologic analysis of an influenza human challenge-transmission trial. *Indoor Air*, 30(6): 1189–1198, 2020.

P. J. Bueno de Mesquita, W. W. Delp, W. R. Chan, W. P. Bahnfleth, and B. C. Singer. Control of airborne infectious disease in buildings: Evidence and research priorities. *Indoor Air*, 32(1):e12965, 2022.

G. Buonanno, L. Morawska, and L. Stabile. Quantitative assessment of the risk of airborne transmission of SARS-CoV-2 infection: Prospective and retrospective applications. *Environment international*, 145:106112, 2020a.

G. Buonanno, L. Stabile, and L. Morawska. Estimation of airborne viral emission: Quanta emission rate of SARS-CoV-2 for infection risk assessment. *Environment international*, 141:105794, 2020b.

H. C. Burridge, S. Fan, R. L. Jones, C. J. Noakes, and P. Linden. Predictive and retrospective modelling of airborne infection risk using monitored carbon dioxide. *Indoor and Built Environment*, 31(5):1363–1380, 2022.

H. C. Burridge, S. Bontitsopoulos, C. Brown, H. Carter, K. Roberts, C. Vouriot, D. Weston, M. Mon-Williams, N. Williams, and C. Noakes. Variations in classroom ventilation during the COVID-19 pandemic: Insights from monitoring 36 naturally ventilated classrooms in the UK during 2021. *Journal of Building Engineering*, 63: 105459, 2023.

A. Cammarata and G. Cammarata. Dynamic assessment of the risk of airborne viral infection. *Indoor air*, 31(6):1759–1775, 2021.

L. Chen, G. Ban, E. Long, G. Kalonji, Z. Cheng, L. Zhang, and S. Guo. Estimation of the SARS-CoV-2 transmission probability in confined traffic space and evaluation of the mitigation strategies. *Environmental Science and Pollution Research*, 28:42204–42216, 2021.

S.-C. Chen and C.-M. Liao. Modelling control measures to reduce the impact of pandemic influenza among schoolchildren. *Epidemiology & Infection*, 136(8): 1035–1045, 2008.

S.-C. Chen, C.-M. Liao, S.-S. Li, and S.-H. You. A probabilistic transmission model to assess infection risk from Mycobacterium tuberculosis in commercial passenger trains. *Risk Analysis: An International Journal*, 31(6):930–939, 2011.

C. H. Cheong and S. Lee. Case Study of Airborne Pathogen Dispersion Patterns in Emergency Departments with Different Ventilation and Partition Conditions. *International journal of environmental research and public health*, 15(3):510, 2018.

C. H. Cheong, B. Park, and S. Lee. Design method to prevent airborne infection in an emergency department. *Journal of Asian Architecture and Building Engineering*, 17(3): 581–588, 2018.

W.-H. Ching, M. Leung, D. Leung, Y. Li, and P. Yuen. Reducing risk of airborne transmitted infection in hospitals by use of hospital curtains. *Indoor and Built Environment*, 17(3):252–259, 2008.

Climate.OneBuilding. Climate Data. `https://climate.onebuilding.org/WMO_Region_6_Europe/GBR_United_Kingdom/index.html`, 2022. Accessed: 01/09/2022.

S. Coldrick, A. Kelsey, M. J. Ivings, T. G. Foat, S. T. Parker, C. J. Noakes, A. Bennett, H. Rickard, and G. Moore. Modeling and experimental study of dispersion and deposition of respiratory emissions with implications for disease transmission. *Indoor air*, 32(2):e13000, 2022.

K. K. Coleman, D. J. W. Tay, K. S. Tan, S. W. X. Ong, T. S. Than, M. H. Koh, Y. Q. Chin, H. Nasir, T. M. Mak, J. J. H. Chu, et al. Viral load of severe acute respiratory syndrome coronavirus 2 (SARS-CoV-2) in respiratory aerosols emitted by patients with coronavirus disease 2019 (COVID-19) while breathing, talking, and singing. *Clinical Infectious Diseases*, 74(10):1722–1728, 2022.

H. Dai and B. Zhao. Association of the infection probability of COVID-19 with ventilation rates in confined spaces. In *Building Simulation*, volume 13, pages 1321–1327. Springer, 2020.

S. K. Das, J.-e. Alam, S. Plumari, and V. Greco. Airborne virus transmission under different weather conditions. *AIP advances*, 12(1):015019, 2022.

T. Dbouk and D. Drikakis. Weather impact on airborne coronavirus survival. *Physics of Fluids*, 32(9):093312, 2020.

T. Dbouk and D. Drikakis. Fluid dynamics and epidemiology: Seasonality and transmission dynamics. *Physics of Fluids*, 33(2):021901, 2021.

T. Dbouk and D. Drikakis. The computational fluid dynamics-based epidemic model and the pandemic scenarios. *Physics of Fluids*, 34(2):027104, 2022a.

T. Dbouk and D. Drikakis. Natural ventilation and aerosol particles dispersion indoors. *Energies*, 15(14):5101, 2022b.

H. De Man, H. Van Den Berg, E. Leenen, J. Schijven, F. Schets, J. Van Der Vliet, F. Van Knapen, and A. de Roda Husman. Quantitative assessment of infection risk from exposure to waterborne pathogens in urban floodwater. *Water research*, 48: 90–99, 2014.

S. Ding, J. S. Lee, M. A. Mohamed, and B. F. Ng. Infection risk of SARS-CoV-2 in a dining setting: Deposited droplets and aerosols. *Building and environment*, 213: 108888, 2022.

W. Dols and B. Polidoro. Contam user guide and program documentation version 3.2. 2015-09-04 2015. doi: https://doi.org/10.6028/NIST.TN.1887.

A. Dowd. Hospital bed occupancy rates in england reach dangerously high levels. *BMJ*, 374, 2021. doi: 10.1136/bmj.n2079. URL `https://www.bmj.com/content/374/bmj.n2079`.

N. Eichler, C. Thornley, T. Swadi, T. Devine, C. McElnay, J. Sherwood, C. Brunton, F. Williamson, J. Freeman, S. Berger, et al. Transmission of severe acute respiratory syndrome coronavirus 2 during border quarantine and air travel, New Zealand (Aotearoa). *Emerging infectious diseases*, 27(5):1274, 2021.

S. Emmerich, C. Howard-Reed, and S. Nabinger. Validation of multizone IAQ model predictions for tracer gas in a townhouse. *Building Services Engineering Research and Technology*, 25(4):305–316, 2004.

S. J. Emmerich. Validation of multizone IAQ modeling of residential-scale buildings: A review. *Transactions-American Society of Heating Refrigerating and Air Conditioning Engineers*, 107(2):619–628, 2001.

S. J. Emmerich and W. S. Dols. Model validation study of carbon monoxide transport due to portable electric generator operation in an attached garage. *Journal of building performance simulation*, 9(4):397–410, 2016.

S. J. Emmerich, D. Heinzerling, J.-i. Choi, and A. K. Persily. Multizone modeling of strategies to reduce the spread of airborne infectious agents in healthcare facilities. *Building and Environment*, 60:105–115, 2013.

A. R. Escombe, C. C. Oeser, R. H. Gilman, M. Navincopa, E. Ticona, W. Pan, C. Martínez, J. Chacaltana, R. Rodríguez, D. A. J. Moore, et al. Natural ventilation for the prevention of airborne contagion. *PLoS medicine*, 4(2):e68, 2007.

J. O. Falkinham III. Mycobacterial aerosols and respiratory disease. *Emerging infectious diseases*, 9(7):763, 2003.

F. Fantozzi, G. Lamberti, F. Leccese, and G. Salvadori. Monitoring CO2 concentration to control the infection probability due to airborne transmission in naturally ventilated university classrooms. *Architectural Science Review*, pages 1–13, 2022.

C. A. Faulkner, J. E. Castellini Jr, W. Zuo, D. M. Lorenzetti, and M. D. Sohn. Investigation of HVAC operation strategies for office buildings during COVID-19 pandemic. *Building and Environment*, 207:108519, 2022.

K. P. Fennelly. Particle sizes of infectious aerosols: Implications for infection control. *The Lancet Respiratory Medicine*, 8(9):914–924, 2020. ISSN 2213-2600.

K. P. Fennelly and E. A. Nardell. The relative efficacy of respirators and room ventilation in preventing occupational tuberculosis. *Infection Control & Hospital Epidemiology*, 19(10):754–759, 1998.

W. J. Fisk, O. Seppanen, D. Faulkner, and J. Huang. Economic benefits of an economizer system: Energy savings and reduced sick leave. 2004.

T. G. Foat, B. Higgins, C. Abbs, T. Maishman, S. Coldrick, A. Kelsey, M. J. Ivings, S. T. Parker, and C. J. Noakes. Modeling the effect of temperature and relative humidity on exposure to SARS-CoV-2 in a mechanically ventilated room. *Indoor Air*, 32(11): e13146, 2022.

F. Franchimon, C. E. Pernot, E. Khoury, and J. Bronswijk. The feasibility of indoor humidity control against avian influenza. In *Proceedings of the 11th International Conference on Indoor Air Quality and Climate, Indoor Air*, 2008.

L. Gammaitoni and M. C. Nucci. Using a mathematical model to evaluate the efficacy of TB control measures. *Emerging infectious diseases*, 3(3):335, 1997.

N. Gao, J. Niu, M. Perino, and P. Heiselberg. The airborne transmission of infection between flats in high-rise residential buildings: Tracer gas simulation. *Building and Environment*, 43(11):1805–1817, 2008.

J. García-Tobar. A comparative study of indoor radon levels between two similar dwellings using CONTAM Software. *Environments*, 5(5):59, 2018.

J. García-Tobar. Weather-dependent modelling of the indoor radon concentration in two dwellings using CONTAM. *Indoor and Built Environment*, 28(10):1341–1349, 2019.

C. Gilkeson, M. Camargo-Valero, L. Pickin, and C. Noakes. Measurement of ventilation and airborne infection risk in large naturally ventilated hospital wards. *Building and environment*, 65:35–48, 2013.

D. T. Gillespie. A general method for numerically simulating the stochastic time evolution of coupled chemical reactions. *Journal of computational physics*, 22(4): 403–434, 1976.

J. F. Guest, T. Keating, D. Gould, and N. Wigglesworth. Modelling the annual NHS costs and outcomes attributable to healthcare-associated infections in England. *BMJ open*, 10(1):e033367, 2020.

W. Guo, Y. Fu, R. Jia, Z. Guo, C. Su, J. Li, X. Zhao, Y. Jin, P. Li, J. Fan, et al. Visualization of the infection risk assessment of SARS-CoV-2 through aerosol and surface transmission in a negative-pressure ward. *Environment international*, 162:107153, 2022.

Y. Guo, H. Qian, Z. Sun, J. Cao, F. Liu, X. Luo, R. Ling, L. B. Weschler, J. Mo, and Y. Zhang. Assessing and controlling infection risk with Wells-Riley model and spatial flow impact factor (SFIF). *Sustainable Cities and Society*, 67:102719, 2021.

J. K. Gupta, C.-H. Lin, and Q. Chen. Risk assessment of airborne infectious diseases in aircraft cabins. *Indoor air*, 22(5):388–395, 2012.

G. Guyot, S. Sayah, S. Guernouti, and A. Mélois. Role of ventilation on the transmission of viruses in buildings, from a single zone to a multizone approach. *Indoor air*, 32(8):e13097, 2022.

C. N. Haas. Quantitative microbial risk assessment and molecular biology: Paths to integration. *Environmental Science & Technology*, 54(14):8539–8546, 2020.

C. N. Haas, J. B. Rose, and C. P. Gerba. *Quantitative microbial risk assessment*. John Wiley & Sons, 1999.

T. M. Habeebullah, I. H. Abd El-Rahim, and E. A. Morsy. Impact of outdoor and indoor meteorological conditions on the COVID-19 transmission in the western region of Saudi Arabia. *Journal of environmental management*, 288:112392, 2021.

A. Haddrell, M. Otero-Fernandez, H. Oswin, T. Cogan, J. Bazire, J. Tian, R. Alexander, J. F. Mann, D. Hill, A. Finn, et al. Differences in airborne stability of SARS-CoV-2 variants of concern is impacted by alkalinity of surrogates of respiratory aerosol. *Journal of the Royal Society Interface*, 20(203):20230062, 2023.

A. Haddrell, H. Oswin, M. Otero-Fernandez, J. F. Robinson, T. Cogan, R. Alexander, J. F. Mann, D. Hill, A. Finn, A. D. Davidson, et al. Ambient carbon dioxide concentration correlates with SARS-CoV-2 aerostability and infection risk. *Nature Communications*, 15(1):3487, 2024.

F. Haghighat and A. C. Megri. A Comprehensive Validation of Two Airflow Models — COMIS and CONTAM. *Indoor Air*, 6(4):278–288, 1996.

F. Hamilton, D. Arnold, B. R. Bzdek, J. Dodd, C. White, J. Murray, J. Keller, J. Brown, A. Shrimpton, A. Pickering, et al. Aerosol generating procedures: Are they of relevance for transmission of SARS-CoV-2? *The Lancet Respiratory Medicine*, 2021.

K. A. Hamilton, J. Ciol Harrison, J. Mitchell, M. Weir, M. Verhougstraete, C. N. Haas, A. P. Nejadhashemi, J. Libarkin, T. Gim Aw, K. Bibby, et al. Research gaps and priorities for quantitative microbial risk assessment (QMRA). *Risk analysis*, 2024.

E. Hathway, C. Noakes, L. Fletcher, P. Sleigh, I. Clifton, and M. Elliott. The role of nursing activities on the bioaerosol production in hospital wards. *Indoor and Built Environment*, 22(2):410–421, 2013.

Health and Safety Executive (HSE). Ventilation in the workplace. `https://www.hse.gov.uk/ventilation/overview.htm`, 2023. Accessed: 10/05/2023.

W. Hiwar, H. Kharrufa, M. King, N. Salman, L. Fletcher, and C. Noakes. Multiplate air passive sampler to measure deposition rate of airborne microorganisms over time. In *Proceedings of the 16th Conference of the International Society of Indoor Air Quality and Climate: Creative and Smart Solutions for Better Built Environments, Indoor Air 2020*, volume 1, pages 708–713. International Society of Indoor Air Quality and Climate (ISIAQ), 2021a.

W. Hiwar, M.-F. King, F. Shuweihdi, L. A. Fletcher, S. J. Dancer, and C. J. Noakes. What is the relationship between indoor air quality parameters and airborne microorganisms in hospital environments? A systematic review and meta-analysis. *Indoor Air*, 31(5):1308–1322, 2021b.

A. T. Hodgson, S. J. Nabinger, and A. K. Persily. Volatile organic compound concentrations and emission rates measured over one year in a new manufactured house. 2004.

C. M. Issarow, N. Mulder, and R. Wood. Modelling the risk of airborne infectious disease using exhaled air. *Journal of theoretical biology*, 372:100–106, 2015.

M. Jayaweera, H. Perera, B. Gunawardana, and J. Manatunge. Transmission of COVID-19 virus by droplets and aerosols: A critical review on the unresolved dichotomy. *Environmental research*, 188:109819, 2020.

D. Juher, J. Ripoll, and J. Saldaña. Analysis and Monte Carlo simulations of a model for the spread of infectious diseases in heterogeneous metapopulations. *Physical Review E*, 80(4):041920, 2009.

J. Jung, J. Lee, S. Jo, S. Bae, J. Y. Kim, H. H. Cha, J. Y. Lim, S. H. Kwak, M. J. Hong, et al. Nosocomial Outbreak of COVID-19 in a Hematologic Ward. *Infection & Cheomotherapy*, 53(2):332–341, 2021.

W. O. Kermack and A. G. McKendrick. A contribution to the mathematical theory of epidemics. *Proceedings of the royal society of london. Series A, Containing papers of a mathematical and physical character*, 115(772):700–721, 1927.

M. Kidd, A. Richter, A. Best, N. Cumley, J. Mirza, B. Percival, M. Mayhew, O. Megram, F. Ashford, T. White, et al. S-variant SARS-CoV-2 lineage B1. 1.7 is associated with significantly higher viral load in samples tested by TaqPath polymerase chain reaction. *The Journal of infectious diseases*, 223(10):1666–1670, 2021.

K. G. King, G. L. Delclos, E. L. Brown, S. T. Emery, J. M. Yamal, and R. J. Emery. An assessment of outpatient clinic room ventilation systems and possible relationship to disease transmission. *American Journal of Infection Control*, 49(6):808–812, 2021a.

M.-F. King, C. Noakes, P. Sleigh, and M. Camargo-Valero. Bioaerosol deposition in single and two-bed hospital rooms: A numerical and experimental study. *Building and Environment*, 59:436–447, 2013.

M.-F. King, C. J. Noakes, and P. A. Sleigh. Modeling environmental contamination in hospital single-and four-bed rooms. *Indoor Air*, 25(6):694–707, 2015.

M. F. King, A. M. Wilson, M. López-García, J. Proctor, D. G. Peckham, I. J. Clifton, S. J. Dancer, and C. J. Noakes. Why is mock care not a good proxy for predicting hand contamination during patient care? *Journal of Hospital Infection*, 109:44–51, 2021b. ISSN 15322939.

M. Kitajima, W. Ahmed, K. Bibby, A. Carducci, C. P. Gerba, K. A. Hamilton, E. Haramoto, and J. B. Rose. SARS-CoV-2 in wastewater: State of the knowledge and research needs. *Science of The Total Environment*, 739:139076, 2020.

L. D. Knibbs, L. Morawska, S. C. Bell, and P. Grzybowski. Room ventilation and the risk of airborne infection transmission in 3 health care settings within a large teaching hospital. *American journal of infection control*, 39(10):866–872, 2011.

L. D. Knibbs, L. Morawska, and S. C. Bell. The risk of airborne influenza transmission in passenger cars. *Epidemiology & Infection*, 140(3):474–478, 2012.

G. Ko, H. A. Burge, E. A. Nardell, and K. M. Thompson. Estimation of tuberculosis risk and incidence under upper room ultraviolet germicidal irradiation in a waiting room in a hypothetical scenario. *Risk Analysis*, 21(4):657–674, 2001.

G. Ko, K. M. Thompson, and E. A. Nardell. Estimation of tuberculosis risk on a commercial airliner. *Risk Analysis: An International Journal*, 24(2):379–388, 2004.

A. Kozajda, K. Jeżak, and A. Kapsa. Airborne Staphylococcus aureus in different environments—a review. *Environmental Science and Pollution Research*, 26: 34741–34753, 2019.

J. Lai, K. K. Coleman, S.-H. S. Tai, J. German, F. Hong, B. Albert, Y. Esparza, D. Rastogi, A. Srikakulapu, P. Kalliomäki, et al. Relative efficacy of masks and respirators as source control for viral aerosol shedding from people infected with SARS-CoV-2: A controlled human exhaled breath aerosol experimental study. *EBioMedicine*, 2024.

A. Laitinen, M. Korhonen, K. Keskinen, O. Kaario, and V. Vuorinen. Large-eddy simulation of buoyant airflow in an airborne pathogen transmission scenario. *Building and Environment*, 241:110462, 2023.

Z. Lau, I. M. Griffiths, A. English, and K. Kaouri. Predicting the spatio-temporal infection risk in indoor spaces using an efficient airborne transmission model. *Proceedings of the Royal Society A*, 478(2259):20210383, 2022.

V. Leprince and F. R. Carrie. Comparative analysis of window airing models proposed in prEN 16798-7 and influence of internal resistances. In *Proceedings of the CLIMA*, 2016.

H. Li, S. N. Shankar, C. T. Witanachchi, J. A. Lednicky, J. C. Loeb, M. M. Alam, Z. H. Fan, K. Mohamed, A. Eiguren-Fernandez, and C.-Y. Wu. Environmental surveillance and transmission risk assessments for SARS-CoV-2 in a fitness center. *Aerosol and air quality research*, 21(11), 2021a.

J. Li, Z. Cheng, Y. Zhang, N. Mao, S. Guo, Q. Wang, L. Zhao, and E. Long. Evaluation of infection risk for SARS-CoV-2 transmission on university campuses. *Science and Technology for the Built Environment*, 27(9):1165–1180, 2021b.

T. Li, Z. Yang, B. Di, and M. Wang. Hand-foot-and-mouth disease and weather factors in Guangzhou, southern China. *Epidemiology & Infection*, 142(8):1741–1750, 2014.

Y. Li. Basic routes of transmission of respiratory pathogens — A new proposal for transmission categorization based on respiratory spray, inhalation, and touch. *Indoor Air*, 31(1):3, 2021.

Y. Li, G. M. Leung, J. Tang, X. Yang, C. Chao, J. Z. Lin, J. Lu, P. V. Nielsen, J. Niu, H. Qian, et al. Role of ventilation in airborne transmission of infectious agents in the built environment - A multidisciplinary systematic review. *Indoor air*, 17(1):2–18, 2007.

Y. Li, H. Qian, J. Hang, X. Chen, P. Cheng, H. Ling, S. Wang, P. Liang, J. Li, S. Xiao, et al. Probable airborne transmission of SARS-CoV-2 in a poorly ventilated restaurant. *Building and environment*, 196:107788, 2021c.

C.-M. Liao, C.-F. Chang, and H.-M. Liang. A probabilistic transmission dynamic model to assess indoor airborne infection risks. *Risk Analysis: An International Journal*, 25(5):1097–1107, 2005.

P. F. Linden. The fluid mechanics of natural ventilation. *Annual review of fluid mechanics*, 31(1):201–238, 1999.

J. O. Lloyd-Smith, S. J. Schreiber, P. E. Kopp, and W. M. Getz. Superspreading and the effect of individual variation on disease emergence. *Nature*, 438(7066):355–359, 2005.

K. J. Lomas, R. Giridharan, C. A. Short, and A. Fair. Resilience of 'Nightingale' hospital wards in a changing climate. *Building Services Engineering Research and Technology*, 33(1):81–103, 2012.

M. López-García, M. F. King, and C. J. Noakes. A Multicompartment SIS Stochastic Model with Zonal Ventilation for the Spread of Nosocomial Infections: Detection, Outbreak Management, and Infection Control. *Risk Analysis*, 39(8):1825–1842, 2019.

J. Ma, X. Qi, H. Chen, X. Li, Z. Zhang, H. Wang, L. Sun, L. Zhang, J. Guo, L. Morawska, et al. Coronavirus disease 2019 patients in earlier stages exhaled millions of severe acute respiratory syndrome coronavirus 2 per hour. *Clinical Infectious Diseases*, 72 (10):e652–e654, 2021.

J. Mao and N. Gao. The airborne transmission of infection between flats in high-rise residential buildings: A review. *Building and Environment*, 94:516–531, 2015.

J. Mao, W. Yang, and N. Gao. The transport of gaseous pollutants due to stack and wind effect in high-rise residential buildings. *Building and Environment*, 94:543–557, 2015.

X. Mei and G. Gong. Predicting airborne particle deposition by a modified Markov chain model for fast estimation of potential contaminant spread. *Atmospheric environment*, 185:137–146, 2018.

V. Melkumov, G. Kuznetsova, A. Panin, and M. Y. Panov. Using air exchange to reduce the probability of spreading coronavirus infection. *Russian Journal of Building Construction and Architecture*, (4):14–20, 2020.

A. Mikszewski, L. Stabile, G. Buonanno, and L. Morawska. The airborne contagiousness of respiratory viruses: A comparative analysis and implications for mitigation. *Geoscience Frontiers*, page 101285, 2021.

D. Miller, M.-F. King, J. Nally, J. R. Drodge, G. I. Reeves, A. M. Bate, H. Cooper, U. Dalrymple, I. Hall, M. López-García, S. T. Parker, and C. J. Noakes. Modeling the factors that influence exposure to SARS-CoV-2 on a subway train carriage. *Indoor Air*, 32(2):e12976, 2022.

S. L. Miller, W. W. Nazaroff, J. L. Jimenez, A. Boerstra, G. Buonanno, S. J. Dancer, J. Kurnitski, L. C. Marr, L. Morawska, and C. Noakes. Transmission of SARS-CoV-2 by inhalation of respiratory aerosol in the Skagit Valley Chorale superspreading event. *Indoor air*, 31(2):314–323, 2021.

D. K. Milton, M. P. Fabian, B. J. Cowling, M. L. Grantham, and J. J. McDevitt. Influenza virus aerosols in human exhaled breath: Particle size, culturability, and effect of surgical masks. *PLoS pathogens*, 9(3):e1003205, 2013.

N. Mingotti, D. Grogono, G. Dello Ioio, M. Curran, K. Barbour, M. Taveira, J. Rudman, C. S. Haworth, R. A. Floto, and A. W. Woods. The impact of hospital-ward ventilation on airborne-pathogen exposure. *American Journal of Respiratory and Critical Care Medicine*, 203(6):766–769, 2021.

L. Morawska, G. Johnson, Z. Ristovski, M. Hargreaves, K. Mengersen, S. Corbett, C. Y. H. Chao, Y. Li, and D. Katoshevski. Size distribution and sites of origin of droplets expelled from the human respiratory tract during expiratory activities. *Journal of aerosol science*, 40(3):256–269, 2009.

T. A. Myatt, M. H. Kaufman, J. G. Allen, D. L. MacIntosh, M. P. Fabian, and J. J. McDevitt. Modeling the airborne survival of influenza virus in a residential setting: The impacts of home humidification. *Environmental Health*, 9(1):1–7, 2010.

National Institute of Standards and Technology. NIST CONTAM. `https://www.nist.gov/services-resources/software/contam`, 2022. Accessed: 17/05/2022.

W. W. Nazaroff, M. Nicas, and S. L. Miller. Framework for evaluating measures to control nosocomial tuberculosis transmission. *Indoor Air*, 8(4):205–218, 1998.

NHS. Examples of Aerosol Generating Procedures - University Hospitals Birmingham NHS Foundation Trust. `https://www.uhb.nhs.uk/coronavirus-staff/aerosol-generating-procedures.htm`, 2021. Accessed: 21-01-2022.

NHS. NHS England Respiratory Disease. `https://www.england.nhs.uk/ourwork/clinical-policy/respiratory-disease/`, 2022. Accessed: 07/09/2021.

NHS England. *Health building note 04-01 (HBN04-01): Adult in-patient facilities*. 2009.

NHS England. *Health building note 00-10 PartD (HBN00-10): Design for flooring, walls, ceilings, sanitary ware and windows: Part D: Windows and associated hardware*. 2013.

NHS England. *HTM03-01 Specialised ventilation for healthcare buildings*. 2021.

NHS England. NHS Net Zero Building Standard. `https://www.england.nhs.uk/publication/nhs-net-zero-building-standard/`, 2023. Accessed: 28/07/2023.

M. Nicas. An analytical framework for relating dose, risk, and incidence: An application to occupational tuberculosis infection. *Risk Analysis*, 16(4):527–538, 1996.

P. V. Nielsen. Fifty years of CFD for room air distribution. *Building and Environment*, 91:78–90, 2015.

NIST. Results Export Tool. `https://pages.nist.gov/CONTAM-apps/webapps/contam_results_exporter/index.htm`, 2022. Accessed: 22/10/2022.

NIST. NIST CONTAM Input Data. `https://www.nist.gov/el/energy-and-environment-division-73200/nist-multizone-modeling/software/contam/input-data`, 2023a. Accessed: 17/05/2023.

NIST. NIST CONTAM Weather File Creator 2.0. `https://www.nist.gov/el/energy-and-environment-division-73200/nist-multizone-modeling/software/contam-weather-file`, 2023b. Accessed: 17/05/2023.

C. Noakes, P. Sleigh, A. Escombe, and C. Beggs. Use of CFD analysis in modifying a TB ward in Lima, Peru. *Indoor and Built Environment*, 15(1):41–47, 2006a.

C. J. Noakes and P. A. Sleigh. Mathematical models for assessing the role of airflow on the risk of airborne infection in hospital wards. *Journal of the Royal Society Interface*, 6, dec 2009.

C. J. Noakes, C. B. Beggs, P. A. Sleigh, and K. G. Kerr. Modelling the transmission of airborne infections in enclosed spaces. *Epidemiology and Infection*, 134(5):1082–1091, oct 2006b.

C. J. Noakes, M. A. I. Khan, and C. A. Gilkeson. Modeling infection risk and energy use of upper-room ultraviolet germicidal irradiation systems in multi-room environments. *Science and Technology for the Built Environment*, 21(1):99–111, 2015.

Office for National Statistics (ONS). Deaths registered in England and Wales: 2022. Statistical Bulletin: `https://www.ons.gov.uk/peoplepopulationandcommunity/birthsdeathsandmarriages/deaths/bulletins/deathsregistrationsummarytables/2022`, 2023. Released: 15/12/2023; Accessed: 03/07/2024.

H. P. Oswin, A. E. Haddrell, M. Otero-Fernandez, J. F. Mann, T. A. Cogan, T. G. Hilditch, J. Tian, D. A. Hardy, D. J. Hill, A. Finn, et al. The dynamics of SARS-CoV-2 infectivity with changes in aerosol microenvironment. *Proceedings of the National Academy of Sciences*, 119(27):e2200109119, 2022.

H. Pang, E. Lambertini, R. L. Buchanan, D. W. Schaffner, and A. K. Pradhan. Quantitative microbial risk assessment for Escherichia coli O157: H7 in fresh-cut lettuce. *Journal of food protection*, 80(2):302–311, 2017.

S. K. Pani, N.-H. Lin, and S. RavindraBabu. Association of COVID-19 pandemic with meteorological parameters over Singapore. *Science of the Total Environment*, 740: 140112, 2020.

J. Pantelic and K. W. Tham. Assessment of the mixing air delivery system ability to protect occupants from the airborne infectious disease transmission using Wells–Riley approach. *Hvac&R Research*, 18(4):562–574, 2012.

S. Park, Y. Choi, D. Song, and E. K. Kim. Natural ventilation strategy and related issues to prevent coronavirus disease 2019 (COVID-19) airborne transmission in a school building. *Science of the total environment*, 789:147764, 2021.

S. Parker, C. Coffey, J. Gravesen, J. Kirkpatrick, K. Ratcliffe, B. Lingard, and J. Nally. Contaminant ingress into multizone buildings: An analytical state-space approach. In *Building Simulation*, volume 7, pages 57–71, 2014.

B. Pavilonis, A. M. Ierardi, L. Levine, F. Mirer, and E. A. Kelvin. Estimating aerosol transmission risk of SARS-CoV-2 in New York City public schools during reopening. *Environmental Research*, 195:110805, 2021.

L. F. Pease, N. Wang, T. I. Salsbury, R. M. Underhill, J. E. Flaherty, A. Vlachokostas, G. Kulkarni, and D. P. James. Investigation of potential aerosol transmission and infectivity of SARS-CoV-2 through central ventilation systems. *Building and Environment*, 197:107633, 2021.

S. Peng, Q. Chen, and E. Liu. The role of computational fluid dynamics tools on investigation of pathogen transmission: Prevention and control. *Science of The Total Environment*, page 142090, 2020.

Z. Peng, A. P. Rojas, E. Kropff, W. Bahnfleth, G. Buonanno, S. J. Dancer, J. Kurnitski, Y. Li, M. G. Loomans, L. C. Marr, et al. Practical indicators for risk of airborne transmission in shared indoor environments and their application to COVID-19 outbreaks. *Environmental science & technology*, 56(2):1125–1137, 2022.

F. Pérez-Rodríguez, A. Valero, E. Carrasco, R. M. García, and G. Zurera. Understanding and modelling bacterial transfer to foods: A review. *Trends in Food Science & Technology*, 19(3):131–144, 2008.

A. Persily and L. de Jonge. Carbon dioxide generation rates for building occupants. *Indoor air*, 27(5):868–879, 2017.

A. K. Persily and E. M. Ivy. Input data for multizone airflow and IAQ analysis. 2001.

N. Pica and N. M. Bouvier. Environmental factors affecting the transmission of respiratory viruses. *Current opinion in virology*, 2(1):90–95, 2012.

J. Piret and G. Boivin. Pandemics throughout history. *Frontiers in microbiology*, 11: 631736, 2021.

B. Polidoro, L. C. Ng, W. S. Dols, et al. Contam results export tool. *Technical Note-1912. Gaithersburg, MD: National Institute of Standards and Technology*, 2016.

K. A. Prather, L. C. Marr, R. T. Schooley, M. A. McDiarmid, M. E. Wilson, and D. K. Milton. Airborne transmission of SARS-CoV-2. *Science*, 370(6514):303–304, 2020.

J. C. Pringle, J. Leikauskas, S. Ransom-Kelley, B. Webster, S. Santos, H. Fox, S. Marcoux, P. Kelso, and N. Kwit. COVID-19 in a correctional facility employee following multiple brief exposures to persons with COVID-19—Vermont, July–August 2020. *Morbidity and Mortality Weekly Report*, 69(43):1569, 2020.

H. Qian, Y. Li, P. V. Nielsen, C.-E. Hyldgaard, T. W. Wong, and A. Chwang. Dispersion of exhaled droplet nuclei in a two-bed hospital ward with three different ventilation systems. *Indoor air*, 16(2):111–128, 2006.

H. Qian, Y. Li, P. V. Nielsen, and X. Huang. Predicting spatial distribution of infection risk of airborne transmission diseases in a hospital ward. In *Proceedings of healthy buildings*, 2007.

H. Qian, Y. Li, P. V. Nielsen, and X. Huang. Spatial distribution of infection risk of SARS transmission in a hospital ward. *Building and Environment*, 44(8):1651–1658, 2009.

H. Qian, Y. Li, W. Seto, P. Ching, W. Ching, and H. Sun. Natural ventilation for reducing airborne infection in hospitals. *Building and Environment*, 45(3):559–565, 2010.

F. Y. Ramírez-Castillo, A. Loera-Muro, M. Jacques, P. Garneau, F. J. Avelar-González, J. Harel, and A. L. Guerrero-Barrera. Waterborne pathogens: Detection methods and challenges. *Pathogens*, 4(2):307–334, 2015.

R. Reichman and Y. Dubowski. Gaseous pollutant transport from an underground parking garage in a Mediterranean multi-story building — Effect of temporal resolution under varying weather conditions. In *Building Simulation*, volume 14, pages 1511–1523, 2021.

P. L. Remington, W. N. Hall, I. H. Davis, A. Herald, and R. A. Gunn. Airborne transmission of measles in a physician's office. *Jama*, 253(11):1574–1577, 1985.

J. Ren, Y. Wang, Q. Liu, and Y. Liu. Numerical study of three ventilation strategies in a prefabricated COVID-19 inpatient ward. *Building and Environment*, 188:107467, 2021.

E. Riley, G. Murphy, and R. Riley. Airborne spread of measles in a suburban elementary school. *American journal of epidemiology*, 107(5):421–432, 1978.

S. Robertson, S. D. Lawn, A. Welte, L.-G. Bekker, and R. Wood. Tuberculosis in a South African prison - A transmission modelling analysis. *South African Medical Journal*, 101(11):809–813, 2011.

L. Rocha-Melogno, K. Crank, M. H. Bergin, G. C. Gray, K. Bibby, and M. A. Deshusses. Quantitative risk assessment of COVID-19 aerosol transmission indoors: A mechanistic stochastic web application. *Environmental Technology*, pages 1–12, 2021.

B. R. Rowe, A. Canosa, A. Meslem, and F. Rowe. Increased airborne transmission of COVID-19 with new variants, implications for health policies. *Building and environment*, page 109132, 2022.

S. Rudnick and D. Milton. Risk of indoor airborne infection transmission estimated from carbon dioxide concentration. *Indoor air*, 13(3):237–245, 2003.

U. Ryan, N. Hijjawi, and L. Xiao. Foodborne cryptosporidiosis. *International journal for parasitology*, 48(1):1–12, 2018.

M. Sadyś. Effects of wind speed and direction on monthly fluctuations of Cladosporium conidia concentration in the air. *Aerobiologia*, 33(3):445–456, 2017.

SAGE. EMG/Transmission Group/SPI-B: COVID-19 Transmission in Hotels and Managed Quarantine Facilities (MQFs). https://www.gov.uk/government/publications/emg-covid-19-transmission-in-hotels-and-managed-quarantine-facilities-mqfs-9-september-2021, 2021.

S. Sampath, A. Khedr, S. Qamar, A. Tekin, R. Singh, R. Green, and R. Kashyap. Pandemics throughout the history. *Cureus*, 13(9), 2021.

G. Scheuch. Breathing is enough: For the spread of influenza virus and SARS-CoV-2 by breathing only. *Journal of aerosol medicine and pulmonary drug delivery*, 33(4): 230–234, 2020.

W. Seto. Airborne transmission and precautions: Facts and myths. *Journal of Hospital Infection*, 89(4):225–228, 2015.

Y. Shang, J. Dong, L. Tian, F. He, and J. Tu. An improved numerical model for epidemic transmission and infection risks assessment in indoor environment. *Journal of Aerosol Science*, 162:105943, 2022.

K.-W. Shi, C.-W. Wang, and S. C. Jiang. Quantitative microbial risk assessment of Greywater on-site reuse. *Science of the Total Environment*, 635:1507–1519, 2018.

C. A. Short, C. J. Noakes, C. A. Gilkeson, and A. Fair. Functional recovery of a resilient hospital type. *Building Research & Information*, 42(6):657–684, 2014.

P. Shrestha, J. W. DeGraw, M. Zhang, and X. Liu. Multizonal modeling of SARS-CoV-2 aerosol dispersion in a virtual office building. *Building and Environment*, 206:108347, 2021.

A. J. Shrimpton, J. Brown, T. Cook, C. Penfold, J. P. Reid, and A. E. Pickering. Quantitative evaluation of aerosol generation from upper airway suctioning assessed during tracheal intubation and extubation sequences in anaesthetized patients. *Journal of Hospital Infection*, 124:13–21, 2022.

J. A. Soller, M. E. Schoen, T. Bartrand, J. E. Ravenscroft, and N. J. Ashbolt. Estimated human health risks from exposure to recreational waters impacted by human and non-human sources of faecal contamination. *Water research*, 44(16):4674–4691, 2010.

S. Stelzer-Braid, B. G. Oliver, A. J. Blazey, E. Argent, T. P. Newsome, W. D. Rawlinson, and E. R. Tovey. Exhalation of respiratory viruses by breathing, coughing, and talking. *Journal of medical virology*, 81(9):1674–1679, 2009.

L. G. Stensballe, J. K. Devasundaram, and E. A. SIMOES. Respiratory syncytial virus epidemics: The ups and downs of a seasonal virus. *The Pediatric infectious disease journal*, 22(2):S21–S32, 2003.

R. Sturm. Stochastic modeling of particle deposition in lungs of cystic fibrosis patients. *International Scholarly Research Notices*, 2011, 2011.

C. Sun and Y.-H. Hsieh. Global analysis of an SEIR model with varying population size and vaccination. *Applied Mathematical Modelling*, 34(10):2685–2697, 2010.

C. Sun and Z. Zhai. The efficacy of social distance and ventilation effectiveness in preventing COVID-19 transmission. *Sustainable cities and society*, 62:102390, 2020.

M. Swami and S. Chandra. Correlations for pressure distribution on buildings and calculation of natural-ventilation airflow. *ASHRAE transactions*, 94(1):243–266, 1988.

G. N. Sze To and C. Y. H. Chao. Review and comparison between the Wells–Riley and dose-response approaches to risk assessment of infectious respiratory diseases. *Indoor air*, 20(1):2–16, 2010.

J. W. Tang, P. Wilson, N. Shetty, and C. J. Noakes. Aerosol-transmitted infections — A new consideration for public health and infection control teams. *Current treatment options in infectious diseases*, 7(3):176–201, 2015.

K.-A. Thompson, J. V. Pappachan, A. M. Bennett, H. Mittal, S. Macken, B. K. Dove, J. S. Nguyen-Van-Tam, V. R. Copley, S. O'Brien, P. Hoffman, et al. Influenza aerosols in UK hospitals during the H1N1 (2009) pandemic - The risk of aerosol generation during medical procedures. *PloS one*, 8(2):e56278, 2013.

W. Timpitak and N. Pochai. A mathematical model of risk assessment on airborne infection in a room with an outlet ventilation system. *Engineering Letters*, 30(2), 2022.

Y.-C. Tung and S.-C. Hu. Infection risk of indoor airborne transmission of diseases in multiple spaces. *Architectural Science Review*, 51(1):14–20, 2008.

UK Health Security Agency. UKHSA Advisory Board: Preparedness for infectious disease threats. `https://www.gov.uk/government/publications/ukhsa-board-meeting-papers-january-2023/ukhsa-advisory-board-preparedness-for-infectious-disease-threats`, 2023. Released: 24/01/2023; Accessed: 05/07/2024.

S. Verma, M. Dhanak, and J. Frankenfield. Visualizing the effectiveness of face masks in obstructing respiratory jets. *Physics of Fluids*, 32(6):061708, 2020.

C. Vouriot, H. Burridge, C. Noakes, and P. Linden. Seasonal variation in airborne infection risk in schools due to changes in ventilation inferred from monitored carbon dioxide. *Indoor Air*, 31(4):1154–1163, 2021.

C. C. Wang, K. A. Prather, J. Sznitman, J. L. Jimenez, S. S. Lakdawala, Z. Tufekci, and L. C. Marr. Airborne transmission of respiratory viruses. *Science*, 373(6558): eabd9149, 2021.

L. L. Wang, W. S. Dols, and Q. Chen. Using CFD capabilities of CONTAM 3.0 for simulating airflow and contaminant transport in and around buildings. *Hvac&R Research*, 16(6):749–763, 2010.

X. Wang, S. Ma, B. Zhao, G. Deng, H. She, K. Xu, L. Hao, Y. Deng, Q. Li, Z. Yu, et al. Correlations between the viral loads and symptoms in the SARS-CoV-2-infected patients. *MedComm*, 4(4), 2023.

Z. Wang, E. R. Galea, A. Grandison, J. Ewer, and F. Jia. A coupled Computational Fluid Dynamics and Wells-Riley model to predict COVID-19 infection probability for passengers on long-distance trains. *Safety science*, 147:105572, 2022.

D. D. Weber and R. J. Kearney. Natural convective heat transfer through an aperture in passive solar heated buildings. *In proceedings of 5th National Passive Solar Conference, ASES*, pages 1037–1041, 1980.

W. F. Wells. On air-borne infection: Study II. Droplets and droplet nuclei. *American journal of Epidemiology*, 20(3):611–618, 1934.

W. F. Wells et al. Airborne contagion and air hygiene. an ecological study of droplet infections. *Airborne Contagion and Air Hygiene. An Ecological Study of Droplet Infections.*, 1955.

C. M. Williams, M. Abdulwhhab, S. S. Birring, E. De Kock, N. J. Garton, E. Townsend, M. Pareek, A. Al-Taie, J. Pan, R. Ganatra, et al. Exhaled Mycobacterium tuberculosis output and detection of subclinical disease by face-mask sampling: Prospective observational studies. *The Lancet Infectious Diseases*, 20(5):607–617, 2020.

A. M. Wilson, M.-F. King, M. López-García, I. J. Clifton, J. Proctor, K. A. Reynolds, and C. J. Noakes. Effects of patient room layout on viral accruement on healthcare professionals' hands. *Indoor air*, 31(5):1657–1672, 2021a.

A. M. Wilson, M. H. Weir, S. F. Bloomfield, E. A. Scott, and K. A. Reynolds. Modeling COVID-19 infection risks for a single hand-to-fomite scenario and potential risk reductions offered by surface disinfection. *American journal of infection control*, 49(6): 846–848, 2021b.

A. M. Wilson, K. Canter, S. E. Abney, C. P. Gerba, E. R. Myers, J. Hanlin, and K. A. Reynolds. An application for relating legionella shower water monitoring results to estimated health outcomes. *Water Research*, 221:118812, 2022.

J. Wilson, G. Carson, S. Fitzgerald, M. J. Llewelyn, D. Jenkins, S. Parker, A. Boies, J. Thomas, K. Sutcliffe, A. Sowden, et al. Are medical procedures that induce coughing or involve respiratory suctioning associated with increased generation of aerosols and risk of SARS-CoV-2 infection? A rapid systematic review. *Journal of Hospital Infection*, 116:37–46, 2021c.

N. Wilson, C. Calabria, A. Warren, A. Finlay, A. O'Donovan, G. Passerello, N. Ribaric, P. Ward, R. Gillespie, R. Farrel, et al. Quantifying hospital environmental ventilation using carbon dioxide monitoring - A multicentre study. *Anaesthesia*, 79(2):147–155, 2024.

T.-w. Wong, C.-k. Lee, W. Tam, J. T.-f. Lau, T.-s. Yu, S.-f. Lui, P. K. Chan, Y. Li, J. S. Bresee, J. J. Sung, et al. Cluster of SARS among medical students exposed to single patient, Hong Kong. *Emerging infectious diseases*, 10(2):269, 2004.

S. G. Wood, J. Craske, and H. C. Burridge. Relating quanta conservation and compartmental epidemiological models of airborne disease outbreaks in buildings. *Scientific Reports*, 13(1):17335, 2023.

World Health Organization. *International travel and health: Situation as on 1 January 2012*. World Health Organization, 2012.

World Health Organization. The top 10 causes of death. `https://www.who.int/news-room/fact-sheets/detail/the-top-10-causes-of-death`, 2020. Released: 09/12/2020; Accessed: 05/07/2024.

World Health Organization. Global technical consultation report on proposed terminology for pathogens that transmit through the air. Technical report, Geneva, 2024.

Z. Xia, H. Guan, Z. Qi, and P. Xu. Multi-Zone Infection Risk Assessment Model of Airborne Virus Transmission on a Cruise Ship Using CONTAM. *Buildings*, 13(9): 2350, 2023.

C. Yan, Z.-c. Gui, and J.-t. Wu. Quantitative microbial risk assessment of bioaerosols in a wastewater treatment plant by using two aeration modes. *Environmental Science and Pollution Research*, 28:8140–8150, 2021.

S. Yan, L. Wang, M. J. Birnkrant, Z. Zhai, and S. L. Miller. Multizone Modeling of Airborne SARS-CoV-2 Quanta Transmission and Infection Mitigation Strategies in Office, Hotel, Retail, and School Buildings. *Buildings*, 13(1):102, 2022a.

S. Yan, L. L. Wang, M. J. Birnkrant, J. Zhai, and S. L. Miller. Evaluating SARS-CoV-2 airborne quanta transmission and exposure risk in a mechanically ventilated multizone office building. *Building and Environment*, page 109184, 2022b.

C. Younes, C. A. Shdid, and G. Bitsuamlak. Air infiltration through building envelopes: A review. *Journal of Building physics*, 35(3):267–302, 2012.

C. Zemouri, S. Awad, C. Volgenant, W. Crielaard, A. Laheij, and J. De Soet. Modeling of the transmission of coronaviruses, measles virus, influenza virus, Mycobacterium tuberculosis, and Legionella pneumophila in dental clinics. *Journal of Dental Research*, 99(10):1192–1198, 2020.

Z. Zhai and H. Li. Distributed probability of infection risk of airborne respiratory diseases. *Indoor and Built Environment*, page 1420326X211030324, 2021.

S. Zhang and Z. Lin. Dilution-based evaluation of airborne infection risk - Thorough expansion of Wells-Riley model. *Building and Environment*, 194:107674, 2021.

X. Zhang, Z. Ji, Y. Yue, H. Liu, and J. Wang. Infection risk assessment of COVID-19 through aerosol transmission: A case study of South China seafood market. *Environmental science & technology*, 55(7):4123–4133, 2020.

X. Zhao, S. Liu, Y. Yin, T. Zhang, and Q. Chen. Airborne transmission of COVID-19 virus in enclosed spaces: An overview of research methods. *Indoor air*, 32(6):e13056, 2022.

S. Zhu, S. Jenkins, K. Addo, M. Heidarinejad, S. A. Romo, A. Layne, J. Ehizibolo, D. Dalgo, N. W. Mattise, F. Hong, et al. Ventilation and laboratory confirmed acute respiratory infection (ARI) rates in college residence halls in College Park, Maryland. *Environment international*, 137:105537, 2020.